

# MHD Models of Relativistic Magnetic Reconnection

Matthew Tanguy Bohan

Submitted in accordance with the requirements for the degree of Doctor  
of Philosophy

The University of Leeds  
Department of Applied Mathematics

September 2009

The candidate confirms that the work submitted is his own and that appropriate credit has been given where reference has been made to the work of others. This copy has been supplied on the understanding that it is copyright material and that no quotation from the thesis may be published without proper acknowledgement.

# Abstract

There has been mounting evidence over the last few years that magnetic reconnection is powering high energy emissions from many relativistic astrophysical objects. These include black hole magnetospheres, active galactic nuclei and magnetars. The emissions from magnetars currently show the strongest evidence with quiescent periods followed by short rise times of the flares.

If this is combined with the recent development of a relativistic resistive magnetohydrodynamical code by Komissarov, it is an opportune time for relativistic magnetohydrodynamical models of magnetic reconnection. The two main types of reconnection to be studied are the tearing mode and Petschek reconnection. Both are expected to be analogous to the reconnection found in solar flares with magnetic energy being released with very short rise times due to a resistive instability.

The relativistic tearing mode is an instability found in current sheets and is investigated analytically by the reproduction of order of magnitude calculations and the linear analysis of the tearing mode for magnetodynamics. This is used to analyse the results of numerical simulations.

Relativistic Petschek reconnection is caused by a small area of anomalous resistivity giving a much smaller reconnection region with magnetic energy also being released at shock waves as well as the reconnection region. This is investigated analytically by the reproduction of order of magnitude calculations. This is used to analyse the results of numerical simulations.

The results of both sets of simulations are discussed including their implications and suggestions for future work. The results and analyses are compared to observations of magnetars with good agreement.

For my family



“The sciences do not try to explain, they hardly even try to interpret, they mainly make models. By a model is meant a mathematical construct which, with addition of certain verbal interpretations, describes observed phenomena. The justification of such a mathematical construct is solely and precisely that it is expected to work.”

-John Von Neumann



# Acknowledgements

The author wishes to thank the following people:

Prof. Komissarov for his unwavering support and guidance,

Nick Camus and Dr. Barkov for their numerous discussions and time,

Dr. Boxall for proof reading this document,

Christian Groh for his advice in presenting this document,

Sam Peck for his statistical advice and general support,

and Prof.'s Lyubarsky and Lyutikov for their correspondence.





# Contents

Abstract . . . . .	ii
Dedication . . . . .	iii
Quote . . . . .	v
Acknowledgements . . . . .	vii
Contents . . . . .	ix
List of figures . . . . .	xiv
List of tables . . . . .	xxi
<b>1 Introduction</b>	<b>1</b>
1.1 Magnetic reconnection and its development . . . . .	1
1.2 Magnetars and Blazars . . . . .	5
1.3 Motivation . . . . .	8
1.4 Dimensionless parameters . . . . .	10
1.5 Important works in relativistic magnetic reconnection . . . . .	14
1.5.1 Steady state relativistic Sweet Parker reconnection . . . . .	14
1.5.2 The tearing mode in relativistic force-free electrodynamics . . . . .	17

1.5.3	Order of magnitude calculations of relativistic Sweet Parker and Petschek reconnection . . . . .	21
1.6	Alternative models to study relativistic magnetic reconnection . . . . .	22
1.6.1	Hall magnetohydrodynamics . . . . .	22
1.6.2	Plasma kinetics . . . . .	24
1.7	Aims of the thesis . . . . .	25
<b>2</b>	<b>The model</b>	<b>27</b>
2.1	The equations . . . . .	27
2.2	Conservation laws . . . . .	31
<b>3</b>	<b>Numerics</b>	<b>35</b>
3.1	Conservative methods . . . . .	35
3.2	The Riemann problem and Godunov's method . . . . .	37
3.2.1	The Riemann problem . . . . .	37
3.2.2	Godunov's method . . . . .	40
3.3	The no magnetic monopole condition . . . . .	42
3.3.1	Augmented system . . . . .	43
3.3.2	Constrained transport . . . . .	46
3.3.3	Comparison of the augmented system and constrained transport . . . . .	47
3.4	The stiff, resistive term . . . . .	47
3.5	Implementation of the code . . . . .	50

3.6	Convergence of the solution . . . . .	53
3.6.1	The relativistic tearing mode . . . . .	54
3.6.2	Relativistic Petschek reconnection . . . . .	58
3.7	Boundary conditions, domain size and Courant number . . . . .	62
3.7.1	The relativistic tearing mode . . . . .	62
3.7.2	Relativistic Petschek reconnection . . . . .	63
3.8	Limitations . . . . .	64
3.9	Conversion to dimensional results . . . . .	67
<b>4</b>	<b>The relativistic tearing mode</b>	<b>69</b>
4.1	Mathematics of the relativistic Sweet-Parker current sheet and tearing mode	69
4.1.1	An order of magnitude calculation for the relativistic Sweet-Parker current sheet . . . . .	70
4.1.2	Analysis of the relativistic tearing mode . . . . .	75
4.2	Numerical Simulations . . . . .	88
4.2.1	The numerical model . . . . .	88
4.2.2	Physical description of the relativistic tearing mode and its structure	98
4.2.3	Linear growth rates of the relativistic tearing mode . . . . .	102
4.2.4	Dispersion relations of the relativistic tearing mode . . . . .	106
4.2.5	Comparison of the linear growth rates to the observations of flare rise times in Magnetars . . . . .	114

4.2.6	The non-linear development of the relativistic tearing mode and comparison of the relativistic tearing mode in magnetohydrodynamics to magnetodynamics . . . . .	117
4.2.7	Comparison of the simulations with the theoretically predicted values for the relativistic tearing mode . . . . .	124
4.2.8	The reconnection electric field . . . . .	125

## **5 Relativistic Petschek reconnection 133**

5.1	An order of magnitude calculation for relativistic Petschek reconnection .	133
5.1.1	Jump conditions for a slow shock . . . . .	134
5.1.2	The reconnection region . . . . .	140
5.1.3	Relativistic Petschek reconnection with $B_z \neq 0$ . . . . .	142
5.2	Numerical simulations . . . . .	145
5.2.1	The numerical model . . . . .	145
5.2.2	Physical description and structure of relativistic Petschek reconnection . . . . .	148
5.2.3	Motivation and organisation of the regimes investigated for relativistic Petschek reconnection . . . . .	151
5.2.4	Anti-parallel relativistic Petschek reconnection . . . . .	157
5.2.5	Relativistic Petschek reconnection with a small $B_z \neq 0$ component, where $2\alpha\sqrt{\zeta} \approx 1$ . . . . .	160
5.2.6	Comparison of relativistic Petschek reconnection for different relativistic Lundquist numbers . . . . .	173

5.2.7	Relativistic Petschek reconnection with a small $B_z \neq 0$ component, where $\alpha \ll 1/2\sqrt{\zeta}$ . . . . .	175
5.2.8	The reconnection electric field . . . . .	178
5.2.9	Relativistic Petschek reconnection with a large $B_z \neq 0$ component, where $\alpha \gg 1/2\sqrt{\zeta}$ . . . . .	182
5.2.10	Comparison of the Poynting and kinetic energy fluxes for the different values of $\alpha$ . . . . .	183
<b>6</b>	<b>Discussion</b>	<b>185</b>
6.1	A summary of the research into magnetohydrodynamical models of relativistic reconnection . . . . .	185
6.2	The relativistic tearing mode . . . . .	188
6.3	Relativistic Petschek reconnection . . . . .	193
6.4	Future research . . . . .	198
	<b>Appendix</b>	<b>200</b>
A	Estimation of the relativistic Lundquist number for magnetars . . . . .	201
B	Estimation of the magnetisation parameter for magnetars . . . . .	204
C	Estimation of the plasma beta for magnetars . . . . .	206
	<b>Bibliography</b>	<b>208</b>



# List of figures

1.1	A sketch diagram of magnetic reconnection . . . . .	2
3.1	The fan of the waves emanating from the origin for each eigenvalue of an $m$ - dimensional system . . . . .	40
3.2	Grid convergence for different spatial resolutions . . . . .	55
3.3	Details of grid convergence . . . . .	56
3.4	Comparison of uniform and non-uniform grids . . . . .	57
3.5	A comparison of the reconnection electric field $E^* = \mathbf{E}(0, 0)$ for different resolutions in the $y$ direction . . . . .	59
3.6	The $v_x$ component of the velocity showing the central outflow velocity and the undesired flow along the boundary . . . . .	60
3.7	The $v_x$ velocities for the different resolutions along the boundary . . . . .	61
3.8	A magnified view of the $v_x$ velocities for the different resolutions along the boundary . . . . .	61
3.9	The plasma pressure along the top boundary . . . . .	62
4.1	A sketch diagram of the relativistic Sweet-Parker current sheet . . . . .	71

4.2	Quasi-equilibrium variables for a current sheet . . . . .	91
4.3	Comparison of the growth rate of the perturbation of the standard case with $\lambda = 12$ for periodic and free flow boundary conditions and for a Harris current sheet . . . . .	94
4.4	The initial set-up of the plasma pressures for a Harris current sheet . . . .	94
4.5	A current sheet undergoing the relativistic tearing mode reconnection . .	100
4.6	Secondary tearing . . . . .	101
4.7	The variables in the linear growth phase of the current sheet . . . . .	103
4.8	The $B_y$ perturbation to the background state in the linear growth phase of the relativistic tearing mode . . . . .	104
4.9	Linear growth rates for $\eta = 10^{-3}$ . . . . .	105
4.10	Linear growth rates for $\eta = 10^{-4}$ . . . . .	105
4.11	Linear growth rates for $\beta = 0.1$ . . . . .	107
4.12	Linear growth rates for $\beta = 0.05$ . . . . .	107
4.13	Linear growth rates for the isothermal case . . . . .	108
4.14	Linear growth rates for the magnetisation parameter of $\varsigma = 1.25$ with state variables $\rho_0 = 0.5$ and $p_0 = 0.1$ . . . . .	108
4.15	The linear regime, including the settling period, for $\lambda = 4$ , $\eta = 10^{-3}$ and $\beta = 0.32$ for perturbation amplitudes of $10^{-3}$ and $10^{-5}$ , with the initial perturbation subtracted from the solutions for comparison . . . . .	109
4.16	The linear regime, including the settling period, for $\lambda = 4$ , $\eta = 10^{-3}$ and $\beta = 0.1$ for perturbation amplitudes of $10^{-3}$ and $10^{-5}$ , with the initial perturbation subtracted from the solutions for comparison . . . . .	109



4.17	The linear regime, including the settling period, for $\lambda = 4$ , $\eta = 10^{-3}$ and $\beta = 0.05$ for perturbation amplitudes of $10^{-3}$ and $10^{-5}$ , with the initial perturbation subtracted from the solutions for comparison . . . . .	110
4.18	Growth rate as a function of wavelength for various plasma betas and isothermal cases . . . . .	111
4.19	Growth rate as a function of wavelength for $\eta = 10^{-3}$ and $10^{-4}$ . . . . .	112
4.20	Growth rate as a function of wavelength with state variables $p_0 = \rho_0 = 0.1$ with $\varsigma = 6.25$ and $\rho_0 = 0.5$ , $p_0 = 0.1$ with $\varsigma = 1.25$ . . . . .	113
4.21	A sketch diagram of the magnetic field of a magnetar before a flare . . . .	115
4.22	Saturation of the perturbation for a resistivity of $\eta = 10^{-3}$ and plasma beta of $\beta = 0.32$ . . . . .	118
4.23	The standard case with wavelength 4 and the perturbation applied at time 11.501 . . . . .	119
4.24	The early behaviour of the perturbation applied at time 11.501 . . . . .	119
4.25	Comparison of perturbation values to determine the onset of saturation of the perturbation . . . . .	121
4.26	Convergence of growth rates to the isothermal case for decreasing plasma betas compared to the magnetodynamical case . . . . .	122
4.27	Extrapolation of the plasma beta to zero at time 61.194 from figure 4.26 . .	123
4.28	Evolution of the reconnection electric field for various plasma betas . . .	128
4.29	Evolution of the reconnection electric field for the isothermal case . . . .	128
4.30	Evolution of the reconnection electric field for $\eta = 10^{-4}$ . . . . .	129

4.31	Evolution of the reconnection electric field for state variables $p_0 = \rho_0 = 0.1$ with $\varsigma = 6.25$ and $\rho_0 = 0.5$ , $p_0 = 0.1$ with $\varsigma = 1.25$ . . . . .	129
4.32	A comparison of the structure of an X-point and an O-point . . . . .	130
5.1	A sketch diagram of relativistic Petschek reconnection . . . . .	134
5.2	Early evolution of relativistic Petschek reconnection . . . . .	149
5.3	Later evolution of relativistic Petschek reconnection . . . . .	150
5.4	The hydrodynamical variables for relativistic Petschek reconnection . . .	152
5.5	The magnetic field for relativistic Petschek reconnection . . . . .	153
5.6	The electric field and current density for relativistic Petschek reconnection	154
5.7	The plasma pressure at time 24.754 for anti-parallel relativistic Petschek reconnection when the resolution has been halved in both directions . . .	154
5.8	A zoomed in image of the relativistic slow shocks for the velocity and magnetic fields for relativistic Petschek reconnection . . . . .	155
5.9	The resolution in the $y$ direction across the current sheet . . . . .	158
5.10	A comparison of the plasma pressures along the $x$ -axis for 50 and 100 grid points per unit length . . . . .	159
5.11	Comparison of the plasma pressure at time 30.945 for values of $\alpha$ of $\pi/12$ , $\pi/6$ and $\pi/4$ . . . . .	162
5.12	Comparison of the plasma pressure at time 30.945 for values of $\alpha$ of $\pi/3$ and $5\pi/12$ . . . . .	163
5.13	The plasma pressure, density and charge density for relativistic Petschek reconnection when $\alpha = \pi/12$ . . . . .	164

5.14	The three components of the velocity field for relativistic Petschek reconnection when $\alpha = \pi/12$ . . . . .	165
5.15	The three components of the magnetic field for relativistic Petschek reconnection when $\alpha = \pi/12$ . . . . .	166
5.16	The three components of the electric field for relativistic Petschek reconnection when $\alpha = \pi/12$ . . . . .	167
5.17	The three components of the velocity field for relativistic Petschek reconnection with $\alpha = \pi/6$ . . . . .	169
5.18	The three components of the magnetic field for relativistic Petschek reconnection with $\alpha = \pi/6$ . . . . .	170
5.19	Indication of the rotational shock . . . . .	171
5.20	The three components of the velocity field for relativistic Petschek reconnection with $\alpha = \pi/6$ and $L_u = 16 \times 10^2$ . . . . .	176
5.21	The three components of the magnetic field for relativistic Petschek reconnection with $\alpha = \pi/6$ and $L_u = 16 \times 10^2$ . . . . .	177
5.22	Evolution of the reconnection electric field $E^*$ , of anti-parallel and $\alpha \ll 1/2\sqrt{\zeta}$ for relativistic Petschek reconnection . . . . .	180
5.23	Evolution of the reconnection electric field $E^*$ for relativistic Petschek reconnection with different Lundquist numbers . . . . .	180
5.24	Evolution of the reconnection electric field $E^*$ for relativistic Petschek reconnection with $2\alpha\sqrt{\zeta} \sim 1$ and larger . . . . .	181
5.25	Outflow velocity along the $y$ axis where the outflow velocity is plotted along the $y$ axis at time 61.846 for $\alpha = \pi/4, \pi/3$ and $5\pi/12$ . . . . .	182

5.26 Comparison of the Poynting flux and kinetic flux in the outflow when	
$\alpha \ll 1/2\sqrt{\varsigma}$ and when $2\alpha\sqrt{\varsigma} \sim 1$ . . . . .	184

# List of tables

1.1	A table of dimensionless parameters . . . . .	13
4.1	Values of the relativistic Lundquist number for given values of $\eta$ . . . . .	95
4.2	Values of the background Alfvén speed, Lorentz factor and magnitude of the magnetic field for a given $\beta$ . . . . .	97
4.3	The magnetisation parameter for different values of the plasma beta . . . . .	98
4.4	The fastest growth rates of the relativistic tearing mode . . . . .	116
4.5	Agreement of numerical simulations with Lyubarsky’s prediction of $v_{in} = L_u^{-1}$ . . . . .	125
4.6	A table of the outflow velocity and Lorentz factor for the fastest growing modes of each case . . . . .	126
5.1	A table comparing the predictions for anti-parallel relativistic Petschek reconnection with simulations . . . . .	160
5.2	A table comparing the predictions and simulations for relativistic Petschek reconnection with magnetic field lines not anti-parallel with simulations . . . . .	173

5.3 A table comparing the predictions and simulations for relativistic Petschek reconnection for  $\alpha = \frac{\pi}{6}$  for external Lundquist numbers of  $S_u = 16 \times 10^2$  and  $12 \times 10^3$  . . . . . 174

5.4 A table comparing predictions and simulations of relativistic Petschek reconnection in the regime  $\alpha \ll 1/2\sqrt{\zeta}$  with  $\alpha = 5^\circ$  . . . . . 178

# Chapter 1

## Introduction

The introduction is split into three sections: a short background on magnetic reconnection giving its historical setting, general information on magnetars and the motivation and application of the research.

### 1.1 Magnetic reconnection and its development

Magnetic reconnection is a topological change of the structure of the magnetic field where magnetic field lines that are twisted and stretched break and reconnect with each other. This can release magnetic energy stored in the magnetic fields.

The basic idea is shown as a sketch in figure 1.1 where oppositely aligned magnetic field lines AC and CD move towards each other and reconnect to give the new field lines AB and CD which are retreating from each other.

Magnetic reconnection was first suggested in the 1940s as an effective method of releasing stored magnetic energy into kinetic energy or heating and was largely thought of in the context of solar physics. There were several developments over the intervening years

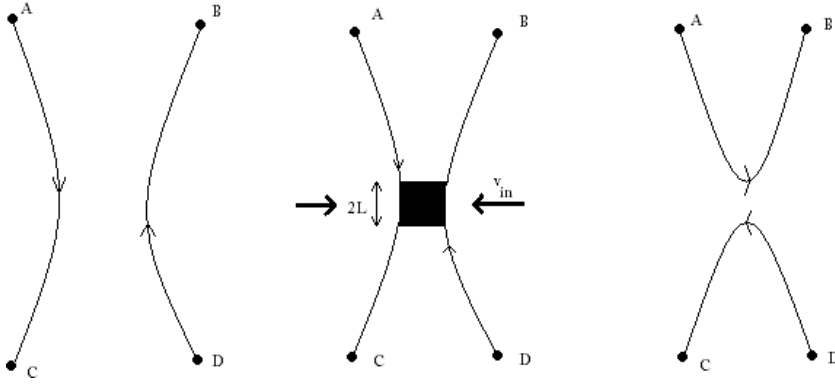


Figure 1.1: A sketch diagram of magnetic reconnection. From left to right: the field lines AC and BD approach each other, when close together approach each other with a velocity  $v_{in}$  and a current sheet (the shaded region) of length  $2L$  forms where the field lines will reconnect and after reconnection the field lines AB and CD retreat away from each other.

and Cowling’s review in [4] gives a pleasant overview of the early years of solar physics including the dynamo theory and the original ideas that led to magnetic reconnection.

The first major development happened in 1956 at a symposium held by the International Astronomical Union in Stockholm where Sweet presented his work on “The neutral point theory of solar flares” which is recorded in [44]. This was followed by a more mathematical work of Parker on Sweet’s mechanism [37]. Together with a final paper by Sweet [45], this provided the basis for the first model of reconnection using neutral points and long thin current sheets.

The Sweet-Parker model has a long thin current sheet (also known as the neutral line) of length  $2L$  and width  $2l$  between two regions of oppositely aligned magnetic fields. These create an inflow through the diffusive magnetic field being frozen to the plasma. Outside the current sheet the magnetic pressure is very high and is balanced inside by the plasma pressure. In the current sheet the sharp magnetic gradient inside the thin layer allows the resistivity to act on them and allows them to slip through the plasma and reconnect. When the magnetic field reconnects, the energy contained in it is transferred to



the plasma as kinetic energy (with some being converted into heat). The plasma pressure and tension force in the remaining magnetic field then cause the plasma inside the sheet to be evacuated, forming an outflow.

The inflow velocity therefore gives an estimate of how much magnetic flux is reconnected as it is transported into the current sheet. The setup is identical to that shown in figure 4.1 in chapter 4. If an order of magnitude calculation is made for the steady state, a measure of the reconnection rate is found to be

$$v_{in} = S_u^{-\frac{1}{2}}, \quad (1.1)$$

where  $S_u$  is the external relativistic Lundquist number (using the length scale  $L$ , of the current sheet). The derivation of this is not presented here as it is almost identical to the relativistic one presented in chapter 4, except that in the non-relativistic case the speed of light is replaced by the Alfvén speed. The derivation can be found in [39]. A point of note is that in the non-relativistic Sweet-Parker model, if a small perpendicular component of the magnetic field is present it will not affect the reconnection rate.

Linear analysis was done on the current sheets by Furth et al. in [11] and the tearing mode was one of three resistively driven instabilities identified. This is where long wavelengths cause a current sheet to split into multiple parallel filaments.

This is caused by the instability causing the current sheet to thin by a small perturbation to the magnetic field which grows and causes a strong magnetic tension force which pulls the magnetic field lines out along the current sheet. The thinning in the sheet is accompanied by the formation of magnetic islands. These can be stable forming a steady state (as found in simulations with periodic boundary conditions) or ejected as plasmoids which are closed rings of plasma containing plasma (as found in simulations with free flow boundary conditions). The growth of the perturbation will continue until non-linear terms become dominant. The tearing mode is important as it affects not just current sheets, but

sheared magnetic fields as well. The tearing mode is found to have a maximum growth rate  $\omega$ , of

$$\omega = (\tau_d \tau_a)^{-\frac{1}{2}}, \quad (1.2)$$

where  $\tau_d$  is the diffusive time scale and  $\tau_a$  is the Alfvén crossing time. The derivation of this is not presented here as it is almost identical to the derivation for magnetodynamics in chapter 4, except that in the non-relativistic case the speed of light is replaced by the Alfvén speed.

The next major event in the development of reconnection happened when Kantrowitz suggested to Petschek that energy could be liberated from the magnetic field not just at the reconnection region but at standing magnetohydrodynamic waves as well. This was presented in [38] and with standing switch-off shocks used to greatly reduce the reconnection region giving a greater rate of reconnection.

Petschek's model for reconnection has four standing switch-off shock waves (a type of slow shock) emanating from a much shorter current sheet. The shorter current sheet will be similar to the Sweet-Parker model and the plasma flow will be diffusely dominated. The increase in reconnection rate associated with Petschek reconnection will therefore come from the shock waves. Switch-off shocks get their name from taking the upstream magnetic field and leaving it perpendicular to the shock front downstream. The shocks propagate at the Alfvén speed into the medium and accelerate the plasma which passes through them to the Alfvén speed parallel to the shock front with the acceleration being powered by the drop in magnetic energy density across the shock. The setup is identical to that shown in figure 5.1 in chapter 5. A good introductory work on Petschek reconnection is presented in [51] by Uzdensky based on his talk given at the Petschek memorial symposium. Petschek reconnection is presented without too much technical detail and applications in different astrophysical situations.

From an order of magnitude calculation, an estimate of the reconnection rate for Petschek reconnection is found to be

$$M_e = \frac{\pi}{8 \log R_u}, \quad (1.3)$$

where  $M_e$  is the external Alfvén Mach number defined as the ratio of the external plasma velocity and Alfvén speeds  $M_e = \frac{v_e}{v_{a,e}}$  and  $R_u$  is the Lundquist number. The derivation of this is not presented here as it is almost identical to the derivation for relativistic magnetohydrodynamics found in chapter 5, except that the speed of light is replaced by the Alfvén speed in the non-relativistic case. The reconnection rate is now only weakly dependent on the Lundquist number and so is much faster than the Sweet-Parker model for the large Lundquist numbers expected.

The Sweet-Parker model has been found to be related to Petschek's through the tearing mode. As the tearing mode acts upon the Sweet-Parker steady state, the thin current sheet forms between the emerging magnetic islands. The thin forming current sheet is used as the basis for models of anomalous resistivity to trigger Petschek reconnection. For example Ugai in [50] uses this concept with the relative electron-ion drift velocity  $V_d$ , which is dependent on the magnitude, to trigger fast Petschek reconnection from the tearing mode acting on a Sweet-Parker setup.

The mechanism of Sweet-Parker and Petschek reconnection have both been generalised to relativistic resistive magnetohydrodynamics in Lyubarsky's paper [29], and are detailed in chapters 4 and 5 for completeness.

## 1.2 Magnetars and Blazars

Neutron stars are produced at the ends of the lives of massive stars with initial masses  $M_{int}$ , of  $8M_\odot < M_{int} < 25M_\odot$  where  $M_\odot$  is the mass of the sun (see [16],) and are

composed almost entirely of neutrons. A magnetar is a neutron star with a super strong magnetic field of  $B = 10^{15}$  Gauss or  $10^{11}$  Tesla and is expected to spin rapidly. They were first predicted theoretically by Duncan & Thompson in 1992 in [8]. The birth rate of magnetars is predicted to be 1 – 3 per 1000 years per galaxy as given by [16] and in a separate analysis in [10].

Magnetars are observed as sources of X-ray bursts with the expected life time of the magnetar as an X-ray emitter being  $\sim 10^4$  yr (see [23]). The magnitude of these bursts is phenomenal, with the magnetar SGR 1806 – 20 being observed on the 27<sup>th</sup> of December in 2004 as “even surpassing the full moon brightness for 0.2 seconds” (see [36]). This is due to the super strong magnetic fields which are thought to power X-ray flares. In observational work magnetars are separated into two classes, anomalous X-ray pulsars and soft gamma-ray repeaters, both of which display X-ray flares and quiescent X-ray emission. The quiescent phase happens over a long period with the flare occurring over a short period of about 80 – 200 milliseconds followed by an observable tail which lasts a few seconds (see [9]).

This is all in good analogy with solar flares where magnetic energy may build up over very long time periods and then lose stability and release the energy on the Alfvén time scale. The short rise time is inconsistent with a crustal deformation as shown in [30] and this points to a magnetospheric origin to the flare. The instability that causes the loss of equilibrium can be dynamical or resistive. The work in this thesis is based on resistive instabilities.

The analogy with solar flares goes further, with the X-ray flares being thought as being caused by a similar mechanism as those found in the solar corona. The energy for magnetar flares is stored in the neutron star in its formation. This will include electric currents in its interior. These will be slowly pushed into the magnetosphere through slow plastic deformations of the crust. This causes a slow twisting of the field lines in the magnetosphere. This will slowly build up until dynamic equilibrium is lost

where significant reorganisation of the magnetic field will occur with thin current sheets being formed and magnetic dissipative process commencing. The loss of stability in the magnetic fields will occur on the Alfvén crossing time. This will result in magnetic energy being released as kinetic energy and radiation. The reconfiguration of the magnetic topology also allows magnetic loops to form that in time will break away from the star. This is similar to coronal mass ejections in the solar corona where active magnetic regions caused by a slow build up of magnetic shear from either displacements of magnetic footpads by the photosphere or the emergence and submergence of magnetic flux through the photosphere (see [1]). This builds up until dissipative effects become important allowing the magnetic field lines to reconnect and power the mass ejection from the solar corona on the short time scale.

Blazars are a type of compact active galactic nuclei that are extreme energy sources (and thought to represent the most powerful sources) with beamed jets with a violently variable optical continuum (see [33]). In [33] a typical jet of a blazar is modelled using the gamma-ray jet of blazar 3C 279 to constrain the parameters. It was found that in the relativistic jet gamma-rays are produced by a synchrotron self-Compton mechanism. In [13] gamma-ray bright blazars are found as a continuum including flat-spectrum radio quasars and BL Lacs using the spectral energy distributions. This is done with two models, synchrotron self Compton and external Compton mechanisms (note that the external mechanism, synchrotron self-Compton mechanism is included in this).

In [14] the fast TeV variability of two observed blazars is found to be caused by a compact emitting regions moving with the jet bulk. The physical cause for this is found to be a dissipative reconnection event in a Poynting flux dominated jet. The reconnection event is found to be able to power TeV flares. This is expected to be a Petschek type event with a large magnetisation parameter  $\varsigma$  and triggered by a current driven instability that is dissipative, such as the tearing mode.

Another interesting case is the variability in jets emanating from blazars. The variation is

thought to be caused by the still potent Poynting flux in the jet reconnecting inside the jet. This is described in [15].

### 1.3 Motivation

With magnetic reconnection being a well studied subject in the Earth's magnetopause (see [34] for example) and in solar physics (see [49] for example) the theory is being brought to bear on relativistic astrophysics, specifically to explain the energy release in soft gamma ray bursts and anomalous X ray pulsars thought to occur in magnetars and blazars. The physical question motivating this research is “Is relativistic magnetic reconnection a viable candidate to power highly energetic flares in magnetars?”. Within this question the theory has now been developed to the point where numerical simulations are required to backup the order of magnitude predictions as will be presented in section 1.5.

With the work by Komissarov et al. giving interesting parallels between magnetic reconnection in resistive magnetohydrodynamics and magnetodynamics (also known as force free electrodynamics) in [27], the order of magnitude analyses done by Lyubarsky in [29] and the advent of the first relativistic resistive magnetohydrodynamical code (detailed in [26]) provided a good opportunity for a numerical relativistic resistive magnetohydrodynamical investigation of relativistic magnetic reconnection.

In the resistive magnetodynamical work on reconnection in [27] the rise time of reconnection was found to be the same as for resistive magnetohydrodynamics, with a linear time scale of

$$\tau = (\tau_d \tau_c)^{\frac{1}{2}}, \quad (1.4)$$

where  $\tau_d$  is the diffusive time scale and  $\tau_c$  is the light crossing time for

magnetodynamics and the Alfvén time for magnetohydrodynamics. This was found to be due to the similarity of the equations and suggests that reconnection in resistive relativistic magnetohydrodynamics will lie between the two extremes of a completely electromagnetic dominated environment and the non-relativistic case with a linear growth time close to  $\tau$ .

This work suggested that the rise time in the magnetodynamical model would be close to the observed times as documented in [31] for a magnetar. In astrophysics relativistic magnetic reconnection is thought to be important in many high energy astrophysical phenomena where the excessively strong magnetic field is thought to be the power source. These include pulsar wind nebulae, active galactic nuclei jets, gamma ray bursts and magnetars. Of these, magnetars have the most evidence for being powered by magnetic reconnection. This is shown in section 1.2.

The location of reconnection in magnetars is suspected to be in the magnetosphere and, in correspondence with M. Lyutikov, he has confirmed that this will be very collisionless. This prompts the question of applicability of a magnetohydrodynamical approach. This is discussed at length in [39], where it is found to be quite useful as long as the limitations are kept in mind. For the most part their argument carries over to relativistic magnetohydrodynamics in that even though it does not describe the motion of individual particles it always describes the bulk motion of a plasma as long as it can support an electric field in its own frame of reference. Another reason that supports this approach is that for a strong magnetic field the particles will thread along the field lines impeding motion across them. This gives long range interaction along the field lines and perpendicular to them short range interactions which are described by magnetohydrodynamical equations. A final reason in favour of using the magnetohydrodynamical approach is that inside the current sheet the plasma is expected to be highly compressed creating a collisional environment, outside the current sheet will still be collisionless though.

The major difficulty of conducting numerical simulations of relativistic magnetic reconnection is the stiff term introduced by the resistivity. This term adds in a second, faster time scale to the system which can cause fast convergence to a solution, but not necessarily to the physically realistic one. This is dealt with in an analytic way in the code used in this is discussed in section 3.4.

## 1.4 Dimensionless parameters

When performing numerical simulations it is important that the parameters are in the right regime for the phenomena being studied. For relativistic resistive magnetohydrodynamical simulations of relativistic magnetic reconnection these are the relativistic Lundquist number  $L_u$ , the plasma beta  $\beta$  and the magnetisation parameter  $\varsigma$

The relativistic Lundquist number is the relativistic generalisation of the Lundquist number  $R_u$ , which itself is a generalisation of the magnetic Reynolds number  $R_m$ . They have the definitions

$$R_m = \frac{vl}{\eta}, \quad R_u = \frac{v_a l}{\eta} \quad \text{and} \quad L_u = \frac{cl}{\eta}, \quad (1.5)$$

where  $v$  is a typical velocity of the plasma,  $l$  is a typical length scale,  $v_a$  is the Alfvén velocity,  $c$  is the speed of light and  $\eta$  is the resistivity. These give a measure of the importance of the inertia, using a typical velocity of the system, to magnetic diffusion for a plasma. For  $R_m$  the velocity of the fluid is used while for  $R_u$  the Alfvén velocity is used since it is a more characteristic velocity of an astrophysical plasma. For the relativistic Lundquist number the Alfvén velocity is replaced with the speed of light which is more appropriate for relativistic situations.

An estimate for the relativistic Lundquist number for magnetars is found in Komissarov et al. [27]. Komissarov has kindly provided the details of this and these will be presented



in the appendix in A.

This is

$$L_u = 1.54 \times 10^8 \left( \frac{l}{R_{NS}} \right) \left( \frac{B}{B_Q} \right)^{\frac{1}{2}} \lambda^{\frac{1}{2}}. \quad (1.6)$$

The prefactor roughly represents a maximum value for the relativistic Lundquist number. As  $l \approx R_{NS}$ ,  $B \sim B_Q$  and  $\lambda^{\frac{1}{2}}$  will be small, around  $\frac{1}{10}$  the relativistic Lundquist number will be around  $10^6$ .

The plasma beta is defined as the ratio of the plasma pressure to the magnetic pressure and is defined as

$$\beta = \frac{p}{p_m} = \frac{8\pi p}{B^2}, \quad (1.7)$$

where  $p$  is the plasma pressure,  $p_m$  is the magnetic pressure and  $B$  is the magnetic field strength. This is important in relativistic reconnection as the inflow region will be dominated by the magnetic pressure and the outflow by the plasma pressure. As the total pressure  $p_t = p + p_m$  is approximately constant across both regions the plasma beta gives a measure of the conversion of magnetic energy to kinetic in the reconnection process. In the inflow region it is expected to be small with  $\beta \ll 1$ .

In appendix C the upper and lower limits are estimated for the plasma beta in the magnetosphere of a magnetar. This uses the Goldreich Julian density arguments of [18], the additional matter not accounted for in this method provided by pair production found by Hirschman and Arons in [21] and an estimation of the temperature of the magnetosphere of  $\approx 10\text{keV}$  from [46]. This gave a range of

$$10^{-20} \leq \beta \leq 10^{-17}. \quad (1.8)$$

The magnetisation parameter is defined as a comparison of the magnetic energy density and the plasma energy density and, following [29], is defined as

$$\varsigma = \frac{B^2}{4\pi\rho c^2\gamma^2}, \quad (1.9)$$

where  $B$  is the magnetic field,  $\rho$  is the plasma density and  $\gamma$  is the Lorentz factor. This is not quite the plasma energy density, but is accurate for the inflow region in reconnection as will be shown in chapters 4 and 5. The magnetisation parameter is expected to be  $\varsigma \gg 1$  for relativistic reconnection (and for a magnetar).

For the relativistic tearing mode, as the inflow pressure was kept the same as the inflow density the magnetisation parameter was superceded by the plasma beta  $\beta = 2p/B^2$ , as a measure of the magnetisation of the plasma. If the magnetisation parameter is considered in units where  $c = 1$  and the factor  $\sqrt{4\pi}$  is absorbed into the electromagnetic fields and if the Lorentz factor is  $\approx 1$  as is expected for the tearing mode (see section 4.1.1), then

$$\varsigma = \frac{B^2}{\rho}. \quad (1.10)$$

Since, in the majority of the simulations presented in this work, the inflow region the thermodynamic variables were initialised and stayed at  $p = \rho = 0.1$ , equation 1.10 can be written

$$\varsigma = \frac{B^2}{p} = 2\beta^{-1}. \quad (1.11)$$

Then a range for the plasma beta of  $\beta = 0.32$  to  $0.05$  gives a magnetisation range of  $\varsigma = 6.25$  to  $40$  which is acceptable given the code's limitations (see section 3.8). The largest value of the plasma beta gives a background Alfvén velocity of  $0.75c$  which is acceptable in simulations which require that the characteristic speed of the plasma be relativistic.

		Equation of the parameter		Estimation of the
Name	Symbol	Dimensional	Non-dimensional	parameter for a magnetar
The magnetisation parameter	$\varsigma$	$\frac{B^2}{4\pi\gamma^2\rho c^2}$	$\frac{B^2}{\gamma^2\rho}$	$10^{14} \leq \varsigma \leq 10^{17}$
The plasma beta	$\beta$	$\frac{8\pi p}{B^2}$	$\frac{2p}{B^2}$	$10^{-20} \leq \beta \leq 10^{-17}$
The relativistic Lundquist number	$L_u$	$\frac{lc}{\eta}$	$\frac{l}{\eta}$	$10^6$

Table 1.1: A table of dimensionless parameters.

For relativistic Petschek reconnection the magnetisation parameter is measured in the inflow region and the same magnitude of the magnetic field and density are used to initialise all the simulations of relativistic Petschek reconnection. The inflow velocity caused by the reconnection is never more than a third of the speed of light, and so the Lorentz factor may be ignored. The initial magnitude of the magnetic field  $|B| = 2.5$  and density of  $\rho = 0.1$  give a magnetisation parameter of around  $\varsigma = 62.5$ . This is much larger than one, but not massively so. It would be preferable to increase this, but higher values than this are unachievable due to the limitations of the code used.

In appendix B upper and lower limits are found for the magnetisation parameter based on the Goldreich Julian density arguments of [18] and the additional matter not accounted for in this method provided by pair production found by Hirschman and Arons in [21] as

$$10^{14} \leq \varsigma \leq 10^{17}. \quad (1.12)$$

A list of the dimensionless parameters with their formulation in dimensional and dimensionless form is presented in table 1.1.

## 1.5 Important works in relativistic magnetic reconnection

With the growing evidence that magnetic reconnection is not only important in solar physics and in the Earth's magnetosphere, but in high energy astrophysics as well. Three of the most important works in magnetohydrodynamical models are presented below with a short summary and review of each paper.

### 1.5.1 Steady state relativistic Sweet Parker reconnection

In June 2003 Lyutikov and Uzdensky published [32] in which they described steady state relativistic Sweet Parker reconnection in 2-dimensions. They first consider the steady state equations and the outflow along the  $x$ -axis finding a similar scaling for both the four-velocity and the magnetic field, that of the current sheet thickness. Then the assumptions that the plasma is incompressible and the magnetisation parameter and relativistic Lundquist number are both large  $\varsigma$ ,  $L_u \gg 1$ , to first estimate the current in the reconnection layer as

$$J_z \sim \frac{B}{l} \sim \frac{\gamma_{in} v_{in} B_{in}}{\eta} \quad (1.13)$$

where the subscript “in” denotes variables in the inflow region,  $l$  is the width of the current sheet and the other variables have their usual meaning. This is then used to approximate the relativistic Ohm's law to get

$$v_{in} \gamma_{in} \sim \frac{\eta}{l}, \quad (1.14)$$

which written in terms of the relativistic Lundquist number is

$$v_{in}\gamma_{in} \sim \frac{L}{l}L_u^{-1}, \quad (1.15)$$

where  $L$  is the length of the reconnection region (as shown in figure 4.1).

Then the energy flux and particle conservation equations with the same assumptions give

$$v_{in}\gamma_{in}L = \gamma_{out}l \quad (1.16)$$

and

$$v_{in} = \varsigma \frac{l}{L}, \quad (1.17)$$

where  $v_{out}$  has been dropped as they expected it to be approximately the speed of light (unity).

The momentum flux

$$\partial_y \left( (w + B_z^2) u^2 + \frac{1}{2} B_z^2 \right) = 0 \quad (1.18)$$

where  $w$  is the plasma enthalpy and  $u$  is the four-velocity, is also considered and simplified using conservation of mass and magnetic flux to give

$$\rho u \partial_y u + \frac{1}{2} \partial_y (\rho \varsigma) = 0. \quad (1.19)$$

where the assumption that the Alfvén speed is approximately unity  $B_z^2 = \varsigma \rho$ , has been used.

This shows that the plasma compressibility only becomes important when these two terms are equal, when

$$u \sim \sqrt{\varsigma} \sim u_a, \quad (1.20)$$

where  $u_a$  is the four-Alfvén velocity.

With equations 1.15, 1.17 and condition 1.20 they then separate relativistic steady state Sweet Parker reconnection into three regimes where the ratio of the length to the width of the reconnection region and the inflow are both predicted. The three regimes are:-

**Non-relativistic inflow,  $v_{in} \ll 1$ .**

Using the inflow assumption that  $v_{in} \ll 1$  to give the inflow Lorentz factor as unity  $\gamma_{in} = 1$ , in equation 1.15 and combining with equation 1.17 gives

$$\frac{l}{L} \sim (\varsigma L_u)^{-\frac{1}{2}}. \quad (1.21)$$

If this is then combined with equation 1.17 again to eliminate the ratio of the dimensions of the reconnection region to give

$$v_{in} \sim \sqrt{\frac{\varsigma}{L_u}} \sim \frac{2}{L_u} \gamma_a \quad (1.22)$$

where  $\gamma_a = (2\varsigma)^{1/2}$  is the Lorentz factor of an Alfvén wave in the inflow region.

As  $v_{in} \ll 1$  this gives  $\varsigma \ll L_u$  and the inflow is inversely proportional to the square root of the relativistic Lundquist number as found in the non-relativistic case.

**Relativistic sub-Alfvénic flow,  $1 \ll \gamma_{in} \ll (2\varsigma)^{-1/2}$**

Using  $v_{in} \approx 1$  in equation 1.17 and 1.15 and combining gives

$$v_{in} \sim \frac{\varsigma}{L_u}. \quad (1.23)$$

Using all this in equation 1.16 gives the outflow Lorentz factor as

$$\gamma_{out} \sim \frac{\varsigma^2}{L_u}. \quad (1.24)$$

As  $v_{in} \approx 1$  this means that  $\varsigma \gg L_u$ . Comparing the ratio of the inflow and Alfvén Lorentz factors

$$\frac{\gamma_{in}}{\gamma_a} \sim \frac{\sqrt{\varsigma/2}}{L_u} \quad (1.25)$$

and since the inflow velocity needs to be sub-Alfvénic to satisfy condition 1.20 for the plasma to be incompressible this requires

$$\varsigma \ll 2L_u^2 \quad (1.26)$$

and hence the incompressible relativistic inflow regime is for a magnetisation parameter in the range  $L_u \ll \varsigma \ll L_u^2$ .

**Relativistic super-Alfvén inflow,  $\gamma_{in} \sim (2\varsigma)^{1/2}$**

In this regime the incompressibility assumption breaks down and the full set of equations should be considered to make any predictions.

This is a strong start to relativistic magnetic reconnection with three main shortcomings, the non-relativistic Alfvén speed is used instead of the relativistic one, the assumption that the outflow will be relativistic which is shown to be false in [29] and that the momentum and energy equations are not solved consistently.

### 1.5.2 The tearing mode in relativistic force-free electrodynamics

In December 2003 Lyutikov published [30] in which an analytic study into the tearing mode in relativistic force-free electrodynamics (also known as magnetodynamics) and

presents evidence that the flares and burst events in anomalous X-ray pulsars and soft Gamma-ray repeaters have magnetospheric origins.

To study the tearing mode in relativistic force-free electrodynamics the equations were first derived. This was done assuming the plasma is force free which requires the condition that  $B^2 \gg \rho c^2$  (or in the notation of this work the magnetisation parameter is  $\varsigma \gg 1$ ) and that the energy released in the system leaves it as a form of radiation rather than with the plasma as is normal in magnetic reconnection. The first equation derived is Ohm's law in which the motion of the particles across the field is governed by the drift velocity  $\mathbf{v}_\perp$  given by

$$\mathbf{v}_\perp = \frac{\mathbf{E} \times \mathbf{B}}{B^2} \quad (1.27)$$

which gives the plasma rest frame as the frame where the drift velocity is zero. Then the covariant Ohm's law

$$F^{\alpha\beta} u_\beta = \eta^{\alpha\beta} (g_\beta^\gamma - u_\beta u^\gamma) j_\gamma, \quad (1.28)$$

where  $F^{\alpha\beta}$  is the Maxwell tensor,  $u_{\beta}$  and  $j_\gamma$  are the four velocity and current density,  $g_\beta^\gamma$  is the metric of space time and the tensor resistivity is given by

$$\eta^{\alpha\beta} = \eta \frac{b^\alpha b^\beta}{b^2}, \quad (1.29)$$

where the four vector of the magnetic field is given by  $b_\alpha = \gamma \{(\mathbf{v} \cdot \mathbf{b}), \mathbf{B}\}$ , can be simplified using the choice of the parallel velocity to the magnetic field lines as part of the co-ordinate system as  $v_\parallel = 0$  and ignoring the Poynting flux for the bulk motion to give

$$\mathbf{J} = \frac{\nabla \cdot (\mathbf{E} (\mathbf{E} \times \mathbf{B}))}{B^2} + \frac{1}{\eta \sqrt{1 - \left(\frac{\mathbf{E} \times \mathbf{B}}{B^2}\right)^2}} \frac{(\mathbf{E} \cdot \mathbf{B}) \mathbf{B}}{B^2}. \quad (1.30)$$



The other equations needed are given by taking the limit of vanishing state variables  $p, \rho \rightarrow 0$  in the equations of resistive magnetohydrodynamics and reintroducing the electric field by

$$\mathbf{E} = \mathbf{E}_{\parallel} + \mathbf{E}_{\perp} = \frac{(\mathbf{E} \cdot \mathbf{B}) \mathbf{B}}{B^2} - \mathbf{v} \times \mathbf{B}. \quad (1.31)$$

The governing equations are then Maxwell equations

$$\partial_t \mathbf{B} = -\nabla \times \mathbf{E} \quad \text{and} \quad \partial_t \mathbf{E} = \nabla \times \mathbf{B} - \mathbf{J}. \quad (1.32)$$

This is complex system where there is no frame where the electric field is zero and the Ohm's law 1.30 must be substituted into the Maxwell equations to give a closed system for the electromagnetic fields and solved with the condition that  $\nabla \cdot \mathbf{B} = 0$ .

The approximation of these equations will break down when high velocities are achieved which from equation 1.27 is when  $E \rightarrow B$ .

With the governing equations found, several candidates for current sheets are discussed including sheared force-free sub-layer ones which are described in chapters 4 and 5 of this work and a magnetic rotational discontinuity where  $\mathbf{E} = 0$  and the magnitude of the magnetic field is a constant  $B^2 = \text{const}$ .

With this a boundary layer type stability analyses was done, similar to that done in section 4.1.2, finding width of the resistive sub layer to be  $\epsilon L$  where  $L$  is the width of the current sheet and the small parameter is given by

$$\epsilon \sim \frac{\Gamma L^3 k_x}{\eta} \quad (1.33)$$

where  $k_x$  is the  $x$  component of the wavenumber and  $\Gamma$  is the growth rate. This also gives the growth rate as

$$\Gamma \sim (\tau_d \tau_a)^{-\frac{1}{2}} \quad (1.34)$$

where  $\tau_d$  and  $\tau_a$  are the resistive and Alfvénic time scales respectively. This estimate is the same as found for the tearing mode in non-relativistic magnetohydrodynamics. The similarities are investigated in [27] and found to be due to the similarity of the equations being solved. This extension also found a more succinct boundary layer stability analysis.

The six reasons given in favour of the magnetospheric origin of the flares are in brief:-

- The observed pulse profile change after the flare which matches the simpler magnetospheric conditions expected after the event with a magnetospheric origin,
- The softening spectrum after a flare matching weaker current sheets in the post flare state,
- A typical rise time of  $\approx 0.01$ s which is consistent with the tearing mode in force-free electrodynamics,
- The random pulse profile of soft Gamma-ray emitters which is natural for current sheets in the magnetosphere,
- The pulsed fraction increases in the tails of strong bursts with a profile similar to persistent emission which fits better with magnetospheric origin where activity can continue after the burst than if the burst was associated with a hot spot on the surface of the neutron star,
- Short soft Gamma-ray burst events have harder spectra than more intense ones which is consistent with short events being due to reconnection and long events having a large contribution from surface heating.

This is a well explained paper with a lot of technical detail giving a good background to the relativistic tearing mode and through its extension in [27] directly leading to this work.

### 1.5.3 Order of magnitude calculations of relativistic Sweet Parker and Petschek reconnection

In 2005 Lyubarsky published [29] in which he presents a generalisation of resistive magnetohydrodynamics Sweet Parker and Petschek reconnection to the relativistic regime by considering both the energy and momentum equations. In general the Alfvén velocity is found to be close to the speed of light and with the classical model generalising to the relativistic regime in a straightforward (if more complex) way, the reconnection rate may be found by substituting  $v_a = c$  in the classical formulae.

In relativistic Sweet Parker reconnection the outflow is found to be only mildly relativistic, highly compressed and relativistically hot with a small anti-parallel component of the incoming magnetic field having no effect on the dynamics.

In relativistic Petschek reconnection the outflow is found to have a large Lorentz factor and again be relativistically hot. The compression ratio is very high, to such a degree that even a small anti-parallel component of the incoming magnetic field can alter the structure and lead to the majority of the energy of the system leaving as the Poynting flux rather than the kinetic flux.

The details are not presented here as they are presented in detail in chapter 4 for the relativistic Sweet Parker reconnection and in chapter 5 for relativistic Petschek reconnection where they provide the framework for studying the results of numerical simulations and are hence presented in detail for completeness.

## 1.6 Alternative models to study relativistic magnetic reconnection

Two different models used to study plasmas and reconnection are presented here with a small review and reasons why they are not used compared to relativistic magnetohydrodynamics.

These are Hall magnetohydrodynamics and plasma kinetics.

### 1.6.1 Hall magnetohydrodynamics

Hall magnetohydrodynamics came from the concerns of Lighthill on the neglect of terms in the generalised Ohm's law,

$$\mathbf{E} + \mathbf{v} \times \mathbf{B} = \sigma^{-1} \mathbf{J} + \frac{m_e}{ne^2} \left( \frac{\partial \mathbf{J}}{\partial t} + \nabla \cdot (\mathbf{J} \mathbf{v} + \mathbf{v} \mathbf{J}) \right) - n^{-1} \nabla \cdot \mathbf{P}_e + (ne)^{-1} \mathbf{J} \times \mathbf{B}, \quad (1.35)$$

in the derivation of magnetohydrodynamics. The terms on the right hand side of equation 1.35 are, from left to right, the resistive term, the current inertial terms, the electron stress tensor and the Hall term. In the derivation of magnetohydrodynamics only the resistive term is kept, giving the familiar equations. To decide on which terms are important they are scaled and compared to the convective electric field  $\mathbf{v} \times \mathbf{B}$ . Using this very large or small values indicate whether they are important. If this is inconclusive then an analysis of kinetic dynamics is needed. For example in [39] it is suggested that the Hall term is important in reconnection in the Earth's magnetosphere.

When studying Hall magnetohydrodynamics several combinations of the terms on the right side of equation 1.35 are used. In [41] magnetic reconnection is studied using the Hall and resistive terms. This is done for an incompressible plasma and compared

to resistive magnetohydrodynamics finding this to be a limiting case of the more general theory and that reconnection is independent of the resistive mechanism in Hall magnetohydrodynamics. In both [7], where just the Hall term is used with a plasma pressure which may become anisotropic and in [3], where all the terms except the resistive one are used, magnetic reconnection is studied and found that for an electron-positron plasma the Hall current cancels out. In these fast reconnection was triggered by a localised effective resistivity caused by the non-isotropy of the plasma pressure. This was found to be analogous to an anomalous resistivity for traditional resistive magnetohydrodynamics.

The Hall effect is often ignored in magnetohydrodynamical simulations, as mathematically it is difficult to deal with. It is a non-linear term that greatly complicates the already stiff Ohm's law.

It is argued in [46] that in the magnetosphere of a magnetar, where they predict the magnetic reconnection events to happen, will be a photon electron-positron pair plasma and hence from [7] and [3], the Hall term may be ignored. As the photon-pair plasma is caused by the deposition of phenomenal amount of energy in the magnetosphere, it is not unreasonable to assume that other magnetically dominated candidates for relativistic reconnection will also have pair plasmas and hence it can be expected that the Hall effect is un-important in reconnection in these as well. Hence it is neglected in this work.

As the plasmas involved in relativistic reconnection are expected to be collisionless, as stated as one of the properties of the magnetosphere of a magnetar in [2], the inertial terms the generalised Ohm's law 1.35 can be dropped. The final remaining term in the generalised Ohm's law is also dropped in this work as the pressures are assumed to be isotropic and it is the non-isotropic terms that have been found to cause reconnection or affect the dynamics in non-relativistic magnetohydrodynamics as shown in [3] and [5].

### 1.6.2 Plasma kinetics

Plasma kinetic models are based upon the Vlasov equations, also known as the Vlasov-Maxwell system, a system of non-linear integration-differentiation equations. This system was devised in 1938 by Vlasov to deal with problems found in the kinetic models based on the Boltzmann equation. This approach is based on equations for distribution functions of the electrons and ions coupled with Maxwell's equations. The charge density and current density are also dependent on the distribution functions. The equations, as first written down in [52], are

$$\frac{\partial f_\alpha}{\partial t} + \mathbf{v} \cdot \nabla f_\alpha - (\mathbf{E} + \mathbf{v} \times \mathbf{B}) \cdot \frac{\partial f_\alpha}{\partial \mathbf{p}} = 0, \quad (1.36)$$

$$\frac{\partial \mathbf{E}}{\partial t} + \mathbf{J} = \nabla \times \mathbf{B}, \quad \frac{\partial \mathbf{B}}{\partial t} + \nabla \times \mathbf{E} = \mathbf{0}, \quad (1.37)$$

$$\nabla \cdot \mathbf{E} = q, \quad \nabla \cdot \mathbf{B} = 0, \quad (1.38)$$

$$q = e_\alpha \int f_\alpha d^3 \mathbf{p}, \quad \mathbf{J} = e_\alpha \int f_\alpha \mathbf{v} d^3 \mathbf{p}, \quad (1.39)$$

where  $\alpha$  can be  $i$  for ions or  $e$  for electrons and if repeated, is summed over. The distribution function and charge for each species is  $f_\alpha$  and  $e_\alpha$ . Finally  $\mathbf{E}$ ,  $\mathbf{B}$  are the electric and magnetic fields and the charge density and current density are  $q$  and  $\mathbf{J}$  respectively. This is in units where the speed of light is  $c = 1$  and the factor of  $\sqrt{4\pi}$  is absorbed into the electromagnetic field.

These equations are complicated to implement. This is shown in [6], where magnetic reconnection simulations are performed comparing periodic and free flow boundary conditions and the difficulties in implementing free flow boundary conditions for kinetic

models. These difficulties are made worse by generalising to the relativistic regime and hence the relativistic magnetohydrodynamical approach is normally used in this regime.

## 1.7 Aims of the thesis

The work in this thesis is to present the first numerical studies of the tearing mode and Petschek reconnection in the relativistic regime using a resistive magnetohydrodynamical model.

The simulations of the relativistic tearing mode will investigate the exponential growth (or linear growth on a log - time graph) and the dispersion relation. This will be done in the same manner as the investigation into the tearing mode in magnetodynamics in [27] with a boundary layer approach to analyse the linear growth stage and give the dispersion relation. The linear growth rates will then be compared to the observational rise time presented in [31]. The non-linear development of the relativistic tearing mode is investigated and the effects of the plasma beta on the maximum growth rate. The results of the simulations will then be compared to the order of magnitude predictions presented in [29]. Finally the reconnection electric field given by  $E^* = \mathbf{E} \cdot \mathbf{0}$ , is presented as an alternate measure of the growth and evolution of the reconnection of the magnetic field lines. In each of these investigations a standard model was deviated from. The deviations are varying the plasma beta, magnetisation parameter, relativistic Lundquist number and the isothermal case.

The simulations of relativistic Petschek reconnection will investigate anti-parallel and non-anti-parallel reconnection. The simulations will be done to attempt to confirm the prediction on relativistic Petschek reconnection presented in [29]. To do this the angled relativistic Petschek reconnection simulations will be split into three sections, a very small angled magnetic field in the inflow, a larger yet still small angled magnetic field in the inflow which is expected to change the structure of the reconnection and when the angle

of the magnetic field in the inflow is large up to being almost parallel. In the angled case the relativistic Lundquist number is also varied to see its effect on the reconnection. Finally the Poynting and kinetic fluxes are compared in the outflow jet for the different angles.



# Chapter 2

## The model

To study relativistic reconnection a continuum magnetohydrodynamics model was used. In the following sections the basics of the model are described.

### 2.1 The equations

The equations of relativistic resistive magnetohydrodynamics in covariant form are

$$\nabla_\beta \mathbf{F}^{\alpha\beta} = \mathbf{I}^\alpha, \quad (2.1)$$

$$\nabla_\beta {}^* \mathbf{F}^{\alpha\beta} = 0, \quad (2.2)$$

$$\nabla_\beta \mathbf{T}^{\alpha\beta} = 0, \quad (2.3)$$

$$\nabla_\alpha \rho \mathbf{u}^\alpha = 0, \quad (2.4)$$

where  $\mathbf{F}^{\alpha\beta}$  is the Maxwell tensor,  ${}^* \mathbf{F}^{\alpha\beta}$  is the Faraday tensor or the dual of the Maxwell tensor, the four vector of the current density is  $\mathbf{I}^\alpha$ , the four vector of velocity is  $\mathbf{u}^\alpha$  and the proper rest mass density is  $\rho$ .

The energy-momentum tensor  $\mathbf{T}^{\alpha\beta}$  is made up of two parts, the electromagnetic contribution  $\mathbf{T}_{(f)}^{\alpha\beta}$  and the matter contribution  $\mathbf{T}_{(m)}^{\alpha\beta}$ .

$$\mathbf{T}^{\alpha\beta} = \mathbf{T}_{(f)}^{\alpha\beta} + \mathbf{T}_{(m)}^{\alpha\beta}, \quad (2.5)$$

where the electromagnetic field contribution is

$$\mathbf{T}_{(f)}^{\alpha\beta} = \mathbf{F}^{\alpha\gamma} \mathbf{F}^{\beta}_{\gamma} - \frac{1}{4} (\mathbf{F}^{\mu\nu} \mathbf{F}_{\mu\nu}) \mathbf{g}^{\alpha\beta}, \quad (2.6)$$

and the matter contribution is

$$\mathbf{T}_{(m)}^{\alpha\beta} = w \mathbf{u}^{\alpha} \mathbf{u}^{\beta} + p \mathbf{g}^{\alpha\beta}. \quad (2.7)$$

In these equations units where the speed of light is one and the factor of  $\sqrt{4\pi}$  is absorbed into the electromagnetic fields the above tensors are, starting with the four velocity are

$$\mathbf{u}^{\alpha} = (\gamma, \gamma \mathbf{v}), \quad (2.8)$$

where  $\mathbf{v}$  is the plasma velocity measured by the inertial observer and the Lorentz factor is given by  $\gamma = (1 - v^2)^{-\frac{1}{2}}$ . The Maxwell tensor is given by

$$\mathbf{F}^{\alpha\beta} = \begin{pmatrix} 0 & E_x & E_y & E_z \\ -E_x & 0 & B_z & -B_y \\ -E_y & -B_z & 0 & B_x \\ -E_z & B_y & -B_x & 0 \end{pmatrix} \quad (2.9)$$

where the electric field is given by

$$E^i = F^{0i} \quad (2.10)$$

and the magnetic field by

$$B^i = \frac{1}{2} e^{ijk} F_{jk}. \quad (2.11)$$

The Faraday tensor is given by

$${}^* \mathbf{F}^{\alpha\beta} = e^{\alpha\beta\mu\nu} \mathbf{F}_{\mu\nu} \quad (2.12)$$

and its components can then be found from the Maxwell tensor. To do this the Levi-Civita alternating tensor of space-time  $e^{\alpha\beta\mu\nu}$  is used.

As relativistic magnetic reconnection is to be studied in the frame work of special relativity, the metric used is that of special relativity

$$g^{\alpha\beta} = \begin{pmatrix} -1 & 0 & 0 & 0 \\ 0 & 1 & 0 & 0 \\ 0 & 0 & 1 & 0 \\ 0 & 0 & 0 & 1 \end{pmatrix}. \quad (2.13)$$

The four velocity of electric current is

$$\mathbf{I}^\alpha = (q, \mathbf{J}) \quad (2.14)$$

where  $q$  is the charge density and  $\mathbf{J}$  is the current density.

In the matter tensor the relativistic enthalpy is defined as  $w = \rho(1 + \iota) + p$  where  $\iota$  is the internal energy and  $p$  is the plasma pressure. This definition differs from the non-relativistic one by the inclusion of the rest mass energy. If the equation of state  $p = (\Gamma - 1)\rho\iota$  is used the internal energy can be eliminated between the two equations to give

the relativistic enthalpy used in the code  $w = \rho + p \frac{\Gamma}{\Gamma-1}$ . In this  $\Gamma$  is the ratio of specific heats and in the code  $\Gamma = \frac{4}{3}$ , for a polytropic equation of state.

If we use the co-ordinate basis of the global inertial frame of special relativity, equations 2.1 to 2.4 split into the more familiar Maxwell's equations, 2.15 to 2.18. Total energy density, momentum density and matter conservation are given by equations 2.19 to 2.21.

$$\partial_t \mathbf{E} - \nabla \times \mathbf{B} + \mathbf{J} = \mathbf{0}. \quad (2.15)$$

$$\nabla \cdot \mathbf{E} = q. \quad (2.16)$$

$$\partial_t \mathbf{B} + \nabla \times \mathbf{E} = \mathbf{0}. \quad (2.17)$$

$$\nabla \cdot \mathbf{B} = 0. \quad (2.18)$$

$$\partial_t e + \nabla \cdot \mathbf{P} = 0. \quad (2.19)$$

$$\partial_t \mathbf{P} + \nabla \cdot \mathbf{\Pi} = \mathbf{0}. \quad (2.20)$$

$$\partial_t \rho \gamma + \nabla \cdot (\rho \gamma \mathbf{v}) = 0. \quad (2.21)$$

In these equations, as before  $\mathbf{E}$  and  $\mathbf{B}$  are the electric and magnetic fields,  $\mathbf{J}$  is the current density,  $q$  is the charge density,  $e$  is the total energy density given by

$$e = \frac{1}{2}(E^2 + B^2) + w\gamma^2 - p, \quad (2.22)$$

the energy density flux or the momentum density is given by

$$\mathbf{P} = \mathbf{E} \times \mathbf{B} + w\gamma^2 \mathbf{v}, \quad (2.23)$$

and the stress tensor is

$$\mathbf{\Pi} = -\mathbf{E}\mathbf{E} - \mathbf{B}\mathbf{B} + w\gamma^2 \mathbf{v}\mathbf{v} + \left( \frac{1}{2} (E^2 + B^2) + p \right) \delta, \quad (2.24)$$

and as before  $\gamma$  is the Lorentz factor,  $\mathbf{v}$  is the velocity as measured by the inertial observer and  $E = |\mathbf{E}|$  and  $B = |\mathbf{B}|$  are the magnitudes of the electric and magnetic fields. Finally  $\delta$  is the Kronecker delta symbol.

In the model a scalar conductivity (or resistivity) is used. This is introduced in the equation for the current density which in covariant form is

$$\mathbf{I}_\alpha = \sigma \mathbf{F}_{\alpha\mu} \mathbf{u}^\mu + q_0 \mathbf{u}_\alpha, \quad (2.25)$$

where  $q_0$  is the charge density as measured in the fluid frame and given by  $q_0 = -I_\alpha u^\alpha$ ,  $\sigma = 1/\eta$  is the conductivity and  $\eta$  is the resistivity.

In the global inertial frame of special relativity this is

$$\mathbf{J} = \sigma\gamma (\mathbf{E} + \mathbf{v} \times \mathbf{B} - (\mathbf{E} \cdot \mathbf{v}) \mathbf{v}) + q\mathbf{v}, \quad (2.26)$$

and the charge density is given by

$$q = \sigma\gamma \mathbf{E} \cdot \mathbf{v} + \gamma q_0. \quad (2.27)$$

Note that we can combine equations 2.16 and 2.15 to get the conservation law for the electric charge density,

$$\partial_t q + \nabla \cdot \mathbf{J} = 0. \quad (2.28)$$

## 2.2 Conservation laws

The general form of a conservation law is

$$\frac{\partial Q}{\partial t} + \nabla \cdot \mathbf{F} = s, \quad (2.29)$$

where  $Q$  is the conserved quantity,  $\mathbf{F}$  is the flux vector and  $s$  is the source term.

If we take an integral over the volume  $V$  of this we get

$$\iiint_V \left( \frac{\partial Q}{\partial t} + \nabla \cdot \mathbf{F} \right) dV = \iiint_V s dV. \quad (2.30)$$

Assuming that we can take the differential out and using Gauss law

$$\iiint_V \nabla \cdot \mathbf{F} dV = \iint_S \mathbf{F} \cdot d\mathbf{S},$$

where

$$d\mathbf{S} = \mathbf{n} dS \quad (2.31)$$

and  $\mathbf{n}$  is the outward pointing normal on the surface  $S$  bounding the volume  $V$ , we get

$$\frac{\partial}{\partial t} \iiint_V Q dV + \iint_S \mathbf{F} \cdot d\mathbf{S} = \iiint_V s dV. \quad (2.32)$$

The integral form of the conservation law shows where it acquired its name from. The amount of quantity  $Q$  in the arbitrary volume  $V$  varies over time by the amount that moves in and out through the surface  $S$  via the flux and the amount that is created or destroyed by the source  $s$ .

Using the idea of a conservation law we can rewrite 2.15, 2.17, 2.19 2.20 and 2.21 in conservation law form as

$$\frac{\partial \mathbf{Q}}{\partial t} + \nabla \cdot \mathcal{F} = \mathcal{S}, \quad (2.33)$$

where the vector of conserved quantities  $\mathbf{Q}$  and the source vector  $\mathcal{S}$  are given by

$$\mathcal{Q} = \begin{pmatrix} \rho \\ \frac{1}{2}(E^2 + B^2) + w\gamma^2 - p \\ \varepsilon^{ilm} E_l B_m + w\gamma^2 v^i \\ E^i \\ B^i \end{pmatrix}, \quad \mathcal{S} = \begin{pmatrix} 0 \\ 0 \\ 0^i \\ -J^i \\ 0^i \end{pmatrix} \quad (2.34)$$

and the flux tensor  $\mathcal{F}$  is

$$\mathcal{F} = \begin{pmatrix} \rho\gamma v^j \\ \varepsilon^{jlm} E_l B_m + w\gamma^2 v^j \\ -E^i E^j - B^i B^j + w\gamma^2 v^i v^j + \left(\frac{1}{2}(E^2 + B^2) + p\right) \delta^{ij} \\ -\varepsilon^{ijk} B_k \\ \varepsilon^{ijk} E_k \end{pmatrix}, \quad (2.35)$$

where  $\varepsilon^{ijk}$  is the Levi-Civita alternating tensor and the conservation laws are in descending order, matter, energy, momentum, electric and magnetic fields.





# Chapter 3

## Numerics

The code used to investigate relativistic reconnection is a multi-dimensional resistive relativistic magnetohydrodynamic scheme developed by Prof. Komissarov and parallelised by Dr. Barkov.

The details of the serial code were published in [26].

In the following, the basics and points of interest of the code will be noted upon.

### 3.1 Conservative methods

As shown in section 2.2 the equations of relativistic resistive magnetohydrodynamics are conservative. As such it is expected that any numerical scheme for these equations should also be conservative. Before considering the properties of a conservative numerical scheme the equations must first be discretised. To do this the equations are considered in one spatial dimension and the definition of the differential of the function  $f(x)$

$$\frac{df(x)}{dx} = \lim_{h \rightarrow 0} \frac{f(x+h) - f(x)}{h}. \quad (3.1)$$

If now instead of taking the limit the function is approximated by

$$\frac{df(x)}{dx} = \frac{f(x+h) - f(x)}{h} \quad (3.2)$$

and the  $x$  - axis is split up into discrete sections of length  $h$ . Note that this is not a unique representation as

$$\begin{aligned} \frac{df(x)}{dx} &= \lim_{h \rightarrow 0} \frac{f(x+h) - f(x)}{h}, \\ &= \lim_{h \rightarrow 0} \frac{f(x) - f(x-h)}{h}, \\ &= \lim_{h \rightarrow 0} \frac{f(x+\frac{h}{2}) - f(x-\frac{h}{2})}{h}. \end{aligned} \quad (3.3)$$

If the limit is not taken in any of these equations it provides a first order scheme, where the error is of order  $h$ . There are more ways to discretise a system to first order. If this is done to the one dimensional system of equations using the notation of 2.2 is

$$\frac{Q_{n+1} - Q_n}{\Delta t} + \frac{\mathcal{F}_{i+\frac{1}{2}} - \mathcal{F}_{i-\frac{1}{2}}}{\Delta x} = \mathcal{S}_n, \quad (3.4)$$

where time has been discretised into periods of  $\Delta t$  and space into lengths of  $\Delta x$  and the notation

$$Q_{n+1} = Q(x, n\Delta t) \quad (3.5)$$

is introduced where  $n$  and  $i$  give the position on the grid for time and space. This can be rearranged to give the update of the conserved variables as

$$Q_{n+1} = Q_n + \Delta t \frac{\mathcal{F}_{i-\frac{1}{2}} - \mathcal{F}_{i+\frac{1}{2}}}{\Delta x} + \Delta t \mathcal{S}_n. \quad (3.6)$$

This is in the form of a conservative method with the numerical flux dependent on the conserved quantities,  $\mathcal{F}_{i+\frac{1}{2}} = \mathcal{F}_{i+\frac{1}{2}}(\mathcal{Q}_{i-l_L}^n, \dots, \mathcal{Q}_{i+l_R}^n)$  is an approximation to the numerical flux and  $l_L$  and  $l_R$  denote the boundary values. The consistency condition for the numerical flux is

$$\mathcal{F}_{i+\frac{1}{2}}(\mathcal{V}, \dots, \mathcal{V}) = \mathcal{F}(\mathcal{V}). \quad (3.7)$$

The condition in equation 3.7 is equivalent to all the arguments of the flux function  $\mathcal{F}$  being equal to  $\mathcal{V}$  then the numerical flux is identical to the physical flux when  $\mathcal{Q} = \mathcal{V}$ .

## 3.2 The Riemann problem and Godunov's method

To describe Godunov's method the definition of the Riemann problem is needed. The details of these can be found in many books on numerics ( e.g. [47]) and are documented in the following sections.

### 3.2.1 The Riemann problem

To introduce the Riemann problem it is considered for a strictly hyperbolic constant coefficient system in one dimension with no source,

$$\mathcal{Q}_t + A\mathcal{Q}_x = \mathbf{0}, \quad (3.8)$$

for  $x \in [-\infty, \infty]$  and  $t > 0$  and the initial condition

$$\mathcal{Q}(x, 0) = \begin{cases} \mathcal{Q}_L & \text{if } x < 0, \\ \mathcal{Q}_R & \text{if } x > 0. \end{cases} \quad (3.9)$$

As the system has been assumed to be strictly hyperbolic the eigenvalues are real and distinct and hence can be ordered as

$$\lambda_1 < \lambda_2 < \cdots < \lambda_m. \quad (3.10)$$

Since the system is strictly hyperbolic, it can be diagonalised using the the matrix  $V$  made up of the eigenvectors  $\mathbf{v}^{(i)}$  given by

$$V = (\mathbf{v}^{(1)}, \dots, \mathbf{v}^{(m)}), \quad \text{where} \quad A\mathbf{v}^{(i)} = \lambda_i \mathbf{v}^{(i)}. \quad (3.11)$$

Then using the substitution  $\mathbf{w} = V^{-1}\mathcal{Q}$  and the fact that the system has constant coefficients it can be written as

$$\mathbf{w}_t + V^{-1}AV\mathbf{w}_x = \mathbf{0}, \quad (3.12)$$

and the matrix  $\Lambda = V^{-1}AV$  is diagonal with

$$\Lambda = \begin{pmatrix} \lambda_1 & \cdots & 0 \\ 0 & \ddots & 0 \\ 0 & \cdots & \lambda_m \end{pmatrix} \quad (3.13)$$

and hence the system is decoupled. The decoupled system is much simpler, being

$$\frac{\partial w_i}{\partial t} + \lambda_i \frac{\partial w_i}{\partial x} = 0, \quad \text{for } i = 1, \dots, m. \quad (3.14)$$

This is just the linear advection equation and for the initial condition  $w_i(x, 0) = w_i^{(0)}(x)$  the solution is

$$w_i^{(0)} = w_i^{(0)}(x - \lambda_i t), \quad \text{for } i = 1, \dots, m. \quad (3.15)$$

The solution to the original problem is then found by reversing the transformation by taking  $\mathcal{Q} = V\mathbf{w}$ . Expanding this gives

$$\mathcal{Q}_i = v_i^1 w_i + \cdots + v_i^m w_i, \quad (3.16)$$

or that the solution is an eigenvector expansion of the conserved variables with  $w_i$  being the coefficient of the  $i^{th}$  eigenvector or

$$\mathcal{Q}(x, t) = \sum_{i=1}^m w_i(x, t) \mathbf{v}^{(i)}. \quad (3.17)$$

As the  $w_i$  are known the solution is

$$\mathcal{Q}(x, t) = \sum_{i=1}^m w_i^{(0)}(x - \lambda_i t) \mathbf{v}^{(i)}. \quad (3.18)$$

To satisfy the initial conditions, first it is noted that the initial conditions can be decomposed as a linear combination of the eigenvectors as

$$\mathcal{Q}_L = \sum_{i=1}^m a_i \mathbf{v}^{(i)} \quad \text{and} \quad \mathcal{Q}_R = \sum_{i=1}^m b_i \mathbf{v}^{(i)} \quad (3.19)$$

with constant coefficients  $a_i$  and  $b_i$ . As can be seen in figure 3.1 the left hand state will be given by  $\mathcal{Q}_L$  and the right by  $\mathcal{Q}_R$  with the intervening states unknown. If equation 3.18 is compared to equation 3.19 then it can be seen that

$$w_i^{(0)}(x - \lambda_i t) = \begin{cases} a_i & \text{if } x - \lambda_i t < 0, \\ b_i & \text{if } x - \lambda_i t > 0. \end{cases} \quad (3.20)$$

Then for each point  $(x, t)$  there is a eigenvalue  $\lambda_*$  such that  $\lambda_I < \frac{x}{t} < \lambda_{I+1}$  and hence the integer  $I$  gives the largest value where  $w^{(0)}(x - \lambda_i t) = a_i$  and the solution can be written as

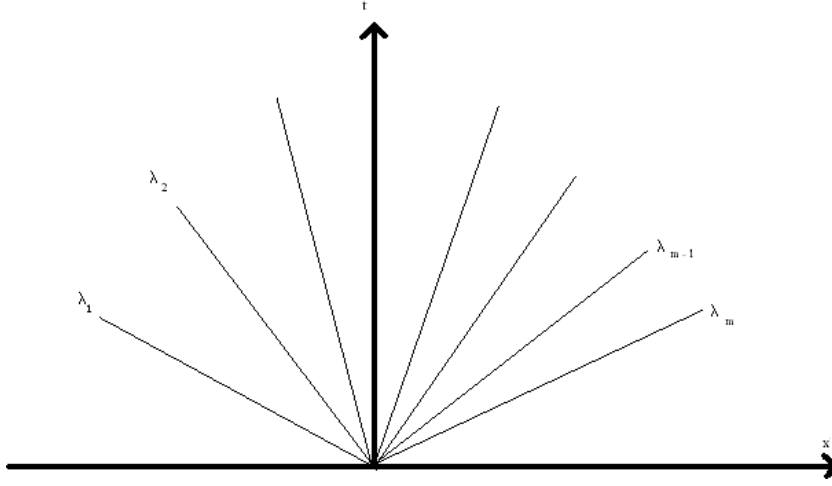


Figure 3.1: The fan of the waves emanating from the origin for each eigenvalue of a  $m$  - dimensional system.

$$\mathcal{Q}(x, t) = \sum_{i=1}^I a_i \mathbf{v}^{(i)} + \sum_{i=I+1}^m b_i \mathbf{v}^{(i)}. \quad (3.21)$$

### 3.2.2 Godunov's method

In 1959 Godunov published his work on a method of numerically solving non-linear systems of hyperbolic conservation laws in [17] and is presented here for one spatial dimension. The method is to solve the hyperbolic system of equations

$$\mathcal{Q}_t + \mathcal{F}(\mathcal{Q})_x = 0 \quad (3.22)$$

where  $\mathcal{Q}$  is the vector of conserved quantities and  $\mathcal{F}$  is the vector of fluxes subject to the initial and boundary conditions

$$\mathcal{Q}(x, 0) = \mathcal{Q}_0(x), \quad \mathcal{Q}(0, t) = \mathcal{Q}_L(t) \quad \text{and} \quad \mathcal{Q}(L, t) = \mathcal{Q}_R(t) \quad (3.23)$$

in the domain  $[0, L]$  for time  $[0, \infty)$ . This is discretised spatially into  $I$  computing cells of length  $\Delta x$  where  $I\delta x = L$  with cell boundaries and centres given by

$$x_{i-1/2} = (i-1)\Delta x, \quad x_{i+1/2} = i\Delta x \quad \text{and} \quad x_i = (i-1/2)\Delta x \quad (3.24)$$

and temporally discretised as  $t^n = n\Delta t$ . The solution is then denoted in each cell and time step by  $\mathcal{Q}(x_i, t^n) = \mathcal{Q}_i^n$ . This discretisation imposes the condition of the time step, for a given spatial step, that

$$2 \leq \frac{\Delta x}{a_{max}\Delta t} \quad (3.25)$$

where  $a_{max}$  is the maximum wave velocity at time  $t^n$  to prevent wave interaction. The Godunov method then assumes a constant solution in each cell giving a piece-wise solution over all. Then the solution in each cell is the solution to the Riemann problem centred at the cell boundary  $x_{i+1/2}$  for  $\mathcal{Q}_i^{n+1}$  with the initial condition  $\mathcal{Q}_i^n$  and left and right constant states  $\mathcal{Q}_i^n$  and  $\mathcal{Q}_{i+1}^n$ . The cell averages are defined for some initial data  $\tilde{\mathcal{Q}}(x, t^n)$  as

$$\mathcal{Q}_i^{n+1} = \frac{1}{\Delta x} \int_{x_i}^{x_{i+1}} \tilde{\mathcal{Q}}(x, t^{n+1}) dx. \quad (3.26)$$

As the problem has been decomposed into a piece-wise constant set of data the Riemann problem can now be solved for each interface between the cells. The solution will be a similarity one, depending only on the ratio  $\frac{x}{t}$  as seen in section 3.2.1 and will be denoted by  $\mathcal{Q}_{m+1/2}^n$ , the vector of conserved variables at the interface. Then the global solution  $\hat{\mathcal{Q}}$  in the domain  $(x, t) \in [0, L] \times [t^n, t^{n+1}]$  is defined by the piece-wise solution

$$\hat{\mathcal{Q}}(x, t) = \mathcal{Q}_{m+1/2}^n \left( \frac{x - x_{m+1/2}}{t - t^n} \right). \quad (3.27)$$

Since the global solution is known in terms of  $\mathcal{Q}_{m+1/2}^n$  the Godunov method can advance it from time  $t^n$  to  $t^{n+1}$  defining new average values. To do this the integral over  $[x_{i-1/2}, x_{i+1/2}] \times [t^n, t^{n+1}]$  is taken over equation of equation 3.22 then

$$\begin{aligned} \int_{x_{i-1/2}}^{x_{i+1/2}} \tilde{\mathcal{Q}}(x, t^{n+1}) dx = \int_{x_{i-1/2}}^{x_{i+1/2}} \tilde{\mathcal{Q}}(x, t^n) dx + \int_0^{\Delta x} \mathcal{F}[\tilde{\mathcal{Q}}(x_{i-1/2}, t)] dt \\ - \int_0^{\Delta x} \mathcal{F}[\tilde{\mathcal{Q}}(x_{i+1/2}, t)] dt. \end{aligned} \quad (3.28)$$

From the time constraint given in equation 3.25 which stops any wave interaction and using the assumption that the solution is piece-wise constant the last two terms of equation 3.28 are constant. Then using equation 3.26 this becomes

$$\mathcal{Q}_i^{n+1} = \mathcal{Q}_i^n + \frac{\Delta t}{\Delta x} (\mathcal{F}_{i-1/2} - \mathcal{F}_{i+1/2}). \quad (3.29)$$

This form of Godunov's method is easily implemented as a computational scheme. Extensions of this include allowing straight line solution instead of constant solution in each cell called slope limiting or as the solution uses averages an approximate Riemann solver can be sometimes used.

### 3.3 The no magnetic monopole condition

From the equation 2.18,

$$\nabla \cdot \mathbf{B} = 0, \quad (3.30)$$

we get the condition of no magnetic monopoles.

Taking the divergence of equation 2.17,



$$\partial_t \mathbf{B} + \nabla \times \mathbf{E} = \mathbf{0}, \quad (3.31)$$

we get

$$\partial_t (\nabla \cdot \mathbf{B}) = 0. \quad (3.32)$$

This shows that if we begin with no magnetic monopoles this will remain the case.

Similarly taking the divergence of equation 2.15 and using 2.16 we get the conservation of electric charge 2.28, the conservation of electric charge as a direct consequence.

This shows that, as long as 2.15 and 2.16 hold, the electric charge is always conserved.

Unfortunately these do not hold true for a general numerical scheme. Due to truncation errors in areas of high electric or magnetic gradients this can lead to a large corruption of the numerical solution.

Two different methods were used in the code to deal with this. The first was an augmented system and then constrained transport was used for the final simulations and was found to give greater accuracy.

### 3.3.1 Augmented system

In an augmented system we add two new variables (or pseudo-potentials) that are evolved. This modifies the equations to keep the no magnetic monopole condition and the continuity of electric charge.

To keep the no magnetic monopole condition we modify 2.18 and 2.17 by introducing the new variable  $\Phi$  as shown below

$$\partial_t \Phi + \nabla \cdot \mathbf{B} = -\kappa \Phi, \quad (3.33)$$

$$\partial_t \mathbf{B} + \nabla \times \mathbf{E} + \nabla \Phi = \mathbf{0}. \quad (3.34)$$

By taking the time derivative of 3.33, the divergence of 3.34 and combining these equations we find that  $\Phi$  satisfies the telegraph equation

$$\partial_t^2 \Phi + \kappa \partial_t \Phi = \nabla^2 \Phi. \quad (3.35)$$

In the non-dimensionalised units (of  $c = 1$ ) the telegraph equation describes a hyperbolic wave moving with the speed of light and decaying for  $\kappa > 0$ . This leads to  $\Phi$  evolving towards  $\Phi = 0$ , assuming that the boundary conditions do not stop this.

If instead the Laplacian  $\nabla^2$  is taken of 3.33 and the divergence of 3.34 is again taken we can combine to get

$$\partial_t^2 (\nabla \cdot \mathbf{B}) + \kappa \partial_t (\nabla \cdot \mathbf{B}) = \nabla^2 (\nabla \cdot \mathbf{B}), \quad (3.36)$$

and hence  $\nabla \cdot \mathbf{B}$  also obeys the telegraph equation and will behave like  $\Phi$ , decaying to zero (for the right boundary conditions) as desired.

In the same way as before we introduce the new variable  $\Psi$  in equations 2.16 and 2.15 as shown below

$$\partial_t \Psi + \nabla \cdot \mathbf{E} = q - \kappa \Psi, \quad (3.37)$$

$$\partial_t \mathbf{E} - \nabla \times \mathbf{B} + \mathbf{J} + \nabla \Psi = \mathbf{0}. \quad (3.38)$$

Taking the time derivative of 3.37 and the divergence of 3.38 and combining using conservation of charge 2.28 we get the telegraph equation for  $\Psi$ ,

$$\partial_t^2 \Psi + \kappa \partial_t \Psi = \nabla^2 \Psi. \quad (3.39)$$

So the behaviour of  $\Psi$  will be the same as  $\Phi$  and will tend to zero if not interrupted by the boundary conditions. Also if the Laplacian is taken of 3.37 and combined with the divergence of 3.38 then using the conservation of charge 2.28 we get the telegraph equation for  $\nabla \cdot \mathbf{E} - q$ ,

$$\partial_t^2 (\nabla \cdot \mathbf{E} - q) + \kappa \partial_t (\nabla \cdot \mathbf{E} - q) = \nabla^2 (\nabla \cdot \mathbf{E} - q), \quad (3.40)$$

hence  $\nabla \cdot \mathbf{E} - q$  will behave like  $\Psi$  and decay to zero as desired.

Note that the same constant  $\kappa$  was used in each case. A different one could be used in each case, but this has no advantage. In the simulations of relativistic reconnection the decay constant in the telegraph equation was set to  $\kappa = 10$  which gives a decay time of 0.1. This is much faster than the diffusive time scale of the system and is equal to the light crossing time.

For an augmented system we then evolve

$$\partial_t \Phi + \nabla \cdot \mathbf{B} = -\kappa \Phi, \quad (3.41)$$

$$\partial_t \mathbf{B} + \nabla \times \mathbf{E} + \nabla \Phi = \mathbf{0}, \quad (3.42)$$

$$\partial_t \Psi + \nabla \cdot \mathbf{E} = q - \kappa \Psi, \quad (3.43)$$

$$\partial_t \mathbf{E} - \nabla \times \mathbf{B} + \mathbf{J} + \nabla \Psi = \mathbf{0}, \quad (3.44)$$

$$\partial_t q + \nabla \cdot \mathbf{J} = 0, \quad (3.45)$$

$$\partial_t e + \nabla \cdot \mathbf{P} = 0, \quad (3.46)$$

$$\partial_t \mathbf{P} + \nabla \cdot \mathbf{\Pi} = 0, \quad (3.47)$$

$$\partial_t \rho \gamma + \nabla \cdot (\rho \gamma \mathbf{v}) = 0, \quad (3.48)$$

where

$$e = \frac{1}{2}(E^2 + B^2) + w\gamma^2 - p, \quad (3.49)$$

$$\mathbf{P} = \mathbf{E} \times \mathbf{B} + w\gamma^2 \mathbf{v}, \quad (3.50)$$

$$\mathbf{\Pi} = -\mathbf{E}\mathbf{E} - \mathbf{B}\mathbf{B} + w\gamma^2 \mathbf{v}\mathbf{v} + \left(\frac{1}{2}(E^2 + B^2) + p\right)\delta, \quad (3.51)$$

$$\mathbf{J} = \sigma\gamma(\mathbf{E} + \mathbf{v} \times \mathbf{B} - (\mathbf{E} \cdot \mathbf{v})\mathbf{v}) + q\mathbf{v}, \quad (3.52)$$

and the new dynamic variables are used to control the  $\nabla \cdot \mathbf{B} = \nabla \cdot \mathbf{E} - q = 0$  conditions.

### 3.3.2 Constrained transport

The method of constrained transport uses a choice of the representation of  $\nabla \cdot \mathbf{B}$  to algebraically keep the numerical approximation exactly zero. This is often done using

an off-centred representation of  $\nabla \cdot \mathbf{B}$ . This method has the advantage of being simple to implement and disadvantage of being more diffusive than a normal scheme.

This approach was found to be better than the augmented system and was hence the method implemented in the version of the code used for simulations.

For further information about constrained transport, Komissarov in [25] gives a brief overview, Tóth in [48] gives a detailed, thorough review and Gammie et al. in [12] give an implementation of a code on general relativistic magnetohydrodynamics.

### **3.3.3 Comparison of the augmented system and constrained transport**

In discussion with the architect of the code Prof. Komissarov, it was unknown why the augmented system performed poorly compared to the constrained transport. It is likely the difference comes from how close  $\nabla \cdot \mathbf{B}$  is kept to zero.

In the augmented system decaying superluminal waves work to move the system to be in a state where there are no magnetic monopoles. This means that there can be areas where  $\nabla \cdot \mathbf{B}$  is non-zero and if this occurs in a complex region of the system will pollute the solution with errors and make it more likely to crash.

The constrained transport keeps  $\nabla \cdot \mathbf{B}$  identically zero algebraically everywhere in the domain. This comes at an increase in computing time but avoids the suggested problem for the augmented system.

## **3.4 The stiff, resistive term**

In section 2.1 we introduced the current density in the global inertial frame of special relativity, as shown in equation 2.26.

One of the differences between resistive and ideal MHD is that we introduce a new time scale, the resistive time scale  $\frac{L^2}{\eta}$  where  $L$  is a typical length scale of the problem. In current sheets used for reconnection this can be a very fast time scale. This may seem like a boon, causing the solution to quickly assume the correct values. Unfortunately this is not the case as truncation errors may cause convergence to an unphysical solution. To overcome this we may increase the temporal resolution which requires a much smaller time step. This will cause longer run times and make the running of the code unfeasible.

A simple method to deal with this is to use a time splitting technique on the time step and use an analytic solution on the resistive time step.

For this time splitting technique the time step will be split into three sections, first a resistive half step, then an ideal full step and then another half resistive time step. This idea was first developed by Strang, [43].

This is done by splitting the source term of 2.33 into two parts,  $\mathcal{S} = \mathcal{S}_a + \mathcal{S}_b$ , where

$$\mathcal{S}_a = \begin{pmatrix} 0 \\ 0 \\ 0^i \\ -qv^i \\ 0^i \end{pmatrix} \quad \text{and} \quad \mathcal{S}_b = \begin{pmatrix} 0 \\ 0 \\ 0^i \\ -J_c^i \\ 0^i \end{pmatrix} \quad (3.53)$$

where the notation  $0^i$  is

$$0^i = (0, 0, 0)^T \quad (3.54)$$

The reduced current density  $\mathbf{J}_c$  is given by

$$\mathbf{J}_c = \sigma\gamma (\mathbf{E} + \mathbf{v} \times \mathbf{B} - (\mathbf{E} \cdot \mathbf{v}) \mathbf{v}) . \quad (3.55)$$

The time splitting technique is now to advance

$$\frac{\partial \mathbf{Q}}{\partial t} = \mathcal{S}_b \quad (3.56)$$

over a half step and then advance the solution over a full time step by

$$\frac{\partial \mathbf{Q}}{\partial t} + \nabla \cdot \mathcal{F} = \mathcal{S}_a \quad (3.57)$$

and finally over the half step 3.56 again.

The main advantage of this approach is that the half step can be solved analytically and hence adds very little to the computational cost whilst dealing with the stiff term.

To solve for the half step we start with the only evolving component of 3.56,

$$\partial_t \mathbf{E} = -\mathbf{J}_c. \quad (3.58)$$

Upon splitting this into components parallel,  $\parallel$ , and perpendicular,  $\perp$ , to the velocity direction  $\mathbf{v}$  the following equations are found

$$\partial_t \mathbf{E}_{\parallel} + \sigma \gamma (\mathbf{E}_{\parallel} - (\mathbf{E} \cdot \mathbf{v}) \mathbf{v}) = \mathbf{0}, \quad (3.59)$$

$$\partial_t \mathbf{E}_{\perp} + \sigma \gamma (\mathbf{E}_{\perp} + \mathbf{v} \times \mathbf{B}) = \mathbf{0}. \quad (3.60)$$

The solution to these equations using the initial value  $\mathbf{E}^0$  is

$$\mathbf{E}_{\parallel} = \mathbf{E}_{\parallel}^0 \exp \left( -\frac{\sigma}{\gamma} t \right), \quad (3.61)$$

$$\mathbf{E}_{\perp} = \mathbf{E}_{\perp}^0 + (\mathbf{E}_{\perp}^0 - \mathbf{E}_{\perp}^*) \exp(-\sigma \gamma t). \quad (3.62)$$

Due to neither  $\mathbf{B}$  or  $\mathbf{v}$  being updated in the half time steps we may treat  $\mathbf{E}_{\perp}^* = -\mathbf{v} \times \mathbf{B}$  as a constant.

It can be noted that these solutions decay to the ideal MHD electric field values of  $\mathbf{E}_{\parallel} = 0$  and  $\mathbf{E}_{\perp}^* = -\mathbf{v} \times \mathbf{B}$ , with the perpendicular component decaying faster than the parallel value approaches zero.

### 3.5 Implementation of the code

This section describes the implementation of the code as detailed in [27]. The code is a Godunov type scheme.

As in section 2.2 the system of hyperbolic conservation laws for relativistic resistive magnetohydrodynamics can be written as

$$\frac{\mathcal{Q}(\mathcal{P})}{\partial t} + \frac{\mathcal{F}^m(\mathcal{P})}{\partial x^m} = \mathcal{S}(\mathcal{P}) \quad (3.63)$$

where  $\mathcal{P}$  is the vector of primitive variables given by

$$\mathcal{P} = \begin{pmatrix} B^i \\ E^i \\ q \\ \rho \\ p \\ v^i \end{pmatrix}. \quad (3.64)$$

and  $B^i$ ,  $E^i$ ,  $q$ ,  $\rho$ ,  $p$  and  $v^i$  are the magnetic field, electric field, charge density, matter density, plasma pressure and velocity field respectively. As in section 3.4 the source vector is split into two terms  $\mathcal{S} = \mathcal{S}_a + \mathcal{S}_b$  where  $\mathcal{S}_b$  contains the stiff terms. Then the system is advanced by a half time step  $\frac{\Delta t}{2}$  for the equation



$$\frac{\partial \mathcal{Q}(\mathcal{P})}{\partial t} = \mathcal{S}_a(\mathcal{P}) \quad (3.65)$$

then by a second order numerical integration over a full time step  $\Delta t$  over

$$\frac{\partial \mathcal{Q}(\mathcal{P})}{\partial t} + \frac{\partial \mathcal{F}^m(\mathbf{P})}{\partial x^m} = \mathcal{S}_a \quad (3.66)$$

and finally over a half step of equation 3.65 again. As described in section 3.4 equation 3.65 is carried out using the analytical solutions equation 3.61 and equation 3.62 which eliminates the time constraints imposed by the stiff term. There is no reason that all the source terms could not be solved in the half time steps of equation 3.65, but it was found in testing to give a reduction of accuracy if this was done. The full time step of equation 3.66 is integrated explicitly as

$$\mathcal{Q}^{n+1} = \mathcal{Q}^n + \Delta t \sum_{m=1}^{N_d} \frac{\mathcal{F}_{m-1/2}^{n+1/2} - \mathcal{F}_{m+1/2}^{n+1/2}}{\Delta x^m} + \Delta t \mathcal{S}_a^{n+1/2} \quad (3.67)$$

where the notation of section 3.2.2 is used and  $N_d$  is the number of dimensions. To find the sources and fluxes after the half time step the solution is advanced by

$$\mathcal{Q}^{n+1/2} = \mathcal{Q}^n + \frac{\Delta t}{2} \sum_{m=1}^{N_d} \frac{\mathcal{F}_{m-1/2}^n - \mathcal{F}_{m+1/2}^n}{\Delta x^m} + \frac{\Delta t}{2} \mathcal{S}_a^n. \quad (3.68)$$

The fluxes at the interfaces are found using the HLL method proposed in [19] which is given by

$$\mathcal{F}_{m+1/2}^n = \frac{\mathcal{F}_{m+1/2}^{R,n} + \mathcal{F}_{m+1/2}^{L,n}}{2} - \frac{\mathcal{Q}_{m+1/2}^{R,n} - \mathcal{Q}_{m+1/2}^{L,n}}{2} \quad (3.69)$$

where the suffix's  $R$  and  $L$  refer to the constant states either side of the interface between two cells. The half time steps have the left and right states found by a piece-wise reconstruction of the primitive variables in each spatial direction and with  $c$  denoting

the cell centre the vector of primitive variables and spatial component in each cell is given by

$$\mathcal{P}^n = \mathcal{P}_c^n \quad \text{in the interval} \quad x_c^m - \frac{\Delta x^m}{2} < x^m < x_c^m + \frac{\Delta x^m}{2}. \quad (3.70)$$

For each cell the auxiliary solution is then used to for a quadratic reconstruction of the solution given by

$$\mathcal{P} = \mathcal{P}^{c, n+1/2} + a_1 (x^m - x_c^m) + \frac{a_2}{2} (x^m - x_c^m)^2 \quad (3.71)$$

with the same inequalities for the spatial variables as before. The coefficients  $a_1$  and  $a_2$  of the expansion are the first and second order derivatives of the reconstructed solution. They are found using a non-linear limiter with  $a_1$  given by

$$a_1 = av \left( \mathcal{P}'_L, \mathcal{P}'_R \right) \quad (3.72)$$

where the right and left numerical approximations of the first derivatives in the  $i^{th}$  cell on the  $x^m$  axis are

$$\mathcal{P}'_L = \frac{\mathcal{P}_i - \mathcal{P}_{i-1}}{\Delta x^m}, \quad \mathcal{P}'_R = \frac{\mathcal{P}_{i+1} - \mathcal{P}_i}{\Delta x^m} \quad (3.73)$$

and the averaging function is given by

$$av(a, b) = \begin{cases} 0 & \text{if } ab < 0 \text{ or } a^2 + b^2 = 0, \\ \frac{a^2 b + ab^2}{a^2 + b^2} & \text{if } ab \geq 0 \text{ and } a^2 + b^2 \neq 0. \end{cases} \quad (3.74)$$

The second non-linear limiter is given by first computing the second derivatives given by

$$\mathcal{P}''_L = \frac{\mathcal{P}_i - 2\mathcal{P}_{i-1} + \mathcal{P}_{i-2}}{(x^m)^2}, \quad \mathcal{P}''_c = \frac{\mathcal{P}_{i+1} - \mathcal{P}_i + \mathcal{P}_{i-1}}{(x^m)^2}, \quad \mathcal{P}''_R = \frac{\mathcal{P}_{i+2} - 2\mathcal{P}_{i+1} + \mathcal{P}_i}{(x^m)^2} \quad (3.75)$$

and then evaluating them in the minmod function giving

$$a_2 = \text{minmod} \left( \mathcal{P}_L'', \mathcal{P}_c'', \mathcal{P}_R'' \right), \quad (3.76)$$

where the minmod function is defined as

$$\text{minmod}(a, b, c) = \begin{cases} 0 & \text{if } ab \leq 0 \text{ or } bc \leq 0, \\ \min(a, b, c) & \text{if } a, b, c > 0, \\ \max(a, b, c) & \text{if } a, b, c < 0. \end{cases} \quad (3.77)$$

The quadratic reconstruction is then used to find the left and right states of each cell and are used to compute the HLL fluxes in equation 3.68. It is useful to note that as the maximum speed of the system is the speed of light, 1 in the dimensionless units used, the constraint on the time step is simplified and the same for each cell.

### 3.6 Convergence of the solution

When performing numerical simulations it is necessary to use an appropriate grid resolution for a problem to ensure that the calculations are accurate, efficient and numerical dissipation does not affect the simulations. To do this it is instructive to compare numerical simulations to an analytic result. Unfortunately the complexity of relativistic MHD equations does not give a straight analytic result to compare to. For the relativistic tearing mode the resolution for an accurate solution is judged by comparison to the heat equation and relativistic Petschek reconnection via a Richardson expansion.

### 3.6.1 The relativistic tearing mode

There is no easy analytic solution to compare the relativistic tearing mode too but as will be seen in chapter 4 to a very close approximation the one-dimensional diffusion equation for a magnetic field is quite accurate approximation of the background state which the small perturbation grows on. This is most easily seen by comparing figures 4.2 and 4.7. As nearly all the complexity of the simulation is in the current sheet, a one-dimensional diffusion equation will capture the greater resolution needed there as opposed to along the sheet. To study this the diffusion equation in one dimension is

$$\frac{\partial B_y}{\partial t} = \eta \frac{\partial^2 B_y}{\partial x^2}, \quad (3.78)$$

is solved using a similarity method with the boundary conditions

$$B_y(0, t) = 0 \text{ and } \lim_{x \rightarrow \infty} B_y(x, t) \rightarrow \mp 1. \quad (3.79)$$

This has the solution

$$B_y(x, t) = \text{erf} \left( \frac{x}{\sqrt{4\eta t}} \right) \quad (3.80)$$

where  $\text{erf}(x)$  is the error function given by

$$\text{erf}(x) = \frac{2}{\sqrt{\pi}} \int_0^x e^{-\beta^2} d\beta. \quad (3.81)$$

In figure 3.2 the error function at  $t = 1$  is advanced to  $t = 9$  and compared to the analytic result  $\text{erf} \left( \frac{x}{\sqrt{36\eta}} \right)$  for a resolution of 25 to 150 in increments of 25 and then 200 to 600 in increments of 100, and then for a resolution of 800 and 1000 grid points over three spatial units of the code. This shows a clear convergence to the analytic solution of the current sheet at a very fast rate. This is seen clearly in figure 3.3 where we have

resolutions of 25 to a 100 as before comparing with a resolution of 300 and the analytic solution again. This shows the fast convergence and no discernible difference between the analytic solution and a resolution of 300. A resolution past 300 is indiscernible from 300 itself or the analytic solution. Overall the resolution between 100 and 200 is very accurate and on closer inspection there are only minute differences. Hence a resolution of 100 grid points per unit length will be used as an economic minimum across the current sheet with a staggered grid and 50 grid points along the current sheet for numerical simulations of the relativistic tearing mode. Due to the size of the domain for relativistic Petschek simulations the resolution was set at 50 grid points in either direction to keep simulation times reasonable. This was combined with a staggered grid in both directions to focus the resolution on the reconnection site and current sheet where the vast majority of the dynamics occurs.

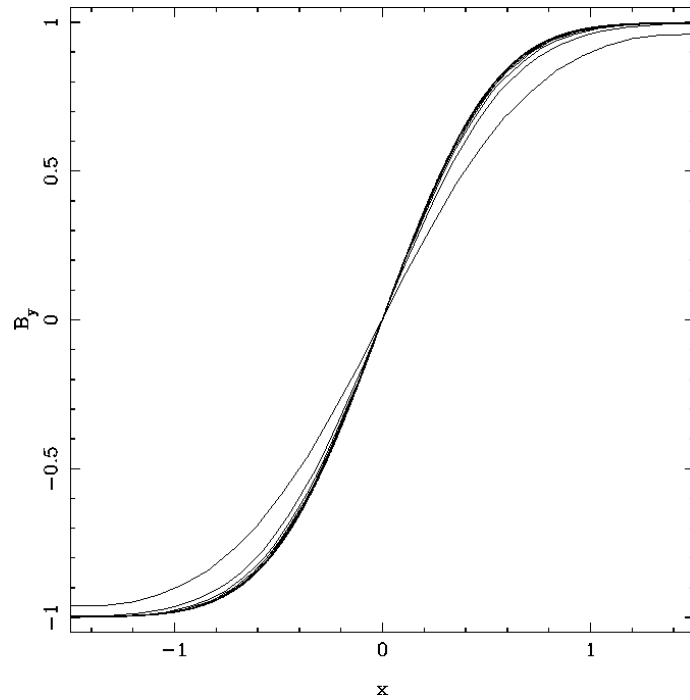


Figure 3.2: Grid convergence of a diffusive current sheet with spatial resolution of 25 to 1000 grid points per 3 unit lengths compared to the analytic solution.

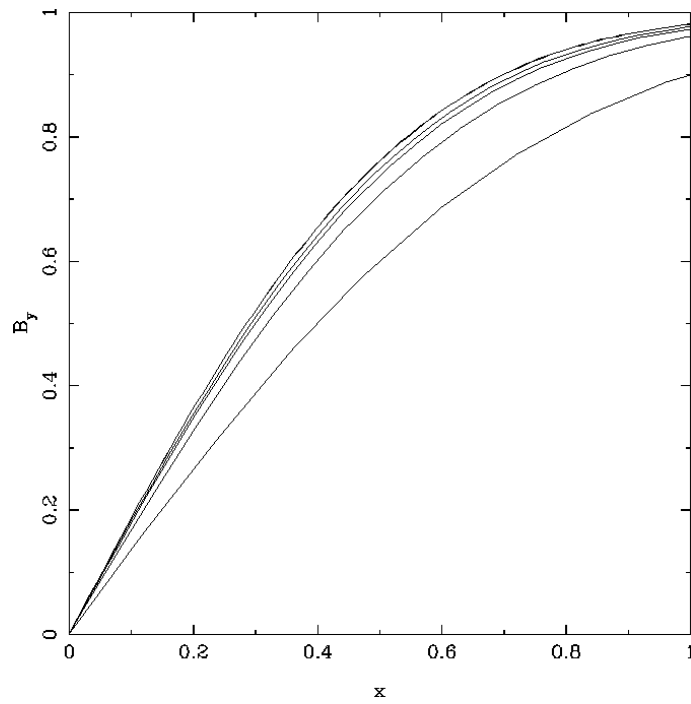


Figure 3.3: An enlarged section of grid convergence for a resolution, from the bottom to the top, of 25 - 100, 300 and the analytic solution.

### A non-uniform grid

In numerical simulations using a non-uniform grid can often lead to greater accuracy where needed and hence a greater economy in run time. Since reconnection in current sheets is the main focus of investigation into relativistic reconnection, their tightly localised and symmetric structure can be used with a non-uniform staggered grid for greater resolution for the same cost.

To do this rather than have a constant spacing between grid points,  $\Delta x$ , a shrinking spacing is used from the boundaries to the centre line. A difference of  $\frac{1}{10}$  was used between the largest and smallest values of  $\Delta x$  to give greater resolution in the centre whilst keeping a good resolution near the boundaries.

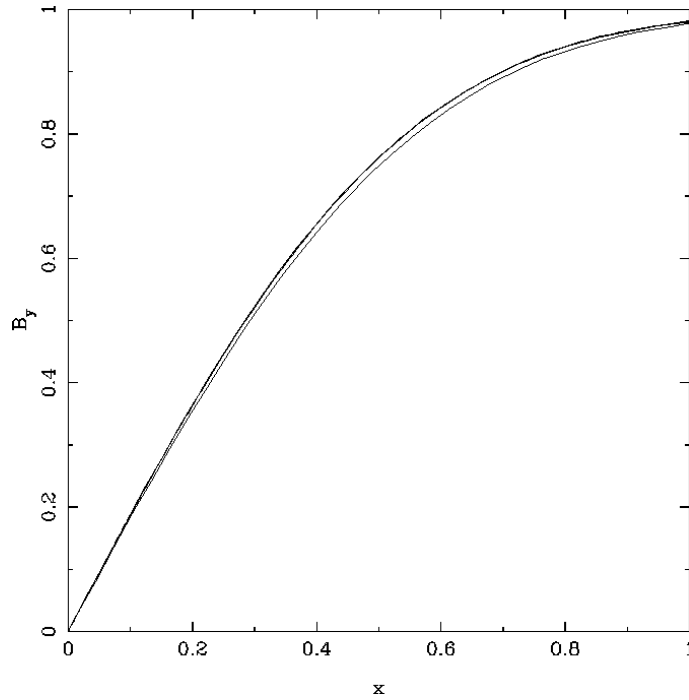


Figure 3.4: Comparison of uniform grid with resolution of 300 and 100 to a non-uniform grid with a resolution of 100 grid points per three unit lengths in one dimension.

In figure 3.4 a non uniform grid with a resolution of 100 is compared to uniform grids of

resolution of 100 and 300. The lower line is the uniform grid with a resolution of 100 and the other two lines are almost concurrent, but on a very close inspection the non uniform grid is slightly more accurate. For a minimum resolution 34 grid points per unit length may now be taken.

This gives a minimum requirement for the resolution for simulations of the tearing mode. This was used in test simulations as a lower limit for the resolution by comparing the difference between solution values until the difference between two numerical solutions was insignificant. The final resolution used to be 50 grid points per unit length across the current sheet.

### 3.6.2 Relativistic Petschek reconnection

Relativistic Petschek reconnection does not have an analogous problem. To test the convergence of the solution simulations were done at various resolutions. The reconnection electric field  $E^* = \mathbf{E} \cdot \mathbf{e}_0$ , is plotted for each different resolution in the  $y$  direction as shown in figure 3.5. This shows a convergence as the resolution increases with the resolution of 50 grid points per unit being in poor agreement with the other resolutions. Figure 3.5 is only shown up to the shortest time for measurements to be taken. This is because an undesired flow was found along the top and bottom boundaries. This is shown in figure 3.6 for a resolution in the  $y$  direction of 125 grid points per unit length. The flow from the centre along the boundary was found for all the simulations, but more pronounced for higher resolution. The undesired boundary flow for the five different resolutions is shown in figure 3.7 at time 12.2. The lowest resolution is almost unaffected whilst the higher resolutions are almost identical. In figure 3.8 the apex of the right hand part of the curve is shown. The difference again is small between the resolutions. This flow causes a pressure drop which crashes the code for high resolutions. The plasma pressure for the boundary flow is shown in figure 3.9 for the resolution in the  $y$  direction of 125 grid points per unit length.



The cause of this flow is unknown. It does not affect the dynamics of relativistic Petschek reconnection, causing the code to crash through the pressure taking a negative value at the boundary. For the lowest resolution of 50 grid points per unit length it did not pose a problem and whilst the solution is not as resolved as desired, it is close to the convergent solution and still gives good quantitative agreement with the order of magnitude predictions in [29]. As such the resolution of 50 grid points per unit length is used for the relativistic Petschek reconnection simulations.

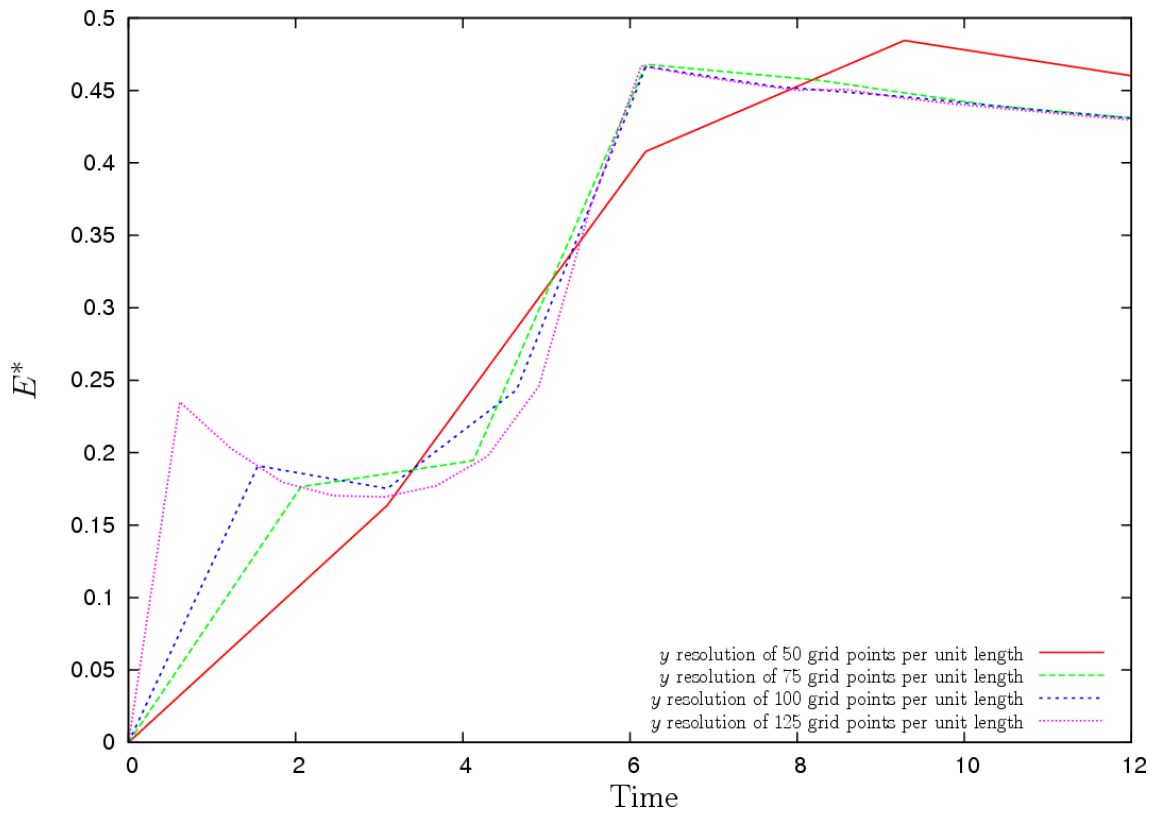


Figure 3.5: A comparison of the reconnection electric field  $E^* = \mathbf{E}(0, 0)$  for different resolutions in the  $y$  direction.

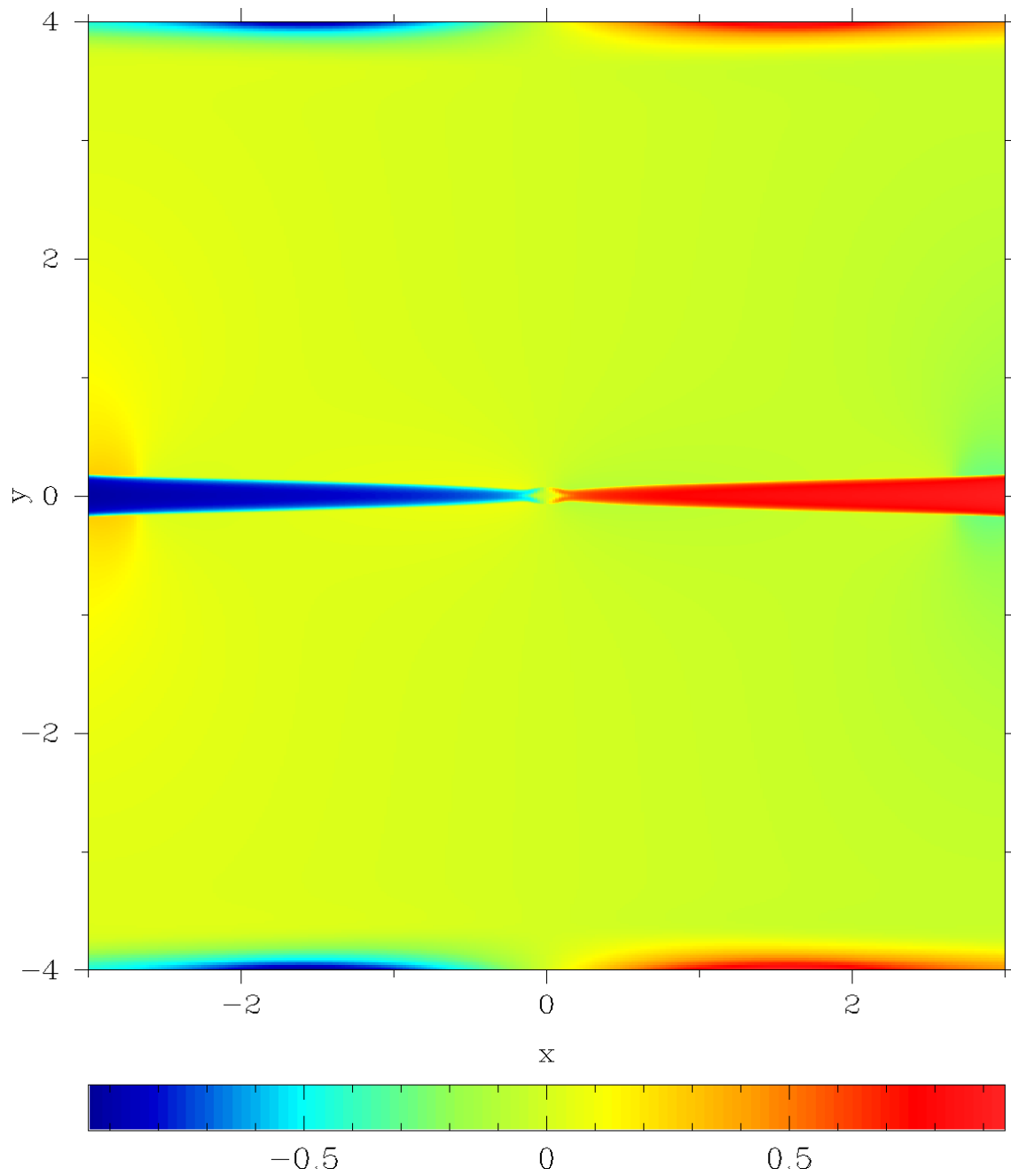


Figure 3.6: The  $v_x$  component of the velocity showing the central outflow velocity and the undesired flow along the boundary at time 13.078, just before the code crashes for the  $y$  resolution of 125 grid points per unit length.

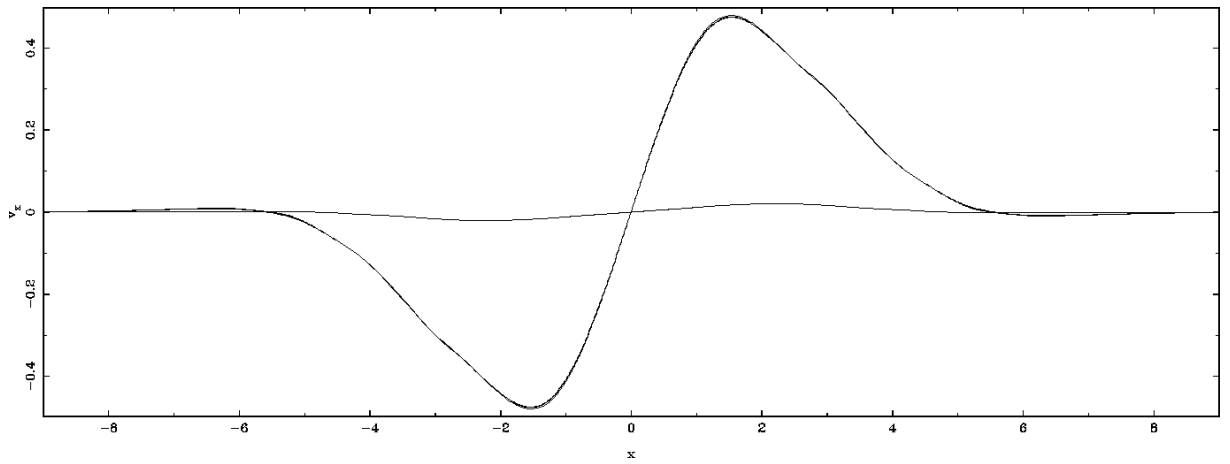


Figure 3.7: The  $v_x$  velocities for the resolutions in the  $y$  direction of 50, 75, 100 and 125 per unit length along the boundary at time 12.2.

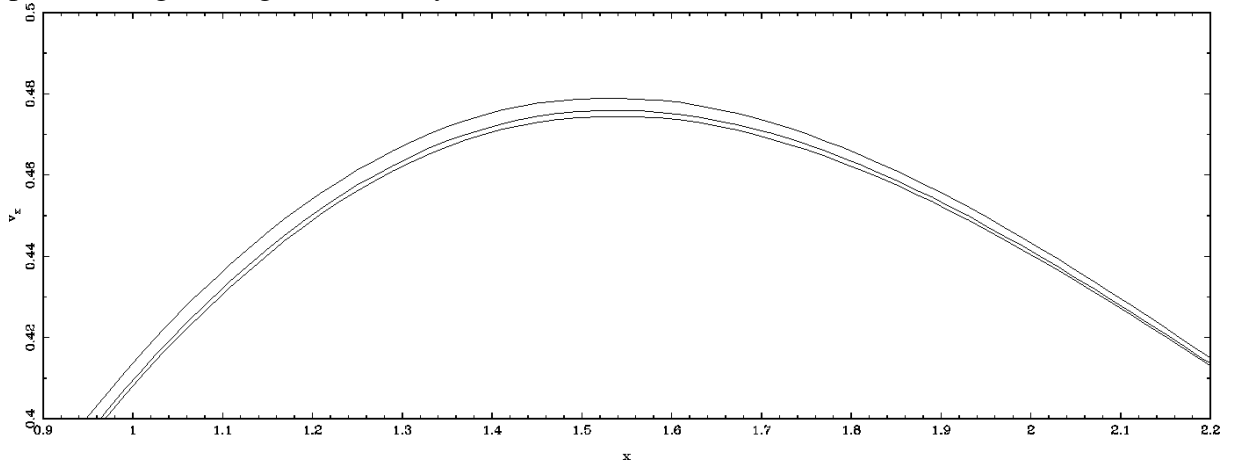


Figure 3.8: A magnified view of the  $v_x$  velocities for the different resolutions in the  $y$  direction of 75, 100 and 125 per unit length along the boundary again at time 12.2.

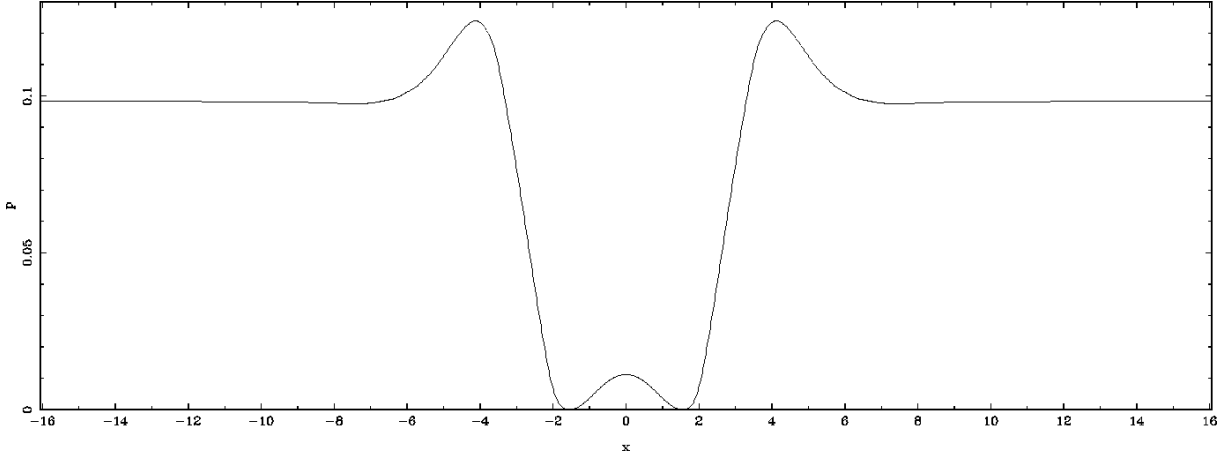


Figure 3.9: The plasma pressure along the top boundary at time 13.078 just before the crash showing the drop to zero corresponding to the parallel flow along the boundary.

### 3.7 Boundary conditions, domain size and Courant number

The choice of boundary conditions, domain size and Courant number were chosen through theory and testing. They are documented separately for the relativistic tearing mode and relativistic Petschek reconnection.

#### 3.7.1 The relativistic tearing mode

The boundary conditions chosen for the relativistic tearing mode are periodic in  $x$  and free flow in  $y$ . The free flow boundaries in  $y$  were chosen as to model, with the initial setup, two regions of oppositely aligned magnetic field each with a large reserve of magnetic energy as described in the physical motivation in chapter 1. When reconnection is triggered this provides a source for more magnetic field lines to be drawn in since they are tied to the plasma by the frozen flux condition. The boundaries in  $x$  could be

chosen to be either periodic or free flow. They were chosen as periodic as the focus of the simulations was the linear growth stage which was unaffected by the choice of boundary conditions. The periodic conditions were also chosen so if time was available the formation of magnetic islands could be studied opposed to the ejection of plasmoids which has been more generally studied.

Free flow boundary conditions allow waves to pass through the boundary and flows through it. This is done by having the derivatives to be zero at the boundary.

With periodic boundary conditions in  $x$  the domain in the  $x$  direction was chosen to be the wavelength of the perturbation. The domain in the  $y$  direction was chosen so that the boundaries did not affect the reconnection region. Through testing this was found to be  $y \in [-2, 2]$ .

In the code, once the spatial grid was set the Courant number  $C_n$ , was used to control the time step via

$$C_n = \frac{\Delta x}{\Delta t} \quad (3.82)$$

where in comparison to equation 3.25 the fastest speed of the system is the speed of light which is one in the units of the code.

The Courant number was set to 0.1 so that the time step was sufficiently small enough to give an accurate solution. The time step was of the order of  $10^{-3}$  with some small variation due to the non-uniformity of the grid in the  $y$  direction.

### 3.7.2 Relativistic Petschek reconnection

The boundary conditions for relativistic Petschek reconnection were chosen to be free flow in both directions. The  $y$  boundaries were chosen for the same reason as for the relativistic tearing mode whilst the  $x$  boundaries are free flow so that the relativistic

jet caused by the reconnection can push out into the plasma and past the boundaries to achieve a steady state. Unfortunately this did not occur with the interface between the jet and the ambient plasma interacting with the boundary and causing it to crash. This is documented in section 3.8.

The domain in the  $y$  direction was chosen to be  $y \in [-4, 4]$  so that the boundaries do not interact with the reconnection region or the shocks emanating from it. The choice of  $y$  boundary was found through initial testing of relativistic Petschek simulations. As the interface between the outflowing jet and ambient plasma interacted with the boundary, causing the simulation to crash, the  $x$  boundary had to be set to allow the solution to settle to a steady state in a region large enough to get accurate data to compare to the theory. This is balanced by the increase of run time with the larger domain. The compromise between these two conditions was to set  $x \in [-16, 16]$  giving an effective region of steady state when the jet started to interface with the boundary of  $x \in [9, -9]$ .

The Courant number was used to control the time step as described in the last section. It was set to  $C_n = 0.1$  to again give an accurate solution. This gave a time step of  $1.03 \times 10^{-3}$ . This is the same for all the relativistic Petschek simulations as the same grid was used for all of them.

### 3.8 Limitations

All numerical codes have some limitations from minor ones, where for example the range of a dimensionless parameter is limited or how hard the system can be driven, to major ones. The code used to conduct simulations of relativistic resistive magnetohydrodynamics has three major problems. These are Alfvén waves interacting with free flow boundaries, the magnetisation parameter (or plasma beta) and the resistivity  $\eta$  and how it affects the resistive half time steps described in section 3.4.

It was found for free flow boundary conditions that rather than pass through the boundaries, Alfvén waves would reflect off them and on reflection increase in magnitude. Whilst this is a problem for the code in general, it does not pose a problem for this work on relativistic reconnection. For the relativistic tearing mode away from the current sheet the solution is a simple inflow with no waves. Along the current sheet only periodic boundary conditions were used and as the Alfvén waves interact with periodic boundaries without any difficulties, the problem Alfvén waves have with free flow boundary conditions does not affect the relativistic tearing mode. Relativistic Petschek reconnection has the same inflow, if seeded up, away from the current sheet and relativistic shocks and along the current sheet the jet is the first wave to reach the boundary and causes the code to crash through problems with the pressure gradients before an Alfvén wave can be reflected off the boundary.

The magnetisation parameter is the ratio of the magnetic energy to the rest mass energy and is defined as

$$\varsigma = \frac{B^2}{\gamma^2 \rho} \quad (3.83)$$

and is a measure of how magnetically dominated the plasma is.

A second parameter that gives a measure of how magnetically dominated the plasma is is the plasma beta  $\beta$  which is the ratio of the plasma pressure to the magnetic pressure  $p_m = \frac{B^2}{2}$  and it is defined as

$$\beta = \frac{2p}{B^2}. \quad (3.84)$$

In any physical situation where relativistic reconnection is expected to be magnetically dominated (with the magnetic energy density dominating the total energy density including the rest mass) it will have  $\varsigma \gg 1$  and  $\beta \ll 1$ .

For the relativistic tearing mode the largest magnetisation parameter is 40 and smallest plasma beta is 0.05. It was found that going any higher with the magnetisation parameter or lower with the plasma beta the code became unreliable and frequently crashed. The cause of this is the routine in the code which finds the primitive variables from the conserved ones. As the plasma becomes more magnetically dominated the contribution to the energy density and momentum density from the plasma pressure and density becomes very small and the iterative process does not converge to physically realistic values, giving one or both as negative.

Relativistic Petschek reconnection has a magnetisation parameter of 65.51 and plasma beta of 0.03 for all the simulations. These are more larger and smaller respectively than the relativistic tearing mode and can take these values due to the reduction of the resistivity in the relativistic Petschek simulations. That the parameters can take more extreme values than the relativistic tearing mode is described in the problems with the resistivity. As before the parameters could not be taken to the desired limits as the same problem with the iterative process affects the plasma pressure and density and hence the parameters.

The resistivity  $\eta$  plays a major role in magnetic reconnection. Outside the current sheet the plasma should behave like an ideal one with the large gradients in the magnetic field in the current sheet acting with the resistivity to give reconnection. As such a small value of the resistivity is required for simulations of relativistic reconnection.

For the relativistic tearing mode the simulations were done with two values of the resistivity  $10^{-3}$  and  $10^{-4}$  to vary the relativistic Lundquist number. Simulations of relativistic Petschek reconnection were all done with a resistivity of  $10^{-2}$  except for one run with  $10^{-3}$ . Attempts at simulations for smaller values of the resistivity crashed before the solution was developed enough to take any measurements.

The inability of lowering the resistivity come from how the stiff resistive term is dealt with. The two resistive half time steps described in section 3.4. In the half time steps only the electric field is evolved as given by equations 3.61 and 3.62 and the energy



density, momentum density and magnetic field are held constant. To keep these constant the plasma pressure and density must change. This can give non-physical results for the energy density, kinetic energy density or the state variables themselves which will cause the code to come to a halt. As a highly magnetised plasma already has problems with finding the plasma pressure and density as described above, the problems with the resistivity exacerbate this.

As the change in the electric field is related to the exponential of the time step as seen in equations 3.61 and 3.62, a smaller time step reduces the magnitude in the change in the electric field and reduces the problems in changing the plasma pressure and density. Unfortunately as this goes like the exponential of the time step it must be greatly reduced for this to have an effect and causes the simulations to be too expensive.

To compare different relativistic Lundquist numbers this was done once for relativistic Petschek reconnection where  $\eta = 10^{-3}$  with a massively increased run time.

### 3.9 Conversion to dimensional results

To compare the numerical results with observations the non-dimensionalised results of the code must be translated back into dimensional units. As the width of the current sheet is known from the simulations  $l_n$  it can be compared to the observed value  $l_d$  to give the factor  $l_o$  which is used to multiply a length by in the code to get it in the dimensional units of  $l_d$  where

$$l_o = \frac{l_d}{l_n}. \quad (3.85)$$

As the speed of light is unity in the units of the code the factor  $t_o$  to multiply a time by to get a dimensional time in the system of units used for the length  $l_d$  and the speed of light is given by

$$t_o = \frac{l_o}{c} = \frac{l_d}{cl_n}. \quad (3.86)$$

To find the general factor to dimensionalise a numerical result a third factor is needed. It is simplest to find the mass  $m_o$  from the magnetic energy since

$$B_o^2 = \frac{m_o}{l_o t_o^2}, \quad (3.87)$$

giving

$$m_o = B_o^2 l_o t_o^2. \quad (3.88)$$

Since the magnetic field factor can be found from  $B_o = B_d/B_n$  and using the definitions for  $l_o$  and  $t_o$  the mass factor is

$$m_o = c^{-2} \left( \frac{B_d}{B_n} \right)^2 \left( \frac{l_d}{l_n} \right)^3. \quad (3.89)$$

The numerical factors are known from the individual simulations. For the relativistic tearing mode  $l_n = 0.1$  and  $B_n = \sqrt{\frac{2p}{\beta}}$  where  $\beta$  is the plasma beta and is varied in different simulations. The simulations of relativistic Petschek reconnection has  $l_n = 0.05$  and  $B_n = 2\sqrt{\frac{5}{3}}$ .

## Chapter 4

### The relativistic tearing mode

The tearing mode and its early development are described in chapter 1 and this chapter will document the tearing mode in relativistic resistive magnetohydrodynamics. The first half of the chapter begins with a sketch of the physical process, followed by the order of magnitude analysis of Lyubarsky (see [29]) and then the linear analyses of the tearing mode in magnetodynamics (see [27]). The second half of the chapter contains the numerical model, investigations, a description of the relativistic tearing mode and the results.

#### 4.1 Mathematics of the relativistic Sweet-Parker current sheet and tearing mode

In section 4.1.1 an order of magnitude calculation, originally done by Lyubarsky in [29], is reproduced to give an order of magnitude value for the important variables of the relativistic tearing mode. In section 4.1.2 the linear analysis of the tearing mode for magnetodynamics is reproduced from the version in a paper by Komissarov et al. in [27] for a framework to study the dispersion relation of the tearing mode in the fully

magnetohydrodynamical setting.

### 4.1.1 An order of magnitude calculation for the relativistic Sweet-Parker current sheet

Following the work of Prof. Lyubarsky in his paper [29] an order of magnitude calculation will be carried out to give properties of the inflow, outflow and ratio of these velocities for the relativistic tearing mode.

To make the problem manageable the following assumptions will be made

- the current sheet has width  $l$  and length  $L$  and is in the  $x$ - $y$  plane,
- there is a scalar resistivity  $\eta$  related to the conductivity  $\sigma$  by  $\eta = \frac{1}{\sigma}$ ,
- a steady state has been achieved,
- the electric force  $q\mathbf{E}$  is negligible in the momentum equation,
- units of the code are used and as such  $c = 1$  and the factor  $4\pi$  is absorbed into the electromagnetic field,
- reconnection was triggered by a small perturbation from zero of  $B_y$ .

The last assumption is justifiable in the linear growth phase where the inflow of magnetic field has balanced the diffusion and the field lines are starting to reconnect. Here the electric field will have just started growing in size and will still be small.

The set-up is illustrated in figure 4.1.

In a steady state there will be equilibrium of the total pressure  $p_t = p + \frac{B^2}{2}$  across the current sheet. Since outside it is magnetically dominated and inside the magnetic field is

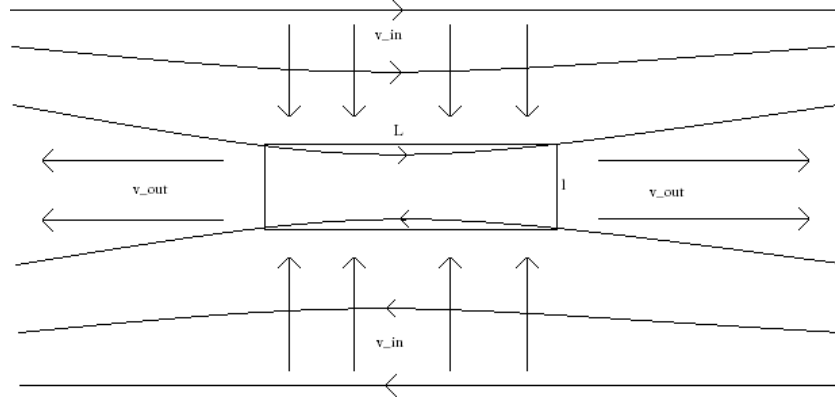


Figure 4.1: A sketch diagram of the relativistic Sweet-Parker current sheet showing the reconnecting region (the box), the magnetic field lines (centred arrows) and the velocity (the headed arrows).

small compared to the pressure ( $\beta > 1$ ) and denoting the constant outer field as  $B_0$ , we have

$$p = \frac{B_0^2}{2}. \quad (4.1)$$

Next we need the momentum equation 2.20 rewritten as conservation of momentum with body forces as a source term. This is

$$\partial_t(w\gamma^2\mathbf{v}) + \nabla \cdot (w\gamma^2\mathbf{v}\mathbf{v} + p\delta) = q\mathbf{E} + \mathbf{J} \times \mathbf{B}. \quad (4.2)$$

With the steady state form an estimate of the outflow velocity  $v_{out}$  can be found. The steady state in the current sheet is

$$\partial_x(wv_{out}^2\gamma_{out}^2 + p) = -J_z B_y. \quad (4.3)$$

In 4.3 the  $J_y B_z$  term in the magnetic force is due to  $J_y = -\partial_x B_z$  and there being very little variation of  $B_z$  in the  $x$  direction.

Next for the steady state Ampère equation 2.17, we get

$$\mathbf{J} = \nabla \times \mathbf{B}. \quad (4.4)$$

Since  $B_y$  is a small perturbation its derivative is ignorable and replacing the  $x$  derivative with  $l$  and  $B_x$  by  $B_0$  we get

$$J_z = -\frac{B_0}{l}. \quad (4.5)$$

Replacing the derivative in equation 4.3 by  $L$  we get

$$wv_{out}^2\gamma_{out}^2 - p = B_0B_y\frac{L}{l}. \quad (4.6)$$

Finally we use the no magnetic monopole condition 2.18 to get  $B_y \sim \frac{l}{L}B_0$  and hence

$$wv_{out}^2\gamma_{out}^2 - p = B_0\frac{L}{l}\left(\frac{l}{L}B_0\right) = B_0^2. \quad (4.7)$$

As we are investigating a relativistically magnetised plasma, in the inflow region the enthalpy can be taken as  $w = 4p$  as the assumption of a relativistically hot plasma. From equation 4.7, for the plasma to be accelerated to high Lorentz factors only if the enthalpy greatly decreases. This cannot happen as the pressure and hence the enthalpy are linked to the external magnetic field by equation 4.1 and are constant.

Hence we have

$$\gamma_{out}, v_{out} \sim 1. \quad (4.8)$$

Far along the current sheet the plasma can attain relativistic speeds if the outer pressure drops, but reconnection rates are judged from the maximum of the magnetic field and the pressure near here will not decrease much.

To get a handle on the ratio of the velocities the steady state energy flux,

$$\nabla \cdot (\mathbf{E} \times \mathbf{B} + w\gamma^2 \mathbf{v}) = 0, \quad (4.9)$$

is considered. In the outflow the Poynting flux will be small compared to the matter outflow and in the inflow the opposite case will be true. So replacing derivatives by length scales and using  $\gamma_{out} \sim 1$  we get

$$\frac{w\mathbf{v}_{out}}{L} = \frac{\mathbf{E} \times \mathbf{B}}{l}. \quad (4.10)$$

In the inflow region there is no magnetic gradient and the resistive terms are unimportant and may be treated as an ideal one and with the charge density being negligible along with equation 4.8, Ohm's law is the same as in the classical case, and hence

$$\mathbf{E} + \mathbf{v} \times \mathbf{B} = 0 \quad (4.11)$$

and with  $\mathbf{v} = v_{in}\hat{\mathbf{y}}$  in the inflow region this gives

$$\mathbf{E} = (-v_{in}B_{z(in)}, 0, v_{in}B_x), \quad (4.12)$$

and hence the  $y$  component of the electromagnetic influx is  $(\mathbf{E} \times \mathbf{B})_y = v_{in}(B_x^2 + B_{z(in)}^2)$ .

Using this, the energy balance is

$$\frac{v_{in}(B_0^2 + B_{z(in)}^2)}{l} = \frac{wv_{out}}{L}. \quad (4.13)$$

From the relativistically hot plasma approximation of the outflow,  $w = 4p$  and by equation 4.1, the ratio of the inflow and outflow is

$$\frac{v_{in}}{v_{out}} \sim \left( \frac{1}{1 + \frac{B_{z(in)}^2}{4p}} \right) \frac{l}{L}. \quad (4.14)$$

As the inflow magnetic field is expected to be close to being anti-parallel it will have  $B_{z(in)}^2 \ll B_x^2 \sim B_0^2 = 2p$  where the last equality is from equation 4.1 and hence equation 4.14 gives

$$\frac{v_{in}}{v_{out}} \sim \frac{l}{L}, \quad (4.15)$$

which means the plasma is roughly incompressible.

If now the  $z$  component of the magnetic field flux  $\nabla \times \mathbf{E} = \mathbf{0}$  is considered then

$$\frac{\partial E_y}{\partial x} = \frac{\partial E_x}{\partial y}, \quad (4.16)$$

and considering this in the inflow and outflow is

$$\frac{E_{y(out)}}{L} = \frac{E_{x(in)}}{l}. \quad (4.17)$$

Then from equation 4.12, in the inflow  $E_{x(in)} = -v_{in}B_{z(in)}$ . In the outflow the resistivity will be important and from Ohm's law

$$E_{y(out)} = v_{out}B_{z(out)} + \eta J_{y(out)}. \quad (4.18)$$

Combining these results with the fact that  $J_y \approx 0$  gives

$$B_{z(in)} = -B_{z(out)} \frac{v_{in}}{v_{out}} \frac{L}{l} \quad (4.19)$$

and hence



$$B_{z(in)} \sim B_{z(out)}. \quad (4.20)$$

So a small  $z$  component of the magnetic field in the inflow will not significantly affect the outflow.

To find  $v_{in}$  the steady state Faraday equation 2.17 is used to find  $E_z$  is a constant. So using the ideal plasma condition 4.11 for outside the sheet,  $E_z \sim v_{in} B_0$  and since inside the sheet  $\gamma_{out}^2 \sim 1$  the usual non-relativistic Ohm's law can be used to give  $E_z = \eta J_z$ . Then, using equation 4.4,  $E_z = \frac{\eta B_0}{l}$ . Combining these gives

$$v_{in} B_0 = \frac{\eta B_0}{l}. \quad (4.21)$$

Upon cancelling and using the definition of the relativistic Lundquist number in code units where the speed of light is one,  $L_u = \frac{l}{\eta}$  we get

$$v_{in} = L_u^{-1}. \quad (4.22)$$

If, instead  $l$  is eliminated from equation 4.21 using equation 4.15 and the result that  $v_{out} \sim 1$  then the inflow velocity can be defined using the external relativistic Lundquist number  $S_u$  which uses the length of the domain  $L$ , instead of the current sheet thickness  $l$  by

$$v_{in} = \sqrt{\frac{\eta}{L}} = S_u^{-\frac{1}{2}}. \quad (4.23)$$

### 4.1.2 Analysis of the relativistic tearing mode

In [30] linear analysis is shown for resistive force-free electrodynamics (magnetodynamics). This is reproduced succinctly using the same method as for incompressible magnetohydrodynamics first produced by Furth et al. in [11] and

reproduced in more clarity in [39] for magnetodynamics with the assumption of constant magnetic energy in [27]. In the same vein as these works an analytic framework for the linear regime of the tearing mode in relativistic resistant magnetohydrodynamics is constructed and its limitations discussed.

To begin first a quasi-equilibrium approximation is made to simplify the equations. To do this three time scales are introduced, the light crossing time,  $\tau_c$ , the diffusive time  $\tau_d$  and the time scale of the tearing mode  $\tau$  where

$$\tau_c = \frac{l}{c} \quad \text{and} \quad \tau_d = \frac{l^2}{\eta}, \quad (4.24)$$

and  $l$  is the width of the current sheet.

Since  $\tau$  gives the global evolution of the current sheet, the light crossing time will be much smaller allowing a small parameter  $\mu_c$  to be defined by

$$\mu_c = \frac{\tau_c}{\tau} \ll 1. \quad (4.25)$$

A quasi-equilibrium current sheet will be slowly diffusing and can be considered stationary compared to growth from an instability. Hence a second small parameter  $\mu_d$  can be defined as

$$\mu_d = \frac{\tau}{\tau_d} \ll 1. \quad (4.26)$$

These two small parameters ensure that the relativistic Lundquist number,  $L_u$  remains large,

$$L_u = \frac{lc}{\eta} = \frac{l^2}{\eta} \cdot \frac{c}{l} = (\mu_d \mu_c)^{-1} \gg 1. \quad (4.27)$$

The final piece of information needed is an idea of the comparative strengths of the magnetic and electric fields. To do this Faraday's equation 2.17 is non-dimensionalised by setting the variable as

$$X = \mathcal{X} \hat{X} \quad (4.28)$$

where  $\hat{X}$  is the dimensionless variable and  $\mathcal{X}$  is the dimensional multiplier. The dimensional multipliers are the global evolution time scale  $\tau$  for time, the current sheet's width  $l$  for length,  $\mathcal{B}$  for the magnetic field and  $\mathcal{E}$  for the electric field. Then Faraday's equation is

$$\frac{l}{\tau} \frac{\partial \hat{\mathbf{B}}}{\partial \hat{t}} + \frac{\mathcal{E}}{\mathcal{B}} \nabla \times \hat{\mathbf{E}} = \mathbf{0}, \quad (4.29)$$

which leads to

$$\frac{\mathcal{E}}{\mathcal{B}} = \mu_c \ll 1. \quad (4.30)$$

Hence the magnetic field is much stronger than the electric field. For simplicity the hats are dropped in the following calculations. With this final piece of information the quasi-equilibrium equations can be found.

The dimensional Ampère equation 2.15 with the Ohm's law 2.26 and taking the Lorentz factor  $\gamma \approx 1$ , as mildly relativistic flows are expected from 4.1.1, gives

$$-\mu_c^2 \partial_t \mathbf{E} + \nabla \times \mathbf{B} = L_u (\mu_c \mathbf{E} + \mu_c \mathbf{v} \times \mathbf{B} - \mu_c^3 (\mathbf{v} \cdot \mathbf{E}) \mathbf{v}) + \mu_c^2 q \mathbf{v}, \quad (4.31)$$

and since  $\mu_c \ll 1$  with terms of order  $\mu_c^2$  and terms of order  $L_u \mu_c^3$  dropped this gives, back in non-dimensionalised code units,

$$\nabla \times \mathbf{B} = \sigma (\mathbf{E} + \mathbf{v} \times \mathbf{B}). \quad (4.32)$$

Making the electric field the subject of equation 4.32 and substituting into the Faraday equation 2.17 gives the induction equation

$$\partial_t \mathbf{B} = \nabla \times (\mathbf{v} \times \mathbf{B}) + \eta \nabla^2 \mathbf{B}. \quad (4.33)$$

The second equation to be approximated is the conservation of momentum equation 2.20 in dimensional form. Using the same units as before and using  $\mathcal{P}$  as the unit of pressure and  $\frac{\mathcal{P}}{c^2}$  as the unit of mass from  $E = mc^2$  to represent the enthalpy  $w$ , we get

$$\begin{aligned} & \mu_c^2 \partial_t \left( \mathbf{E} \times \mathbf{B} + \frac{\beta w}{2} \mathbf{v} \right) \\ &= \nabla \cdot \left( \mathbf{B} \mathbf{B} + \mu_c^2 \mathbf{E} \mathbf{E} - \frac{\beta \mu_c^2 w}{2} \mathbf{v} \mathbf{v} - \left( \frac{1}{2} (B^2 + \mu_c^2 E^2) + \frac{\beta p}{2c^2} \right) \delta \right), \end{aligned} \quad (4.34)$$

using  $\mu_c$  as before and the plasma beta  $\beta = \frac{2\mathcal{P}}{B^2}$ .

If now, as before we drop terms of order  $\mu_c^2$ , the momentum equation becomes the condition for a force-free magnetic field. This occurs as when the equations have been non-dimensionalised they have become an expansion in  $\mu_c$ . As this non-dimensional parameter gives the ratio of the light crossing time to the growth time of the relativistic tearing mode and is taken as small, dropping higher order terms in  $\mu_c$  assumes that the time taken to establish a dynamics equilibrium is very small compared to the time taken for the relativistic tearing mode to evolve. Since the magnetic field is the driving force for relativistic magnetic reconnection, it establishes the global evolution of the system and will move to a force free configuration. This does not help in studying the tearing mode in relativistic magnetohydrodynamics as the matter, which will be dominant inside the current sheet, is ignored.

An interesting approach is to use the assumption that the system is greatly magnetically dominated and as such the plasma beta is small  $\beta \ll 1$ . If this is used as a small parameter it leads to the momentum equation of magnetodynamics,

$$\partial_t (\mathbf{E} \times \mathbf{B}) + \nabla \cdot \left( -\mathbf{B}\mathbf{B} + \frac{1}{2}B^2\delta \right) = \mathbf{0}, \quad (4.35)$$

where the electric field has been dropped due to the magnetic field's dominance from equation 4.30. To rewrite this in a more familiar form for analysis of the tearing mode, the Poynting flux is rewritten using the magnetic energy density  $\rho_{mag}$  and the drift velocity of a charged particle  $\mathbf{V}_{drift}$ , which are defined as

$$\rho_{mag} = \frac{B^2}{2} \quad \text{and} \quad \mathbf{V}_{drift} = \frac{\mathbf{E} \times \mathbf{B}}{B^2}, \quad (4.36)$$

to give

$$\partial_t (2\rho_{mag}\mathbf{V}_{drift}) + \nabla \cdot \left( -\mathbf{B}\mathbf{B} + \frac{1}{2}B^2\delta \right) = \mathbf{0}. \quad (4.37)$$

The standard approach is to use equations 4.33 and 4.37 together to find inner and outer solutions for the current sheet, then match them to get analytic results for the thickness, maximal growth rate and corresponding wavelength and dimensional time scale. Equation 4.33 is the same as for the analysis of resistive magnetohydrodynamics and equation 4.37 is the same as for resistive magnetodynamics. These similarities suggest a similar method will produce a framework to analyse results produced by numerical simulations. Unfortunately this is not feasible, as the system of equations 4.33 and 4.37 is open, with not enough equations to describe all the variables. On further investigation closing this system is only marginally simpler than the full system of equations given in section 2.1. This system is reducible in the number of variables but still not succinct enough for an analytic approach.

To analyse the results of numerical simulations the work presented in [27] for the tearing mode in magnetodynamics will be used as a guide. This is chosen to analyse the results as in the inflow region the plasma is magnetically dominated with the matter expected to have little effects on the evolution except to be pulled into the current sheet with the

magnetic field as it is frozen into the plasma. the second reason for doing this is that there is established theory on it which is well known.

The major limitations of using a magnetodynamic framework are the same as those that inspired this research, the plasma pressure. This is expected to play an important role inside the current sheet. As is shown in figure 4.2, the quasi-equilibrium current sheet has constant total pressure  $p_t$  and so as the magnetic field reconnects inside the sheet the plasma pressure will increase to match the drop in magnetic pressure. This gives very low plasma betas outside the sheet justifying the assumption made in deriving equation 4.37, but large plasma betas inside the sheet. The other difference is the assumption of constant magnetic energy, which to zeroth order is constant in magnetodynamics, but not so in magnetohydrodynamics where the current sheet has been found to be very compressible.

For completeness the derivation of the expected growth rate, time scale and width of the magnetodynamic current sheet will be presented here.

In this the subscripts on the drift velocity  $\mathbf{V}_{drift}$  and magnetic energy density  $\rho_{mag}$  will be dropped and the basic equations of incompressible (constant magnetic energy) quasi-equilibrium magnetodynamics, found using the small parameters  $\mu_c$  and  $\mu_d$ , are

$$\partial_t \mathbf{B} = \nabla \times (\mathbf{V} \times \mathbf{B}) + \eta \nabla^2 \mathbf{B}, \quad (4.38)$$

and taking the curl of 4.37 to get

$$\rho \partial_t (\nabla \times \mathbf{V}) = \frac{1}{4\pi} \nabla \times ((\mathbf{B} \cdot \nabla) \mathbf{B}), \quad (4.39)$$

with the conditions

$$\nabla \cdot \mathbf{B} = 0 \quad \text{and} \quad \nabla \cdot \mathbf{V} = 0. \quad (4.40)$$

Now these equations are perturbed and linearised around the background steady state of a force-free magnetic field

$$\mathbf{B} = \left( B_0 \tanh \left( \frac{y}{l} \right), 0, B_0 \operatorname{sech} \left( \frac{y}{l} \right) \right), \quad (4.41)$$

using the expansion  $\psi = \psi_0 + \psi_1$  where  $\psi_0$  is the background state and

$$\psi_1 = \tilde{\psi}_1(y) e^{i(\mathbf{k} \cdot \mathbf{x}) + \omega t}, \quad (4.42)$$

is the perturbation to the background state. In the perturbation  $\mathbf{x}$  is the position vector,  $\mathbf{k} = (k_x, 0, k_z)$  is the wavenumber vector,  $\omega$  is the growth rate and  $\tilde{\psi}(y)$  is a function of  $y$  and is used to describe more general behaviour than that of a periodic solution.

It is quite straightforward to substitute this into the induction equation 4.38 to get

$$\omega \mathbf{B}_1 = i (\mathbf{B}_0 \cdot \mathbf{k}) \mathbf{V}_1 - V_{y1} \mathbf{B}'_0 + \eta (\mathbf{B}''_1 - k^2 \mathbf{B}_1). \quad (4.43)$$

In the above equation the notation  $' = \frac{d}{dy}$  and  $\psi_{y1}$  is the  $y$  component of the small perturbation vector  $\psi_1$ .

Next the curl of equation 4.39 is taken and when the substitution is made this becomes

$$\begin{aligned} -\omega (\mathbf{V}''_1 - k^2 \mathbf{V}_1) = & \frac{1}{4\pi\rho} \left( 2 (i (\mathbf{B}''_0 \cdot \mathbf{k}) B_{y1} \hat{\mathbf{y}} + i (\mathbf{B}'_0 \cdot \mathbf{k}) B_{y1} \mathbf{k} + i (\mathbf{B}'_0 \cdot \mathbf{k}) B'_{y1} \hat{\mathbf{y}}) \right. \\ & - (i (\mathbf{B}''_0 \cdot \mathbf{k}) \mathbf{B}_1 + 2i (\mathbf{B}'_0 \cdot \mathbf{k}) \mathbf{B}'_1 + i (\mathbf{B}_0 \cdot \mathbf{k}) \mathbf{B}''_1) \\ & \left. + i (\mathbf{B}_0 \cdot \mathbf{k}) k^2 \mathbf{B}_1 - \nabla^2 (B_{y1} \mathbf{B}'_0) \right). \end{aligned} \quad (4.44)$$

From these equations a closed form for  $\tilde{B}_{y1}$  and  $\tilde{V}_{y1}$  can be found by taking the  $y$  components of each. If the exponentials are cancelled as well, this gives

$$\omega \tilde{B}_{y1} = i (\mathbf{B}_0 \cdot \mathbf{k}) \tilde{V}_{y1} + \eta \left( \tilde{B}_{y1}'' - k^2 \tilde{B}_{y1} \right) \quad (4.45)$$

and

$$\omega \left( \tilde{V}_{y1}'' - k^2 \tilde{V}_{y1} \right) = \frac{i (\mathbf{B}_0 \cdot \mathbf{k})}{4\pi\rho} \left( -\frac{(\mathbf{B}_0'' \cdot \mathbf{k})}{(\mathbf{B}_0 \cdot \mathbf{k})} \tilde{B}_{y1} + \tilde{B}_{y1}'' - k^2 \tilde{B}_{y1} \right). \quad (4.46)$$

When  $\mathbf{B}_0 \cdot \mathbf{k}$  is zero in equation 4.46, the second order derivative for the magnetic field is lost. This suggests a boundary layer approach to the problem as a sublayer will develop here. To make things easier, but losing complete generality, the sublayer can be placed in the centre of the current sheet by taking  $\mathbf{k} = k\hat{\mathbf{x}}$ . This also makes the problem symmetric about  $y = 0$ .

The next step is to non-dimensionalise the equations. The obvious start to this is to set

$$\bar{y} = \frac{y}{l}, \quad b = \frac{\tilde{B}_{y1}}{B_0}, \quad \bar{k} = kl, \quad f(\bar{y}) = \frac{B_{0x}}{B_0} = \tanh \bar{y}. \quad (4.47)$$

This also gives  $\frac{d}{dy} = \frac{1}{l^2} \frac{d}{d\bar{y}}$  and hence  $\frac{d^2 f}{dy^2} = \frac{1}{l^2} \frac{d^2 f}{d\bar{y}^2} = f''$ . To complete the non-dimensionalisation we rescale time by the diffusion time  $\tau_d$  and velocity as shown

$$\bar{\omega} = \frac{l^2 \omega}{\eta} \quad \text{and} \quad v = \frac{-ikl^2}{\eta} \tilde{V}_{y1}. \quad (4.48)$$

This gives the non-dimensional versions of 4.45 and 4.46,

$$\bar{\omega} b = -fv + b'' - \bar{k}^2 b \quad (4.49)$$

and

$$\delta \bar{\omega} (v'' - \bar{k}^2) = f \left( -\frac{f''}{f} b + b'' - \bar{k}^2 b \right). \quad (4.50)$$



The parameter  $\delta$  collects all the other terms and will give the expansion parameter. It is given by

$$\delta = \bar{\omega} \frac{4\pi\rho\eta^2}{l^2\bar{k}^2 B_0^2}. \quad (4.51)$$

Within  $\delta$  the factor  $\left(\frac{B_0^2}{4\pi\rho}\right)^{-1}$  appears and looks like the square of the Alfvén speed  $v_a$ . As the Alfvén speed will be approximately the speed of light  $c$ , we can write

$$\frac{B_0^2}{4\pi\rho} \approx v_a^2 \approx c^2. \quad (4.52)$$

Using this and the relativistic Lundquist number,  $L_u = \frac{lc}{\eta}$ , the parameter  $\delta$  can be rewritten as

$$\delta = \frac{\bar{\omega}}{L_u^2 \bar{k}^2} \ll 1. \quad (4.53)$$

This gives a small parameter to use in matched analysis of the current sheet.

Starting with the outer solution, equation 4.50, the variables  $b$  and  $v$  can be expanded in powers of  $\delta$  and keeping the leading order terms gives

$$b'' + (2\text{sech}^2(\bar{y}) - \bar{k}^2) b = 0. \quad (4.54)$$

Using Maple or another suitable program a solution to this can be found with the boundary condition  $b = 0$  as  $\bar{y} \rightarrow \infty$  in analytic form. The solution found is

$$b = \frac{b_0}{\bar{k}} (\tanh \bar{y} + \bar{k}) \left( \frac{1 - \tanh \bar{y}}{1 + \tanh \bar{y}} \right)^{\frac{\bar{k}}{2}}, \quad (4.55)$$

where  $b_0$  is a constant given by  $b(0) = b_0$ .

Now that  $b$  is known,  $v$  can be found from equation 4.45 and due to the simplification of  $k_z = 0$  the  $x$  components of  $\tilde{\mathbf{B}}_1$  and  $\tilde{\mathbf{V}}_1$  can be found from equation 4.41. As a sublayer is expected in the centre of the current sheet, the solution found only applies above the current sheet. Using the other boundary condition,  $b = 0$  as  $\bar{y} \rightarrow -\infty$ , and the symmetry of the problem the full outer solution will be

$$b = \frac{b_0}{\bar{k}} (\tanh |\bar{y}| + \bar{k}) \left( \frac{1 - \tanh |\bar{y}|}{1 + \tanh |\bar{y}|} \right)^{\frac{\bar{k}}{2}}. \quad (4.56)$$

This solution is continuous at  $\bar{y} = 0$ , but its derivative is not. As such we require the jump across the origin  $\Delta$  which is given by

$$\Delta = \left[ \frac{b'}{b} \right]_{0-}^{0+}. \quad (4.57)$$

For this  $b'$  is needed. It is easier to find  $b'_\pm = b'(0\pm)$  separately by replacing  $|\bar{y}|$  by  $\pm\bar{y}$  for  $b'_\pm$  respectively and then differentiating. Using this,  $b'_\pm$  is found to be

$$b'_\pm = \pm \frac{b_0}{\bar{k}} \operatorname{sech}^2 \bar{y} \left( \frac{1 \mp \tanh \bar{y}}{1 \pm \tanh \bar{y}} \right)^{\frac{\bar{k}}{2}} \mp b_0 \left( \frac{1 \pm \tanh \bar{y}}{1 \mp \tanh \bar{y}} \right) \frac{\bar{k} \operatorname{sech}^2 \bar{y}}{(1 \pm \tanh \bar{y})^2}. \quad (4.58)$$

Now  $\Delta$  can be evaluated as

$$\Delta = \left[ \frac{b'}{b} \right]_{0-}^{0+} = \frac{b'_+}{b_+} \Big|_0 - \frac{b'_-}{b_-} \Big|_0 = \left( \frac{1 - \bar{k}^2}{\bar{k}} \right) - \left( \frac{-1 + \bar{k}^2}{\bar{k}} \right), \quad (4.59)$$

and succinctly

$$\Delta = 2 \left( \frac{1 - \bar{k}^2}{\bar{k}} \right). \quad (4.60)$$

To complete the problem the inner solution is required to match to the outer solution. For the inner solution  $\bar{y} \ll 1$  and so the function  $f$  may be approximated by  $f \approx \bar{y}$ . Hence  $f'' \approx 0$ . Using this the equations of the inner solution are

$$\bar{\omega}b = -\bar{y}v + b'' - \bar{k}^2b, \quad (4.61)$$

and

$$\delta (v'' - \bar{k}^2v) = \bar{y} (b'' - \bar{k}^2b). \quad (4.62)$$

If the  $b'' - \bar{k}^2b$  term is eliminated between equations 4.61 and 4.62 then an expression for  $b$  can be found in terms of  $v$  and its derivatives,

$$b = \frac{\delta}{\bar{\omega}\bar{y}} (v'' - \bar{k}^2v) - \frac{\bar{y}v}{\bar{\omega}}. \quad (4.63)$$

If the second derivative of this can be found then equation 4.61 can provide a single equation for  $v$ . The second derivative is

$$b'' = \frac{2\delta}{\bar{\omega}\bar{y}^3} (v'' - \bar{k}^2v) - \frac{2\delta}{\bar{\omega}\bar{y}^2} (v''' - \bar{k}^2v') + \frac{\delta}{\bar{\omega}\bar{y}} (v'''' - \bar{k}^2v'') - \frac{2v'}{\bar{\omega}} - \frac{\bar{y}v''}{\bar{\omega}}, \quad (4.64)$$

and substituting this and  $b$  into equation 4.61 and multiplying through by  $\bar{\omega}\bar{y}^3$  leads to the fourth order equation for  $v$ ,

$$\begin{aligned} \bar{y}^2\delta v'''' - 2\bar{y}\delta v''' + (2\delta - \bar{y}^2\delta\bar{k}^2 - \bar{y}^4 - \delta\bar{y}^2(\bar{\omega} + \bar{k}^2))v'' + (2\delta\bar{k}^2\bar{y} - 2\bar{y}^3)v' \\ + (\delta\bar{k}^2\bar{y}^2(\bar{\omega} + \bar{k}^2) - \bar{y}^4(\bar{\omega} + \bar{k}^2) - \bar{\omega}\bar{y}^4 - 2\delta\bar{k}^2)v = 0. \end{aligned} \quad (4.65)$$

If a stretched variable  $\bar{y} = \zeta\delta^p$  is now introduced the structure of the sublayer can be found by the theory of least degeneracy. In the stretched variable

$$\frac{d^n}{d\bar{y}^n} = \delta^{-np} \frac{d^n}{d\zeta^n} \quad (4.66)$$

and equation 4.65 becomes

$$\begin{aligned} \zeta^2 v'''' - 2\zeta v''' + (2 - \zeta^2 \bar{k}^2 \delta^{2p} - \zeta^4 \delta^{4p-1} - \zeta^2 (\bar{\omega} + \bar{k}^2) \delta^{2p}) v'' + (2\zeta^2 \bar{k}^2 \delta^{3p} - 2\zeta^3 \delta^{4p-1}) v' \\ + (\zeta^2 \bar{k}^2 (\bar{\omega} + \bar{k}^2) \delta^{4p} - \zeta^4 (\bar{\omega} + \bar{k}^2) \delta^{6p-1} - \zeta^4 \bar{\omega} \delta^{6p-1} - 2\bar{k}^2 \delta^{2p}) v = 0. \end{aligned} \quad (4.67)$$

Using the theory of least degeneracy, with  $\delta \ll 1$ , the largest number of terms will be kept if  $p = \frac{1}{4}$  and hence the dimensionless thickness  $\epsilon$  of the sublayer is

$$\epsilon = \delta^{\frac{1}{4}} = \left( \frac{\bar{\omega}}{L_u^2 \bar{k}^2} \right)^{\frac{1}{4}}. \quad (4.68)$$

Though the sublayer's thickness has been found, the inner and outer solutions have not yet been matched. To do this equation 4.61 is rewritten in the stretched variable  $\bar{y} = \zeta \epsilon$ , giving

$$b'' - \epsilon^3 \zeta v - \epsilon^2 (\bar{\omega} + \bar{k}^2) b = 0. \quad (4.69)$$

To second order accuracy this reads

$$b'' - \epsilon^2 (\bar{\omega} + \bar{k}^2) b = 0 \quad (4.70)$$

and, with the symmetry condition  $b(\zeta) = b(-\zeta)$  and with the constant  $b_0$ , has the solution

$$b(\zeta) = b_0 \cosh \left( \sqrt{\bar{\omega} + \bar{k}^2} \epsilon \zeta \right), \quad (4.71)$$

and in the non-stretched variable

$$b(\bar{y}) = b_0 \cosh \left( \sqrt{\bar{\omega} + \bar{k}^2} \bar{y} \right). \quad (4.72)$$

It is straightforward to find  $b'$  and substitute into  $\Delta$  to get

$$\Delta = \left[ \frac{b'(\bar{y})}{b(\bar{y})} \right]_{\bar{y}=-\epsilon}^{\bar{y}=\epsilon} = 2\sqrt{\bar{\omega} + \bar{k}^2} \tanh \left( \sqrt{\bar{\omega} + \bar{k}^2} \epsilon \right). \quad (4.73)$$

As  $\epsilon \ll 1$  the small variable limit can be taken to give  $\tanh \left( \sqrt{\bar{\omega} + \bar{k}^2} \epsilon \right) = \sqrt{\bar{\omega} + \bar{k}^2} \epsilon$  and using the expression for  $\epsilon$  found in equation 4.68 the inner condition reads

$$\Delta = 2 \left( \bar{\omega} + \bar{k}^2 \right) \left( \frac{\bar{\omega}}{L_u^2 \bar{k}^2} \right)^{\frac{1}{4}}. \quad (4.74)$$

Now  $\Delta$  can be matched across the sublayer and equating equations 4.60 and 4.74 gives a relationship between the non-dimensional growth rate  $\bar{\omega}$  and wavenumber  $\bar{k}$  as follows

$$\left( \bar{\omega} + \bar{k}^2 \right) \left( \frac{\bar{\omega}}{L_u^2 \bar{k}^2} \right)^{\frac{1}{4}} = \frac{1 - \bar{k}^2}{\bar{k}}. \quad (4.75)$$

Since the growth rate and hence the left hand side of equation 4.75 is greater than zero, only modes with  $\bar{k} < 1$  will grow. If the limit of  $\bar{k} \ll 1$  is taken then, dropping terms of order greater than  $\bar{k}^{\frac{1}{2}}$ , 4.75 simplifies to

$$\bar{\omega} = \left( \frac{L_u}{\bar{k}} \right)^{\frac{5}{2}}. \quad (4.76)$$

This gives infinite growth as  $\bar{k} \rightarrow 0$  which is not physically realistic. As the e-folding time  $\tau_e$ , the time taken for a function to grow by a factor of  $e$ , must be longer than the diffusive time of the sublayer  $\tau_\epsilon$  in non-dimensional units,

$$\bar{\tau}_e > \bar{\tau}_\epsilon. \quad (4.77)$$

The e-folding time will be given by  $\tau_e = \omega^{-1}$  and in non-dimensional units  $\bar{\tau}_e = \bar{\omega}^{-1}$ , and the sublayers diffusive time will be the diffusive time  $\tau_d$  in the stretched units  $\bar{y} \rightarrow \epsilon \zeta$  and so  $\tau_\epsilon = \frac{l^2 \epsilon^2}{\eta}$  and in non-dimensional units  $\bar{\tau}_\epsilon = \epsilon^2$ . Hence the inequality 4.77 becomes, after a little manipulation,

$$\bar{k} > L_u^{-\frac{1}{4}}. \quad (4.78)$$

As the maximal growth rate is expected for the lowest wavenumber  $\bar{k}^*$ , the maximal growth rate will be for wavenumber  $\bar{k}^* = L_u^{-\frac{1}{4}}$ . Using this in equation 4.76 gives the maximal growth rate  $\bar{\omega}^*$  as

$$\bar{\omega}^* = L_u^{\frac{1}{2}}. \quad (4.79)$$

Since  $\bar{\omega} = \frac{l^2}{\eta}\omega = \frac{\tau_d}{\tau}$  this leads to the dimensional growth rate

$$\tau = (\tau_d \tau_c)^{\frac{1}{2}}. \quad (4.80)$$

## 4.2 Numerical Simulations

Numerical simulations of the relativistic tearing mode were conducted using the code described in chapter 3. The following subsection describes the base model and its extensions. The next subsection physically describes the relativistic tearing mode and its structure and the rest of the section is devoted to the results of the numerical investigations.

### 4.2.1 The numerical model

The simulations were all performed based around a standard model. This model is based on the one-dimensional solution for a force free current sheet found by Low in [28]. This form of the magnetic field was chosen for two reasons, for easy comparison to the relativistic tearing mode in magnetodynamics in [27] and for its useful analytic properties,  $B^2 = \text{const}$  and  $(\mathbf{B} \cdot \nabla) \mathbf{B} = 0$ .

This has an unperturbed state of

$$\mathbf{B} = \left( B_0 \tanh \left( \frac{y}{l} \right), 0, B_0 \operatorname{sech} \left( \frac{y}{l} \right) \right), \quad (4.81)$$

$$\rho_0 = p_0 = 0.1, \quad \mathbf{E} = \mathbf{v} = \mathbf{0}. \quad (4.82)$$

This current sheet has a constant magnetic pressure of  $B_0^2/2$ . This is defined by the background plasma pressure  $p_0$  and the plasma beta which is given by

$$\beta = \frac{2p}{B^2}. \quad (4.83)$$

In Low's original solution there was a non-zero velocity which in these simulations has been replaced by a zero velocity after preliminary investigations showed that the form of the initial velocity profile was irrelevant as the current sheet (perturbed or not) would quickly alter and then set-up its natural profile.

The width of the current sheet is  $2l$ , and it defines the region  $[-l, l]$  where nearly all the rotation of the magnetic field in the current sheet by  $\pi$  happens. In code units it is set to 0.1.

The choice of the background state plasma pressure and density to be equal  $\rho_0 = p_0$  was taken after initial testing. This found that a plasma pressure much larger than the density caused problems in the algorithm that found the primitive variables from the conserved ones as documented in chapter 3. Having the state variables equal results in a highly magnetised inflow which is in line with the observations of relativistic reconnection discussed in chapter 1 and with the small plasma betas does not affect any comparison to magnetodynamical simulations.

To cause the current sheet to tear a perturbation is added to the magnetic field of the form

$$\mathbf{b} = \left( 0, b_0 \sin \left( \frac{2\pi x}{\lambda} \right), 0 \right), \quad (4.84)$$

where  $b_0$  is the amplitude of the perturbation and is set to  $10^{-3}$  and  $\lambda$  is the wavelength.

To check that the initial conditions used are close enough to the quasi-static equilibrium simulations were run on the unperturbed equations with a resistivity of  $\eta = 10^{-3}$  and wavelength of  $\lambda = 4$ , until the evolution moved at the diffusive time scale  $\tau_d$  only. The results for the different variables are shown in figure 4.2.

The results shown in figure 4.2 show some differences to the initial conditions used to simulate the relativistic tearing mode of which only one makes a noticeable difference to the evolution of the tearing mode. For the magnetic field (top left) the only difference is the diffusion of the current sheet, depleting the  $B_z$  component. The diffusion of the magnetic field in the current sheet causes a decrease of the magnetic pressure  $p_m$  which causes the plasma pressure  $p$  to increase to keep the total pressure  $p_t$  constant (as seen at the top right). This dynamic change of the plasma and magnetic pressure keeping the total pressure constant is not accounted for in the initial conditions. The Harris current sheet, described in section 5.2.1, is expected to have a lower value for the maximum value of the perturbation at each time as the plasma pressure is already large in the current sheet, slowing the amount of matter that can enter which by the frozen in flux condition reduces the amount of magnetic field that can enter the current sheet and reconnect. This is shown in figure 4.3. The time taken for the plasma and magnetic pressures to change to keep the total pressure constant is  $\approx 15$  time units.

The left middle panel shows the current density which is given by  $\mathbf{J} = \nabla \times \mathbf{B}$  as expected and the right middle panel shows the electric field given by  $\mathbf{E} \approx \frac{1}{\sigma} \mathbf{J}$  also as expected. The difference in the electric field from  $\mathbf{J} = \sigma \mathbf{E}$  is given by the small contribution from the magnetic field from the  $\mathbf{v} \times \mathbf{B}$  term.

The bottom left panel gives the velocity created by the diffusive movement of the magnetic field and the frozen flux condition and the bottom right gives the density with compression



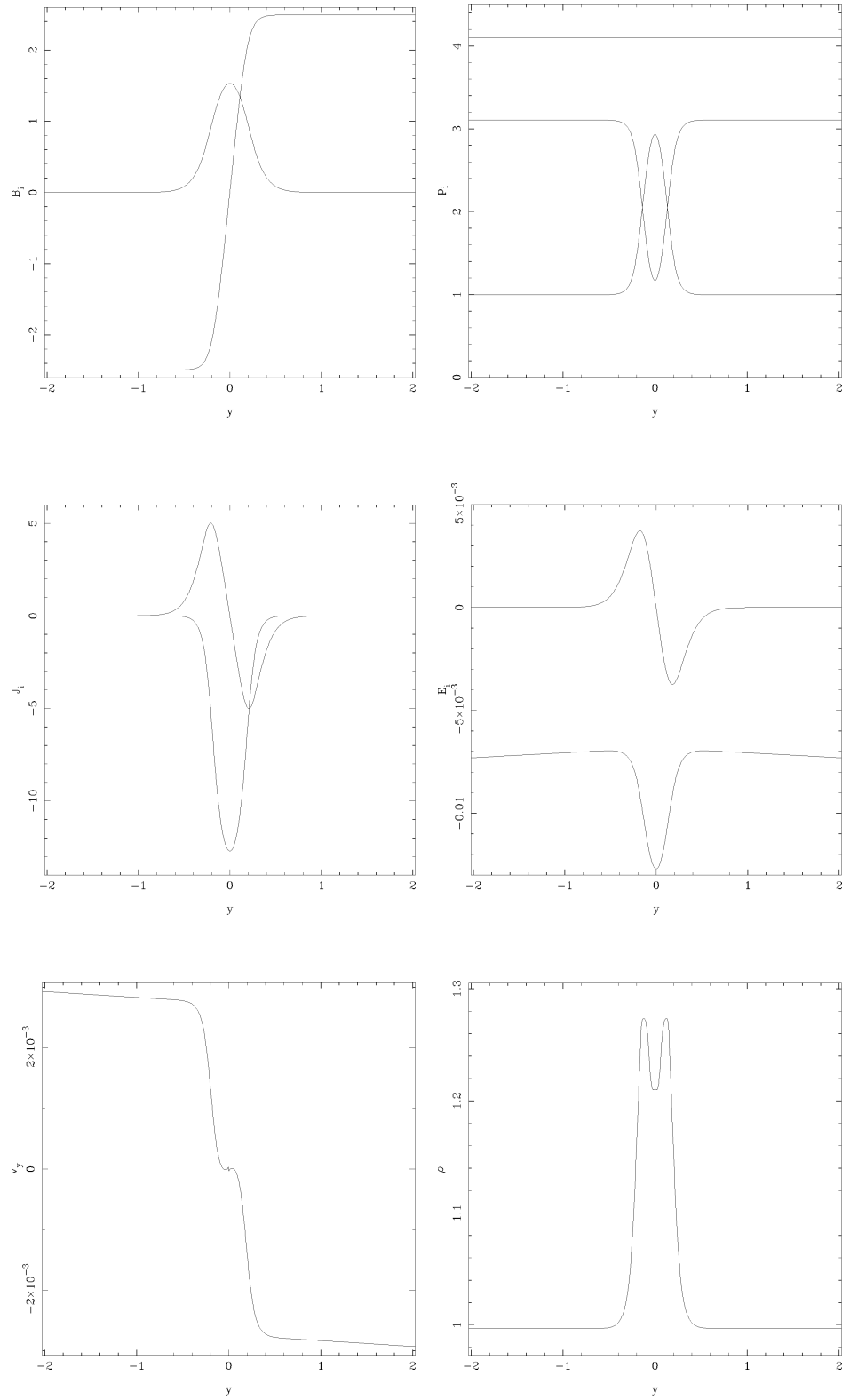


Figure 4.2: Graphs of a current sheet evolved to a quasi-equilibrium state. The variables are, going down the columns from the top left to the bottom right, magnetic field, current density and the velocity and on the right the plasma, magnetic and total pressures, the electric field and the density. The primitive variables not shown ( $B_y$ ,  $E_y$ ,  $v_x$ ,  $v_z$  and  $q$ ) which are all zero.

inside the current sheet matching the plasma brought in by the velocity and negating the need for an outflow.

The simulations were performed using the  $2\frac{1}{2}$  dimensional option of the code where vectors have all three components and  $\partial_z = 0$ . The domain of investigation is  $[-x_0, x_0] \times [-y_0, y_0]$  where  $x_0$  is set by the wavelength and  $y_0$  is chosen so that the boundaries do not interact directly with the current sheet. This was normally set to  $y_0 = 2$  (found again during initial investigations) but was shortened for the smaller wavelengths. The boundaries were free flow at  $\pm y_0$  and periodic at  $\pm x_0$ . The Courant number is  $C_n = 0.1$  in the simulations with a spatial resolution of 50 and 200 grid points per unit length in the  $x$  and  $y$  directions respectively.

To investigate the relativistic tearing mode the force-free model which is based on Low's one-dimensional solution for a force free current sheet described at the start of this section. As periodic conditions were chosen in the  $x$  direction the linear growth phase was repeated with free flow boundaries to be assured that the boundaries had no effect in the linear regime. This is shown to be true in figure 4.3 where the two curves sit on top of one another.

The other main model used in simulations of magnetic reconnection is the Harris current sheet. This is described in equations 5.51 and 5.52. The main difference between the force-free and Harris models is the pressures. In the force-free model the plasma and magnetic pressures are both constants so when reconnection occurs and the magnetic pressure drops, the plasma pressure rapidly grows to keep the total pressure constant. In the Harris current sheet the total pressure is a constant with the plasma and magnetic pressure both being constant in the inflow region and the magnetic pressure dropping to the lower plasma pressure value in the current sheet and the plasma pressure mirroring this to keep the total pressure constant. The initial setup of the different pressures for the Harris current sheet are shown in figure 4.4. This set-up is what the force-free model moves towards (on top of a background of decay of the magnetic field). Hence in the

force-free model there is a longer settling time for the perturbation and as the plasma pressure is lower in the current sheet during the linear growth regime giving a smaller force against the inflowing plasma with its frozen in magnetic field. This allows more magnetic flux to pass through the reconnection region and a larger growth rate. This is shown in figure 4.3.

The force-free model was chosen to conduct simulations of the relativistic tearing mode as it is the magnetohydrodynamical equivalent to the magnetodynamical model used for the tearing mode simulations in [27] and the magnetodynamical simulation presented in this work. As, discussed above, the evolution of the relativistic tearing mode will be very similar for the two models and hence both should react in the same way to the varying of the parameters only the force-free model was used due to the time constraints associated with a thesis.

To investigate the tearing mode four cases were simulated using the force-free model described at the start of this section. These were varying the resistivity  $\eta$ , varying the plasma beta  $\beta$ , varying the magnetisation parameter with  $p_0 \neq \rho_0$  and the isothermal case. Within these regimes the wavelength is again varied to find a relation between it and the parameters.

To investigate the four different regimes a standard model was used with  $L_u = 10^2$ ,  $\beta = 0.32$ ,  $\varsigma = 6.25$  and background total energy  $e = 41/80$  with  $p_0 = \rho_0 = 0.1$ . The deviations from this used to investigate the relativistic tearing mode are denoted in each case.

Three dimensionless parameters are used to characterise different regimes in relativistic magnetohydrodynamics. They are the relativistic Lundquist number  $L_u$ , the plasma beta  $\beta$ , and the magnetisation parameter  $\varsigma$ .

The relativistic Lundquist number, given by

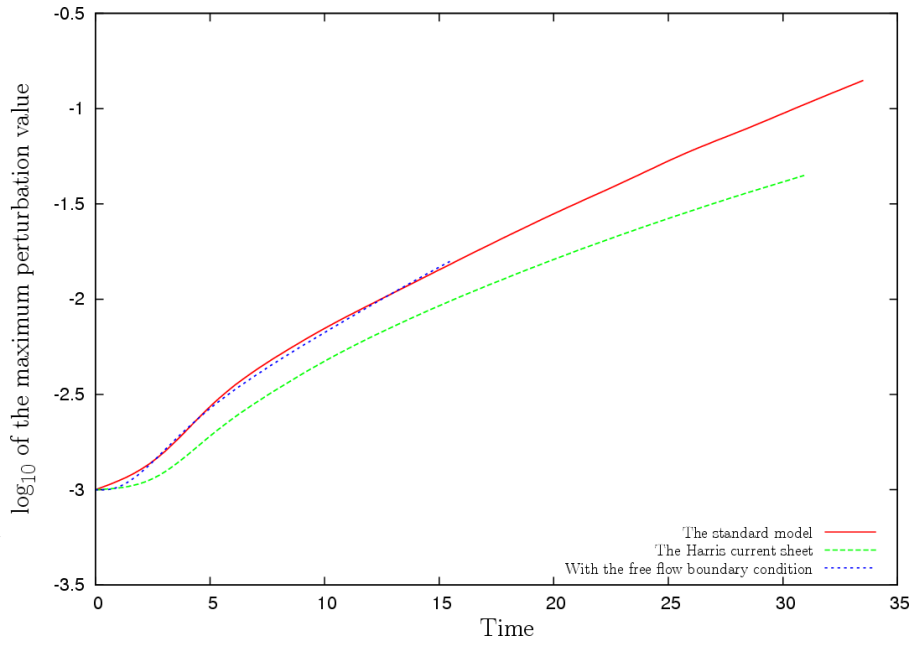


Figure 4.3: Comparison of the growth rate of the perturbation of the standard case with  $\lambda = 12$ ,  $\beta = 0.05$  and  $\eta = 10^{-3}$  for periodic and free flow boundary conditions and for a Harris current sheet

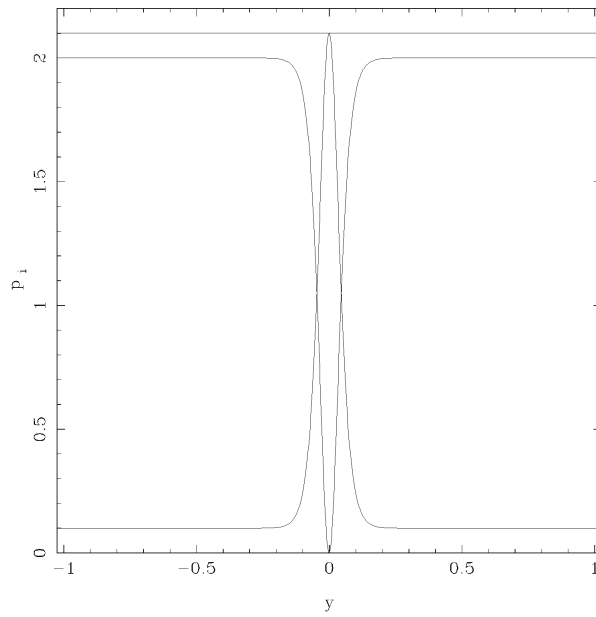


Figure 4.4: The initial set-up of the plasma pressure  $s$  for a Harris current sheet along the line  $x = 0$ . From top to bottom the pressures are the total, magnetic and plasma.

$\eta$	$10^{-3}$	$10^{-4}$
$L_u$	$10^2$	$10^3$

Table 4.1: Values of the relativistic Lundquist number for given values of  $\eta$ .

$$L_u = \frac{l}{\eta}, \quad (4.85)$$

gives a measure of light crossing time scale (a measure of the time needed to reach dynamic equilibrium) versus the diffusive time scale with  $L_u \ll 1$  being magnetically diffusely dominated and  $L_u \gg 1$  giving a fast transition between dynamic equilibria. In the relativistic tearing mode the relativistic Lundquist number is expected to be large, greater than  $10^5$ , so that the relativistic tearing mode is diffusely dominated.

Since the width of the current sheet is fixed at  $l$  the relativistic Lundquist number is dependent on the reciprocal of the resistivity,  $L_u \propto \eta^{-1}$ . In table 4.1 the two values of the resistivity used and their corresponding relativistic Lundquist numbers are given. These are large, but short of the regime expected in physical approximations, but place the simulations in the diffusely dominated regime desired for the relativistic tearing mode.

The plasma beta, defined by

$$\beta = \frac{2p}{B^2} = \frac{p}{p_m}, \quad (4.86)$$

gives a comparison of the plasma pressure to the magnetic pressure with  $\beta \ll 1$  being dominated by the magnetic pressure and  $\beta \gg 1$  being dominated by the plasma pressure. The plasma beta is an important parameter as it identifies two regions in the relativistic tearing mode. In the inflow region, the plasma is magnetically dominated and  $\beta \ll 1$ , whilst in the current sheet where the magnetic field has reconnected the plasma is matter dominated with  $\beta \gg 1$ . As the total pressure, given by  $p_t = p + p_m$ , is a constant across the domain, by defining the background pressure and magnetic field the magnetically

dominated in flow region is defined and the conversely the pressure balance in the current sheet as well.

In the code the once the background plasma pressure was chosen and the plasma beta was chosen, the magnitude of the magnetic field was then calculated from them. Five values of the plasma beta where used in the code and with the corresponding magnetic fields (where the unvaried background plasma pressure of  $p_0 = 0.1$  is used to find them) is presented in table 4.2.

The background Alfvén speed  $c_a$ , is expected to tend to the speed of light (unity in the units being used). This gives a measure of the accuracy of the solutions. For all but one of the regimes simulated the background plasma pressure and density are equal  $p_0 = \rho_0$  and the Alfvén speed given by

$$c_a = \frac{B}{\sqrt{B^2 + w}} \quad (4.87)$$

can be rewritten as

$$c_a = \left(1 + \frac{5}{2}\beta\right)^{-\frac{1}{2}}. \quad (4.88)$$

Using this the background Alfvén speeds and corresponding Lorentz factors  $\gamma_a$ , can be found for the different plasma beta's. These are shown in table 4.2.

It would be preferable if the plasma beta was lower to give a more magnetically dominated inflow region. This was not possible due to the limitations of the code as documented in chapter 3.

The magnetisation parameter, given by

$$\varsigma = \frac{B^2}{\rho\gamma^2} \quad (4.89)$$

$\beta$	$ B $	$c_a$	$\gamma_a$
0.32	$\frac{1}{2}\sqrt{\frac{5}{2}}$	0.75	1.50
0.19	$2\sqrt{\frac{5}{19}}$	0.82	1.76
0.1	$\sqrt{2}$	0.89	2.24
0.075	$2\sqrt{\frac{2}{3}}$	0.92	2.52
0.05	2	0.94	3.00

Table 4.2: Values of the background Alfvén speed, Lorentz factor and magnitude of the magnetic field for a given  $\beta$ .

where  $B$  is the magnetic field,  $\rho$  is the density and  $\gamma$  is the Lorentz factor. This gives a measure of whether the plasma is dominated by the magnetic energy  $\varsigma \gg 1$  or matter dominated  $\varsigma \ll 1$ .

Since the inflow velocity is around  $\approx 0.1$  in all the tearing mode simulations the Lorentz factor is  $\gamma = 1$ . Further, since in all but one set of simulations, the background plasma pressure and density are equal so the magnetisation parameter can be rewritten as

$$\varsigma = \frac{2}{\beta}. \quad (4.90)$$

For the relativistic tearing mode the magnetisation parameter is expected to be large with  $\varsigma \gg 1$ . The standard case has a magnetisation parameter of 6.25 which is not large and is chosen so the code runs for the deviations of the standard model for  $\eta = 10^{-4}$  and the isothermal case. To check the dependence of the relativistic tearing mode on the magnetisation parameter when the background state variables are not equal  $p_0 \neq \rho_0$ , one set of simulations was run with a background plasma pressure of  $p_0 = 0.1$  and density of  $\rho_0 = 0.5$ . This gives a background magnetisation parameter of 1.25. The density was lowered rather than increased due to the known problems with the code documented in chapter 3. This varies magnetisation parameters used for the relativistic tearing mode as

$\beta$	$\varsigma$
0.32	6.25
0.19	10.53
0.1	20
0.075	26.67
0.05	40
0.32	1.25
$\rho_0 = 0.5, p_0 = 0.1$	

Table 4.3: The magnetisation parameter for different values of the plasma beta when the plasma pressure is equal to the density

summed up in table 4.3.

The final regime investigated was the isothermal case, where the temperature is kept constant. This is achieved by using the ideal gas law for the plasma implemented in the code,  $\frac{p}{\rho} = T$  where  $T$  is the temperature. At the end of each time step the plasma pressure was reset as  $p = \rho T_{iso}$  where  $T_{iso}$  is the desired isothermal temperature. For all the isothermal cases studied this was set as  $T_{iso} = 1$ , the initial temperature in the inflow region.

#### 4.2.2 Physical description of the relativistic tearing mode and its structure

Before proceeding to the results, the evolution of the current sheet with and without the perturbation is described.

To explain the process, the relativistic tearing mode in a current sheet starts with two regions of oppositely aligned magnetic field lines in close contact with a sharp gradient



connecting them. The magnetic field then causes a strong current due to Ampère's law. In the connecting region resistivity becomes important and allows the field lines to slip through the plasma and cancel each other out. Since outside this region the plasma is approximately ideal, as there is no gradient for the resistivity to act upon, this causes an inflow through the frozen flux condition. If unperturbed this process will diffuse outwards and establish a stable equilibrium on the diffusive time scale  $\tau_d$  where

$$\tau_d = \frac{l^2}{\eta}, \quad (4.91)$$

and  $2l$  is the width as before.

If the magnetic field is perturbed, then the situation changes, now a small magnetic tension force  $(\mathbf{B} \cdot \nabla) \mathbf{B}$  acts inside the current sheet to move the field lines outwards from the centre along the current sheet. This outflow causes the field lines to reach the centre first and reconnect faster. This causes the centre to thin and the edges to thicken to compensate. The thinning of the current sheet also steepens the magnetic gradient, which with an increasing electric field causing the current density to go up in the connecting region from Ampère's law 2.15. This continues, eventually forming magnetic islands, until one of three things happen: non-linear terms become important, secondary tearing occurs or the current sheet shrinks to a minimum width. If the current sheet reaches a minimum then reconnection will continue at a constant rate. The evolution of the relativistic tearing mode is illustrated in figure 4.5 showing the  $B_z$  component of the magnetic field with the magnetic field tearing and starting to form magnetic islands.

Secondary tearing was found in the isothermal and magnetodynamic simulations. When the current sheet has become very thin it becomes again unstable to tearing with the symmetry of the two islands causing it to form in the centre. Anything forming to either side will be moved into one of the larger islands. Since the current sheet between the two islands is much thinner than originally, the secondary tearing will happen at a much faster rate. This is more likely to happen in longer wavelengths, where the thin current sheet

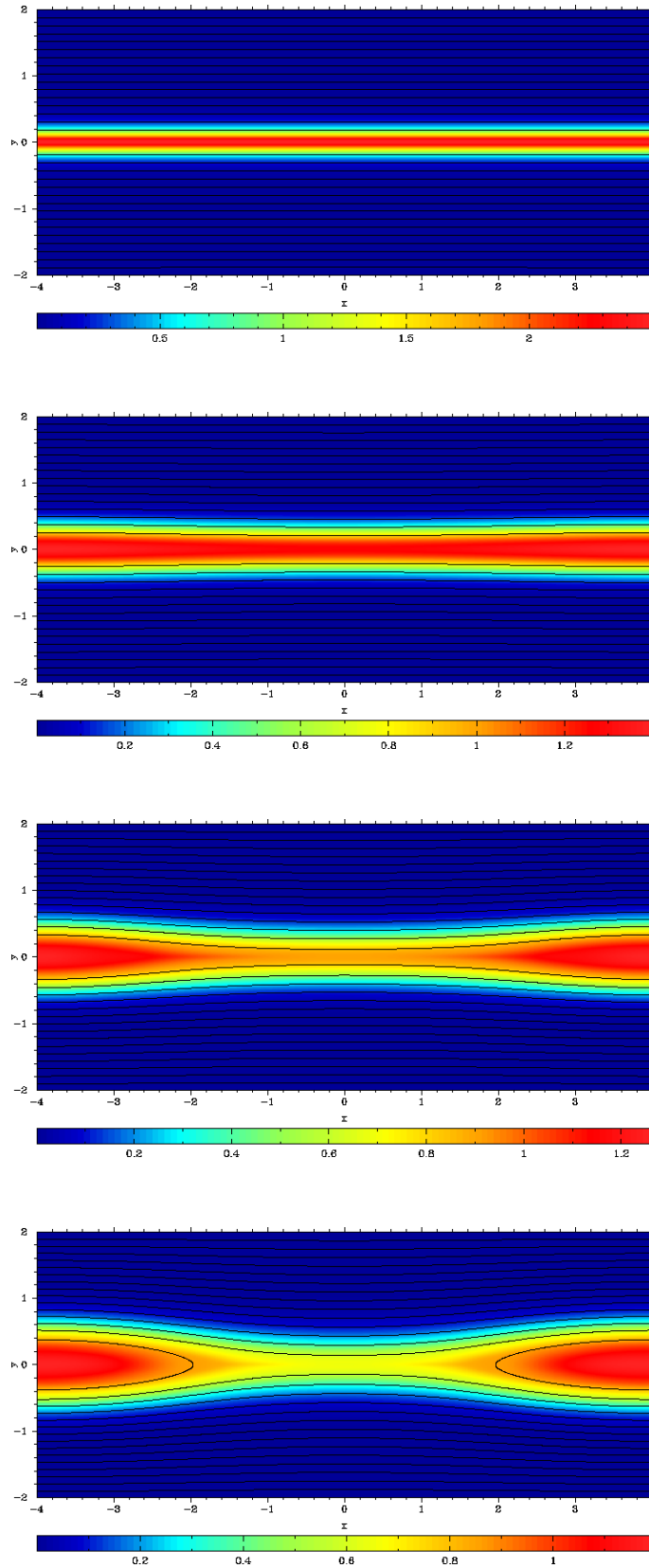


Figure 4.5: A current sheet undergoing the relativistic tearing mode reconnection with  $\eta = 10^{-3}$ ,  $\beta = 0.32$  and a wavelength eight ( $\lambda = 8$ ). The  $B_z$  component of the field is plotted with the contours giving the magnetic field lines for times in descending order of  $t = 0, 23.003, 42.121$  and  $61.195$ .

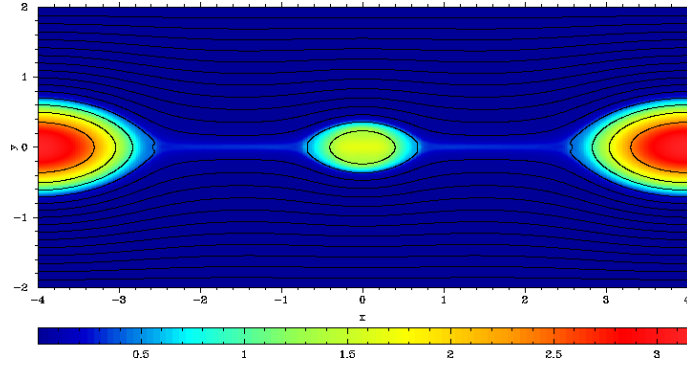


Figure 4.6: An isothermal current sheet with secondary tearing with  $\eta = 10^{-3}$ ,  $\beta = 0.32$  and a wavelength of  $\lambda = 8$ , at time  $t = 61.195$ .

connecting the two magnetic islands will be long enough to allow shorter wavelengths to grow in accordance with the dispersion rates shown in figures 4.18 and 4.19. An image of secondary tearing is shown in figure 4.6.

To illustrate the structure of the current sheet in the linear growth phase, figure 4.7 shows the perturbed version of figure 4.2 at time 11.501. The variables not plotted are very small compared to those that are plotted. The variables are similar to the unperturbed state shown in figure 4.2 except for a greater inflow velocity  $v_y$  and the reconnection electric field  $E_z$  having formed. It is noted that the kink in the  $v_y$  component of the velocity field has gone when compared to figure 4.2. This is because an outflow has now formed towards the  $x$  boundaries along the current sheet and the plasma is no longer being compressed there causing a small flow back towards the inflow region. The current sheet has thinned in the middle due to the growth of the relativistic tearing mode but is otherwise structurally the same as when there is no perturbation present. The major structural changes being brought about by the non-linear terms.

Figure 4.8 shows the  $B_y$  perturbation to the background state in the linear growth phase of the relativistic tearing mode and its evolution from a sine wave in  $x$  to an anti-symmetric maximum and minimum. It is these maximum and minimum which cause the outflow

and grow with the growth of the relativistic tearing mode.

### 4.2.3 Linear growth rates of the relativistic tearing mode

In section 4.1.2 a relation for the growth rate of the tearing mode dependent on the wavenumber is given, showing exponential growth. To display the growth of the perturbation a log of the maximum value of the perturbation - time plot from  $t = 0$  to  $t = 15.5$  in code units showing the linear growth of the maximum of the perturbed magnetic field  $B_y^{max}$  is done for each of the different cases. The standard model is shown in figure 4.9 with parameters  $L_u = 10^2$  and  $\beta = 0.32$ .

The following graphs describe the results of numerical simulations.

Figure 4.9 shows the linear growth rate of the perturbation of the standard set-up, with a resistivity of  $\eta = 10^{-3}$  and plasma beta of  $\beta = 0.32$ , for a series of wavelengths. This shows a maximal linear growth rate for a wavelength of four,  $\lambda = 4$ . The curve for  $\lambda = 2$  shows that it becomes non-linear whilst the others are still growing linearly. The sharp drop-off from the maximal growth rate of  $\lambda = 4$  and the rapid transition to non-linear growth for  $\lambda = 2$  is caused by the maximum growth rate being at the cut-off point for the wavenumber  $k$  as shown in equation 4.75. This feature is common to all the simulations except for the isothermal ones. Another common feature is a short period of settling, typically about 3 time units, where the simulations adapt to the non-natural set-up as described in 4.2.1.

Figure 4.10 has the standard set-up, but with the resistivity changed to  $\eta = 10^{-4}$ . This increases the maximum growth rate, as given by equation 4.79. This is slightly disguised by the long settling period which is likely brought on by the increased competition between the predicted increase in the growth rate from equation 4.79, which increases by a factor of  $\sqrt{10}$ , and the diffusive rate, which has increased by a factor of 10.

Figure 4.11 has the standard set-up, with the plasma beta reduced to  $\beta = 0.1$ , for a greater

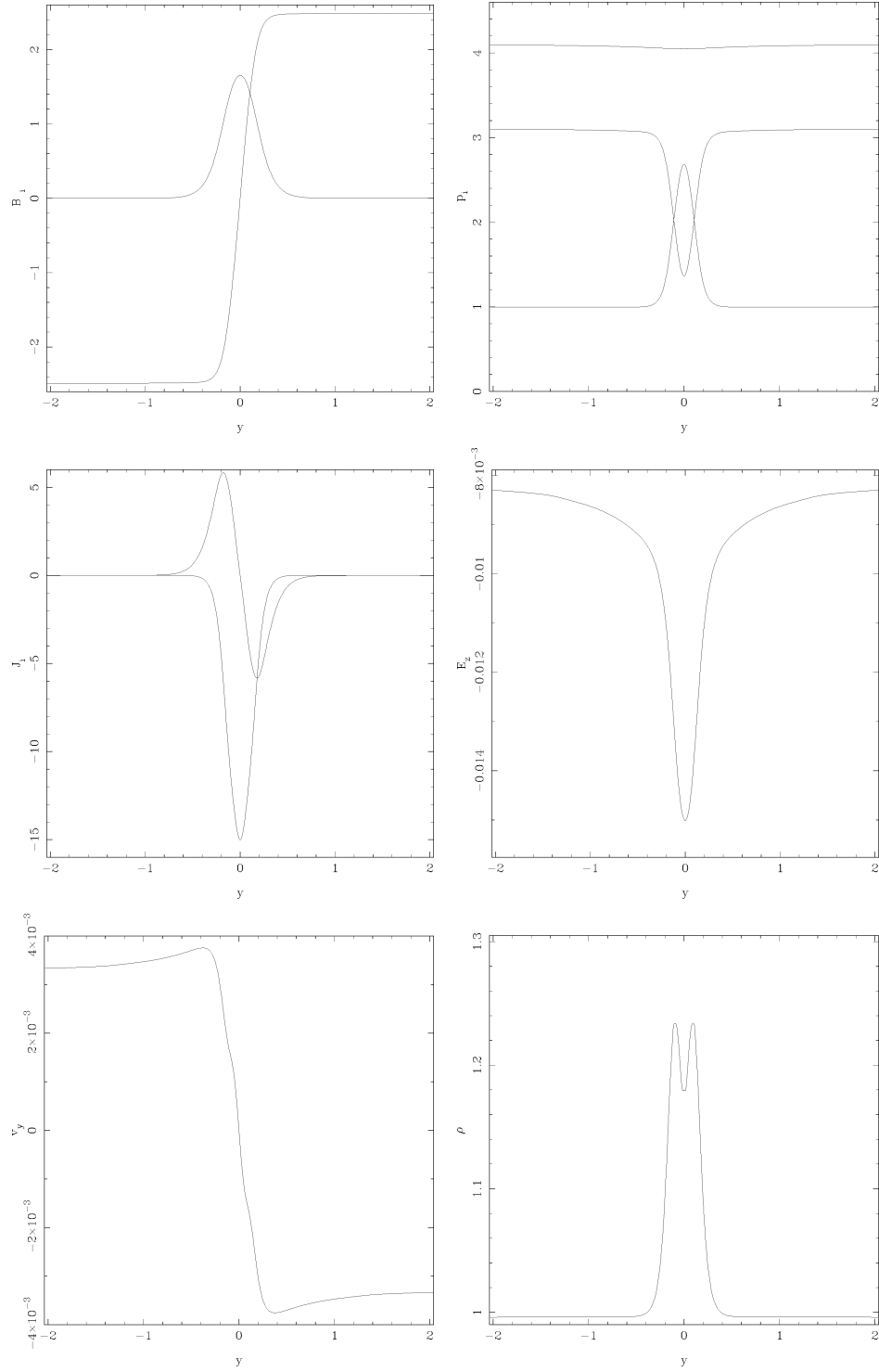


Figure 4.7: Graphs of the current sheet in the linear growth phase with resistivity of  $\eta = 10^{-3}$ , plasma beta of  $\beta = 0.32$  and wavelength of  $\lambda = 4$ . From top left to bottom left the variables are the magnetic field, the current density and the velocity field. From the top right to the bottom right the plasma, magnetic and total pressures, the electric field and the density along the line of  $x = 0$ .

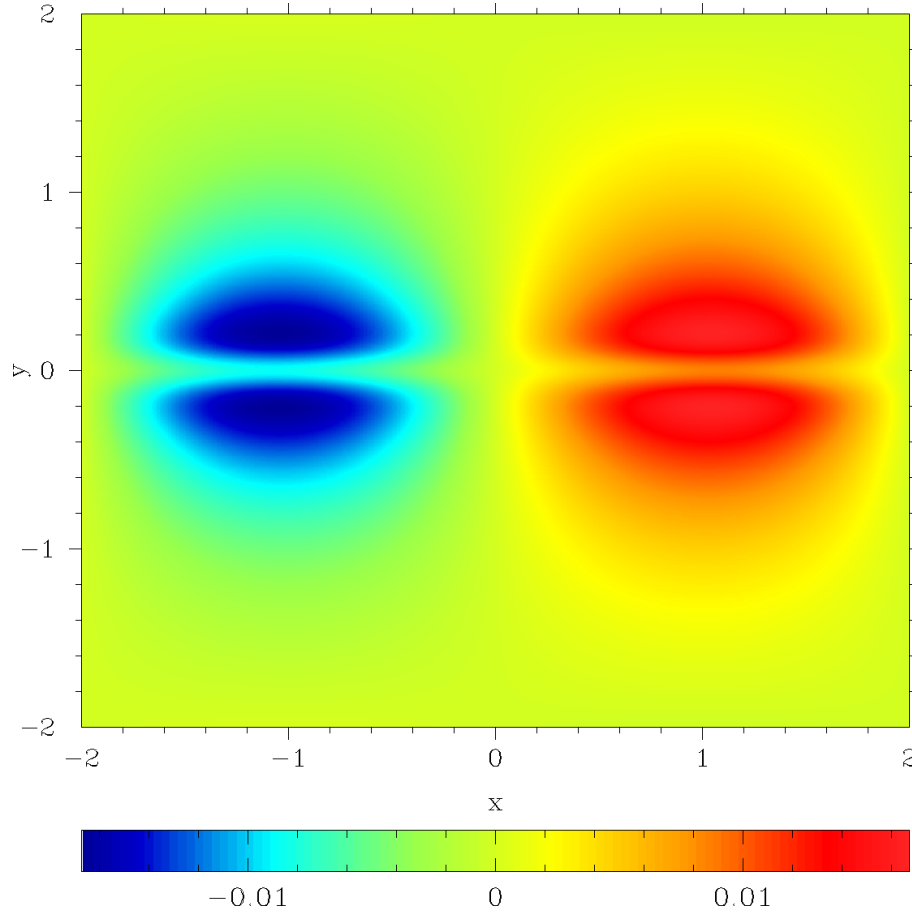


Figure 4.8: The  $B_y$  perturbation to the background state in the linear growth phase of the relativistic tearing mode with resistivity of  $\eta = 10^{-3}$ , plasma beta of  $\beta = 0.32$  and wavelength of  $\lambda = 4$ .

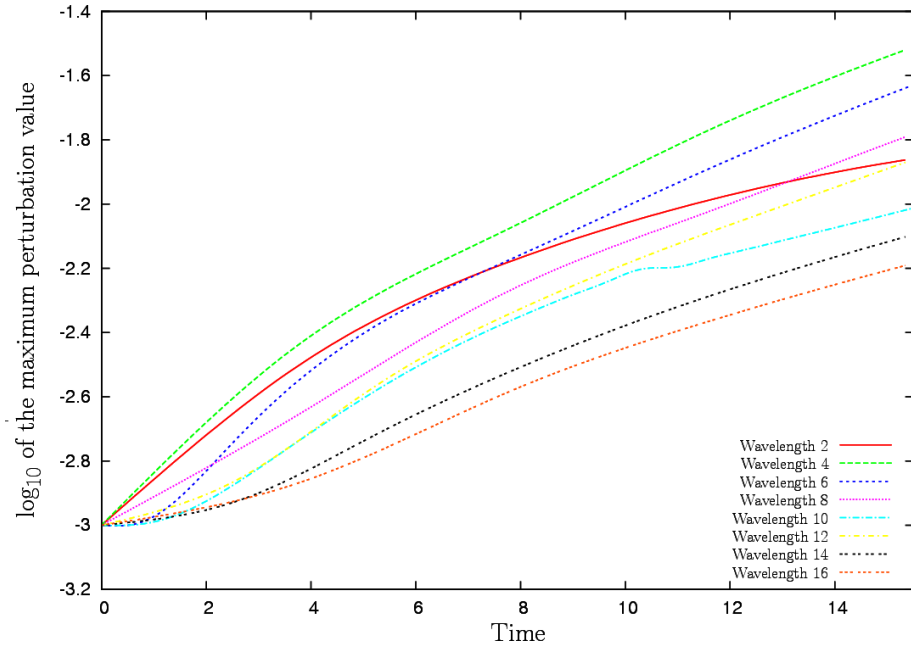


Figure 4.9: Linear growth rate for  $\eta = 10^{-3}$  of the maximum value of the magnetic field perturbation for wavelengths two through sixteen increasing in powers of two on a time -  $\log B_y^{max}$  plot.

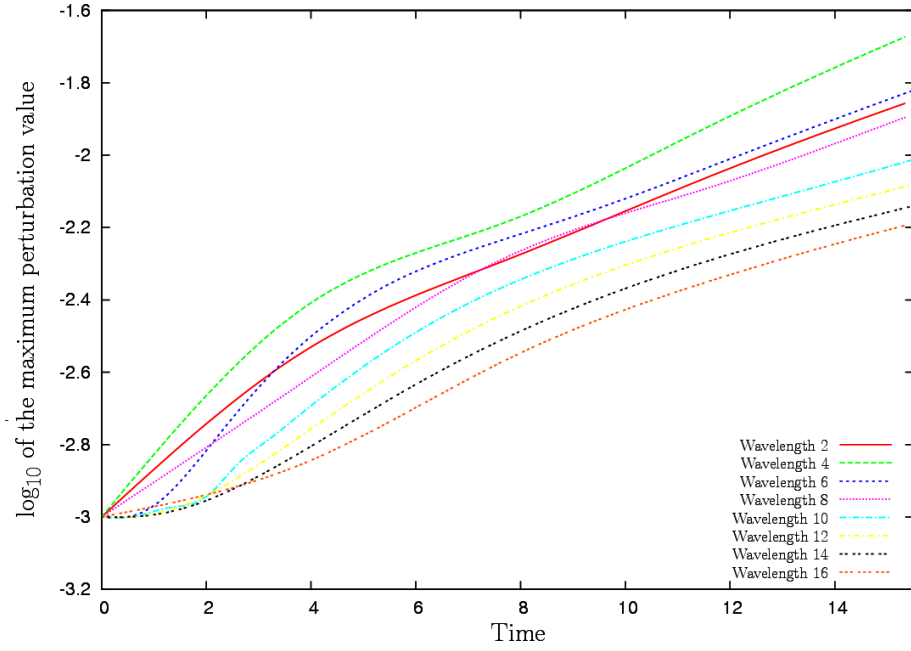


Figure 4.10: Linear growth rate for  $\eta = 10^{-4}$  of the maximum value of the magnetic field perturbation for wavelengths two through sixteen increasing in powers of two on a time -  $\log B_y^{max}$  plot.

dominance of the magnetic pressure (and hence larger magnetisation parameter) in the inflow plasma. This keeps the same structure as the standard model, only with growth rate increasing. The increase in growth rate is due to the greater inflow provided by the increase in the magnetic field in the inflow region.

Figure 4.12 takes the standard set-up and further increases the magnetic field strength, with a plasma beta of  $\beta = 0.05$ . Again this increases the growth rate due to the comparative reduction in the plasma pressure as before, but to a greater extent.

Figure 4.13 is the isothermal version of the standard set-up. As the pressure is reduced to keep the temperature constant the settling time is reduced as the plasma pressure doesn't increase to match the drop in magnetic pressure, a major cause of the resettling time, and with the reduced plasma pressure the growth rate increases greatly. The sharp drop-off of the growth rate for wavenumber is shown again by the almost superposition of wavelengths two and four.

Figure 4.14 shows the standard setup with  $\rho = 0.5$  which changes the magnetisation parameter to  $\varsigma = 1.25$ . This is very similar to the standard case in magnitude.

To verify that the simulations are actually in the linear regime the amplitude of the perturbation was changed to  $10^{-5}$  for three simulations. As, shown in figures 4.15, 4.16 and 4.17, when the magnitude of the initial perturbation is subtracted from the solution the results lie on top of each other. This shows that the perturbation of  $10^{-3}$  is in the linear regime and the solution is the same.

#### 4.2.4 Dispersion relations of the relativistic tearing mode

The gradients from figures 4.9 - 4.13 can be found from the data (in this case using the linear regression suite in the statistics package **R**) and plotted to find the non-dimensional growth rate's dependence on the non-dimensional wavenumber,  $\bar{\omega}(\bar{k})$ . This is done using the results of section 4.1.2. This predicts a maximum growth rate of  $\bar{\omega}^* = L_u^{\frac{1}{2}}$  given by



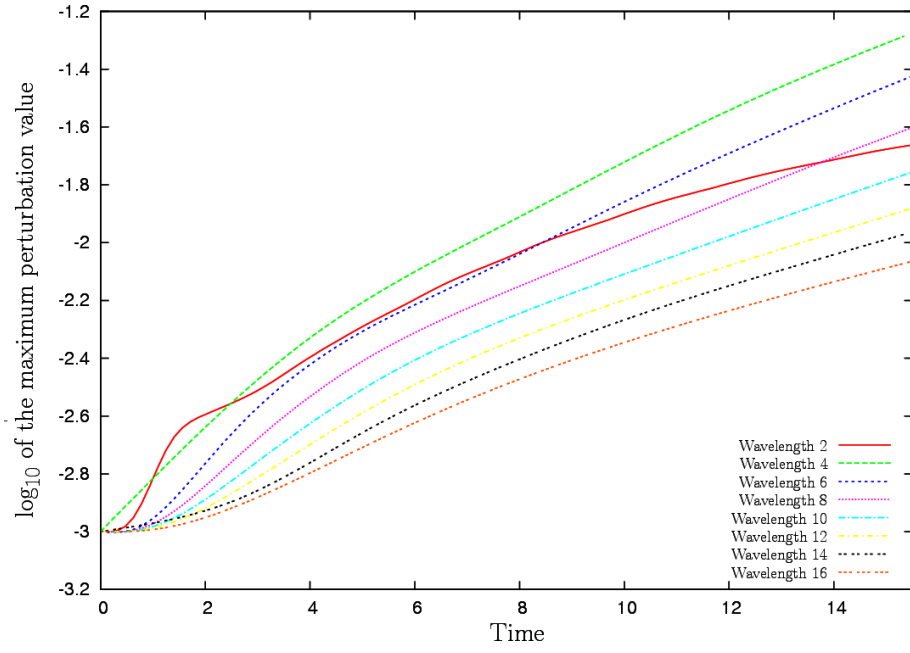


Figure 4.11: Linear growth rate for  $\beta = 0.1$  of the maximum value of the magnetic field perturbation for wavelengths two through sixteen increasing in powers of two on a time -  $\log B_y^{max}$  plot.

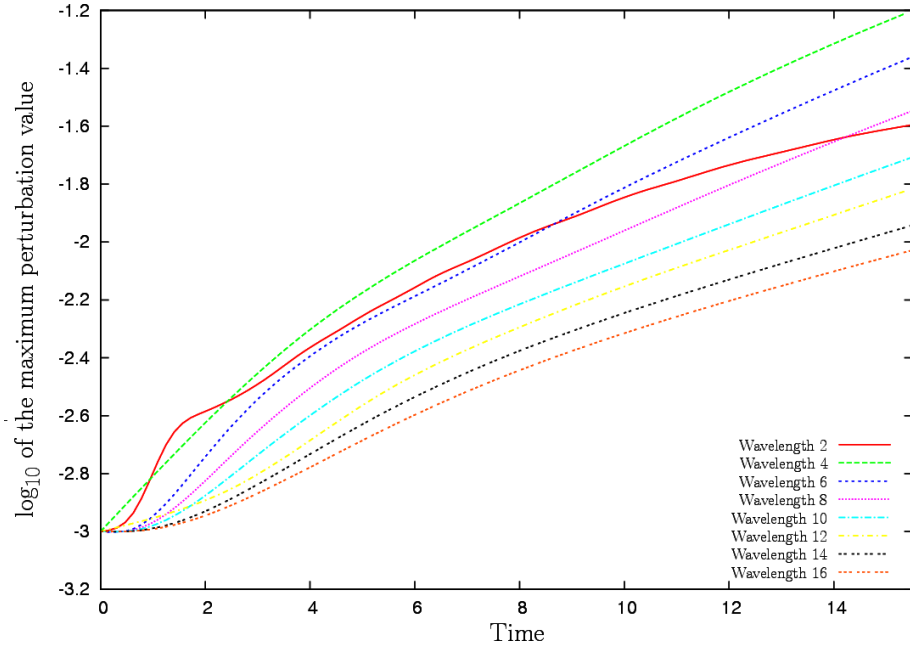


Figure 4.12: Linear growth rate for  $\beta = 0.05$  of the maximum value of the magnetic field perturbation for wavelengths two through sixteen increasing in powers of two on a time -  $\log B_y^{max}$  plot.

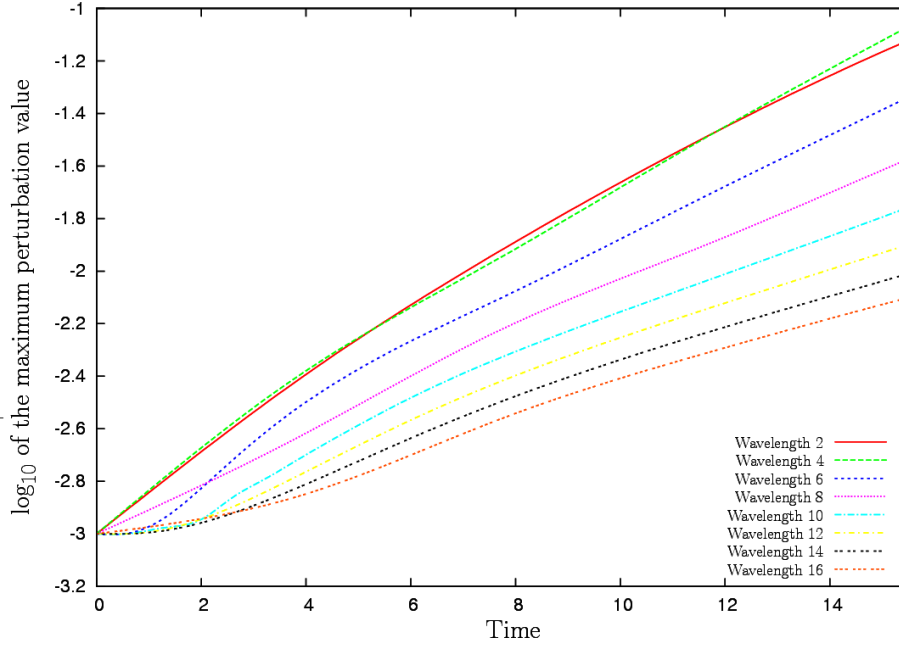


Figure 4.13: Linear growth rate for the isothermal case of the maximum value of the magnetic field perturbation for wavelengths two through sixteen increasing in powers of two on a time -  $\log B_y^{max}$  plot.

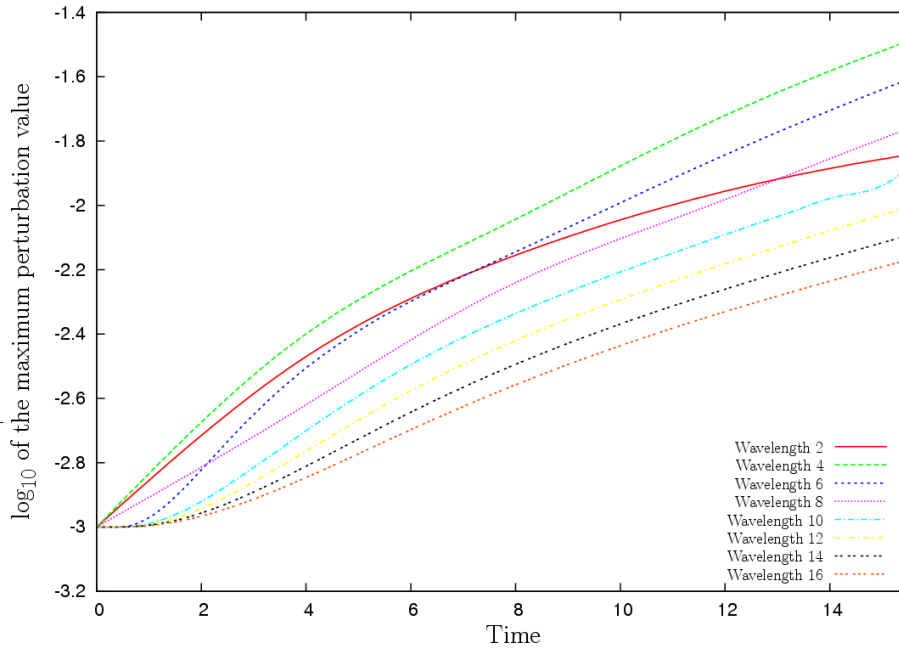


Figure 4.14: Linear growth rates for the magnetisation parameter of  $\zeta = 1.25$  with state variables  $\rho_0 = 0.5$  and  $p_0 = 0.1$  of the maximum value of the magnetic field perturbation for wavelengths two through sixteen increasing in powers of two on a time -  $\log B_y^{max}$  plot.

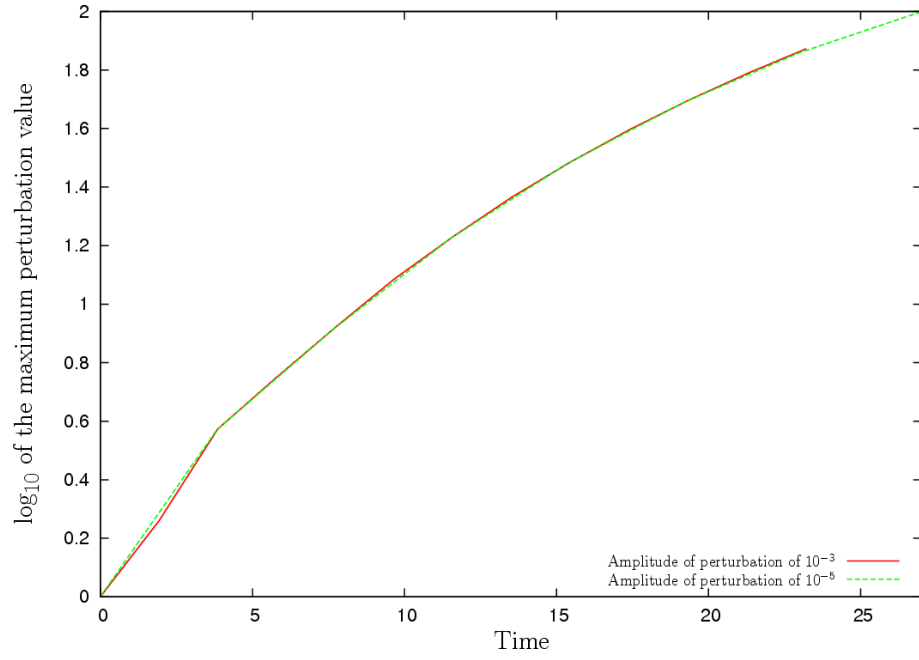


Figure 4.15: The linear regime, including the settling period, for  $\lambda = 4$ ,  $\eta = 10^{-3}$  and  $\beta = 0.32$  for perturbation amplitudes of  $10^{-3}$  and  $10^{-5}$ , with the initial perturbation subtracted from the solutions for comparison.

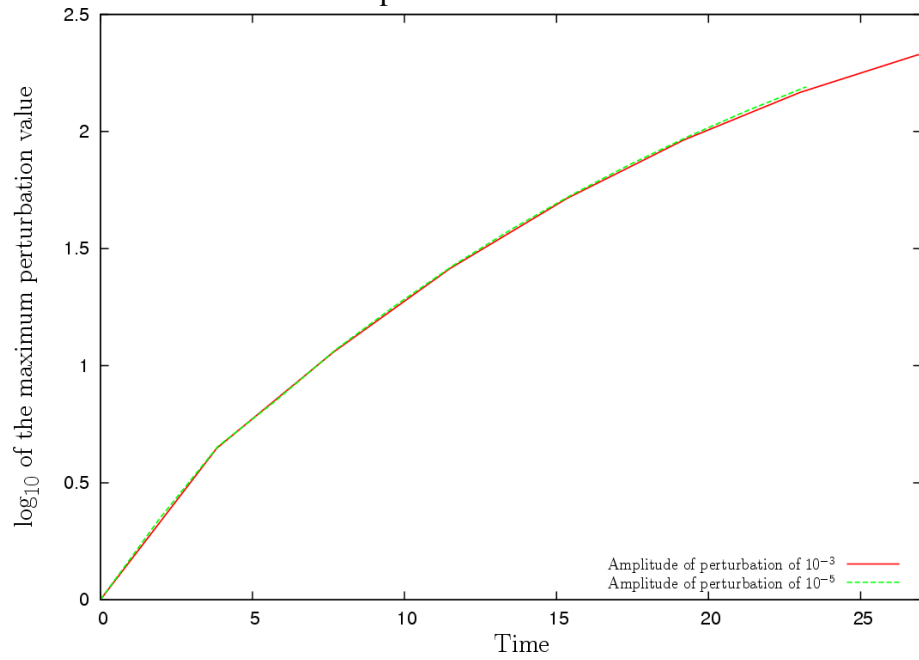


Figure 4.16: The linear regime, including the settling period, for  $\lambda = 4$ ,  $\eta = 10^{-3}$  and  $\beta = 0.1$  for perturbation amplitudes of  $10^{-3}$  and  $10^{-5}$ , with the initial perturbation subtracted from the solutions for comparison.

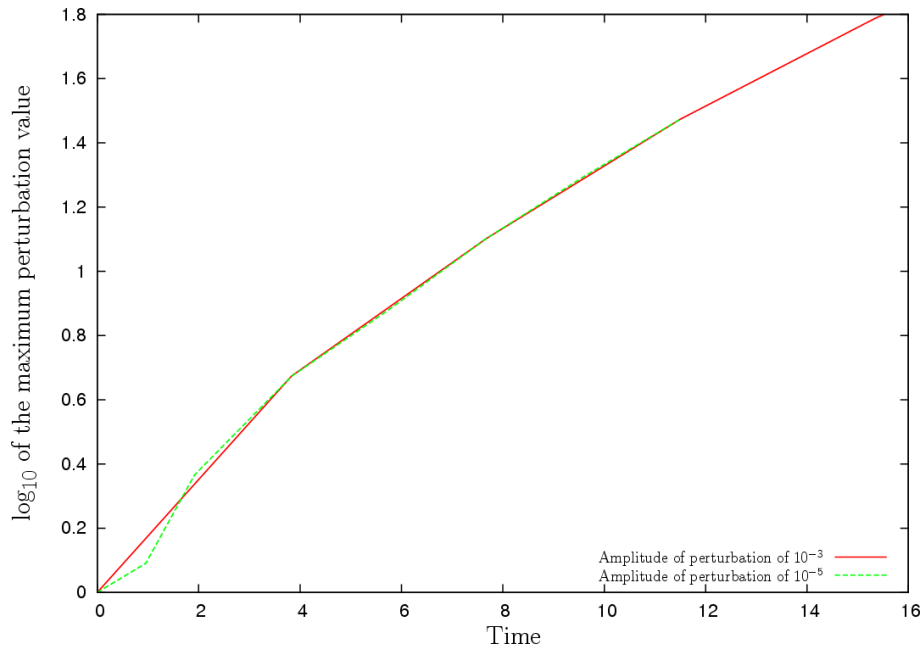


Figure 4.17: The linear regime, including the settling period, for  $\lambda = 4$ ,  $\eta = 10^{-3}$  and  $\beta = 0.05$  for perturbation amplitudes of  $10^{-3}$  and  $10^{-5}$ , with the initial perturbation subtracted from the solutions for comparison

$\bar{k} = L_u^{-\frac{1}{4}}$  and as such the non-dimensional growth rate will be scaled by  $L_u^{\frac{1}{2}}$  and, to scale and place the peak at the origin, the log of the non-dimensional wavenumber divided by the optimum wavenumber is taken.

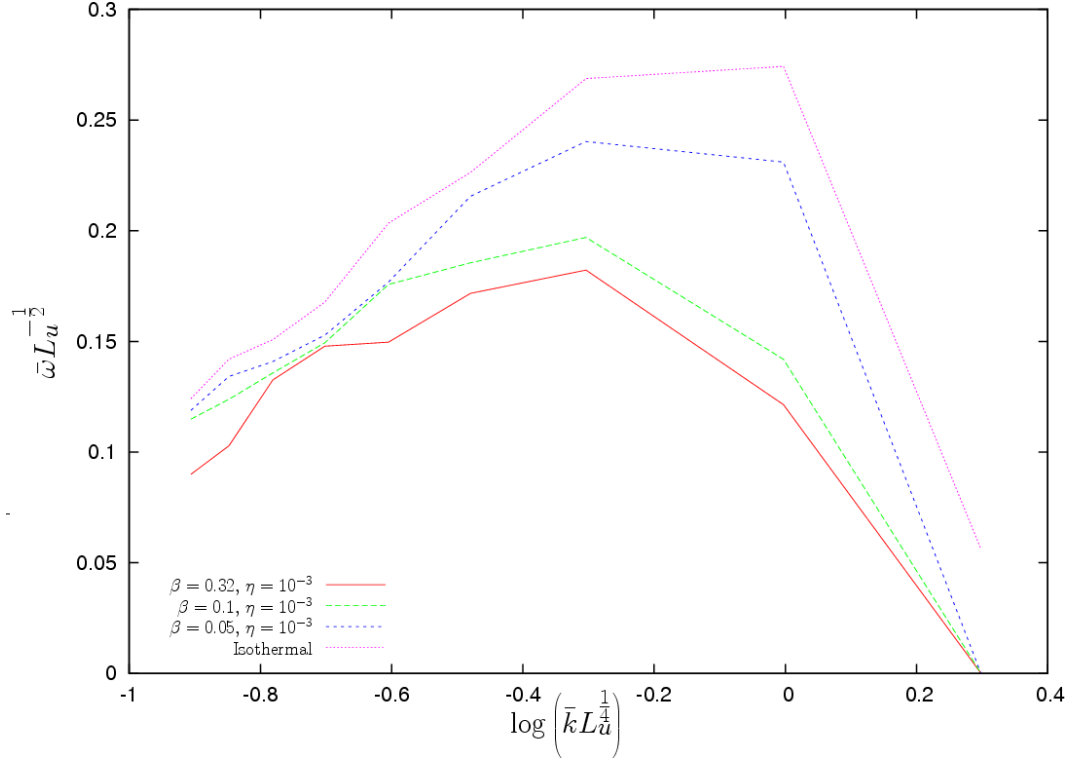


Figure 4.18: Growth rate as a function of wavenumber for  $\beta = 0.32, 0.1, 0.05$  and for the isothermal case.

Figure 4.18 shows the growth rate as a function of wavenumber for the standard model and the three deviations from this of  $\beta = 0.1, 0.05$  and the isothermal case. This has good agreement with the analytic prediction of the value of the wavenumber for the maximum growth rate in 4.1.2 for the isothermal case and the high magnetic pressure dominance (and hence high magnetisation parameter) in the inflow region case of  $\beta = 0.05$ , which is not surprising as the derivation was done for magnetodynamics. The higher plasma beta curves are stretched to the left and flattened in comparison. This is due to the greater effects of the plasma pressure which is not taken into account in the analytic work where

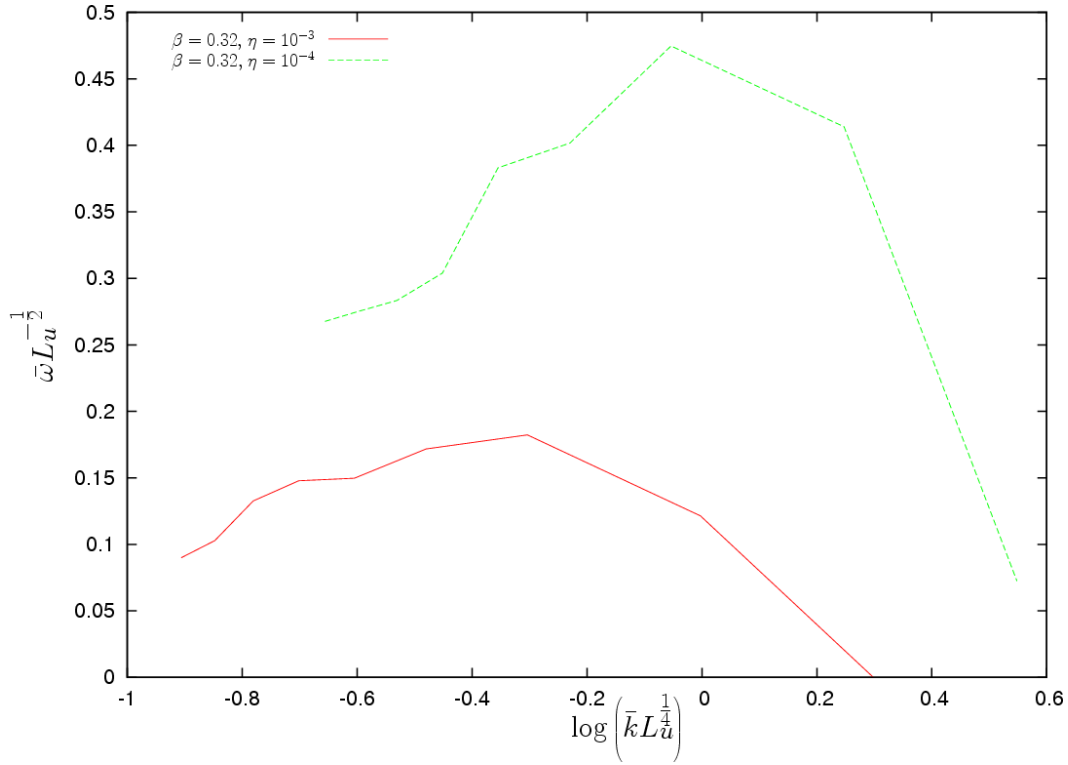


Figure 4.19: Growth rate as a function of wavelength for  $\eta = 10^{-3}$  and  $10^{-4}$ .

it was assumed that the plasma beta is very small (or the magnetisation parameter is very large). The drop-off of the growth rate with the wavenumber is shallower with increasing plasma beta caused by the maximum growth rate occurring for shorter wavenumbers (and longer wavelengths). The non-isothermal cases all cut-off past the wavenumber  $k = \pi$  (wavelength  $\lambda = 2$ ) which points to the cut-off point given by equation 4.75 still existing (if shifted). The isothermal case has a different cut-off point due to the effects of resetting the pressure to keep the temperature constant.

Figure 4.19 shows the growth rate as a function of wavenumber for the standard model with  $\eta = 10^{-3}$  and  $10^{-4}$ . There is a large difference between the two curves and growth rate is more sensitive to the resistivity and hence the relativistic Lundquist number than in magnetodynamics. The curve for  $\eta = 10^{-4}$  has a maximum of about  $\bar{k} = L_u^{-\frac{1}{4}}$

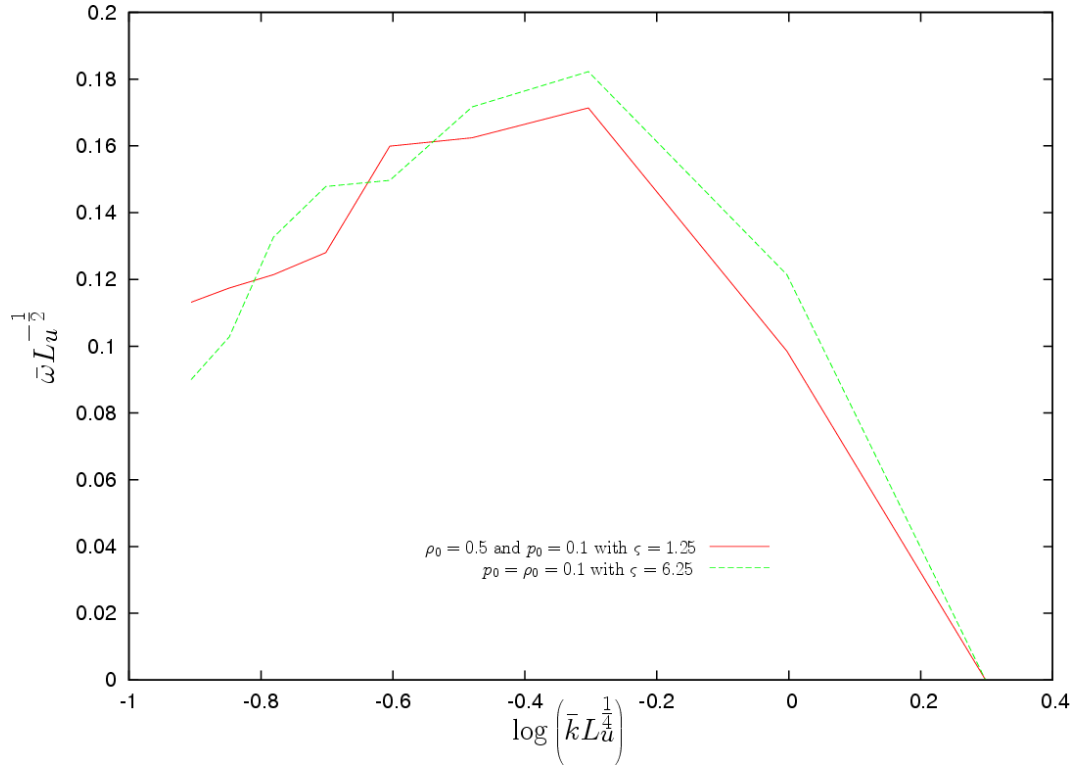


Figure 4.20: Growth rate as a function of wavelength with state variables  $p_0 = \rho_0 = 0.1$  with  $\varsigma = 6.25$  and  $\rho_0 = 0.5, p_0 = 0.1$  with  $\varsigma = 1.25$ .

as predicted in section 4.1.2. This is the result of the greater separation between the wavenumbers for the maximal growth rate and the cut-off point.

Figure 4.20 shows the growth rate as a function of the wavenumber for the standard model with  $p_0 = \rho_0 = 0.1$  with magnetisation parameter  $\varsigma = 6.25$  and  $p_0 = 0.1, \rho_0 = 0.5$  with magnetisation parameter  $\varsigma = 1.25$ . The two curves are very similar with a small reduction in growth rate for the smaller magnetisation parameter. This is caused by the increase in density with the lower magnetisation parameter which requires a greater force to produce the same momentum in the inflow region as a larger magnetisation parameter. As such the growth rate is slightly reduced corresponding to the slight reduction in the inflow. The reduced inflow velocity, to keep the inflow velocity is shown in table 4.5 and the

identical outflow to when the state variables are equal is shown in table 4.6 which with the same electromagnetic momentum flux for the inflow and outflow indicates that the inflow velocity has reduced to keep the inflow momentum density constant.

None of the figures 4.18 - 4.20 reaches the maximal growth rate predicted in 4.1.2. The reduced growth rate is from the effects of the plasma pressure reducing the inflow and slowing the growth of the perturbation. The predictions do accurately predict where the maximum value will occur for lower plasma beta values, larger relativistic Lundquist numbers and the isothermal simulations. This suggests that the magnetodynamical predictions of section 4.1.2 have merit in predicting the wavenumber for the maximum growth rate.

Originally equation 4.75 was to be plotted against the various dispersion relations, but the difference between the predicted growth rates given by magnetodynamics and the growth rates found from relativistic magnetohydrodynamical simulations is so large that they cannot be practically plotted on a single graph. Hence the scaled approach showing the predicted maximum and its corresponding wavenumber was used.

#### **4.2.5 Comparison of the linear growth rates to the observations of flare rise times in Magnetars**

Since the growth rates are known they can be compared to observations of magnetars. From the work on magnetar giant flares and after-glows by Lyutikov in [31] the observed growth rate  $\omega_{ob}$  is found as  $\omega_{ob} = 100s^{-1}$ . The length scale of the current sheet is the typical radius of a neutron star  $R_{NS} \approx 12\text{km}$ . The geometry of a magnetar before a flare is sketched in figure 4.21. This shows a single magnetic field line originating and returning to the magnetar, passing through the magnetosphere where the current sheet caused by oppositely aligned magnetic field lines coming into close contact resides and furthest away from the magnetar is a region of expanding magnetically trapped plasma. The



distance from the magnetar to the magnetosphere is currently unknown. The geometry sketched is similar to the set-up described for a soft gamma ray repeating magnetar in [46].

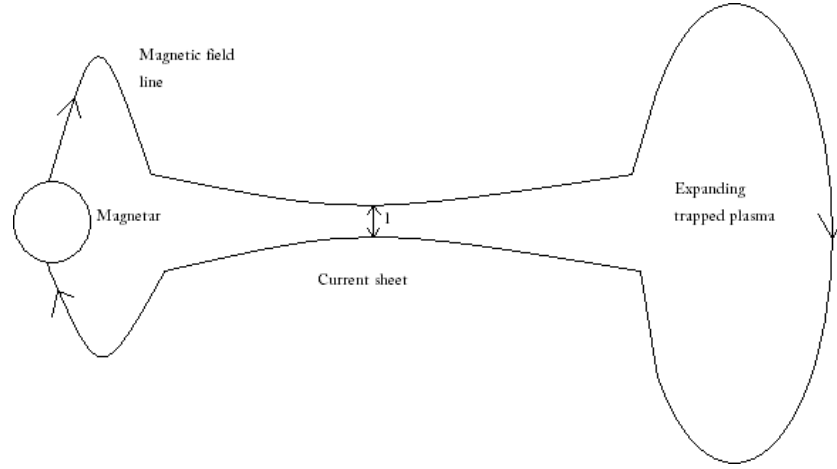


Figure 4.21: A sketch diagram of the magnetic field of a magnetar before a flare

Using the results of section 3.9 with equation 3.86 and the observed values for a magnetar of  $l_d = 10^4 \text{m}$  the numerical growth rates can be converted into S.I. units. This has the time conversion factor of  $t_o = 1/3 \times 10^{-3}$  and hence the conversion factor for the growth rates is  $t_o^{-1} = 3 \times 10^3$ . Conversions can be made to S.I. units and the results of magnetodynamical simulations the fastest growing rates for each case can be compared to the observations. These are presented in table 4.4, where  $\lambda$  is the wavelength,  $\beta$  is the plasma beta and  $\eta$  is the resistivity.

If it is considered that, with the current observational accuracy of compact relativistic objects and that the simulations presented here are quite general and have not been calibrated to any particular physical phenomena or magnetars particularly, then the growth rates compare favourably with the observed value of  $\omega_{ob} = 100 \text{s}^{-1}$  with a small factor of

Case	Growth rate ( $\omega$ ) Code time units	Growth rate, $s^{-1}$ S.I. units
$\lambda = 4, \beta = 0.32, \eta = 10^{-3}$	0.18224	546.72
$\lambda = 8, \beta = 0.32, \eta = 10^{-4}$	0.121152	363.456
$\lambda = 4, \beta = 0.1, \eta = 10^{-3}$	0.185489	556.467
$\lambda = 4, \beta = 0.05, \eta = 10^{-3}$	0.24027	720.81
Isothermal $\lambda = 4, \beta = 0.32, \eta = 10^{-3}$	0.268702	806.106
$\lambda = 4, \beta = 0.32, \eta = 10^{-3}$ $\rho_0 = 0.5$ and $p_0 = 0.1$ with $\varsigma = 1.25$	0.171388	514.16
Magnetodynamics $B_0 = 2.5, \lambda = 4$	0.449932	1349.796

Table 4.4: The fastest growth rates of the relativistic tearing mode for the various cases simulated in time units of the code and S.I. units.

difference being unimportant. This shows that the relativistic tearing mode is a strong candidate for powering magnetar flares.

The main problem with this, as shown in section 4.2.7, is that the plasma outflow which is barely relativistic and has Lorentz factors of  $\approx 1$ . Whilst this is in accord with the predictions for the relativistic tearing mode, it does not match the observations which are expected to have relativistic outflows. This could be solved if the tearing mode led into Petschek reconnection which has the high relativistic outflow as described in sections 5.1.1 and 5.1.3.

### 4.2.6 The non-linear development of the relativistic tearing mode and comparison of the relativistic tearing mode in magnetohydrodynamics to magnetodynamics

The evolution of the perturbation to the current sheet was followed past the linear regime for the case with a resistivity of  $\eta = 10^{-3}$  and plasma beta of  $\beta = 0.32$  for wavelengths of 2, 4, 8 and 16. This is shown in figure 4.22 which shows the saturation of the perturbation for the various modes. The longer wavelengths (smaller wavenumbers) saturate fastest driven by their faster growth rates. This corresponds with the dispersion relation in figures 4.18 and 4.19. The saturation and decay of the perturbation is typical of the tearing mode (as shown in [20]) and is caused by the perturbation acting on the current sheet and changing the structure and increasing with the tearing mode's growth, saturating as the non-linear terms become dominant and their feedback leads to the decay of the perturbation as steady state reconnection is achieved. The final steady state is shown in figure 4.6 with magnetic islands connected by a thin current sheet.

In figure 4.22 the initial settling is seen at the beginning and a saturation at the end of the graph. It is important to separate the causes of the settling and saturation of the perturbation. In the settling the causes can be the perturbation itself settling or the settling of the background state as described in sections 4.2.1 and 4.2.2.

To separate any settling of the perturbation from the settling of the background state the simulation for the standard case with  $L_u = 10^2$ ,  $\beta = 0.32$ ,  $\varsigma = 6.25$  and with a wavelength of 4 was allowed to develop until a time of 11.501 with no perturbation to neglect any effects of the settling of the background state on the perturbation growth. At this time a perturbation of magnitude  $10^{-3}$  was applied as described in section 4.2.1. The resulting growth of the perturbation is shown in figure 4.23. This shows the same settling as before, with the first two time units under-resolved. This region is shown in figure 4.24. It shows an initial small drop in the perturbation value followed by a non-linear growth stage.

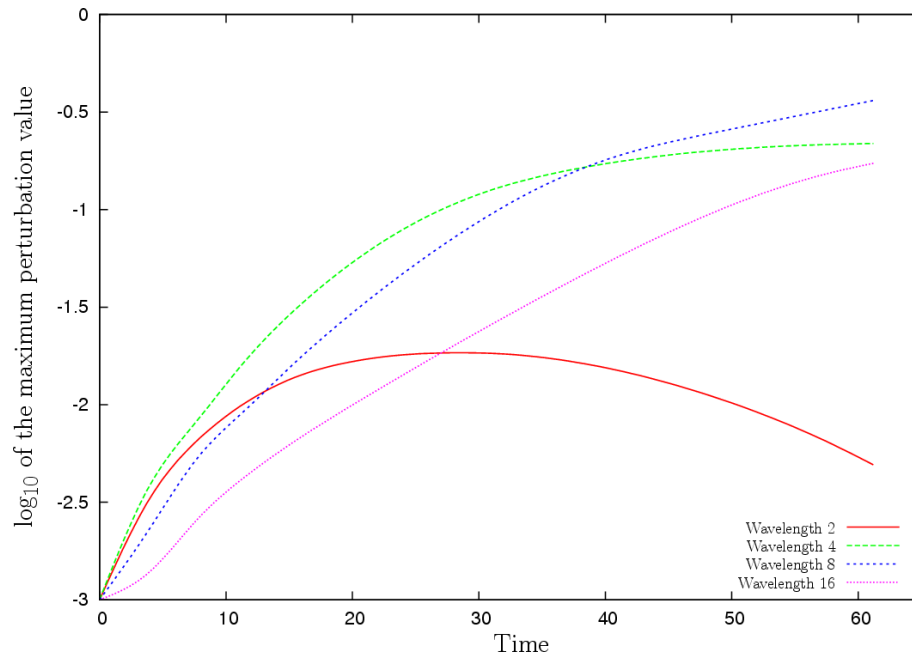


Figure 4.22: Saturation of the perturbation for a resistivity of  $\eta = 10^{-3}$  and plasma beta of  $\beta = 0.32$  for wavelengths 2, 4, 8 and 16.

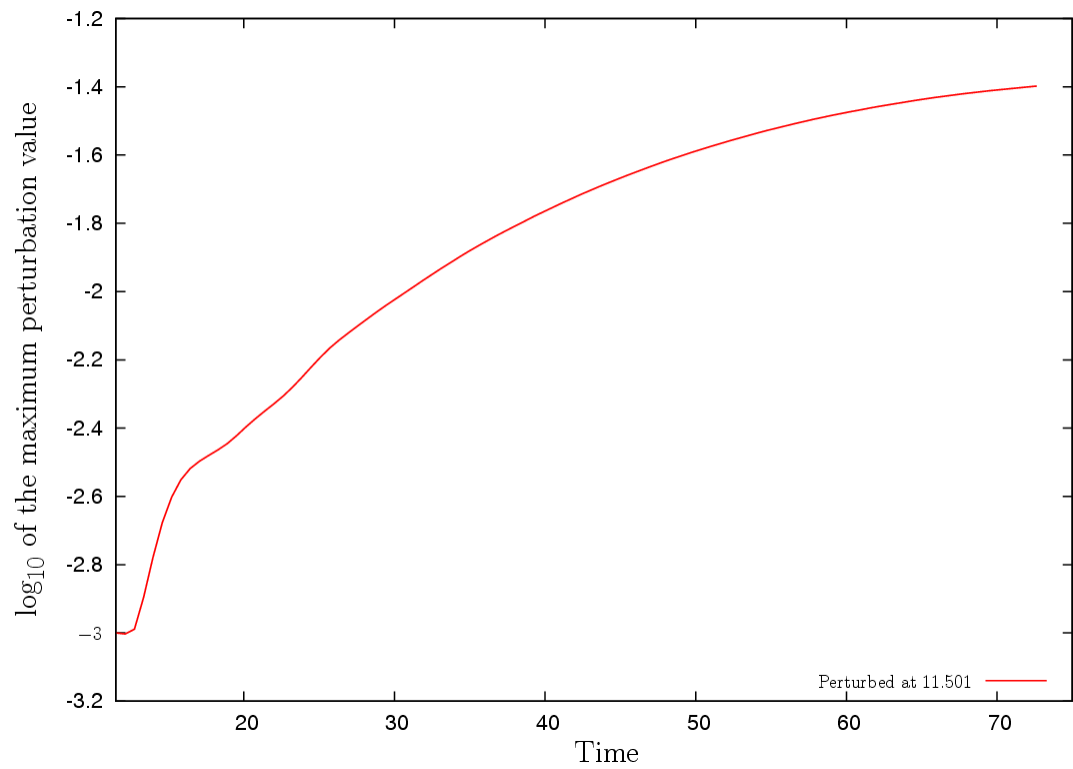


Figure 4.23: The standard case with wavelength 4 and the perturbation applied at time 11.501

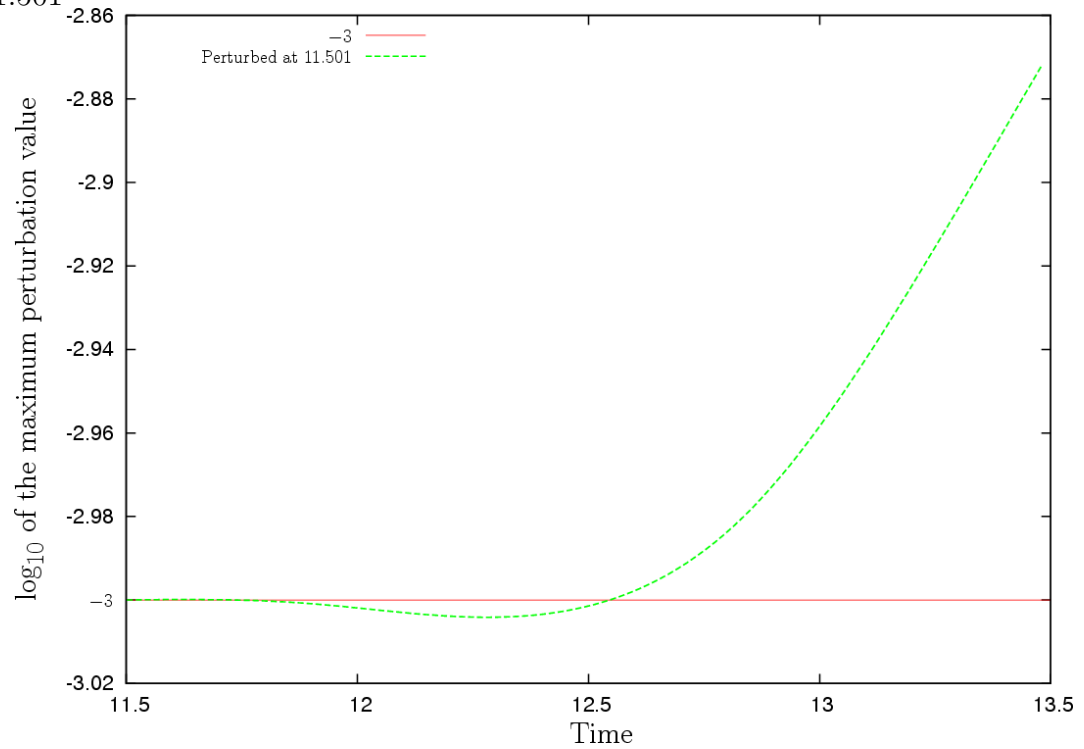


Figure 4.24: The early behaviour of the perturbation applied at time 11.501

This shows that the settling is a property of the perturbation and not an artifact of the background state.

The saturation shown in the figures of the growth rates can be caused by the saturation of the perturbation itself or caused by the diffusion of the current sheet, with the current sheet diffusing away and no longer supporting the perturbation. To investigate this the standard case was simulated with a wavelength of 4 and an initial perturbation of  $10^{-5}$ . As the perturbation is two orders of magnitude smaller it takes longer to grow and if the saturation is caused by the perturbation saturating, will saturate at a later point. The log of the maximum growth rate of the perturbation plotted against time is shown in figure 4.25 which shows the perturbation saturating at the same time as the larger perturbation of  $10^{-3}$ . This shows that the saturation is caused by the diffusion of the current sheet rather than the perturbation itself. This suggests that if the background setup were such that the diffusion of the current sheet were slowed the linear growth regime would last longer and the growth rates could be measured easier. This could be achieved by imposing a constant inflow velocity on the boundary.

The growth rate of the perturbation with plasma beta and the isothermal case for wavelength  $\lambda = 4$  compared to the magnetodynamical case is shown in figure 4.26. As the plasma beta decreases the plasma becomes more magnetically dominated and the plasma pressure has less effect, but, as shown in table 4.4 and the aforementioned figure, even in the isothermal case the plasma pressure has a strong slowing effect on the growth of the tearing mode compared to the magnetodynamical version. This is caused by the dense highly pressurised plasma in the current sheet pushing against the incoming, magnetically frozen in plasma, limiting the amount of magnetic flux which can enter the reconnection region. Hence, it is expected that there is a maximum growth rate that can be achieved by decreasing the plasma beta where the effects of the plasma pressure are no longer affected by increasing the plasma beta value and convergence to a maximal reconnection rate will occur. As an isothermal plasma has a much reduced plasma pressure, it can be thought of

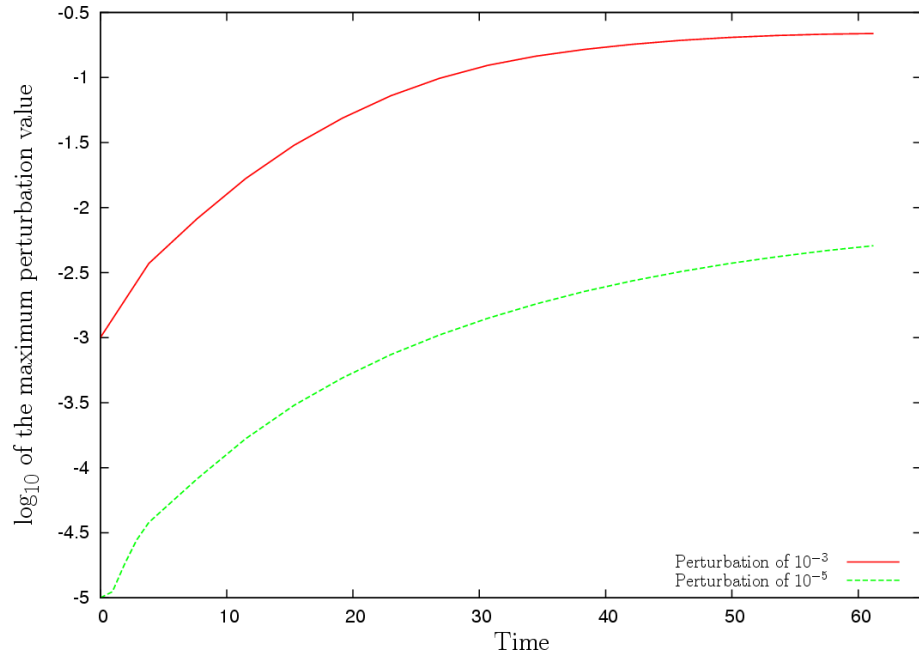


Figure 4.25: Comparison of the perturbations of  $10^{-3}$  and  $10^{-5}$  both with wavelength 4,  $L_u = 10^2$  showing the onset and saturation of the perturbation.

as a upper limit on the maximal growth rates obtainable as the plasma beta goes to zero.

To get a feeling for how the growth rate increases as the plasma beta goes to zero, the maximum perturbation value of each plasma beta at time 61.194 is plotted and extrapolated under a quadratic model to  $\beta = 0$ . The value of the isothermal simulation at this time is also plotted as presented in figure 4.27. This predicts that when  $\beta \rightarrow 0$  the growth rate at time 61.194 will be  $\approx 0.25$ , under the limit of the isothermal simulation (denoted by the filled dot).

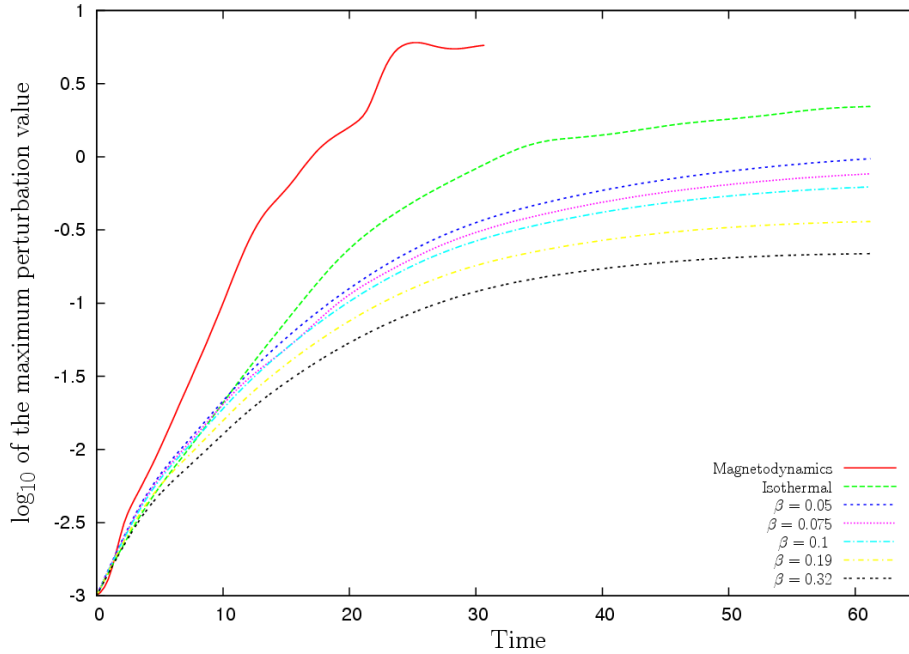


Figure 4.26: Convergence of growth rates to the isothermal case for decreasing plasma betas from  $\beta = 0.32$  to  $\beta = 0.05$  and the magnetodynamical case all with wavelength of  $\lambda = 4$ .



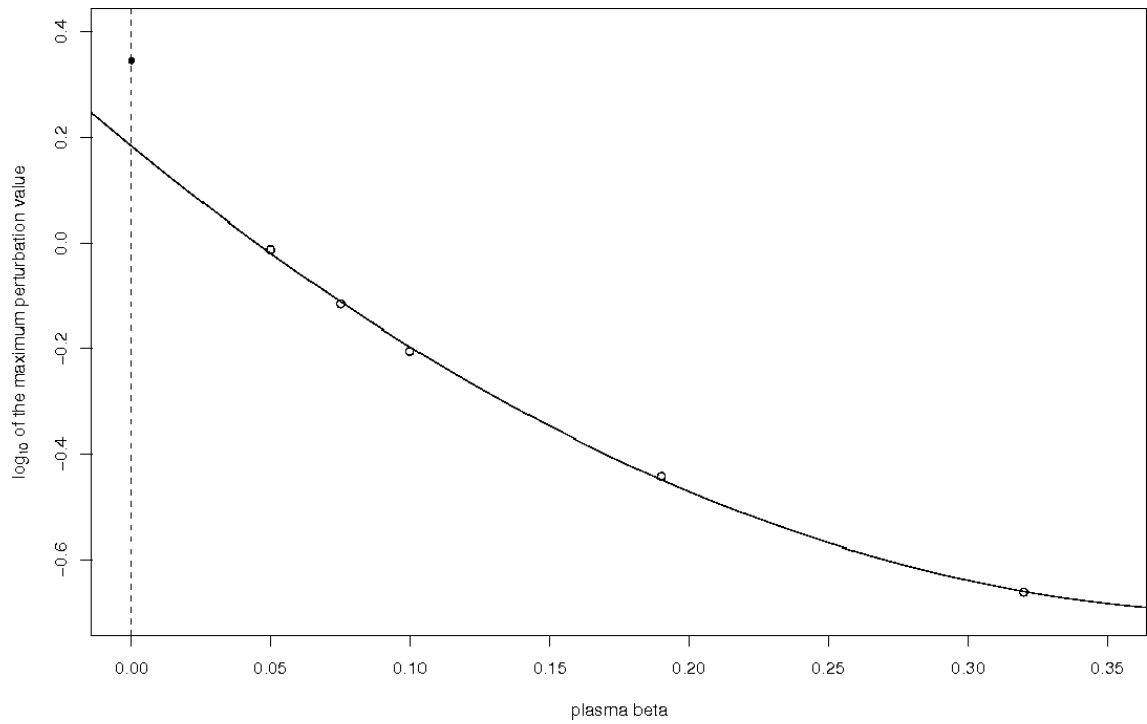


Figure 4.27: Extrapolation of the plasma beta to zero at time 61.194 from figure 4.26.

### 4.2.7 Comparison of the simulations with the theoretically predicted values for the relativistic tearing mode

The numerical simulations can be compared with the order of magnitude prediction of Lyubarsky in section 4.1.1 that

$$v_{in} = L_u^{-1}. \quad (4.92)$$

The values for the fastest growing modes for each case are shown in table 4.5 at time 11.501, just before the end of the linear phase as shown in figures 4.9 - 4.14. The isothermal and lower resistivity  $\eta = 10^{-4}$  cases are very accurate and this is due to the fast growth rate for the isothermal case and the lower resistivity requiring a less magnetically dominated inflow. The other results are at most a factor of 3 out. The cause of this is because the assumption that the inflow region is completely magnetically dominated is not for filled in the simulations. This is not so as seen in the various pressure shown in the top right panel of figure 4.7. As the magnetisation parameter is increased this is expected to be less of a problem as seen in that the decreasing plasma beta gives faster inflows. The compressibility of the plasma inside the current sheet adds to this as well. This is what gives the disagreement between the simulations and the order of magnitude calculations.

In section 4.1.1 it was found that the outflow velocity and Lorentz factor were both approximately  $v_{out}, \gamma_{out} \approx 1$ . The values, which are measured near to the boundaries where they are almost constant, are recorded for each of the fastest growing modes in each case are shown in table 4.6 again for time 11.501 during the linear growth regime.

Case	Inflow velocity ( $v_{in}$ )	$L_u^{-1}$
$\lambda = 4, \beta = 0.32, \eta = 10^{-3}$	$3.3 \times 10^{-3}$	$10^{-2}$
$\lambda = 8, \beta = 0.32, \eta = 10^{-4}$	$10^{-3}$	$10^{-3}$
$\lambda = 4, \beta = 0.1, \eta = 10^{-3}$	$4.1 \times 10^{-3}$	$10^{-2}$
$\lambda = 4, \beta = 0.05, \eta = 10^{-3}$	$4.2 \times 10^{-3}$	$10^{-2}$
Isothermal	$7.4 \times 10^{-3}$	$10^{-2}$
$\lambda = 4, \beta = 0.32, \eta = 10^{-3}$		
$\lambda = 4, \beta = 0.32, \eta = 10^{-3}$ $\rho_0 = 0.5$ and $p_0 = 0.1$ with $\varsigma = 1.25$	$1.6 \times 10^{-3}$	$10^{-2}$

Table 4.5: Agreement of numerical simulations with Lyubarsky's prediction of  $v_{in} = L_u^{-1}$  at time 11.501 in the linear growth phase of the tearing mode.

These all have outflow velocities lower than predicted (which keeps the Lorentz factor  $\approx 1$ ). This is likely due to the current sheet being not fully developed into magnetic islands and having a much larger outflow region. Also the plasma is not incompressible, with a part of the plasma being compressed in the current sheet before being expelled in the outflow compared to the incompressible predictions of section 4.1.1.

The presence of a non-zero  $B_z$  component in the current sheet has been found not to affect the relativistic tearing mode as predicted in section 4.1.1 as it dissipates quickly and is dominated by the plasma pressure in the current sheet. This can be seen by comparing the magnitudes of the plasma pressure and magnetic pressure in the top right panel of figure 4.7 and the top right panel for the rapid dissipation.

### 4.2.8 The reconnection electric field

In experiments of reconnection, either in laboratories or at the Earth's magnetopause, the electric field at the X-point or neutral point is called the reconnection electric field

Case	Outflow velocity ( $v_{out}$ )	Outflow Lorentz factor ( $\gamma_{out}$ )
$\lambda = 4, \beta = 0.32, \eta = 10^{-3}$	0.026	1.0003
$\lambda = 8, \beta = 0.32, \eta = 10^{-4}$	0.23	1.03
$\lambda = 4, \beta = 0.1, \eta = 10^{-3}$	0.04	1.001
$\lambda = 4, \beta = 0.05, \eta = 10^{-3}$	0.054	1.0015
Isothermal $\lambda = 4, \beta = 0.32, \eta = 10^{-3}$	0.2	1.02
$\lambda = 4, \beta = 0.32, \eta = 10^{-3}$ $\rho_0 = 0.5$ and $p_0 = 0.1$ with $\zeta = 1.25$	0.026	1.0003

Table 4.6: A table of the outflow velocity and Lorentz factor for the fastest growing modes of each case

$E^*$  is used to measure the rate of reconnection as a function of time as it is expected to be a source of accelerated particles due to the magnetic field being negligible at the reconnection point. This is often carried over to numerical simulations, e.g. in [50]. For comparison to works that use this the evolution of the reconnection electric field at the X-point  $E^* = |\mathbf{E}(0, 0)|$  with time has been plotted for the fastest growth rates which are recorded in table 4.4 excluding the magnetodynamical case.

Figure 4.28 shows the reconnection electric field for the plasma beta values of  $\beta = 0.32, 0.1, 0.05$ . The reconnection electric field is seen to increase with increasing magnetic dominance of the plasma. The settling period is not seen in the reconnection electric field as, initially it is part of the background electric field caused by the movement of the magnetic field lines.

This quickly drops to the steady reconnection rate with a constant slow decay which corresponds to the saturation of the perturbation as shown in figure 4.22. This is caused by the periodic boundary conditions rather than free flow. The periodic boundaries give an

infinite alternating series of X- and O-points and this stops the formation and ejection of plasmoids and also gives a saturation of the magnetic islands formed by the tearing mode. The saturation slows the rate of reconnection by reducing the amount of magnetic flux which can be reconnected and hence the reconnection magnetic field. The reconnection electric field shown is similar to the electric field found in [40], except they used free flow boundary conditions and hence their reconnection electric field drops to a constant value with no decay.

Figure 4.29 shows the evolution of the reconnection electric field for the isothermal case and how it changes as the current sheet undergoes secondary reconnection, transforming the origin from an X-point (as shown in the final part of figure 4.5) to an O-point (as shown in figure 4.6).

As the current sheet becomes very thin it becomes unstable to secondary tearing caused by shorter wavelengths. To match the sequence of X- and O-points, an O-point forms in the centre of the sheet with two X-points either side. When this happens the changing magnetic field around the origin with the outflow causes the increase in the magnetic reconnection seen in figure 4.29 which dies away back to the slow decay caused by the boundary conditions (as shown in figure 4.28) as the secondary tearing becomes steady and the origin becomes magnetically neutral again. The secondary tearing and the accompanying growth of the reconnection magnetic field from it means there is only a slight decay from the background electric field unlike in figure 4.28.

Figure 4.30 shows the reconnection electric field for a plasma beta of  $\beta = 0.32$  and resistivity of  $\eta = 10^{-4}$ . As can be expected from Ohm's law 2.26, the field is approximately a tenth of the value found for  $\eta = 10^{-3}$ . This can be expected as the non relativistic Ohm's law in the fluid frame is  $\mathbf{J} = \eta^{-1}\mathbf{E}$  which can be expected at the origin. The growth of the reconnection electric field is reminiscent of the secondary tearing found in the isothermal case. Due to the slow growth of the tearing mode this is not obvious from the initial investigation of the data, but on closer inspection this can be

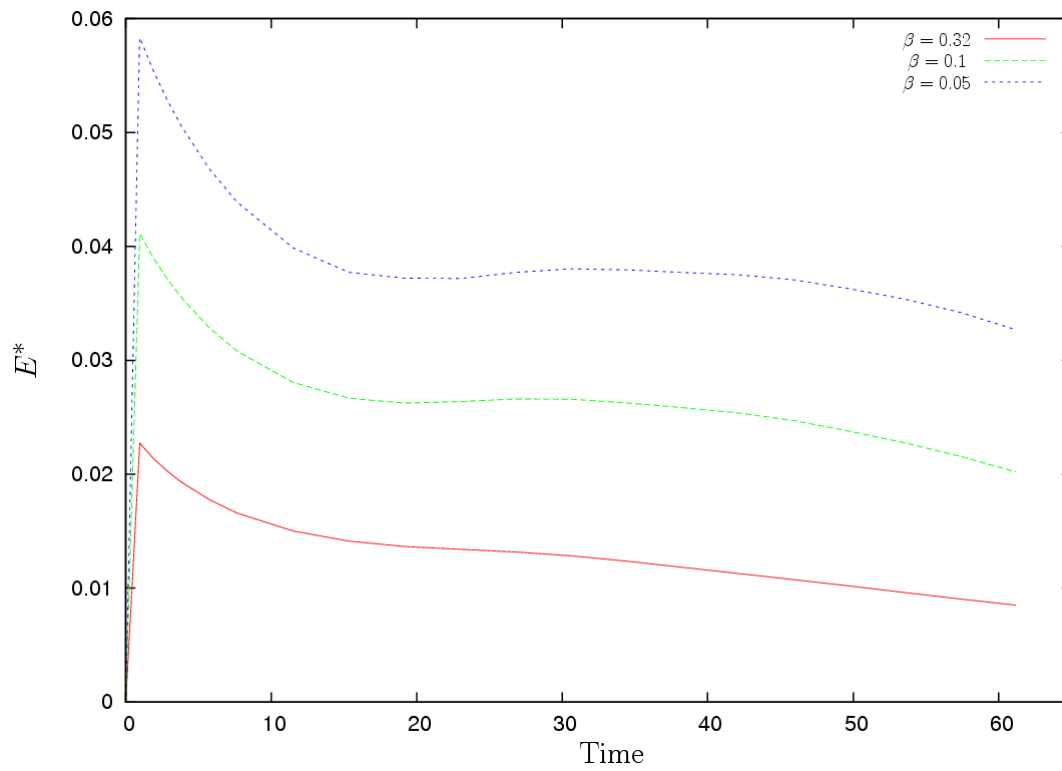


Figure 4.28: Evolution of the reconnection electric field at the X-point for plasma betas,  $\beta = 0.32, 0.1, 0.05$  all with wavelengths  $\lambda = 4$ .

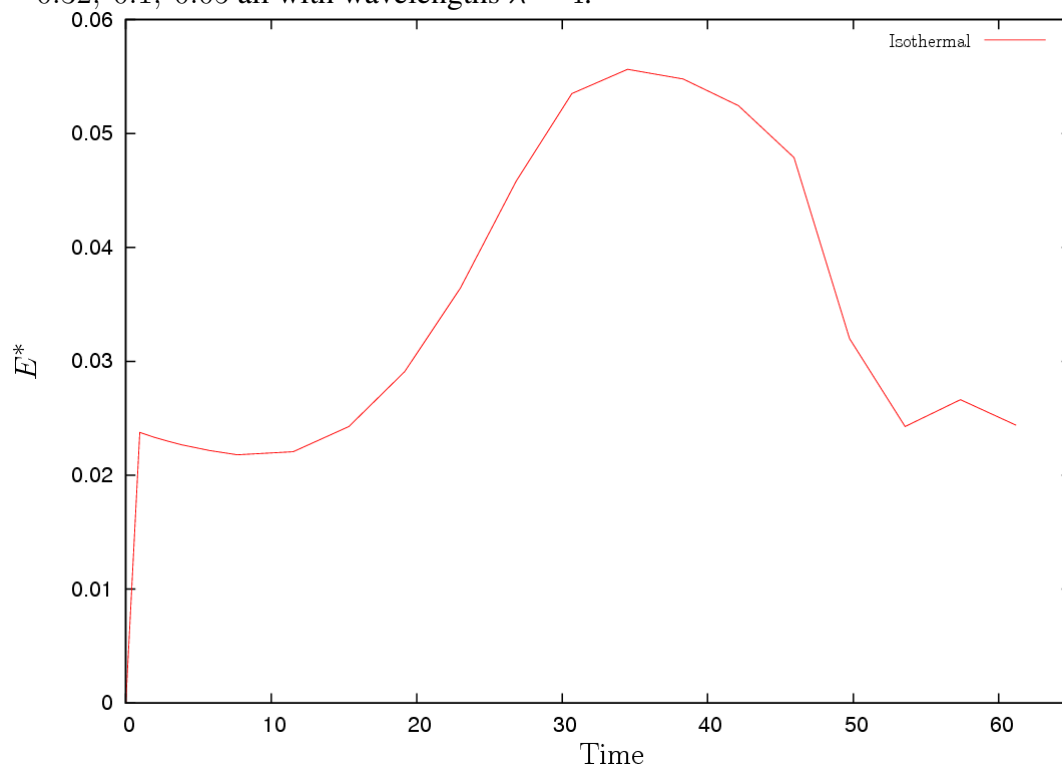


Figure 4.29: Evolution of the reconnection electric field for the isothermal case showing secondary tearing and the X-point transforming to an O-point for wavelength,  $\lambda = 4$ .

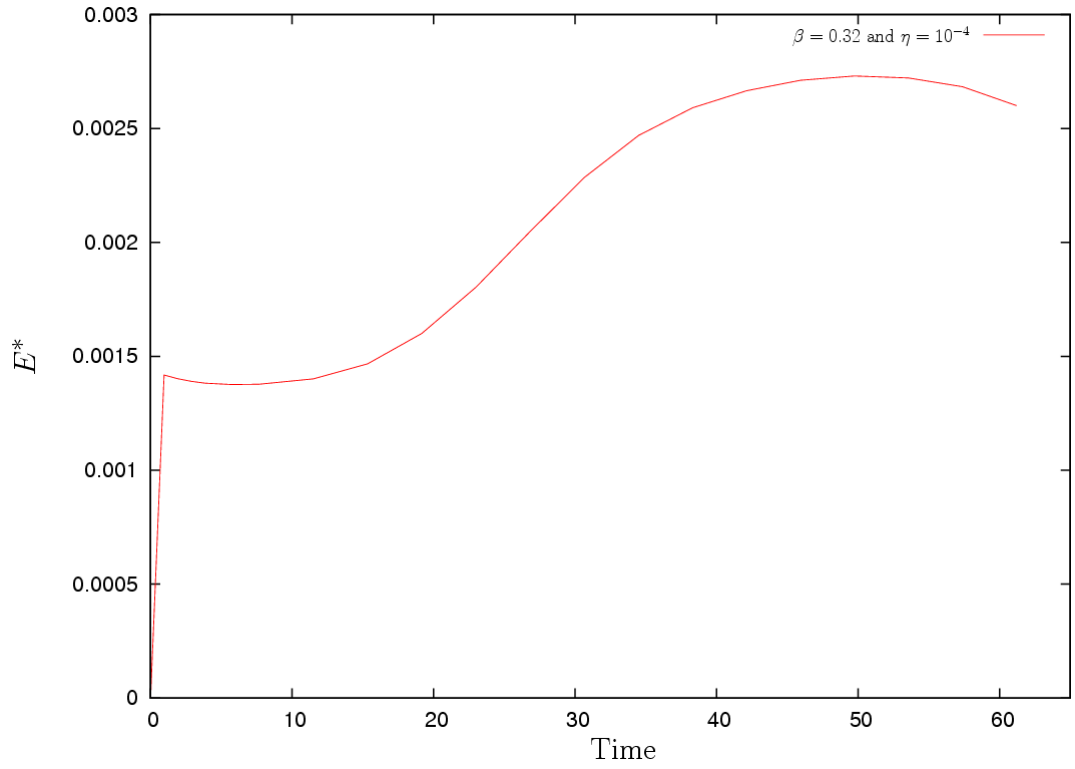


Figure 4.30: Evolution of the reconnection electric field for  $\eta = 10^{-4}$  for wavelength  $\lambda = 8$ .

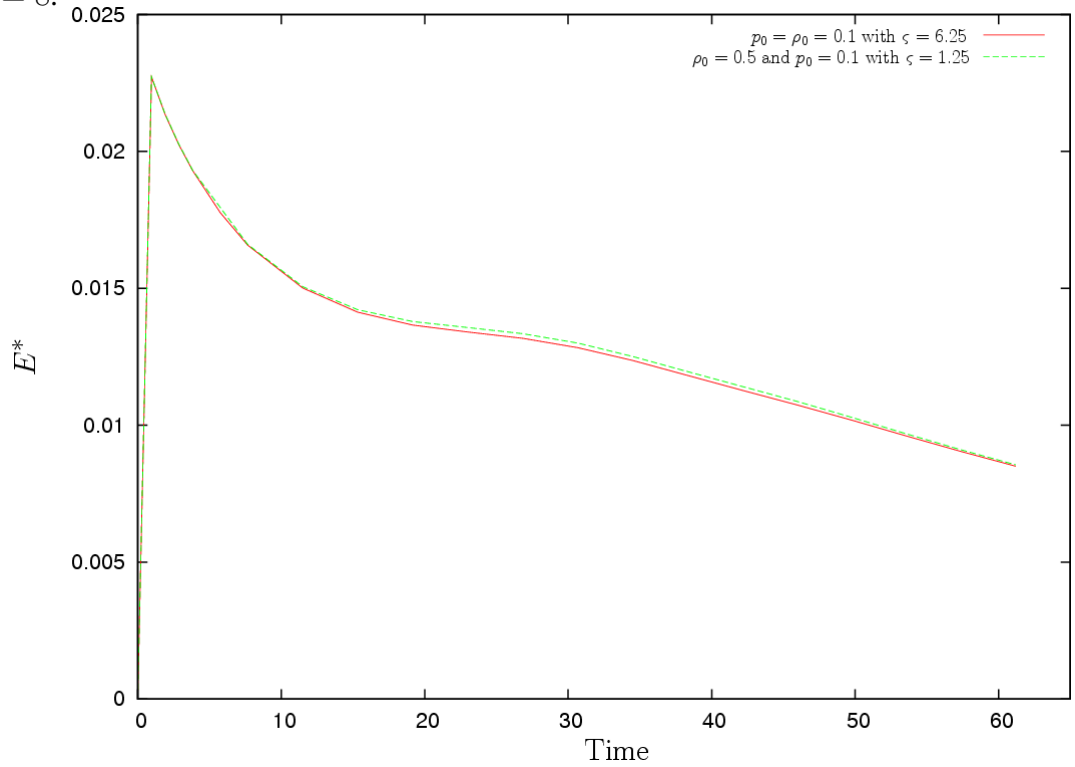


Figure 4.31: Evolution of the reconnection electric field for state variables  $p_0 = \rho_0 = 0.1$  with  $\varsigma = 6.25$  and  $\rho_0 = 0.5, p_0 = 0.1$  with  $\varsigma = 1.25$ .

seen to be secondary tearing, with an O-point forming from the initial X-point. This is shown in figure 4.32 with the X-point found at the same level of resolution and resistivity as wavelength of  $\lambda = 10$  at an earlier time. The secondary tearing is slower than for the isothermal case since the plasma pressure is more dominant in slowing the reconnection process and the resistivity being lower by a factor of 10 gives a slower speed for the magnetic field lines to slip through the plasma in the current sheet. A point of note is that it does not have the same decay from the background electric field to the reconnection electric field found in figure 4.28 as the growth caused by the secondary tearing dominates the reconnection electric field.

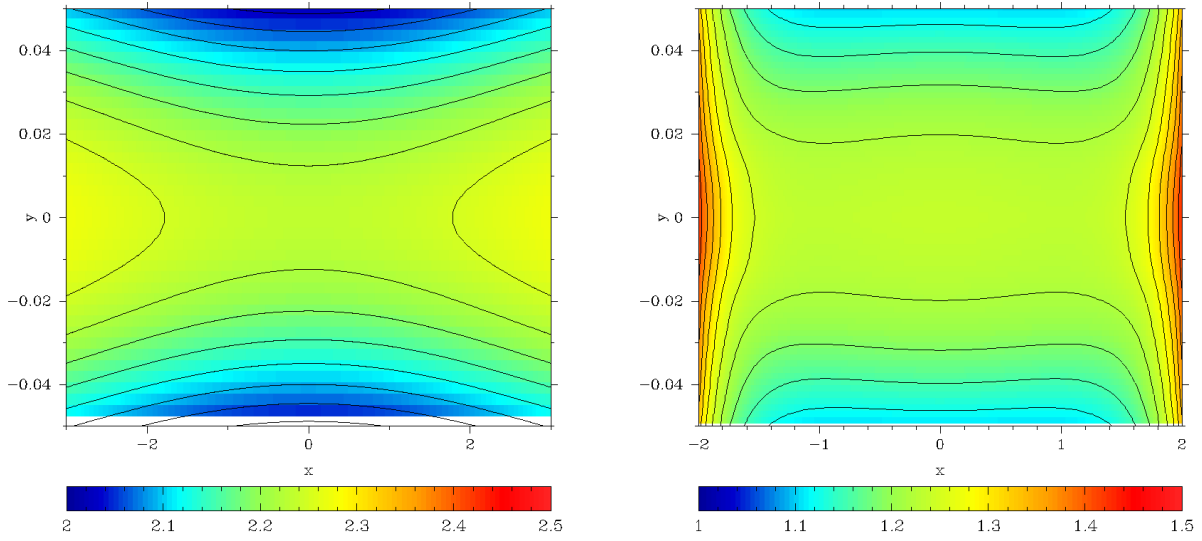


Figure 4.32: A comparison of the X-point for resistivity of  $\eta = 10^{-4}$  and wavelength of  $\lambda = 10$  for time  $t = 61.194$  and the O-point for the same resistivity and a wavelength of  $\lambda = 4$ , for time  $t = 15.464$ . Shown for both cases is the plasma pressure with contour lines.

Figure 4.31 shows the reconnection electric field for state variables  $p_0 = \rho_0 = 0.1$  with  $\varsigma = 6.25$  and  $\rho_0 = 0.5, p_0 = 0.1$  with  $\varsigma = 1.25$ . Despite the variation in the magnetisation parameter, the curves are practically identical. This is due to the magnetisation parameter



being varied by changing the density whilst the reconnection electric field is dependent on the the inflowing magnetic field which is unchanged.



## Chapter 5

# Relativistic Petschek reconnection

In chapter 1 Petschek reconnection and its conception were introduced and in this chapter it will be generalised to the relativistic case via the order of magnitude analysis of Lyubarsky (see [29]). Following this the numerical model is introduced and then relativistic Petschek reconnection is described. The rest of the chapter is dedicated to the results.

### 5.1 An order of magnitude calculation for relativistic Petschek reconnection

To get an idea of the properties of relativistic Petschek reconnection, as in Chapter 4, the order of magnitude work of Lyubarsky in [29] is reproduced. In doing so the same set-up as section 4.1.1 is used. The set-up of Petschek reconnection is shown in figure 5.1, which shows the inflow and outflow, magnetic field lines, smaller reconnection region (of length  $l$ ), relativistic slow shocks, angle between the slow shocks and the  $x$ -axis  $\psi$ , and the angle the magnetic field just upstream of the slow shock makes with the slow shock plane (the  $x$ -axis)  $\theta$ .

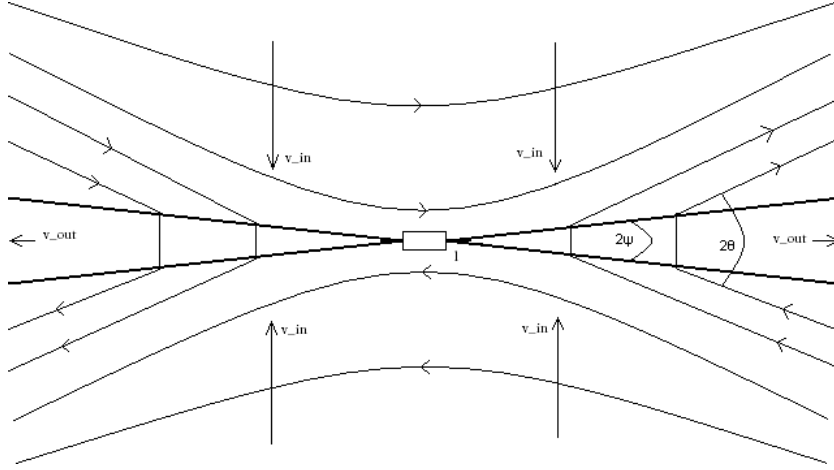


Figure 5.1: A sketch diagram of relativistic Petschek reconnection showing the reconnection region (the box), the magnetic field lines (centred arrows), the velocity (the headed arrows) and the relativistic slow shocks (bold lines).

The length of the current sheet  $L$  is not shown since it will grow as the jet between the relativistic slow shocks pushes out into the unperturbed plasma.

### 5.1.1 Jump conditions for a slow shock

To start the order of magnitude analysis, first the jump conditions at the relativistic slow shocks are considered with the inflow (or upstream flow, denoted by  $_1$ ) being cold,  $w_1 = \rho_1$ , and the outflow (or downstream flow, denoted by  $_2$ ) being relativistically hot,  $w_2 = 4p_2$ . Then in the frame of reference in which the shock is at rest, the conservation of energy and momentum fluxes, in units where  $c = 1$  but the factor of  $4\pi$  is not absorbed into the electromagnetic fields, the density  $\rho$  and enthalpy  $w$  are both measured in the rest frame of the plasma and the electromagnetic fields are measured in the shock frame, the conditions for the matter, energy, normal and tangential momentum, the magnetic field, Gauss's law respectively across the slow shock are in the units of the code

$$\rho_1 \gamma_1 v_{n1} = \rho_2 \gamma_2 v_{n2}, \quad (5.1)$$

$$\rho_1 \gamma_1^2 v_1 + B_{t1} E_t = w_2 \gamma_2^2 v_{n2} + B_{t2} E_t, \quad (5.2)$$

$$\rho_1 \gamma_1^2 v_1^2 + \frac{B_{t1}^2}{2} = w_2 \gamma_2^2 v_{n2}^2 + \frac{B_{t2}^2}{2} + p_2, \quad (5.3)$$

$$-B_n B_{t1} = w_2 \gamma_2^2 v_{n2} v_{t2} - B_n B_{t2}, \quad (5.4)$$

$$E_t = \text{const}, \quad (5.5)$$

$$B_n = \text{const}. \quad (5.6)$$

The final equation needed is the continuity of the transverse magnetic field and is found from Ohm's law, 2.26. Since the reconnection happens inside the small, central reconnection region the resistivity is negligible across the shock and, with the assumption that the charge density and inflow velocity are small, the ideal magnetohydrodynamical condition of infinite conductivity is recovered

$$\mathbf{E} + \mathbf{v} \times \mathbf{B} = \mathbf{0}, \quad (5.7)$$

and then the continuity of the electric field gives

$$E_t = v_1 B_{t1} = v_{n2} B_{t2} - B_n v_{t2}. \quad (5.8)$$

In equations 5.1 to 5.8 the sub-scripts  $n$  and  $t$  are the normal and tangential parts of the vector relative to the shock. In these equations it has been assumed that the inflow velocity is normal to the shock so that  $v_{n1} = v_1$  and  $v_{t1} = 0$  and that  $B_n$  and  $E_t$  are non-zero.

The equations of the jump conditions presented here are based upon the jump conditions for ideal magnetohydrodynamics in [42], for relativistic ideal magnetohydrodynamics in [24] and for electromagnetic fields in [22].

The slow shocks are close to being switch off shocks, where the incoming magnetic field is inclined to the shock and the out-going magnetic field is normal to the shock, and as such the tangential part of the magnetic field can be taken as zero,  $B_{t2} = 0$ . If this is substituted into the second equality in equation 5.8, then

$$v_{t2} = -\frac{B_{t1}}{B_n}v_1. \quad (5.9)$$

If this is then further substituted into the second conservation of momentum flux equation 5.4, the upstream velocity is found as

$$v_1 = \frac{B_n^2}{w_2 \gamma_2^2 v_{n2}}, \quad (5.10)$$

and, using the conservation of energy flux equation 5.2 with the definition of the Lorentz factor,  $\gamma = (1 - v^2)^{-\frac{1}{2}}$ , and the first equality in equation 5.8, the inflow velocity is found in terms of the incoming magnetic field and density,

$$v_1^2 = \frac{B_n^2 (1 - v_1^2)}{\rho_1 + B_{t1}^2 (1 - v_1^2)}. \quad (5.11)$$

Equation 5.11 shows that the inflow velocity is approximately the Alfvén speed since the relativistic Alfvén speed is given by

$$v_a = \frac{B_n}{\sqrt{\rho + B^2}}, \quad (5.12)$$

and in general  $B_{t1} \gg B_n$ . The expression for  $v_1$  can be further simplified if the magnetisation parameter,

$$\varsigma = \frac{B_1^2}{4\pi\rho_1\gamma_1^2}, \quad (5.13)$$

is assumed to be large  $\varsigma \gg 1$ , with the inflow velocity written as

$$v_1^2 = \frac{B_n^2/B_1^2}{\frac{1}{\varsigma} + B_{t1}^2/B_1^2}, \quad (5.14)$$

and then

$$v_1 = \frac{B_n}{B_{t1}} = \tan \theta, \quad (5.15)$$

where the angle  $\theta$  is the angle between the magnetic field just upstream of the relativistic slow shock and the shock plane, as shown in figure 5.1. This derivation has the implicit assumption that  $\theta < \frac{\pi}{4}$ , which is always true in Petschek reconnection as the relativistic slow shocks, which cause the distortion of the incoming magnetic region, are at a small angle to the  $x$ -axis. If neither of the assumptions is true, then the inflow velocity can still be found from the full equation for  $v_1^2$ , equation 5.11.

The tangential part of the outflow velocity can be found from substituting equation 5.11 into equation 5.9 to get

$$v_{t2} = -B_{t1} \sqrt{\frac{1}{\rho_1\gamma_1^2 + B_{t1}^2}}, \quad (5.16)$$

and with the definition of the magnetisation parameter from equation 5.13 and  $\frac{B_{t1}}{B_1} = \cos \theta$ , this is

$$v_{t2} = -\cos \theta \sqrt{\frac{\varsigma}{1 + \varsigma \cos \theta}}. \quad (5.17)$$

If a Taylor expansion in the small parameter  $\frac{1}{\zeta}$  is taken, keeping up to the linear terms, then  $v_{t2}$  in the limit of  $\zeta \gg 1$  is

$$v_{t2} = - \left( 1 - \frac{1}{2\zeta \cos^2 \theta} \right). \quad (5.18)$$

With these  $v_{n2}$ ,  $\gamma_2$  and  $p_2$  can be found. If equations 5.2 and 5.3 are taken as simultaneous equations for  $v_{n2}$  and  $p_2$ , expressing the Lorentz factor in  $v_{t2}$  and  $v_{n2}$  and using  $B_{t2} = 0$  and  $E_t = v_1 B_{t1}$  and  $w_2 = 4p_2$  and then eliminating  $p_2$ ,  $v_{n2}$ , this gives

$$v_{n2} = - (v_{t2}^2 - 1) \frac{(\rho_1 \gamma_1^2 v_1 + v_1 B_{t1}^2)}{4 \left( \rho_1 \gamma_1^2 v_1^2 + \frac{B_{t1}^2}{2} \right)}. \quad (5.19)$$

The pre-factor can be simplified as

$$v_{t2}^2 - 1 = - \frac{\frac{1}{\zeta}}{\frac{1}{\zeta} + \cos^2 \theta}, \quad (5.20)$$

and  $v_{n2}$  becomes

$$v_{n2} = \frac{1}{4\zeta} \left( \frac{1}{\zeta} + \cos^2 \theta \right)^{-1} \frac{(\rho_1 \gamma_1^2 v_1 + v_1 B_{t1}^2)}{4 \left( \rho_1 \gamma_1^2 v_1^2 + \frac{B_{t1}^2}{2} \right)}. \quad (5.21)$$

Using the definition of the magnetisation parameter and  $\cos \theta$  then

$$v_{n2} = \frac{v_1}{4\zeta} \left( \frac{1}{\zeta} + \cos^2 \theta \right)^{-1} \frac{\left( \frac{1}{\zeta} + \cos^2 \theta \right)}{\left( \frac{1}{\zeta} v_1 + \frac{1}{2} \cos^2 \theta \right)}. \quad (5.22)$$

If  $v_{n2}$  is now expressed as a Taylor expansion in  $\frac{1}{\zeta}$  and keeping only up to the linear term, then

$$v_{n2} = \frac{\sin \theta}{2\zeta \cos^3 \theta}. \quad (5.23)$$



With this the Lorentz factor can be expressed as

$$\gamma_2^{-2} = 1 - v_{t2}^2 - v_{n2}^2. \quad (5.24)$$

On substitution and inversion this becomes

$$\gamma_2^2 = \varsigma \cos^2 \theta \left( \frac{4 \cos^4 \theta}{4 \cos^4 \theta - \frac{1}{\varsigma}} \right) \quad (5.25)$$

and since  $\varsigma \gg 1$

$$\gamma_2 = \sqrt{\varsigma} \cos \theta. \quad (5.26)$$

To get the pressure of the outflow, equation 5.2 multiplied by  $v_{n2}$  is subtracted from equation 5.3 to give

$$p_2 = \rho_1 \gamma_1^2 v_1 (v_1 - v_{n2}) + \frac{B_{t2}^2}{8\pi} (1 - 2v_1 v_{n2}). \quad (5.27)$$

If this is then multiplied by  $B_1^{-2}$  then

$$\frac{p_2}{B_1^2} = \frac{1}{\varsigma} (v_1 - v_{n2}) + \frac{1}{2} \cos^2 \theta (1 - 2v_1 v_{n2}). \quad (5.28)$$

Since  $\varsigma \gg 1$  and  $v_{n2} \propto \frac{1}{\varsigma}$ , then

$$p_2 = \frac{B_1^2 \cos^2 \theta}{8\pi}. \quad (5.29)$$

If the angle the outflow makes to the shock is  $\phi$  then

$$\tan \phi = \frac{v_{n2}}{v_{t2}} = \frac{\frac{1}{\varsigma} \tan \theta}{\frac{1}{\varsigma} - 2 \cos^2 \theta}. \quad (5.30)$$

If a Taylor expansion is taken as before, then

$$\tan \phi = -\frac{\tan \theta}{\varsigma \cos^2 \theta}, \quad (5.31)$$

and hence the outflow is strongly relativistic and at an angle  $\phi \sim \frac{1}{\varsigma}$  to the shock plane.

Finally using the conservation of matter equation across a shock 5.1, and since  $v_{n1} \approx v_1$  then the outflow density can be found in terms of the inflow density as

$$\rho_2 = 2\rho_1 \cos^2 \theta \sqrt{\frac{\varsigma}{\cos 2\theta}}. \quad (5.32)$$

Hence the outflow density will be highly compressed.

### 5.1.2 The reconnection region

Petschek's analysis, first presented by Petschek in [38], is sketched in figure 5.1. The current sheet has zero thickness and is located at  $x \in [-l, l]$  with the outer boundaries at  $\pm L$  as described at the start of section 5.1. In the inflow region the magnetic field will be a small perturbation to the background horizontal field  $\mathbf{B} = B_0 \hat{\mathbf{x}}$  and when  $\varsigma \gg 1$  it will have negligible plasma pressure and inertia. With the inflow being approximately the Alfvén velocity from equation 5.11, and  $B_{t1} \approx B_1$ , then

$$v_1 = v_{in} = \frac{B_n}{B_{t1}} \approx \frac{B_y}{B_0}, \quad (5.33)$$

and hence, for  $x \in [-L, -l]$ ,  $B_y = v_{in} B_0$  and, for  $x \in [l, L]$ ,  $B_y = -v_{in} B_0$  (with the sign reversal from  $B_y$  to give the right curvature) in the inflow region. As the Alfvén speed will be non-relativistic in the inflow the electric field will also be negligible and as there is no magnetic gradients plasma acts as an ideal one and hence equation 2.15 gives that the magnetic field will be irrotational and  $\mathbf{B} = \nabla \Phi$ . As with the equation for

no magnetic monopoles 2.18, to find the potential function Laplace's equation must be solved. The last boundary condition needed to solve this is that the field is horizontal at large distances and, with the slow shocks being very narrow, horizontal at  $x = 0$  (the shock plane) as well.

If the normal component of the magnetic field on the  $x$ -axis is considered to be produced by a series of continuous poles along the  $x$ -axis. A pole at  $(\varepsilon, 0)$  will produce a normal component of the magnetic field of

$$\frac{m}{y^2 + (x - \varepsilon)^2}, \quad (5.34)$$

and then the flux produced by the series of poles along the  $x$ -axis will be  $\pi m$  and comparing it with the flux in the upper half plane of  $B_y$  gives

$$m = \frac{B_y}{\pi}. \quad (5.35)$$

So if this is then combined as a perturbation to the horizontal magnetic field  $B_0 \hat{x}$  and using equation 5.33 then the potential is

$$\phi = B_0 x - \frac{v_{in} B_0}{\pi} \left( \int_{-L}^{-l} \ln(y^2 + (x - \varepsilon)^2) d\varepsilon - \int_l^L \ln(y^2 + (x - \varepsilon)^2) d\varepsilon \right). \quad (5.36)$$

Then the  $x$  component of the magnetic field is

$$B_x = \frac{\partial \phi}{\partial x} = B_0 - \frac{2v_{in} B_0}{\pi} \left( \int_{-L}^{-l} \frac{x - \varepsilon}{y^2 + (x - \varepsilon)^2} d\varepsilon - \int_l^L \frac{x - \varepsilon}{y^2 + (x - \varepsilon)^2} d\varepsilon \right), \quad (5.37)$$

and at the origin it is

$$B_x(0) = B_0 - \frac{2v_{in} B_0}{\pi} \left( \int_l^L \varepsilon^{-1} d\varepsilon - \int_{-L}^{-l} \varepsilon^{-1} d\varepsilon \right) \quad (5.38)$$

or, using  $\int x^{-1} dx = \ln |x|$ ,

$$B_x(0) = B_0 \left( 1 - \frac{4v_{in}}{\pi} \ln \frac{L}{l} \right). \quad (5.39)$$

Since reconnection will stop if the magnetic field becomes too large at the origin, an estimate of the maximum reconnection rate is to put  $B_x(0) = 1/2 B_0$  and then

$$v_{in} = \frac{\pi}{8 \ln(L/l)}. \quad (5.40)$$

If equation 4.22 is used with the definition of the Lundquist number for the current sheet,  $L_u = l/\eta$ , then  $l = \eta/v_{in}$ . If this is substituted into equation 5.40 and the external Lundquist number for the inflow, far from the shock plane,  $S_u = L/\eta$ , then the inflow velocity is

$$v_{in} \simeq \frac{\pi}{8 \ln S_u}, \quad (5.41)$$

where the  $\ln v_{in}$  term is dropped compared to  $\ln S_u$ .

Hence as the Lundquist number  $S_u$  will typically be a large number of the order of  $10^5$ - $10^{10}$ , the maximum reconnection rate will be  $\approx 1/10$ .

From equation 5.15, and  $\theta$  being a small angle, the inclination of the magnetic field just upstream of the shock to the shock plane will be  $\theta \approx 1/10$ .

### 5.1.3 Relativistic Petschek reconnection with $B_z \neq 0$

So far it has been assumed that the  $z$  component of the magnetic field is zero in the inflow,  $B_{z(in)} = 0$ . However, unlike the tearing mode, Petschek reconnection is highly compressive, as shown in equation 5.32, and in the outflow the  $z$  component may become large and change the outflow parameters.

To investigate this, a small  $z$  component of the magnetic field is assumed to be in the inflow region,  $B_{z(in)} = \alpha B_0$ , where  $\alpha$  is a small fraction. The  $B_z$  component is the same in the whole domain and unlike the  $B_x$  component does not change sign. As the  $B_x$  does change sign, the magnetic field lines diverge across the  $x$ -axis in the  $z$  direction. Hence the magnetic field lines shrink in the  $x$  direction as they reconnect as in the anti-parallel case, they stretch in the  $z$  direction to connect the divergent inflow regions. To accommodate this, the inflow will be separated from the outflow by a rotational shock. In this section, an order of magnitude calculation is performed. A more detailed analysis is given in the appendix of [29] where it is found that a pair of slow shocks is needed between the rotational ones to satisfy the outflow conditions on the velocity.

If the angle of the rotational shock is  $\psi_r$  to the  $x$ - $z$  plane, it will be much less than the angle the inflow magnetic field makes with the shock plane,  $\psi_r \ll \theta$ . At the upper relativistic rotational shock the magnetic field lines will shrink with the speed of light to connect the inflow to the outflow. The point where this happens will move at the speed  $\sin \alpha$  (since the speed of light is taken as 1) in the  $z$  direction and since  $\alpha$  is a small angle, the speed of the intersection point can be taken as  $\alpha$ . Using the same argument the point of intersection of the incoming magnetic field lines with the relativistic rotational shock will move in the  $y$  direction with speed  $\psi_r$ . At the lower relativistic rotational shock the velocities are the same, but with opposite sign and hence field lines between the two relativistic rotational shocks will be inclined at an angle  $\alpha/\psi_r$  to the  $x$ - $z$  plane. Then, since the  $y$  component is almost perpendicular to the rotational shock, it will not vary much across it. The outflow  $z$  component of the magnetic field can be estimated to be

$$\frac{B_{z(out)}}{B_y} = \frac{\alpha}{\psi_r}, \quad (5.42)$$

and from equation 5.15, using the fact that  $\theta$  is a small angle,  $B_{z(out)}$  is

$$B_{z(out)} = \frac{\alpha\theta}{\psi_r} B_0. \quad (5.43)$$

For  $B_{z(out)}$  to affect the outflow, it must become large enough to match the inflow pressure. In the rest frame of the plasma the outflow magnetic field is  $B_{z(out)} / \gamma_{out}$  and since in the inflow the magnetic field is almost parallel to the  $x$ -axis it will not be transformed, and so a small  $B_z$  in the inflow has no effect on the outflow if

$$B_{z(out)} \ll B_0 \gamma_{out}. \quad (5.44)$$

In this case the derivations of section 5.1.1 govern the outflow parameters. Then, using the small  $\theta$  approximation, equation 5.26 gives  $\gamma_{out} = \sqrt{\varsigma}$  and equation 5.23 gives  $\psi_r = \theta / 2\varsigma$ . If this, along with equation 5.43, is used, the condition for a small  $B_z$  component in the inflow to stay negligible in the outflow is

$$\alpha \ll \frac{1}{2\sqrt{\varsigma}}. \quad (5.45)$$

Even though  $\alpha$  is small, this condition is easily violated as  $\varsigma$  will be very large. If this condition is violated, then at the first point this happens,

$$B_{z(out)} = B_0 \gamma_{out}. \quad (5.46)$$

Since the inflow and outflow are now both magnetically dominated, the energy flux is

$$B_{t1} E_t = B_{t2} E_t, \quad (5.47)$$

and using equation 5.8 this becomes

$$B_0^2 v_{in} = B_{z(out)}^2 \psi_r, \quad (5.48)$$

where the  $B_n v_{t2}$  is dropped as it is small compared to the  $B_{t2} v_{n2}$  term.

Then, using equation 5.43 and the small  $\theta$  approximation, the angle the rotational shock makes to the  $x$ - $z$  plane is

$$\psi_r = \alpha^2 \theta. \quad (5.49)$$

The outflow speed is found in the appendix of [29] and is  $v_{out} = 1 - \alpha^2 / 2$ , which gives the Lorentz factor of the outflow as

$$\gamma_{out} = \frac{1}{\alpha}. \quad (5.50)$$

Equations 5.49 and 5.50 show that, when condition 5.45 is violated, the rotational shock will be much wider, giving a thicker outflow travelling at a slower speed. With the reduced outflow velocity and  $B_z$  magnetic field present, the outflow will be magnetically dominated and there will be a large Poynting flux in the outflow.

As the inflow velocity is unaffected, the reconnection rate given by equation 5.41 will be the same whether  $B_z = 0$  or not.

## 5.2 Numerical simulations

Numerical simulations of relativistic Petschek reconnection were performed using the code described in chapter 3. The following section describes the model and extensions of it and the final section of this chapter describes the results of the simulations.

### 5.2.1 The numerical model

The standard model used to investigate relativistic Petschek reconnection was a Harris current sheet,

$$\mathbf{B} = \left( B_0 \tanh \left( \frac{y}{l} \right), 0, 0 \right), \quad \mathbf{E} = \mathbf{v} = \mathbf{0}, \quad (5.51)$$

$$p = p_0 \left( 1 + \frac{1}{\beta} \left( \operatorname{sech}^2 \left( \frac{y}{l} \right) \right) \right) \quad \text{and} \quad \rho_0 = \frac{1}{10}. \quad (5.52)$$

The constants used were a background pressure of  $p_0 = 0.1$  (equal to the background density), an effective width of the current sheet of  $l = 0.05$  and a plasma beta of  $\beta = 0.03$  then using the definition of the plasma beta

$$\beta = \frac{2p}{B^2}, \quad (5.53)$$

using the background magnetic field of  $B_0 = 2\sqrt{\frac{5}{3}} \approx 2.6$ .

Then the background parameters are, using equation 4.88, the inflow region Alfvén speed is  $c_a = \sqrt{\frac{40}{43}} \approx 0.96$ . This is in good agreement with the expected Alfvén speed in the inflow of  $\approx 1$  and using equation 5.55 the background magnetisation parameter is  $\varsigma = 66\frac{2}{3}$ . Using equation 2.22 with the polytropic equation of state where  $\Gamma = 4/3$ , the background total energy is  $e = 3 \frac{11}{15}$ .

The Harris current sheet was used rather than the constant magnetic field current sheet in chapter 4 for easier comparison to other Petschek simulations. Since the Harris current sheet has constant total pressure it does not suffer the same settling period as the constant magnetic pressure current sheet in chapter 4.

The relativistic Petschek reconnection is triggered by anomalous resistivity rather than a small perturbation. The anomalous resistivity was used as a simple model to imitate the more complex behaviour which will be dependent on the variables of state and the magnetic field by it threading the charged particles along it. This was achieved by setting the anomalous conductivity as



$$\sigma_{an} = \begin{cases} \sigma, & \text{if } r > r_0 \\ \frac{\sigma}{1 + 99 \left( 2 \left( \frac{r}{r_0} \right)^3 - 3 \left( \frac{r}{r_0} \right)^2 + 1 \right)}, & \text{if } r \leq r_0, \end{cases} \quad (5.54)$$

where  $r$  is the radius and  $r_0$  is the radius of the area affected by the anomalous resistivity found by  $\eta_{an} = \sigma_{an}^{-1}$ . To keep the code from crashing and reasonable run times the background conductivity was set to  $\sigma = 100$  and, to produce reliable Petschek reconnection the radius of the anomalous resistivity was set to  $r_0 = 0.1$ . This, with  $l = 0.05$ , gives a corresponding background relativistic Lundquist number of  $L_u = 5$ .

If this trigger for reconnection is compared to the perturbation of order  $10^{-3}$  for the tearing mode, it is much stronger and it comes as no surprise that Petschek reconnection happens instantly due to the very small reconnection region given by  $r_0$ .

The magnetisation parameter  $\varsigma$  will be much greater than one in relativistic Petschek reconnection. In the units of the code it is

$$\varsigma = \frac{B^2}{\rho\gamma^2} \quad (5.55)$$

and is measured in the inflow region. As the magnitude of the magnetic field and density are kept the same for the Petschek simulations, only the Lorentz factor changes from the inflow created by the reconnection. The inflow is between a tenth and a quarter of the speed of light and hence the variation in the Lorentz factor is unimportant. With this, the values of the magnetisation parameter are all that of the anti-parallel case where  $\varsigma = 65.51$ . This is much greater than one, but not massively so. This is limited by the limitations of the code and it would be preferable to have a greater value.

The simulations were performed using the  $2\frac{1}{2}$  dimensional option of the code, where each vector has three components and no  $z$  dependence,  $\partial_z = 0$ . The domain of investigation was  $[-x_0, x_0] \times [-y_0, y_0]$  with free flow boundary conditions in both directions. To stop the  $y$  boundaries affecting the reconnection region or the outflow jet it was set as  $y_0 = 4$ .

Unfortunately when the outflow jet reaches the  $x$  boundaries they interact and cause the code to crash. To allow the Petschek reconnection to reach a steady state and give a large enough region to analyse the  $x$  boundaries were set at  $x_0 = 16$ . The Courant number used for the simulations is  $C_n = 0.1$  and the resolution used is 50 grid points per unit length in each direction.

### 5.2.2 Physical description and structure of relativistic Petschek reconnection

Before the results are presented, the evolution of the current sheet is described.

As with the tearing mode, an inward velocity is produced by the frozen in magnetic field lines moving toward the centre to annihilate by diffusion. When they approach the current sheet where they would annihilate, the region of increased resistivity allows the field lines in the middle to slip through the plasma and meet before the rest of the lines. This leaves the field lines about to annihilate connected in a sharp wedge where a strong magnetic tension force will pull them apart. Although the magnetic field is not completely frozen in, it will move a portion of the fluid with it changing the current sheet from predominantly compression to a fast outflow. Since the magnetic tension force will act very close to the  $x$  axis, the outflow will also be close to the axis and, to match the inflow with the outflow and the near horizontal magnetic field lines with the near vertical ones of the outflow, a slow shock is created. Due to the angle the magnetic field lines make with the slow shock in the inflow and the outflow field lines being normal to the shock, this will be very close to a switch off shock. As the jet moves out into the plasma it will leave behind a steady state Petschek reconnection.

In figures 5.2 and 5.3, the evolution of Petschek reconnection is shown for the plasma pressure from time  $t = 0$ , in the initial set-up described in equations 5.51 and 5.52, till just before the edge of the jet reaches the  $x$  boundary.

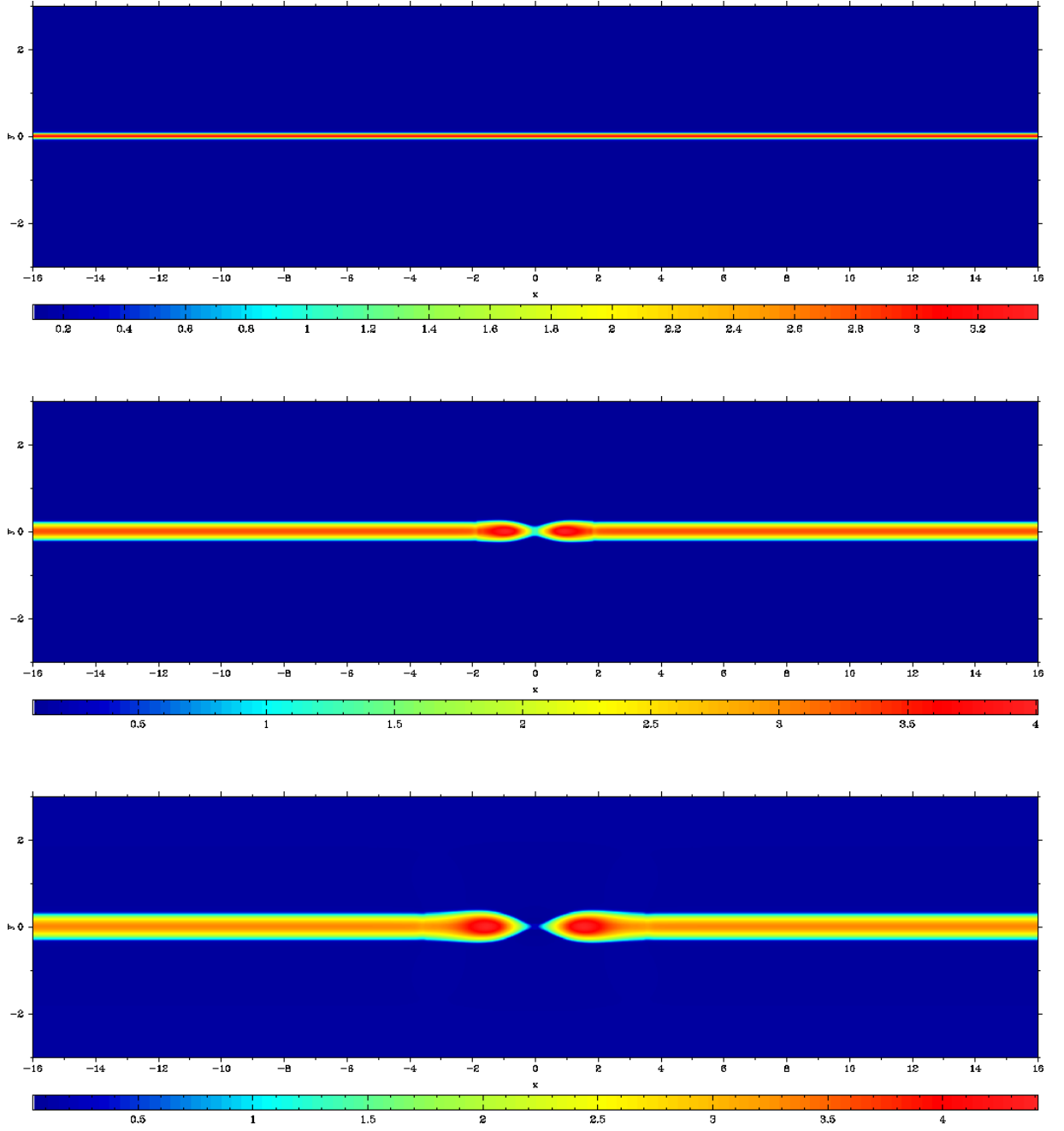


Figure 5.2: The early evolution of the plasma pressure for relativistic Petschek reconnection at times 0, 3.094 and 6.188 with a resistivity of  $\eta = 10^{-2}$  and plasma beta of  $\beta = 0.03$ .

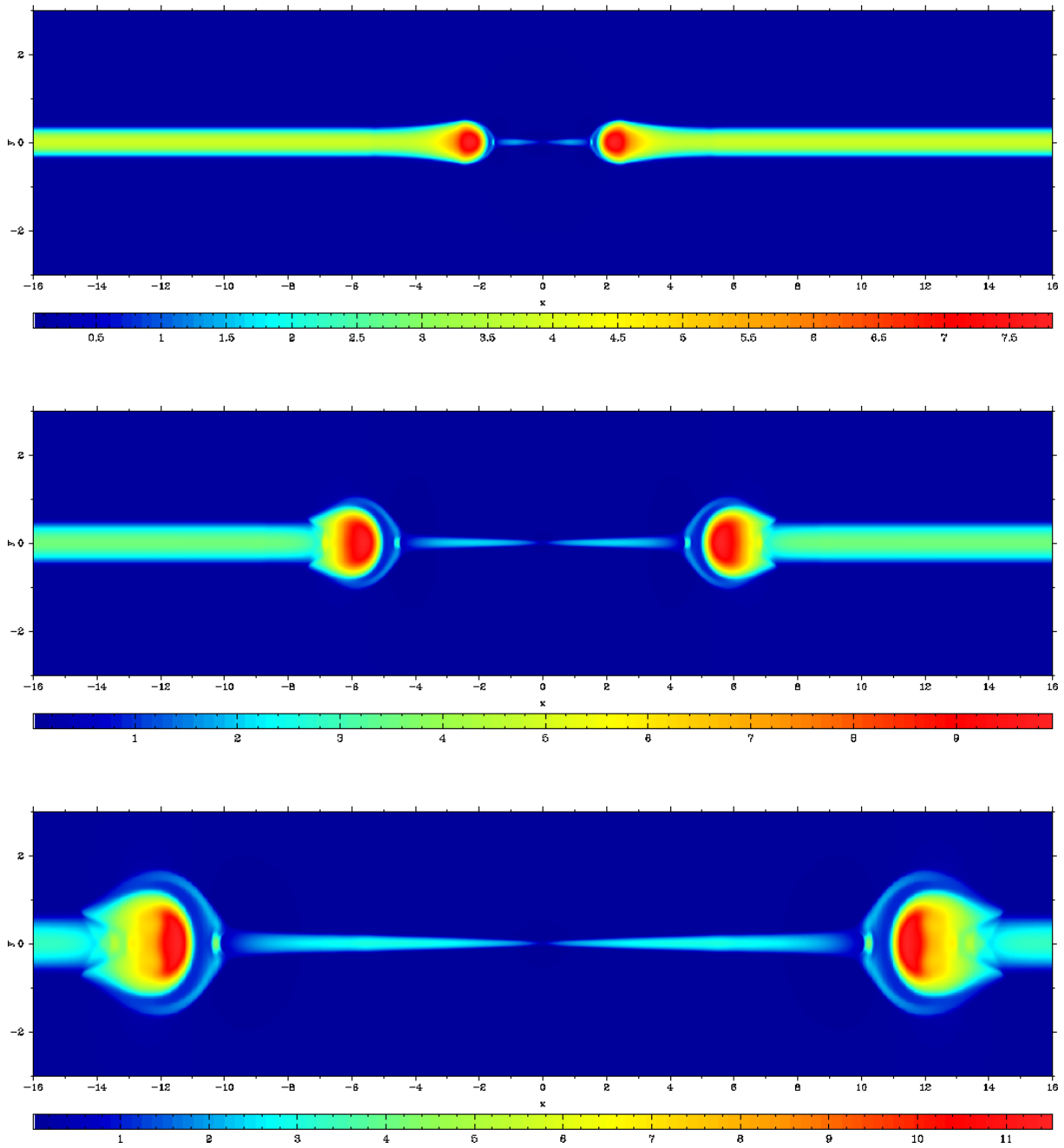


Figure 5.3: The later evolution of the plasma pressure for relativistic Petschek reconnection at times 9.282, 15.467 and 24.754 with a resistivity of  $\eta = 10^{-2}$  and plasma beta of  $\beta = 0.03$ .

To show the structure of Petschek reconnection and illustrate the earlier description, the variables are plotted for a time 24.754. Figure 5.4 shows, from top to bottom, the plasma pressure, density and magnitude of the velocity field with an overlay of the directional field. Note that the  $z$  component of the velocity field is zero.

Figure 5.5 shows the non-zero components of the magnetic field and the magnitude of the magnetic field with the field lines during relativistic Petschek reconnection. The  $z$  component of the magnetic field is zero.

Figure 5.6 shows the  $z$  component of the electric field and the current density. The other components of both vectors are zero.

Figure 5.8 shows a zoomed in image of the relativistic slow shocks for the magnitude of the velocity field with directional arrows and the magnitude of the magnetic field with field lines.

### 5.2.3 Motivation and organisation of the regimes investigated for relativistic Petschek reconnection

To investigate relativistic Petschek reconnection two main regimes were considered. These are motivated by the order of magnitude calculations of Lyubarsky in [29] and the main focus is anti-parallel relativistic Petschek reconnection where  $B_z = 0$  and relativistic Petschek reconnection where the incoming magnetic field lines are angled to each other where  $B_z \neq 0$ .

The anti-parallel relativistic Petschek reconnection simulations are a straightforward extension of the non-relativistic case and are presented in section 5.2.4.

As shown in Lyubarsky's paper [29] and presented here in section 5.1, when  $B_z \neq 0$  it is not a straightforward extension of the non-relativistic theory and has a modified structure. To clearly present this the  $B_z \neq 0$  simulations are split up into the following sections.

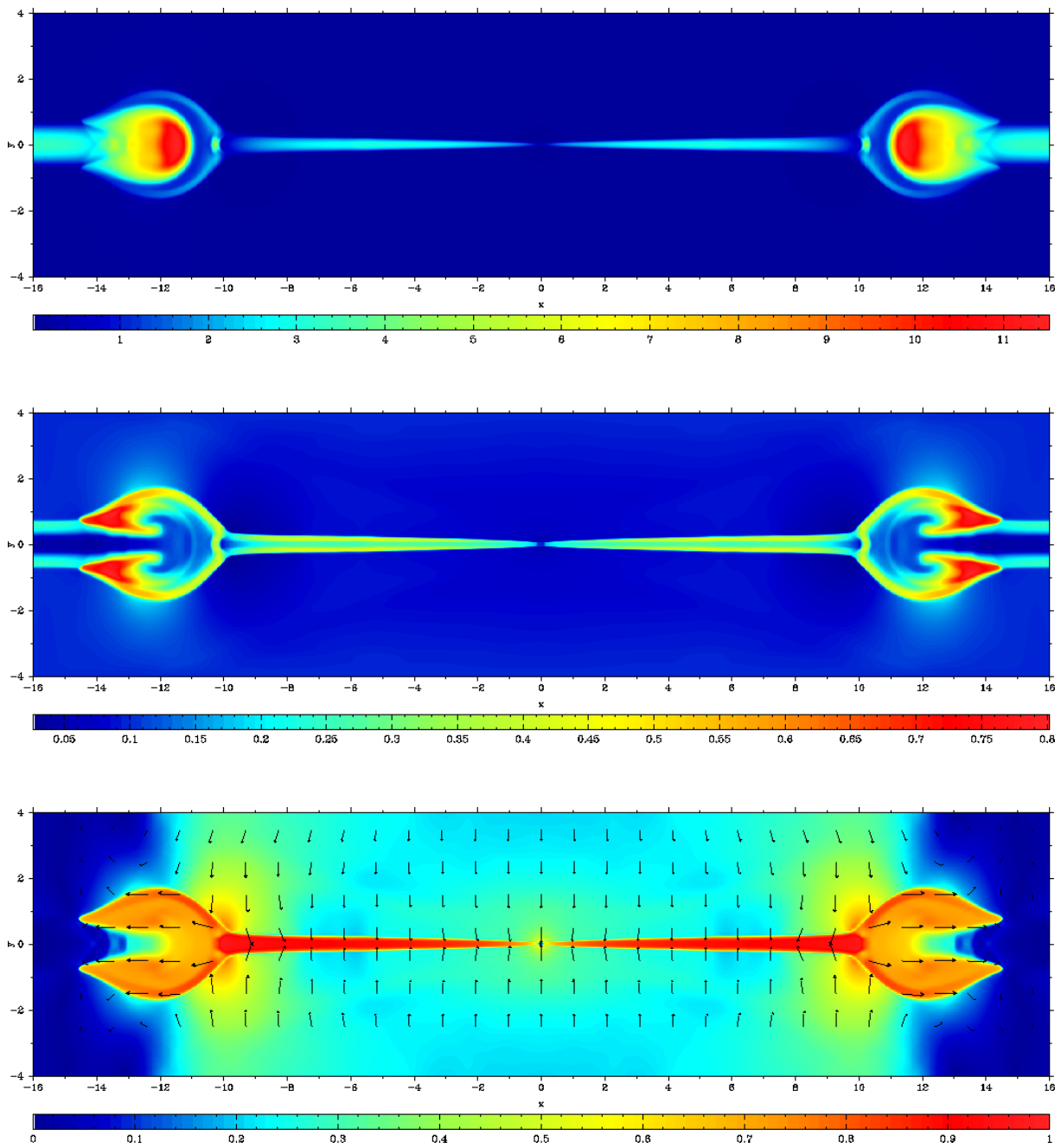


Figure 5.4: The hydrodynamical variables of plasma pressure, density and velocity field for relativistic Petschek reconnection at time 24.754 time units.

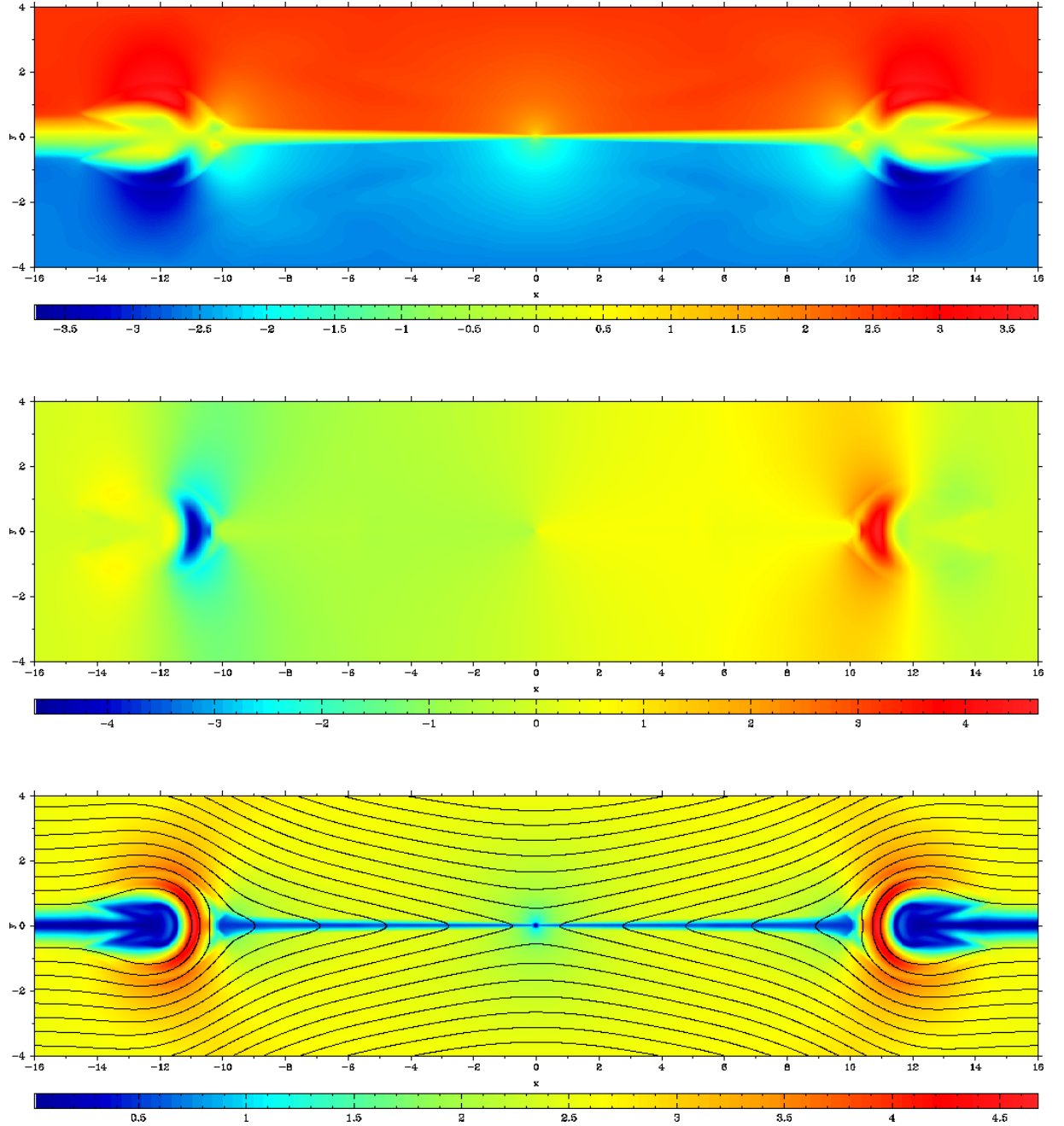


Figure 5.5: The magnetic field for relativistic Petschek reconnection, from top to bottom  $B_x$ ,  $B_y$  and the magnetic field lines with the magnitude of the magnetic field at time 24.754 time units. Note  $B_z = 0$ .

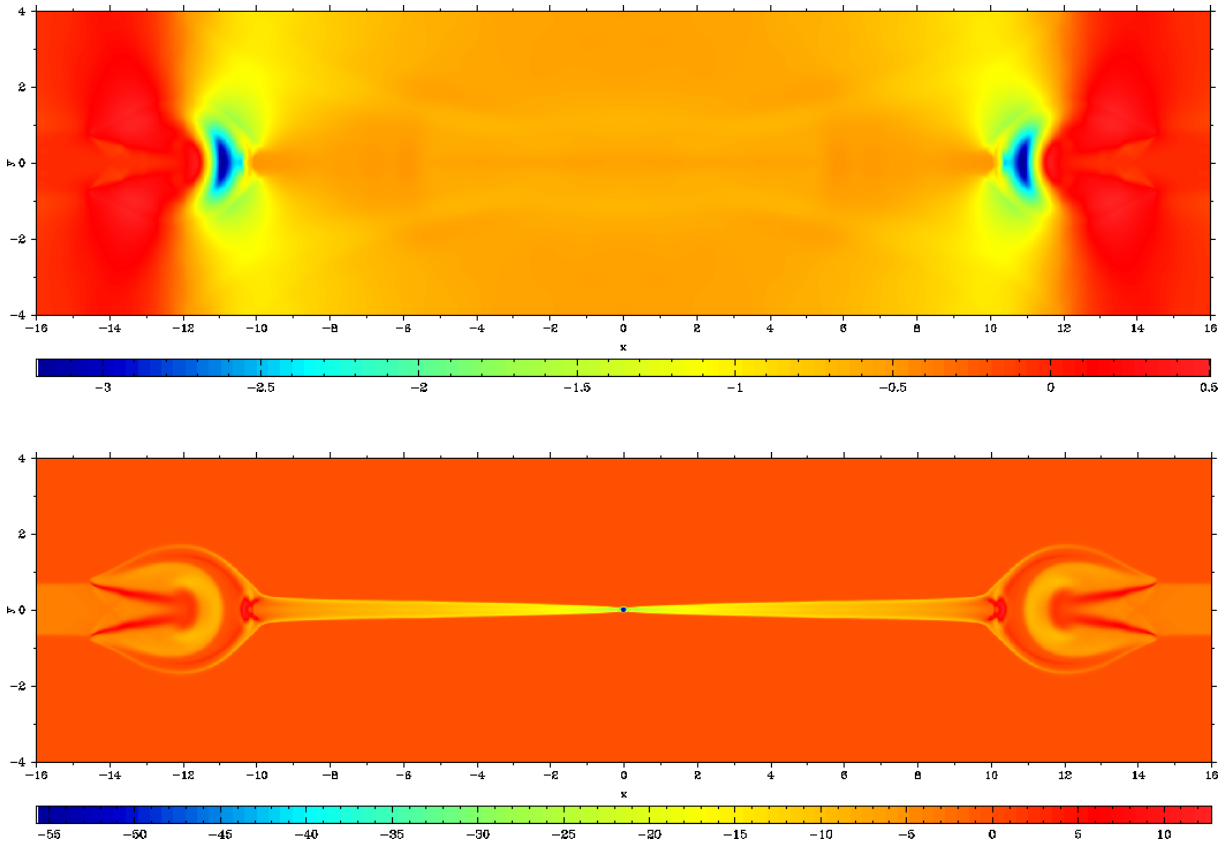


Figure 5.6: The  $z$  component of the electric field and current density for relativistic Petschek reconnection at time 24.754 time units. The  $x$  and  $y$  components of both vectors are zero.

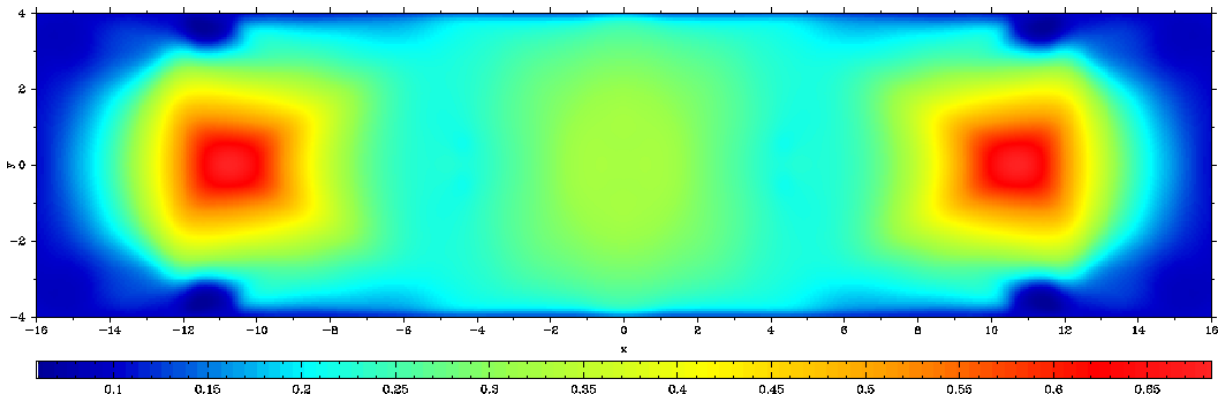


Figure 5.7: The plasma pressure at time 24.754 for anti-parallel relativistic Petschek reconnection when the resolution has been halved in both directions.



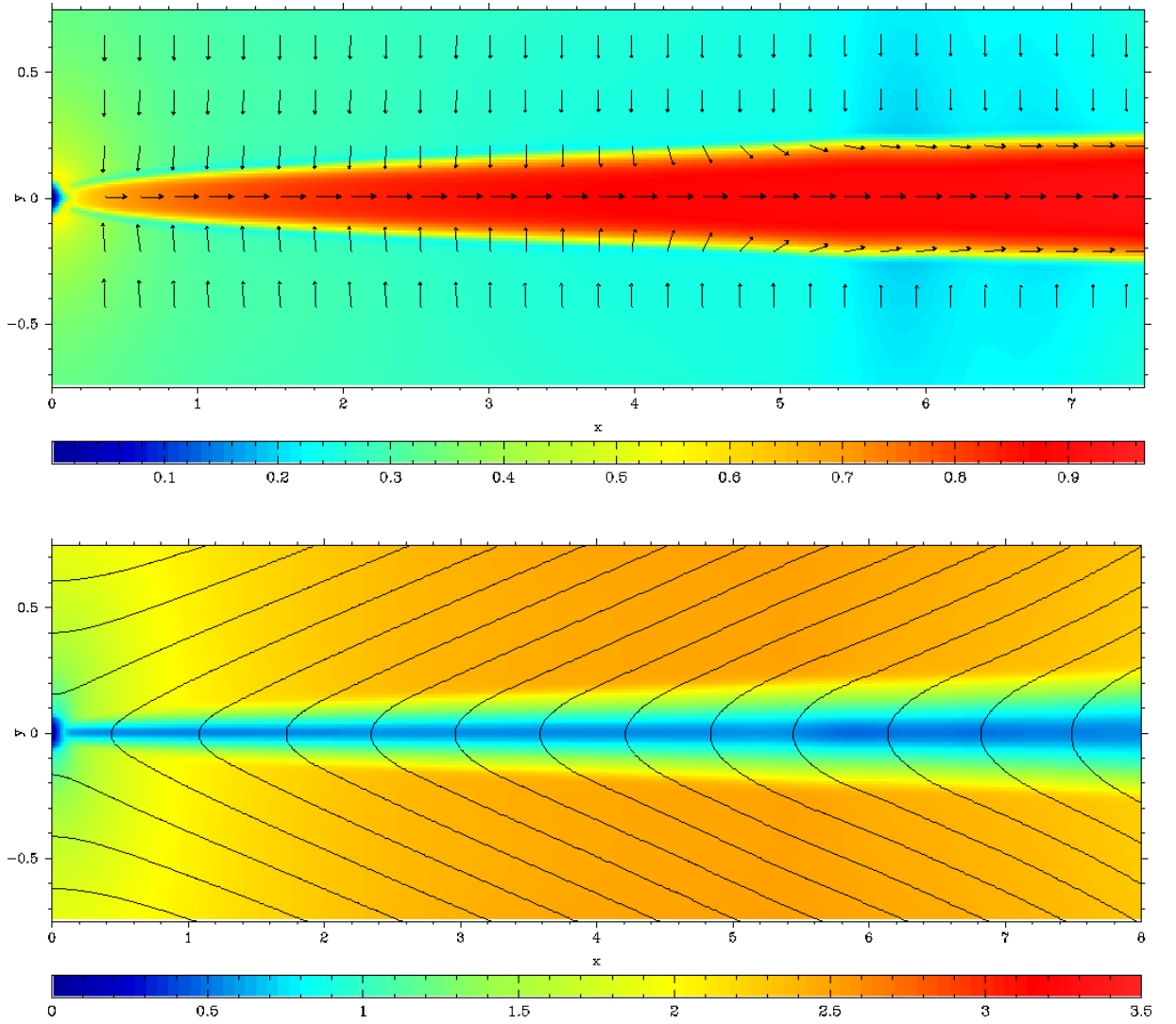


Figure 5.8: A zoomed in image of the relativistic slow shocks for the magnitude of the velocity field with directional arrows and the magnitude of the magnetic field with magnetic field lines for relativistic Petschek reconnection at time 24.754.

To introduce the main differences as described in section 5.1 first simulations where  $B_z \neq 0$  and  $2\alpha\sqrt{\zeta} \approx 0$ , when the condition for structural change has just been violated, are presented in section 5.2.5.

Due to the resources needed to vary the relativistic Lundquist numbers, this was only performed once and the angled case where  $\alpha = \Pi/6$  was chosen for this. As the base case the variation to the relativistic Lundquist number was just presented, the comparison is presented next in section 5.2.6.

With the angled relativistic Petschek reconnection now presented to confirm that a small  $\alpha \ll 1/2\sqrt{\zeta}$  does not affect the structure and reconnection proceeds as if  $B_z = 0$  the case when  $\alpha = \Pi/36$  is presented in section 5.2.7.

To give an overview of relativistic Petschek simulations the reconnection electric field for each is plotted and compared. This gives an easily interpreted graph of the reconnection region as relativistic Petschek reconnection evolves to a steady state. This also provides motivation to whether relativistic Petschek reconnection occurs when the incoming field lines are almost parallel,  $\alpha \gg 1/2\sqrt{\zeta}$  giving a positive result. This is presented in section 5.2.8.

With the reconnection electric fields showing that relativistic Petschek reconnection occurs when  $\alpha \gg 1/2\sqrt{\zeta}$  the simulations are presented here along with their use as a background for relativistic reconnection to occur from. This is presented in section 5.2.9.

The final section describes the effects on how the energy flux is magnetically or materially dominated in the outflow depending on  $\alpha$  and if condition 5.45 is violated. This is presented in section 5.2.10.

To create the relativistic Petschek reconnection when the inflow magnetic field is not anti-parallel, the inflow magnetic field is set at an angle  $\alpha$  to the shock plane in the upper half of the domain. This is done for from  $\alpha = 0$  to  $5\pi/12$ , with  $\alpha$  changing in increments of  $\pi/12$ . The inclination in the magnetic field in each case is mirrored in the lower half of

the domain.

### 5.2.4 Anti-parallel relativistic Petschek reconnection

In figures 5.4 - 5.6 the slow shock is easily seen, separating the inflow and outflow regions. By measuring the magnetic field lines close to the slow shock in figure 5.5, the angle  $\theta$  they make with the shock plane is found to be  $\tan \theta = 0.242$ . Comparing this with the inflow velocity in simulations, measured to be  $v_1 = 0.227$ , which is in good agreement with equation 5.15. To further investigate the predictions made in section 5.1, the magnetisation parameter,  $\cos \theta$  and  $\sin \theta$  are needed. The magnetisation parameter given by equation 5.13 requires the inflow density  $\rho_1 = 0.09$ , Lorentz factor  $\gamma_1 = 1.029$  and the square of the magnetic field  $B_1 = 2.5$  which gives the magnetisation parameter as  $\varsigma = 65.51$ . This is in the regime where  $\varsigma \gg 1$  as required. By measuring the hypotenuse it is found that  $\cos \theta = 0.976$  and  $\sin \theta = 0.236$ , which gives  $\sin^2 \theta + \cos^2 \theta = 1.008$ .

Using this information the formulae of the predictions made in section 5.1 can be compared to the results of the simulations. The outflow velocity normal and transverse to the shock are predicted to be 0.002 and 0.99 and are found in the simulations to be 0.02 and 0.87. These are found by taking the normal and tangential velocity in the outflow region as the relativistic slow shock is approximately the  $x$ -axis. These are not in particularly good agreement. It follows that the expected outflow Lorentz factor found in the simulations of 2.35 is not close to the predicted value of 7.90. The outflow density is found in the simulations to be 0.4145 which does not agree well with the predicted value of 1.465. The angle of the outflow velocity  $\phi$  is predicted to be 0.0153 and from the simulations is calculated from the measured outflow velocities using  $\tan \phi = v_{n2}/v_{t2}$ , which gives  $\phi = 0.0230$ . Like the Lorentz factor, the discrepancy between the two values follows from the discrepancy in the outflow velocity. Finally the plasma pressure is predicted to be 2.9768 and found to be 2.8 in simulations. This is in good agreement.

To investigate this the resolution was looked at to check for numerical dissipation. The base resolution for relativistic Petschek reconnection simulations was based on the resolution used for the relativistic tearing mode with increasing resolution until the expected structure of Petschek reconnection was clearly present. Figure 5.9 shows the number of grid points in the  $y$  direction across the current sheet for the density. It is seen that the resolution for the inflow region and outflow region is sufficient, but the shocks are not clearly resolved.

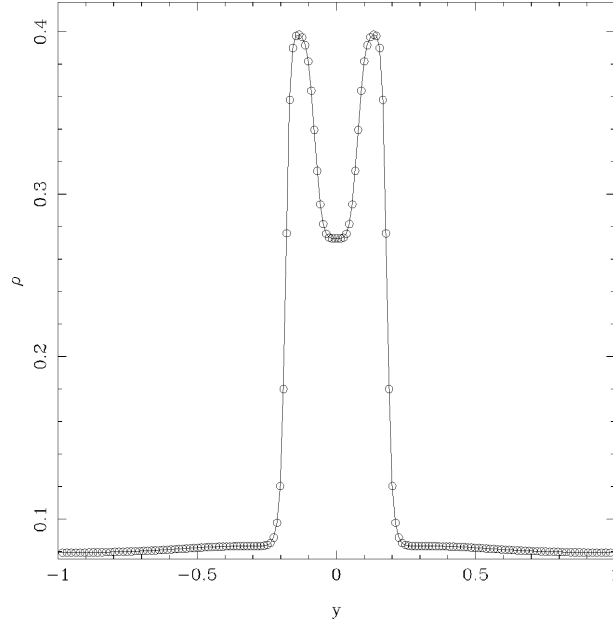


Figure 5.9: The resolution in the  $y$  direction across the current sheet

To further check the resolution the simulation for the anti-parallel case was repeated with the resolution halved in both directions. The reduction was chosen over increasing the resolution due to the much shorter time taken by the reduced simulation. Figure 5.7 shows the plasma pressure at time 24.754 for anti-parallel Petschek reconnection when the resolution has been halved in both directions. This shows the numerical resolution dissipating the structure of reconnection. The low resolution and its effect on resolving the density is shown in figure 5.9.

A simulation was run with double the resolution to see if this improved upon the problem. This run was not as long as desired due to the problem documented in section 3.6.2. This was found to be quantitatively the same as the lower resolution simulation with a slight difference in the magnitude of the variables. This is shown along the  $x$ -axis for the plasma pressure in figure 5.10. This suggests that the resolution used for analysing the results qualitatively captures relativistic Petschek reconnection, but is not quantitatively as accurate as desired. It is an acceptable resolution in comparing to the predictions of section 5.1 which are order of magnitude calculations.

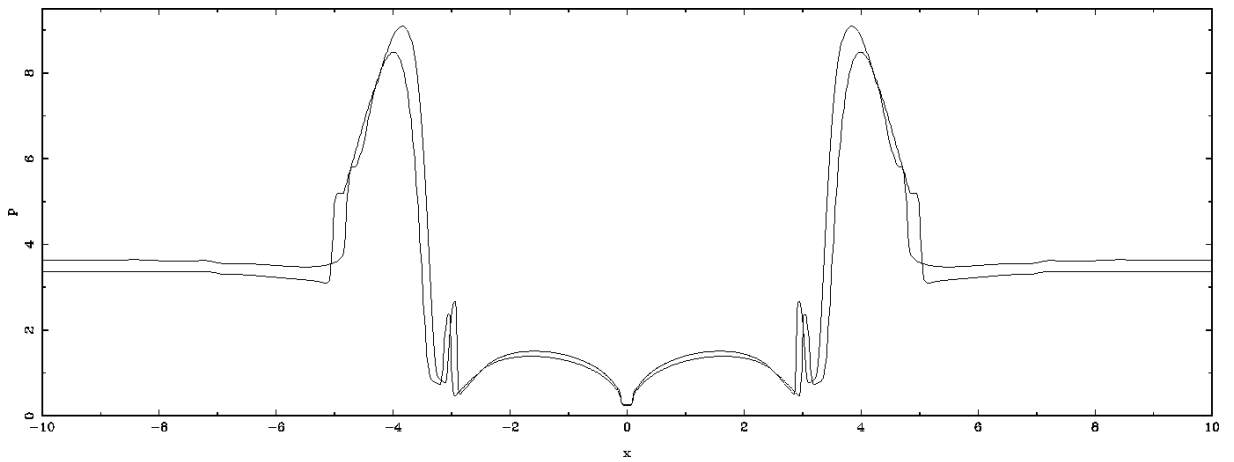


Figure 5.10: A comparison of the plasma pressures along the  $x$ -axis for 50 and 100 grid points per unit length with the lower curve being the higher resolution. The lower resolution curve is slightly advanced at time 12.375 to the higher resolution curve at time 12.268 due to the different time steps and getting them to coincide.

The difference between the variables does not affect the reconnection rate, since this is given by the inflow velocity which is in good agreement.

The comparison of the predictions made in section 5.1 and the simulations are summed up in table 5.1.

Variable	Predicted value	simulated value
$v_1$	0.242	0.227
$v_{n2}$	0.0019	0.02
$v_{t2}$	0.99	0.87
$\gamma_2$	7.90	2.35
$\rho_2$	1.465	0.4145
$p_2$	2.9768	2.8
$\phi$	0.0153	0.0230

Table 5.1: A table comparing the predictions for anti-parallel relativistic Petschek reconnection with simulations.

### 5.2.5 Relativistic Petschek reconnection with a small $B_z \neq 0$ component, where $2\alpha\sqrt{\varsigma} \approx 1$

To create the case where the magnetic field lines in the inflow are not anti-parallel a  $z$  component was added of the magnitude required for the desired angle and then normalised so that the magnitude of the magnetic field  $|B|$  is the same as the anti-parallel case where  $|B_0| = 2\sqrt{5/3}$ . This was done to keep the pressure balance the same as when  $B_z = 0$  in the inflow region. The structure of relativistic Petschek reconnection with  $B_z \neq 0$  is similar to the anti parallel one, but more complicated. There are now two sets of shocks, rotational (where the magnetic and velocity fields rotate with constant magnitude and all others variables stay constant across it) and slow, separating the inflow from the outflow. When  $B_z = 0$  the vectors were all either in the  $x$ - $y$  plane or perpendicular to it, but with the introduction of a small  $z$  component to the magnetic field all the vectors have all three components and it becomes a much richer problem.

To investigate this when  $2\alpha\sqrt{\varsigma} \sim 1$ , the magnetic field in the inflow in the upper half was

varied with  $\alpha = \pi/12$  and  $\pi/6$ , which is mirrored in the lower plane. This was done to investigate the predictions of section 5.1.

As described in section 5.2.1, the inflow is caused by the gradient in the  $x$  component of the magnetic field. To keep the total pressure constant and avoid the settling problems found in the tearing mode simulations, the magnetic field in the inflow is normalised to  $B_0$  and hence the  $B_x$  component is reduced. With the reduction in  $B_x$ , the difference between the upper and lower regions is less which, as the magnetic field is frozen in the plasma, produces a slower inflow. With the slower inflow Petschek reconnection then takes longer to develop. Whilst the anti-parallel case reaches the outer boundary by time 27.849, when  $\alpha = \pi/12$  it reaches the boundary by 34.037. For values of  $\alpha$  greater than this, none reach the boundary by time 61.846. This is shown for  $\alpha \neq 0$  in figure 5.11. If a larger magnetisation parameter was achieved it is expected that the difference in inflow speed will be reduced.

As the structure of relativistic Petschek reconnection is expected to change when the condition 5.45 is violated the primitive independent variables are plotted to illustrate the changes for  $\alpha = \pi/12$  at time 34.037. In plotting these the domain is shrunk to focus on the outflow region and the part of the inflow region immediately surrounding it. The bulbous region where the outflow pushes into the ambient plasma is also ignored. In the first paragraph of this section it was stated that the variables are not just in the  $x$ - $y$  plane or normal to it, but across all the spatial directions. Hence the magnetic contour map and velocity directional field can not be used and all three components of each vector need to be plotted individually. Figure 5.13 shows the plasma pressure, density and charge density. Figures 5.14 - 5.16 show the velocity, magnetic and electric fields.

For the different values of  $\alpha$  where the analyses of section 5.1.3 applies to see how the  $\alpha$  value affects the structure of the reconnection it is instructive to plot the velocity and magnetic fields. This has already been done for  $\alpha = \pi/12$  in figures 5.14 and 5.15. For  $\alpha = \pi/6$  they are presented in figures 5.17 and 5.18 at time 61.846 with the focusing

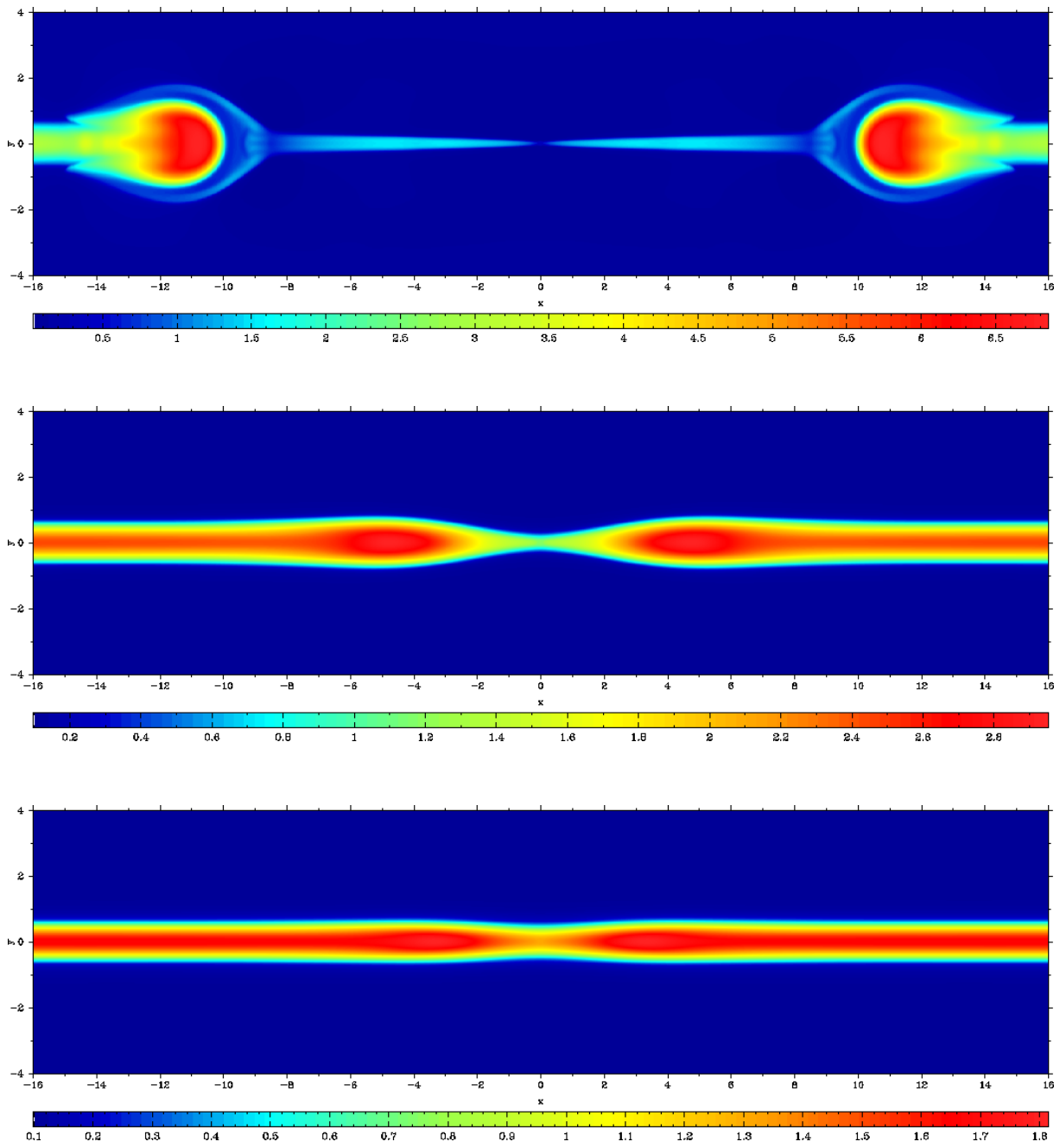


Figure 5.11: Comparison of the plasma pressure at time 30.945 for values of  $\alpha$  of  $\pi/12$ ,  $\pi/6$  and  $\pi/4$  showing the slow development for larger values of  $\alpha$ .



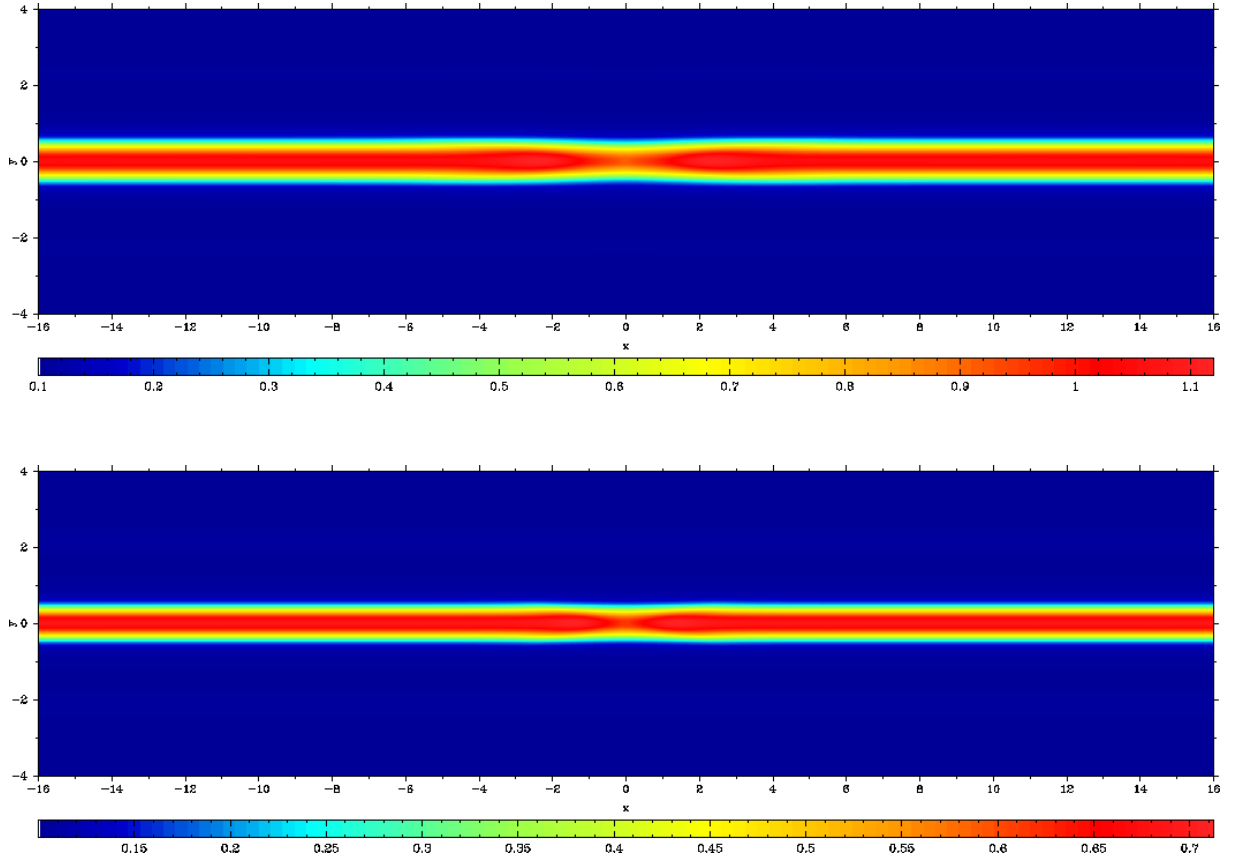


Figure 5.12: Comparison of the plasma pressure at time 30.945 for values of  $\alpha$  of  $\pi/3$  and  $5\pi/12$  showing the slow development for large values of  $\alpha$ .

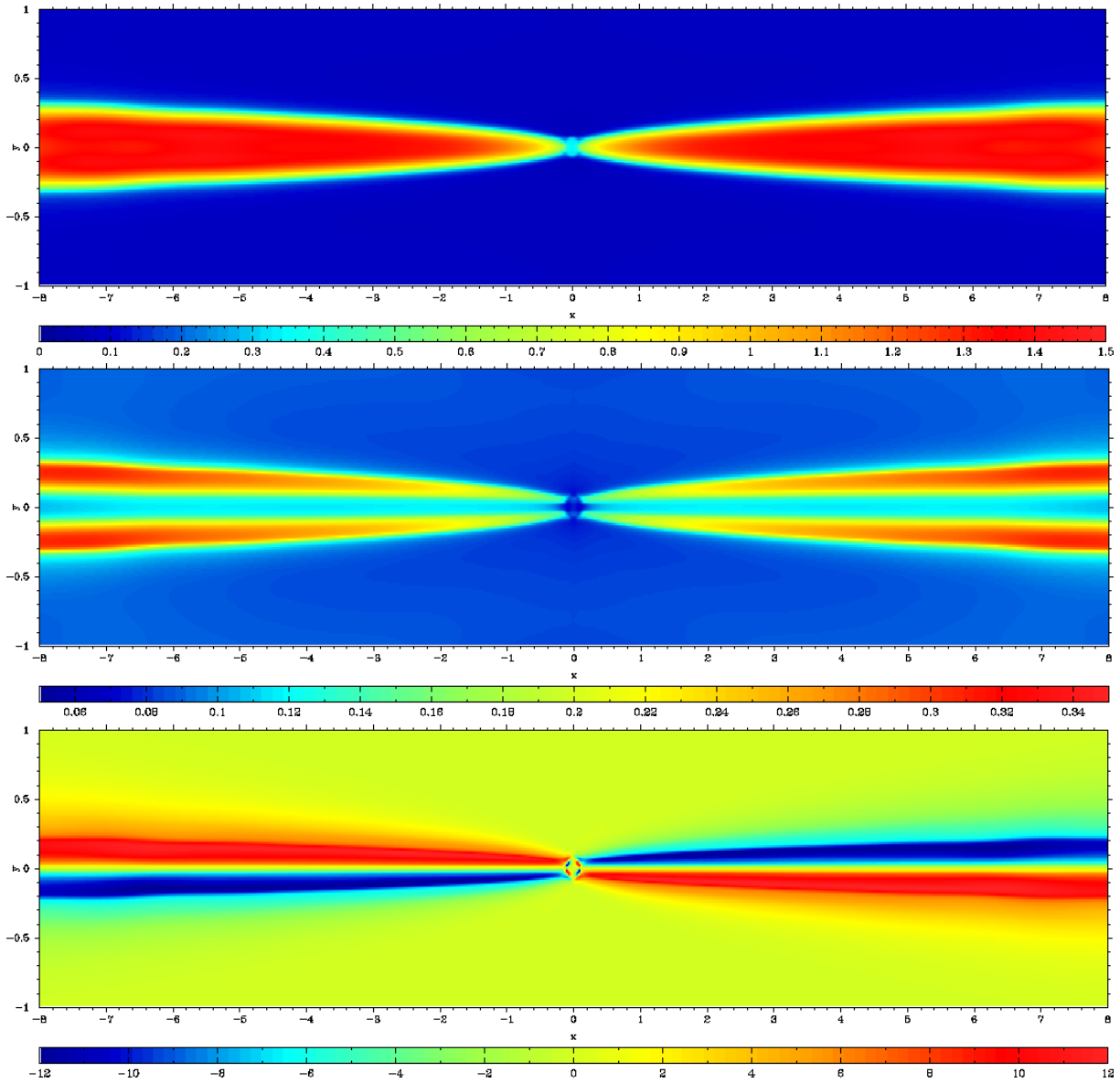


Figure 5.13: From top to bottom the plasma pressure, density and charge density for relativistic Petschek reconnection with  $\alpha = \pi/12$  at time 34.037 focused on the outflow region, excluding the outflow ambient plasma interface.

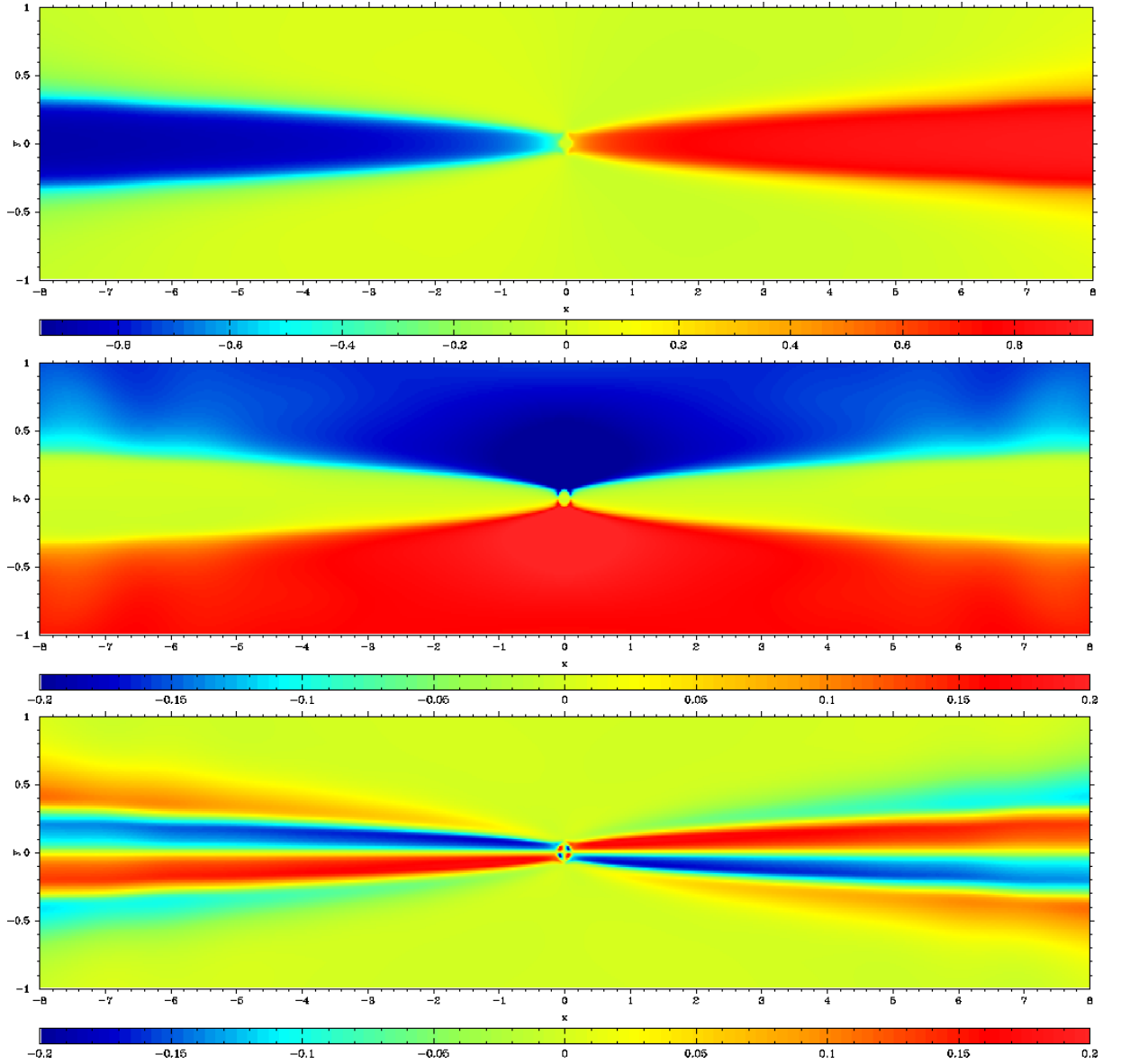


Figure 5.14: From top to bottom the  $v_x$ ,  $v_y$  and  $v_z$  components of the velocity field for relativistic Petschek reconnection with  $\alpha = \pi/12$  at time 34.037 focused on the outflow region, excluding the outflow ambient plasma interface.

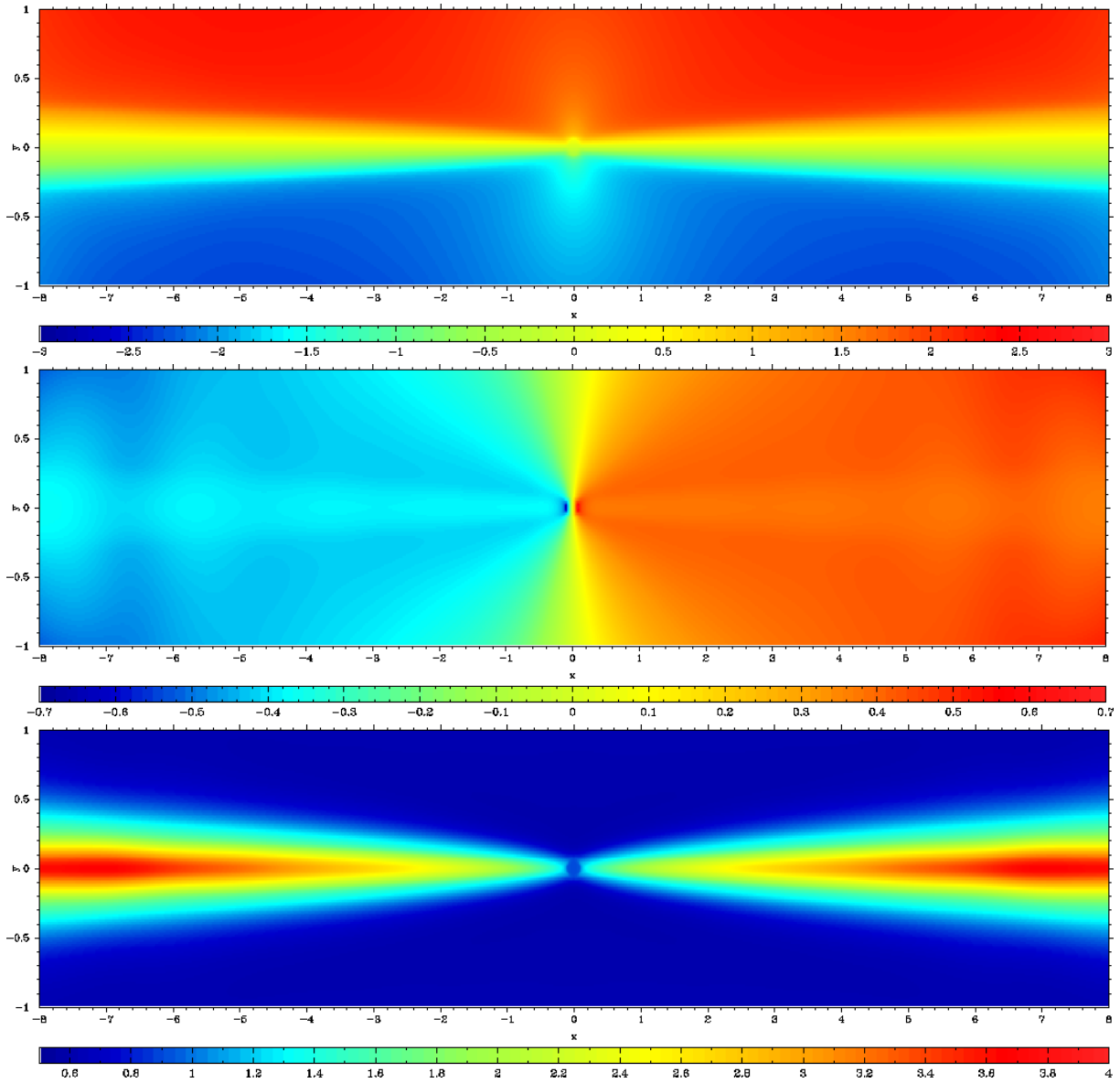


Figure 5.15: From top to bottom the  $B_x$ ,  $B_y$  and  $B_z$  components of the magnetic field for relativistic Petschek reconnection with  $\alpha = \pi/12$  at time 34.037 focused on the outflow region, excluding the outflow ambient plasma interface.

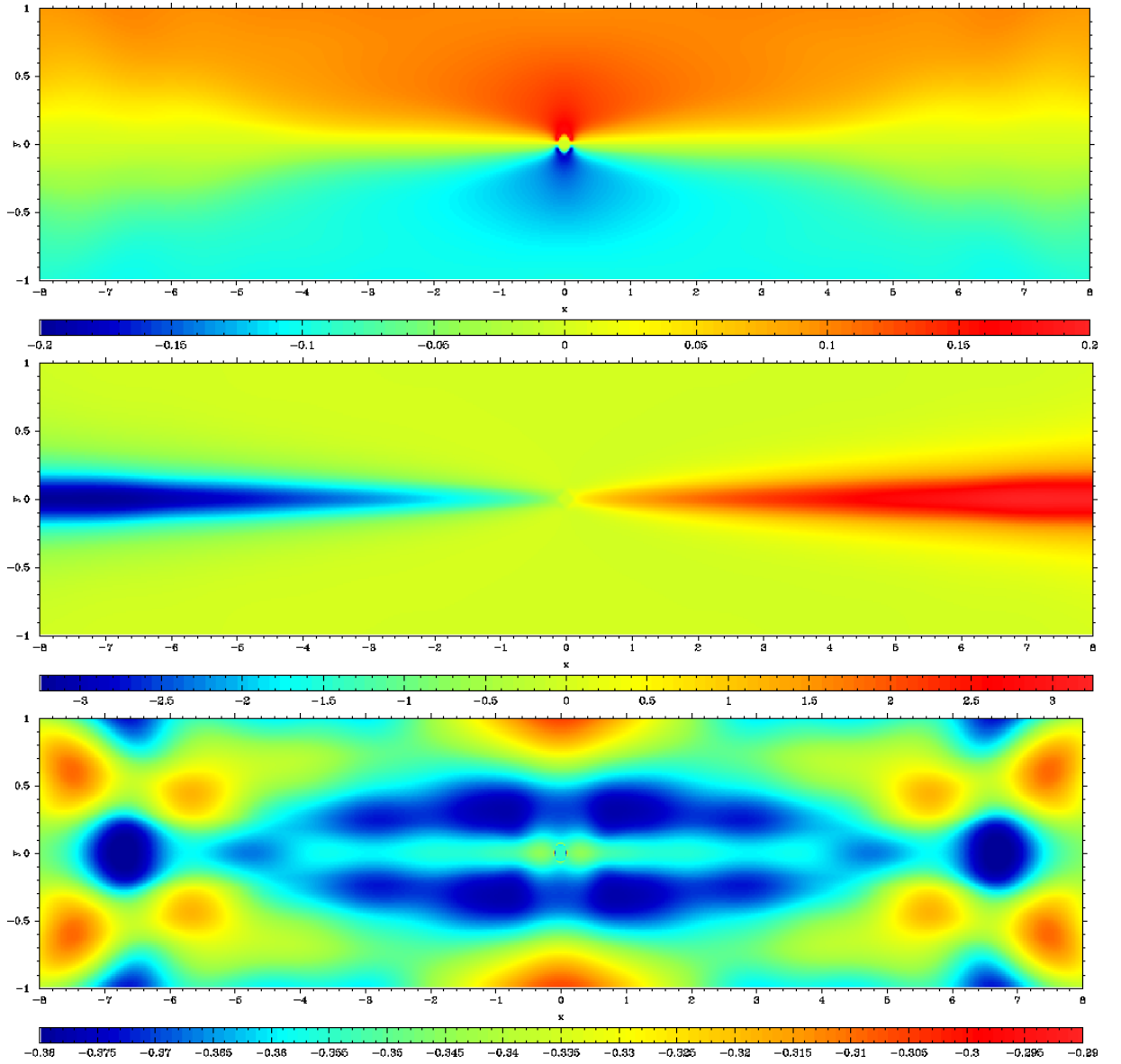


Figure 5.16: From top to bottom the  $E_x$ ,  $E_y$  and  $E_z$  components of the electric field for relativistic Petschek reconnection with  $\alpha = \pi/12$  at time 34.037 focused on the outflow region, excluding the outflow ambient plasma interface.

again on the outflow and surrounding region. These show a similar structure to when  $\alpha = \pi/12$ , but with a reduced magnitude for the velocity field and a slightly reduced magnitude of the magnetic field except for the  $B_z$  component which has increased. This is as expected as there is less magnetic flux reconnecting creating a slower inflow through the frozen flux condition and a slower outflow as the outflow retains the unreconnected magnetic field instead of converting it to kinetic energy. The change in the magnetic field is due entirely to the initial set up.

The relativistic rotational shocks present in this regime are difficult to identify as they have no non-linear steepening, yet are still diffusive. Since the rotational shock is present due to the introduction of a  $z$  component to the magnetic field, this is the obvious variable to look for them. To look for indication of the relativistic rotational shock the directional field of the velocity is overlaid on the  $z$  component of the magnetic field, showing the region where the velocity field changes direction on the interface between the inflow and outflow.

To further investigate this the region where the arrows change direction corresponding to where the value of  $B_z$  changes from the inflow to the outflow is plotted along the line  $x = \text{const}$ . This shows a kink in  $B_z$  in a similar position which points towards a rotational discontinuity. To corroborate this the  $v_z$  component of the velocity field is plotted along the same line showing a deviation from zero which occurs at the same position as the kink in the  $B_z$  component of the magnetic field. As the velocity field is expected to rotate with the magnetic field at a rotational discontinuity, this is positive evidence towards the relativistic rotational shocks existence in the area suggested by the plot of  $B_z$  with the  $x$ - $y$  directional field of the velocity. This is all shown in figure 5.19 for  $\alpha = \pi/6$  at a time of 61.846.

With the kink and the rotation of the velocity field, a region of the rotational shock can be estimated and using this gives estimates on the angle of the rotational shocks  $\psi_r$ , for  $\alpha = \pi/12$ , of  $0.0125 \leq \psi_r \leq 0.0141$  and, for  $\alpha = \pi/6$ , of  $0.0245 \leq \psi_r \leq 0.0265$ .

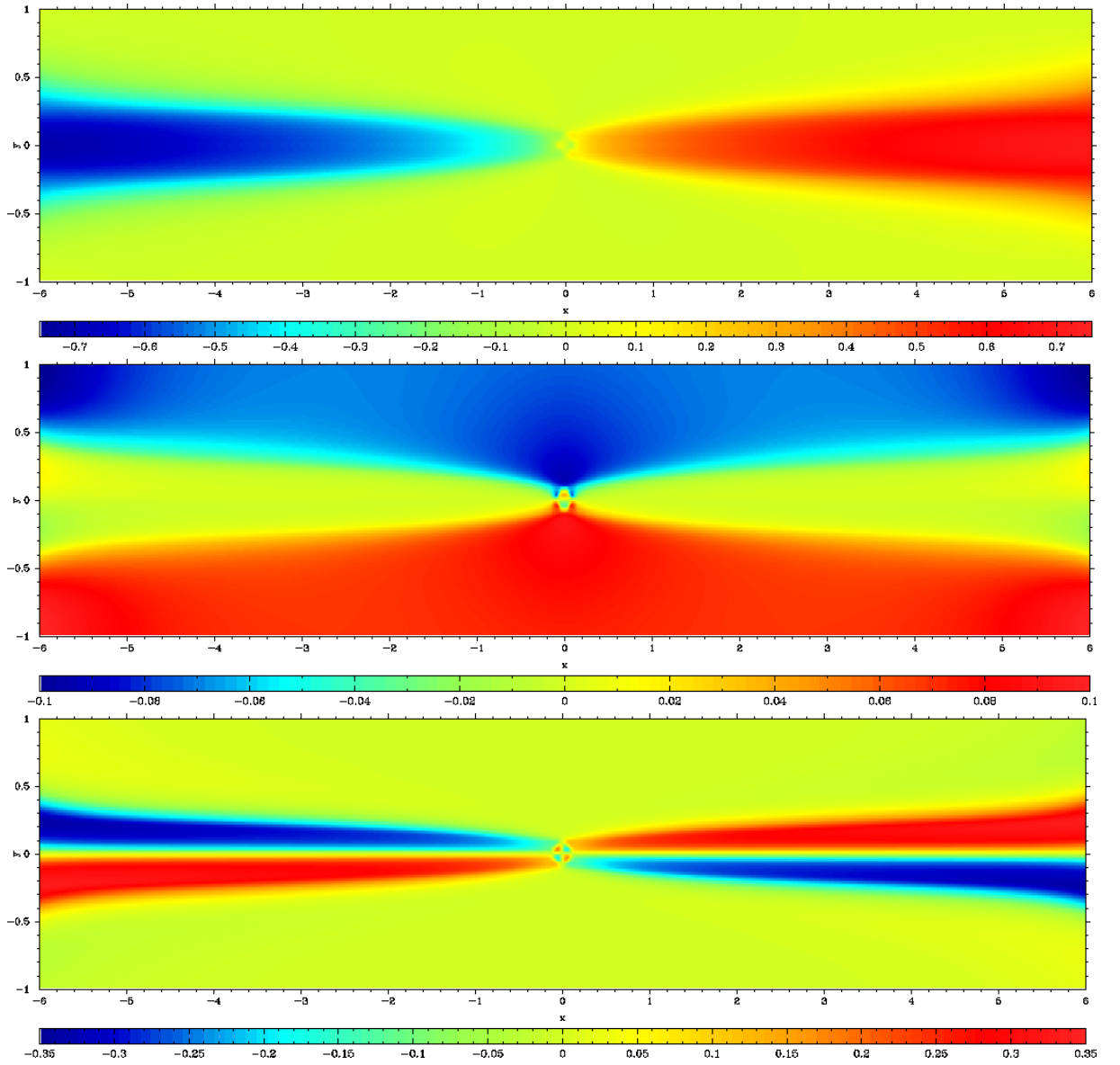


Figure 5.17: From the top to the bottom, the  $v_x$ ,  $v_y$  and  $v_z$  components of the velocity field for relativistic Petschek reconnection with  $\alpha = \pi/6$  at time 61.846.

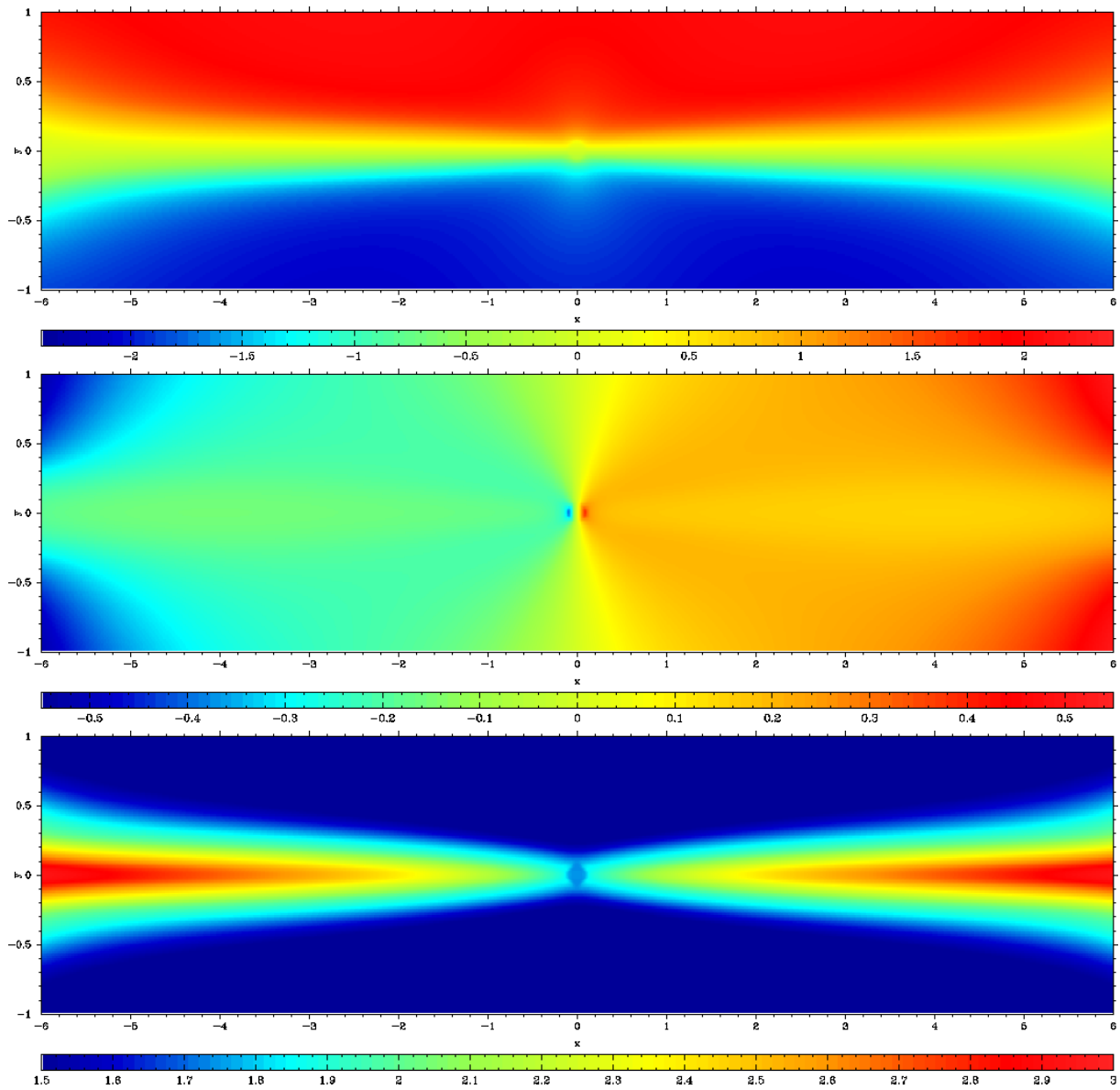


Figure 5.18: From the top to the bottom, the  $B_x$ ,  $B_y$  and  $B_z$  components of the magnetic field for relativistic Petschek reconnection with  $\alpha = \pi/6$  at time 61.846.



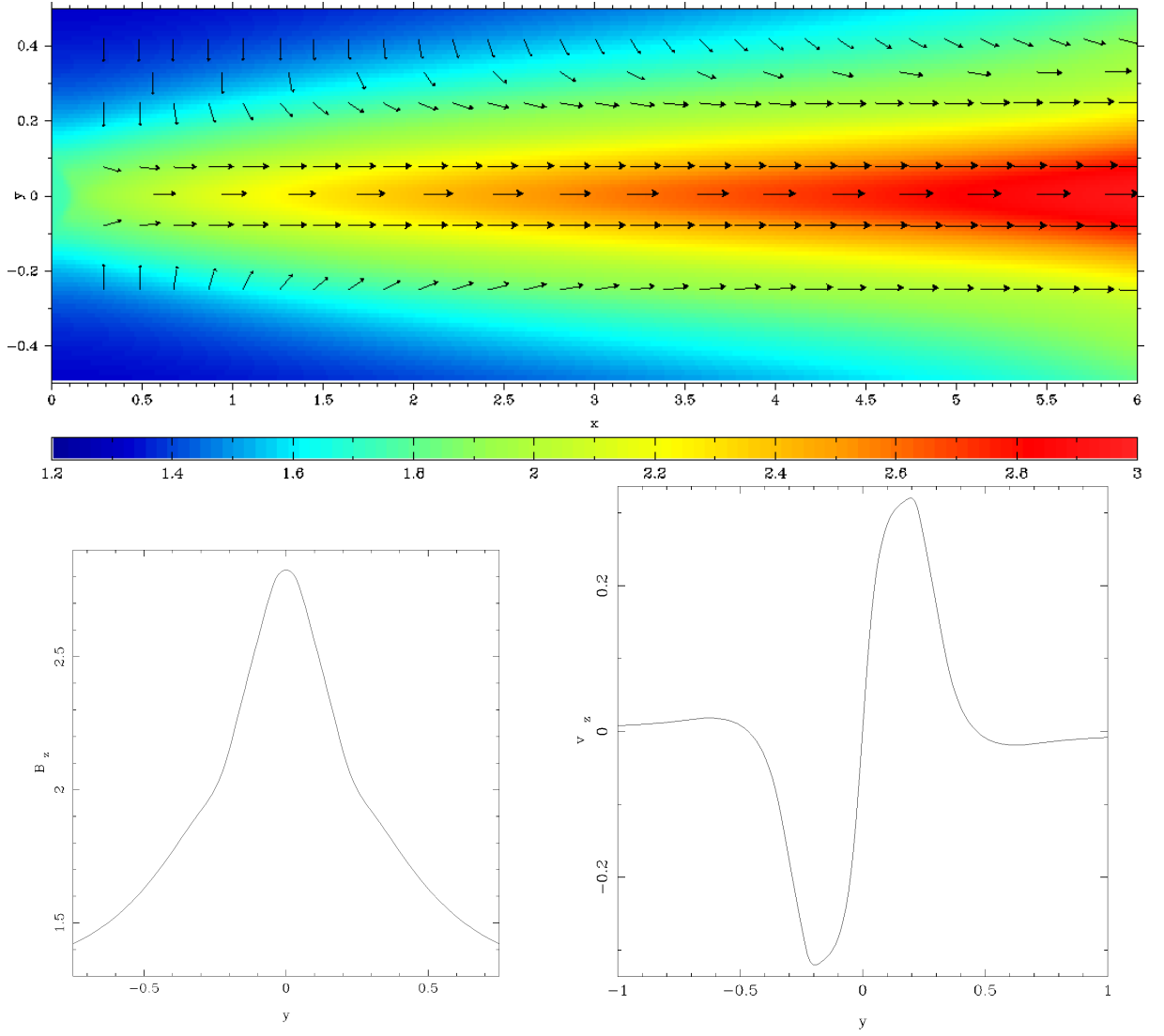


Figure 5.19: Indications of the rotational shock given by : the top image where the  $B_z$  component of the magnetic field with the  $x$ - $y$  directional field plotted on top, the bottom images are shown along the line  $x = 5$  with the left image showing the  $B_z$  component of the magnetic field with the kinks at  $\approx \pm 0.3$  and the right image showing the  $v_z$  component of the velocity field with peaked values corresponding to the kinks in  $B_z$ . All three images are with  $\alpha = \pi/6$  and at time 61.846.

For  $\alpha$  greater than this the reconnection has not developed enough to make any precise measurements. If the angle the magnetic field makes with the shock plane is measured, as for the anti-parallel case, then using equation 5.49 the predicted angle for  $\alpha = \pi/12$  with  $\theta = 0.185$  is  $\psi_r = 0.0127$  and for  $\alpha = \pi/6$  with  $\theta = 0.113$  is  $\psi_r = 0.0310$ . The predictions of equation 5.49 are then in fair agreement with the angles found in the simulations.

In section 5.1.3, for a known value of  $\alpha$  predictions can be made about the outflow velocity and Lorentz factor from  $v_{out} = 1 - \alpha^2/2$  and  $\gamma_{out} = \alpha^{-1}$ . For  $\alpha = \pi/12$ , this gives predicted values for the outflow velocity and Lorentz factor as 0.966 and 3.820 which compare favourably with the values found in the simulations of 0.938 and 2.938. For  $\alpha = \pi/6$  this gives predicted values for the outflow velocity and Lorentz factor as 0.863 and 1.910 which are comparable with the values found in the simulations of 0.733 and 1.470. The discrepancy is likely due to the fact that  $\alpha = \pi/6$ . The magnitude of  $B_z$  is comparable to that of  $B_x$  and the assumption that  $\alpha$  is small starts to break. This is summed up for the two values of  $\alpha$  in table 5.2.

From equation 5.41, the inflow velocity can be estimated as  $v_{in} \simeq 0.12$ . This compares well with the inflows found in the simulations of 0.15 for  $\alpha = \pi/12$  and 0.07 for  $\alpha = \pi/6$ . The differences come from the reduced inflow as described before.

The agreement between the predictions and simulations is much better than for the anti-parallel case. This will be due to the predictions being only dependent on the angle of the inflowing magnetic field, except for  $\psi_r$  which uses  $\theta$  and the in inflow velocity which is dependent on relativistic Lundquist number.

	$\alpha = \frac{\pi}{12}$		$\alpha = \frac{\pi}{6}$	
Quantity	Predicted	Simulated	Predicted	Simulated
$\theta$	Not predicted	0.185	Not predicted	0.113
$\psi_r$	0.0127	0.0125-0.0141	0.0310	0.0245-0.0265
$v_{out}$	0.966	0.938	0.863	0.733
$\gamma_{out}$	3.820	2.938	1.910	1.470
$v_{in}$	0.12	0.15	0.12	0.07

Table 5.2: A table comparing the predictions and simulations for relativistic Petschek reconnection with magnetic field lines not anti-parallel with simulations.

### 5.2.6 Comparison of relativistic Petschek reconnection for different relativistic Lundquist numbers

Increasing the relativistic Lundquist number made the code more likely to crash as the change in the resistivity used to change the relativistic Lundquist number results in larger changes in the electric field in the resistive half time step described in section 3.4 and stabilising this required much smaller time steps which gave excessively long run times. To do this the set up described in section 5.2.1 was altered to have a Courant number of  $C_n = 0.01$  which reduced the time step by a tenth. This helped stabilise the code by giving a smaller jump in the electric field over the half time steps described in section 3.4. Due to the small time step, which required large numerical resources, one simulation of this was done with  $\alpha = \pi/6$  and a background resistivity of  $\eta = 10^{-3}$  which gives an external Lundquist number of  $S_u = 12 \times 10^3$ . The simulation was run for the shortest time for the structure to emerge and be far enough from the ambient outflow interface to allow measurements to be taken. This led to the simulation being run till time 18.546. As the resistivity has been increased the relativistic rotational shock has been further smeared out and only the method of using the velocity field on the  $z$  component of the magnetic

	$S_u = 16 \times 10^2$		$S_u = 12 \times 10^3$	
Quantity	Predicted	Simulated	Predicted	Simulated
$\theta$	Not predicted	0.113	Not predicted	0.172
$\psi_r$	0.0310	0.0245-0.0265	0.0473	0.0469-0.0611
$v_{out}$	0.0863	0.733	0.863	0.860
$\gamma_{out}$	1.910	1.470	1.910	1.956
$v_{in}$	0.1	0.07	0.1	0.096

Table 5.3: A table comparing the predictions and simulations for relativistic Petschek reconnection for  $\alpha = \frac{\pi}{6}$  for external Lundquist numbers of  $S_u = 16 \times 10^2$  and  $12 \times 10^3$ .

field could be used to locate it giving a much larger range.

If now the same method as before is applied, the angle the magnetic field makes with the shock plane in the inflow region is found to be  $\theta = 0.172$ . This is larger than at the lower Lundquist number value. This will be caused by the outflow jet recoil from the jet ambient fluid interface affecting the magnetic field lines. Using the same equations as before the predictions and simulations for the rotational shock angle, outflow velocity and Lorentz factor and the inflow velocity can be made. The range for the rotational shock is 0.0469-0.0611 with the predicted value being  $\psi_r = 0.0473$ . Whilst this is at the lower end, with the large margin of error it is quite acceptable. The inflow velocity and Lorentz factor are predicted to be 0.863 and 1.910 which are nearly identical to the simulated values of 0.860 and 1.956. Finally the inflow velocity is found to be 0.096 which is again very close to the predicted value of 0.1

As shown in table 5.3, with the same limitations, the higher value Lundquist number gives results much closer to the predicted values. The greater agreement for the larger Lundquist number is due to the inflow region being closer to the ideal state and hence closer to the equations used to derive the predicting equations. For larger Lundquist numbers the predictions of section 5.1 are also expected to be more accurate.

For a direct comparison to the case with relativistic Lundquist number of  $L_u = 16 \times 10^2$  the velocity and magnetic fields are presented here in the same format as section 5.2.5 in figures 5.20 and 5.21. In comparison to the lower relativistic Lundquist number the structure is essentially the same and the  $v_x$  and  $v_y$  velocities have both increased. This is due to the magnetic field being more firmly frozen to the plasma in the inflow region from the lower resistivity. During reconnection this is turned into a greater outflow. The  $v_z$  component of the velocity field is the same for relativistic Lundquist numbers. This can be expected as it is generated by the rotation of the magnetic field which should be rotated through the same angle for both relativistic Lundquist numbers. The  $B_x$  component of the magnetic field is the same in each case as set by the initial conditions. The  $B_y$  and  $B_z$  components of the magnetic field have increased in magnitude due to the increased inflow of magnetic flux being drawn in in the same time period.

### 5.2.7 Relativistic Petschek reconnection with a small $B_z \neq 0$ component, where $\alpha \ll 1/2\sqrt{\zeta}$

To confirm that when  $\alpha \ll 1/2\sqrt{\zeta}$  relativistic Petschek reconnection is unaffected by the inclusion of a small  $B_z$  component of the magnetic field, simulations were run with  $\alpha = \pi/36$ . As when  $2\alpha\sqrt{\zeta} \sim 1$ , the structure is more complicated than the anti-parallel case.

Both the analysis for when the condition  $\alpha \ll 1/(2\sqrt{\zeta})$  is violated or not needs the value of  $\theta$  which is found to be 0.211.

If the analysis of the angled case is applied, the results are not consistent with the results of the other angled cases with  $v_{out}$  and  $\gamma_{out}$  predicting values of 0.996 and 11.459 and the simulations giving 0.88 and 2.4. The inflow velocity does not agree with the predictions and the rotational shock is predicted to be  $\psi_r = 0.00161$  which is approximately the shock plane. This suggests that a rotational shock is not needed to deal with the small stretching

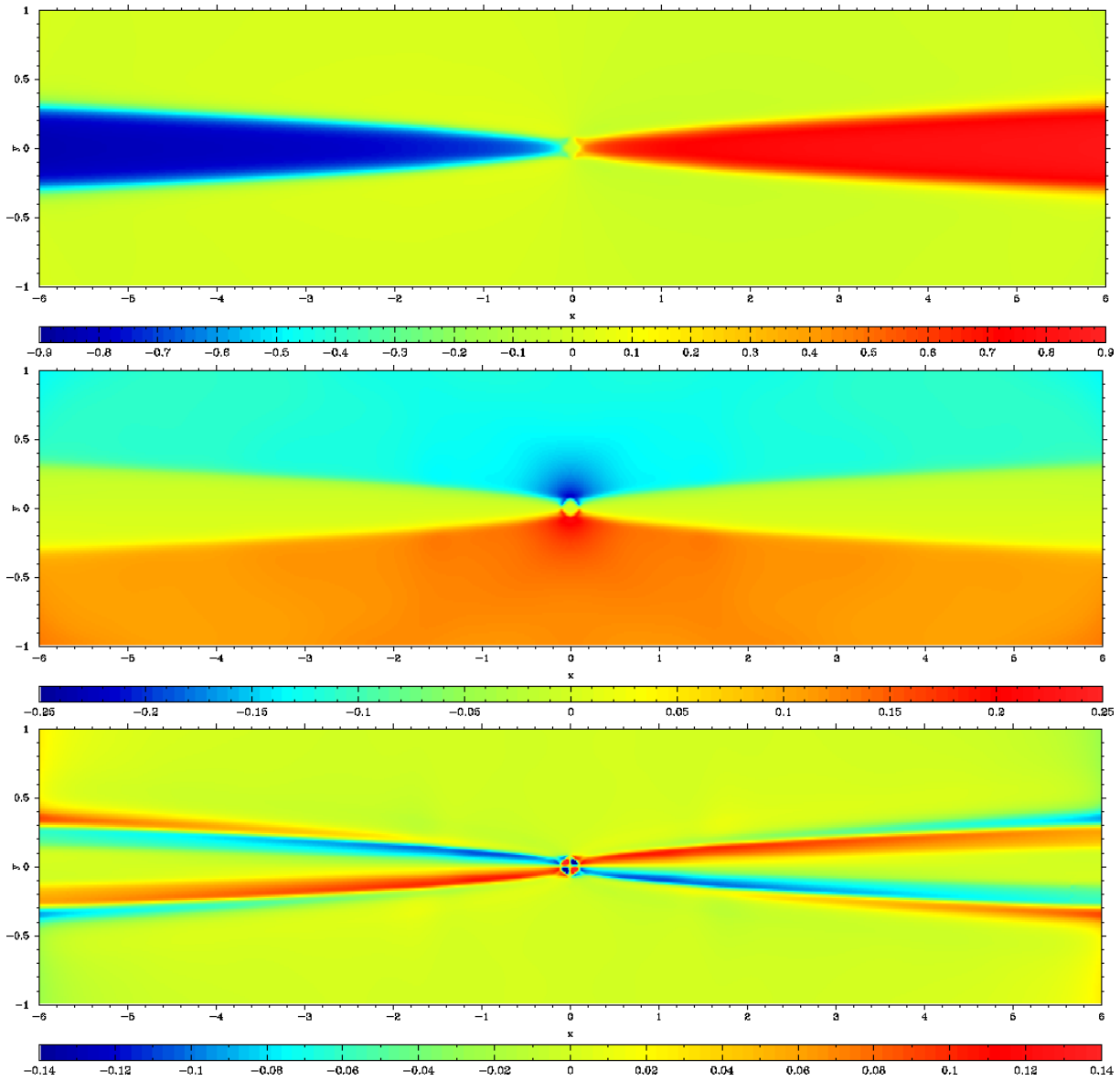


Figure 5.20: From the top to the bottom, the  $v_x$ ,  $v_y$  and  $v_z$  components of the velocity field for relativistic Petschek reconnection with  $\alpha = \pi/6$ ,  $L_u = 16 \times 10^2$  at time 18.546.

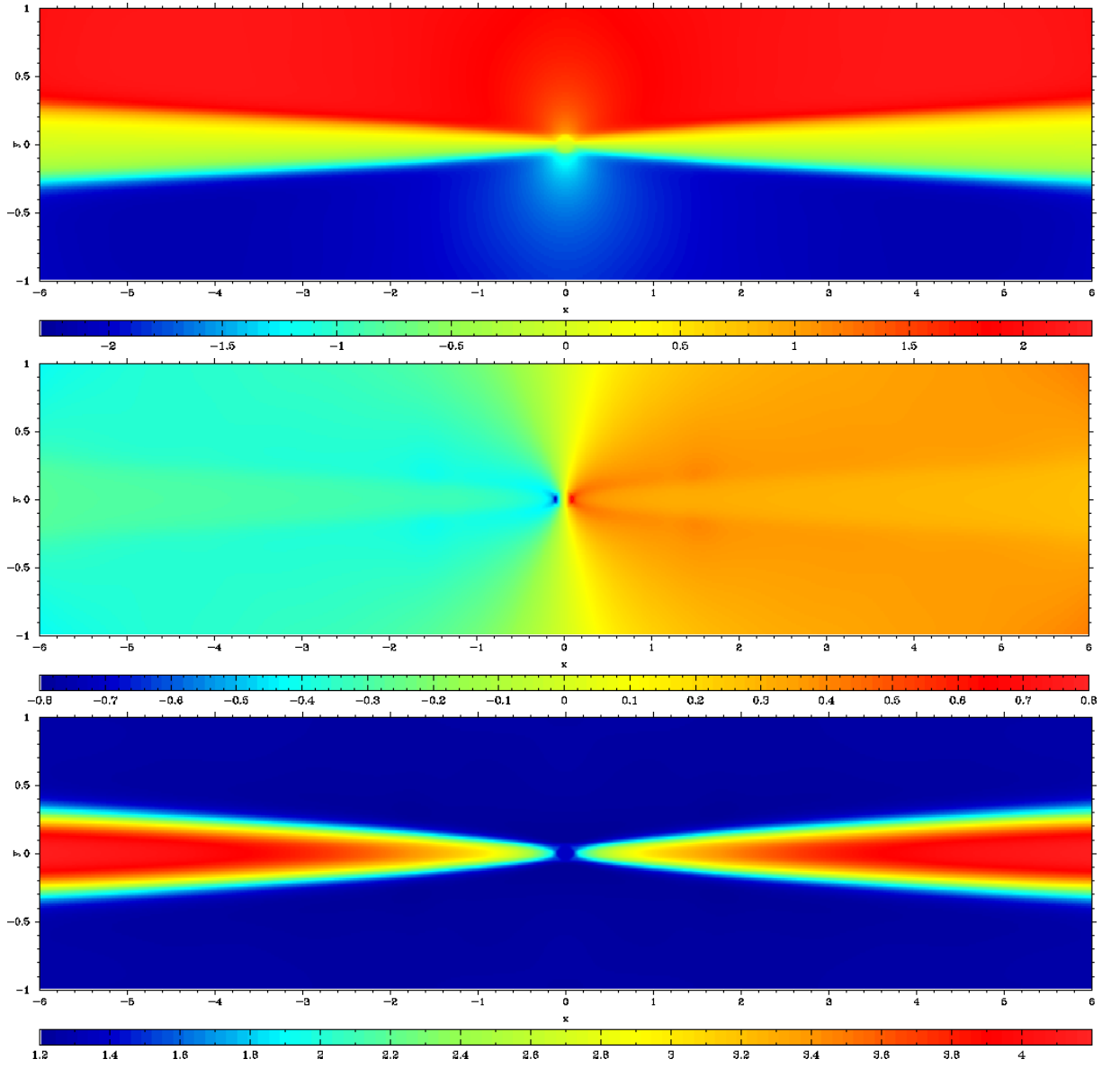


Figure 5.21: From the top to the bottom, the  $B_x$ ,  $B_y$  and  $B_z$  components of the magnetic field for relativistic Petschek reconnection with  $\alpha = \pi/6$ ,  $L_u = 16 \times 10^2$  at time 18.546.

Quantity	Predicted value	Simulated value
$v_{in}$	0.211	0.21
$v_{n2}$	0.00163	0.018
$v_{t2}$	0.99	0.88
$\gamma_2$	8.049	2.4
$\rho_2$	2.209	0.42
$p_2$	2.989	2.8
$\phi$	0.0148	0.0204

Table 5.4: A table comparing predictions and simulations of relativistic Petschek reconnection in the regime where the condition  $\alpha \ll 1/2\sqrt{\zeta}$  holds with  $\alpha = \pi/36$ .

in  $B_z$  between the upper and lower domains and the analysis of when  $\alpha \neq 0$  does not apply.

If the analysis of the anti-parallel case is instead applied, the agreement between the predictions and simulations is similar to the agreement of the anti-parallel case, with poor agreement except for the inflow velocity and outflow pressure. The simulations also reach the outer boundary in roughly the same time as the anti-parallel case, adding further evidence that for  $\alpha \ll 1/2\sqrt{\zeta}$  the structure of the reconnection is not significantly changed. The predictions and simulated values are shown in table 5.4.

### 5.2.8 The reconnection electric field

As stated in section 4.2.2, the reconnection electric field  $E^* = |\mathbf{E}(0)|$  is often used to measure the rate of reconnection. Figure 5.2.8 shows the reconnection electric field for  $\alpha = 0$  (the anti-parallel case),  $\pi/36$  and  $\pi/12$  with external Lundquist number of  $S_u = 16 \times 10^2$ . The graph shows an initial sharp growth, as reconnection commences



and is sustained by the forming outflow jet still being close to the origin, which then settles to a steady reconnection rate. For  $\alpha = \pi/36$ , which is in the regime where the angle will not change the structure, the reconnection electric field closely follows the anti-parallel case with a slight reduction in magnitude. The difference in magnitude will be caused by the slightly reduced  $x$  component of the magnetic field. Also shown is the case when  $\alpha = \pi/12$ , which has a reduced reconnection electric field caused by the reduced  $x$  component of the magnetic field. This shows signs of growing and suggests that the reconnection rate is unaffected by the inclusion of a  $z$  component of the magnetic field as stated in section 5.1.3.

Figure 5.22 shows the reconnection electric field for  $\alpha = \pi/6$  for the external Lundquist numbers  $S_u = 16 \times 10^2$  and  $12 \times 10^3$ . Both cases show the same initial sharp growth and settling at early times. The larger external Lundquist number gives a result five times larger in magnitude. This will be caused by the ten-fold increase in the conductivity. The slow development of the lower Lundquist number allows the reconnection field to begin to grow and suggests that the reconnection rate is unaffected as stated in section 5.1.3.

Figure 5.24 shows the reconnection electric field for  $\alpha = \pi/4, \pi/3$  and  $5\pi/12$  with an external Lundquist number of  $S_u = 16 \times 10^2$ . The figure shows the same initial sharp growth caused by the same commencement of reconnection and sustained by the close proximity of the outflow jet to the origin. This is followed by a decline to a steady state. As these results are in the region where  $\alpha \sim 1$  or greater, the analysis of section 5.1.3 does not apply and the decreased reconnection rate will be caused by the large reduction in the  $x$  component of the inflow magnetic field. The results show that reconnection occurs even when the magnetic field lines in the upper and lower domains are almost parallel, but at a greatly reduced rate. This shows that when the inflow magnetic field lines are almost parallel reconnection still occurs rather than simple diffusion and this happens at a much reduced rate than for  $\alpha \ll 1$ .

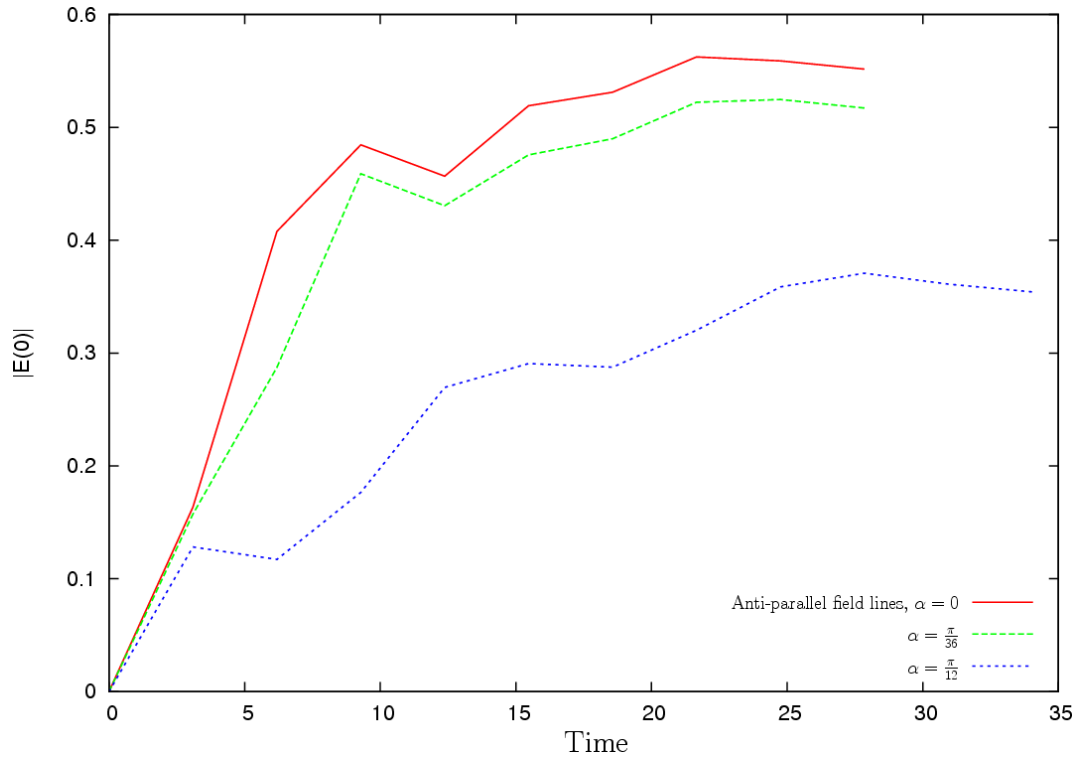


Figure 5.22: Evolution of the reconnection electric field  $E^*$ , with  $\alpha = 0$  (the anti-parallel case),  $\pi/36$  and  $\pi/12$  for relativistic Petschek reconnection.

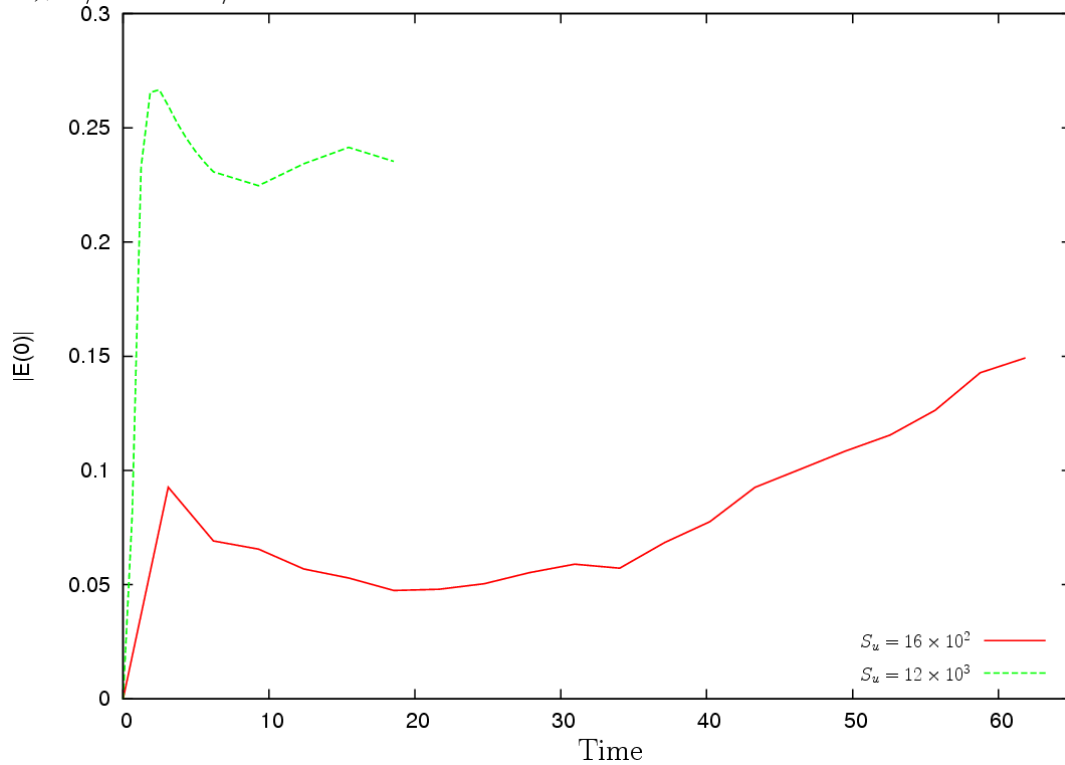


Figure 5.23: Evolution of the reconnection electric field  $E^*$  for relativistic Petschek reconnection with external Lundquist numbers  $S_u = 16 \times 10^2$  and  $12 \times 10^3$  and  $\alpha = \pi/6$ .

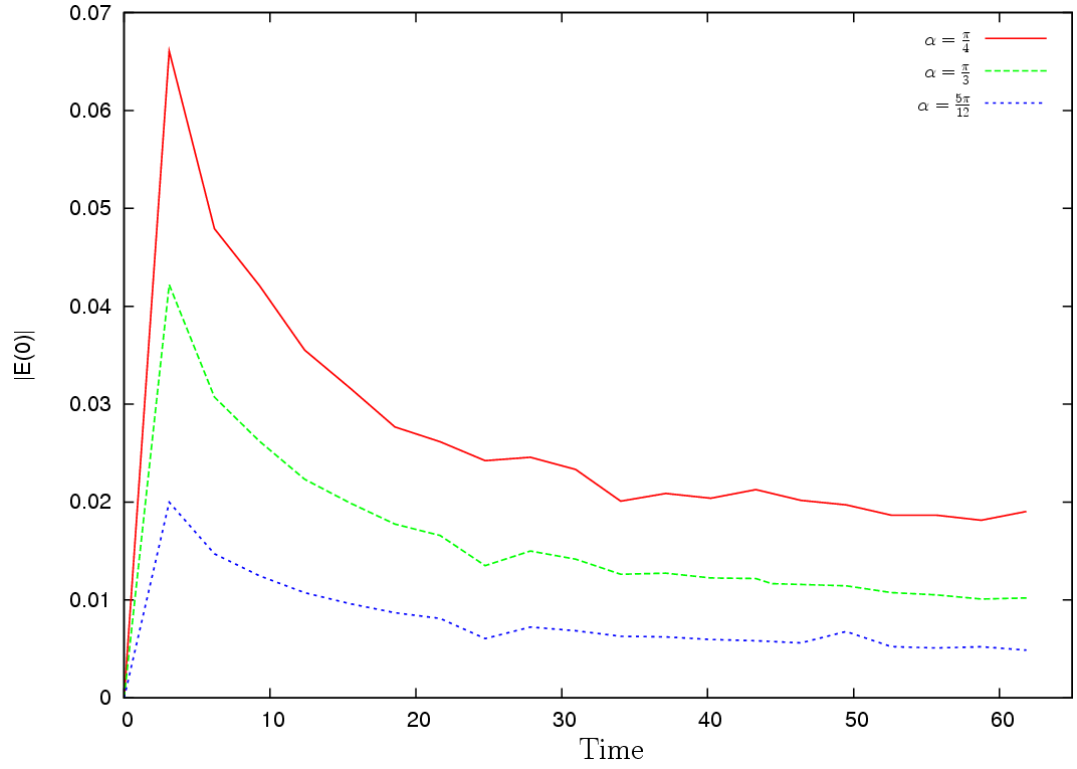


Figure 5.24: Evolution of the reconnection electric field  $E^*$  for relativistic Petschek reconnection with  $\alpha = \pi/4, \pi/3$  and  $5\pi/12$ .

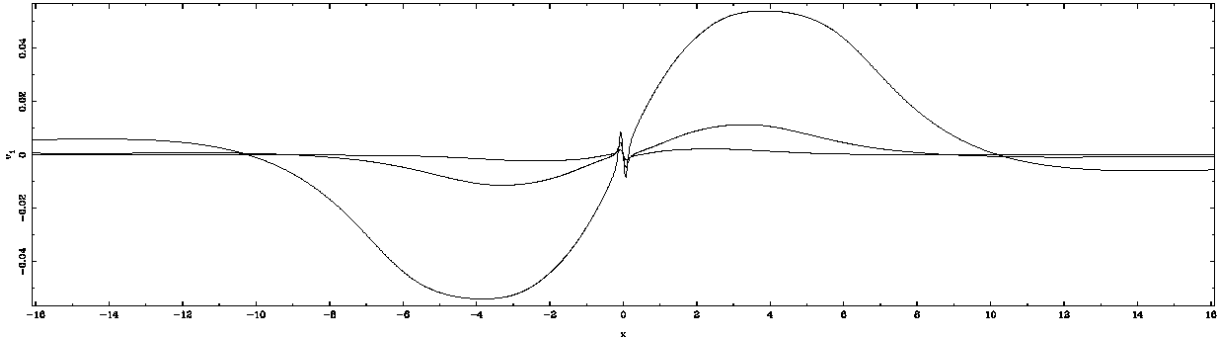


Figure 5.25: Outflow velocity along the  $y$  axis for where the outflow velocity is plotted along the  $y$  axis at time 61.846 for  $\alpha = \pi/4, \pi/3$  and  $5\pi/12$  showing the slower evolution and smaller inflow velocity for increasing values of  $\alpha$ .

### 5.2.9 Relativistic Petschek reconnection with a large $B_z \neq 0$ component, where $\alpha \gg 1/2\sqrt{\zeta}$

When the angle of inclination of the magnetic field is large, to the point where the inflow magnetic field is almost parallel, reconnection still occurs, albeit at a greatly reduced rate as shown in figure 5.24. As with the case when  $\alpha$  is small, the development of the structure of the tearing mode is greatly reduced (as shown in figures 5.11 and 5.12) and the magnitude of the variables is also reduced. This is shown in figure 5.25, where the outflow velocity is plotted along the  $y$  axis at time 61.846 for  $\alpha = \pi/4, \pi/3$  and  $5\pi/12$  with the largest to smallest velocity corresponding to the smallest to largest value of  $\alpha$ .

As with the smaller angle case the slow development will be due to the smaller gradient in the inflow anti-parallel component of the magnetic field giving a lower rate of reconnection. Since the magnetic gradients are much smaller the current sheet does not thicken much through diffusion. The thickening is reduced as the angle increases for large values of  $\alpha$ . The fact that relativistic Petschek reconnection occurs at all in this regime will be to do with the slow diffusion rate allowing the slow development of the relativistic Petschek reconnection.

### 5.2.10 Comparison of the Poynting and kinetic energy fluxes for the different values of $\alpha$

It is predicted through the order of magnitude arguments in section 5.1.3 that when the condition  $\alpha \ll 1/2\sqrt{\zeta}$  is violated the outflow will be magnetically dominated. Hence the Poynting flux will be much larger and the kinetic energy flux  $w\gamma^2\mathbf{v}$  will be much smaller. This is done for  $\alpha = 0$  (the anti-parallel case),  $\pi/36$  and  $\pi/12$  with the results being shown in figure 5.26. The left image shows the kinetic energy flux with  $\alpha$  increasing from top to bottom. This shows a larger kinetic energy flux in the outflow when  $\alpha \ll 1/2\sqrt{\zeta}$  and a smaller one when this condition is violated as expected. The right image shows the Poynting flux with  $\alpha$  decreasing from top to bottom. This shows a smaller Poynting flux in the outflow when  $\alpha \ll 1/2\sqrt{\zeta}$  and a larger one when this condition is violated confirming the predictions of the analysis. Both images are shown along the  $x$  axis.

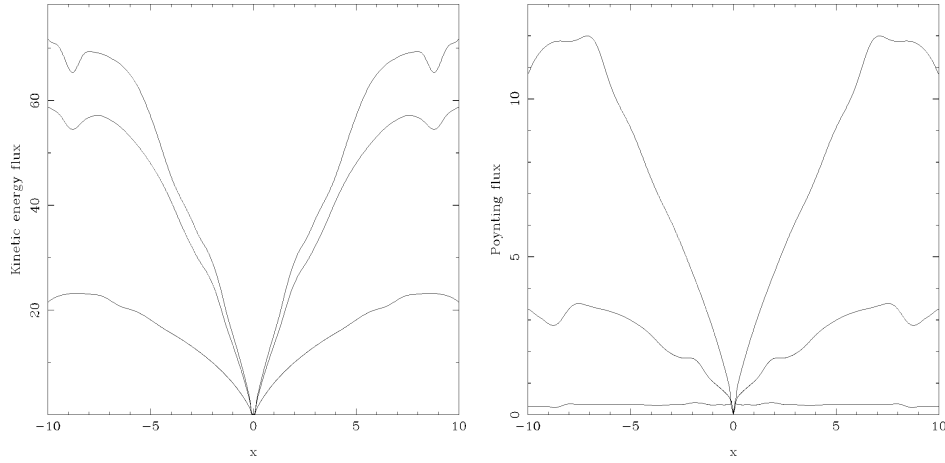


Figure 5.26: Comparison of the Poynting flux and kinetic energy flux in the outflow for  $\alpha = 0$  (the anti-parallel case),  $\pi/36$  and  $\pi/12$ . The left figure shows the kinetic energy flux with increasing  $\alpha$  from top to bottom. The right figure shows the Poynting flux with decreasing  $\alpha$  from top to bottom. Both are shown along the  $x$  axis. The three pairs of simulations are shown for when the simulations have reached the same state of development along the  $x$ -axis rather than for the same time.

## Chapter 6

### Discussion

This final chapter will draw together and discuss the conclusions of the research into magnetohydrodynamical models of relativistic magnetic reconnection. This will start with a summary of the original work in the thesis then proceed with the relativistic tearing mode, then relativistic Petschek reconnection and end with a look at possibilities for future research of magnetohydrodynamical models of relativistic reconnection.

#### **6.1 A summary of the research into magnetohydrodynamical models of relativistic reconnection**

A summary of the original work achieved in this thesis is presented below.

The first simulations of relativistic magnetohydrodynamical models of magnetic reconnection were completed. This included simulations of the relativistic tearing mode and relativistic Petschek reconnection.

For the relativistic tearing mode this was:-

- An investigation of the linear growth rates for different values of the plasma beta, relativistic Lundquist number, magnetisation parameter and the isothermal case. In each of these cases the wavelength was varied as well;
- With the linear growth rates the dispersion relations, relating the growth rate to the wavenumber, were plotted. These were in agreement with the predictions of which wavenumber the maximum growth rate will occur given by the analyses for the tearing mode in magnetodynamics;
- The linear growth rates are also compared to the observed values with good agreement;
- The non-linear growth of the relativistic tearing mode was considered and the reasons for the saturation of the growth rate and its initial settling. The saturated growth rates were compared for a series of plasma beta's, the isothermal case and for magnetodynamics. By extrapolation this indicated that the isothermal case presented a ceiling for the growth rates of the relativistic tearing mode in resistive magnetohydrodynamics;
- The results of the simulations were compared to the order of magnitude predictions of Lyubarsky which are presented in [29] with good agreement for the inflow velocity, but poor agreement with the outflow velocity;
- The reconnection electric field was then considered as a measure of the reconnection rate showing a similarity structure with lower reconnection rate for larger plasma beta's and providing clear evidence to identify secondary tearing for the isothermal case and when varying the relativistic Lundquist number.

For relativistic Petschek reconnection this was:-

- Relativistic Petschek simulations with anti-parallel incoming magnetic field lines with anomalous resistivity were performed. These qualitatively agreed with



Lyubarsky's predictions in [29] and quantitatively for the inflow velocity and the outflow plasma pressure;

- Relativistic Petschek simulations with non-anti-parallel incoming field lines caused by a small non-zero  $B_z = \alpha B_0$  component of the magnetic field where  $B_0$  is the background magnetic field strength and  $\alpha \ll 1$  with anomalous resistivity were performed. These agreed quantitatively and qualitatively with the predictions made in [29];
- The relativistic Lundquist number was varied for when  $B_z \neq 0$  to compare the differences. It was found that a larger relativistic Lundquist number gave a greater agreement with the predictions in [29];
- The limit predicted in [29] where if  $\alpha \ll 1/2\sqrt{\varsigma}$ , where  $\varsigma$  is the magnetisation parameter, relativistic Petschek reconnection goes ahead as if  $B_z = 0$ ;
- The reconnection electric fields were plotted for the different relativistic Petschek reconnection simulations. These show a decrease in the reconnection electric field for increasing values of  $\alpha$  and when  $\alpha \gg 1$  show that reconnection still occurs;
- Relativistic Petschek reconnection was simulated in the regime where  $\alpha \gg 1/2\sqrt{\varsigma}$  or when the incoming magnetic field lines are almost parallel. This showed that relativistic Petschek reconnection still occurs, albeit at a much reduced rate. This is a candidate for a background state from which fast relativistic Petschek reconnection can happen from by a rotation of the incoming magnetic field;
- The outflowing Poynting and kinetic fluxes were compared confirming the prediction in [29] that as the  $\alpha$  increases and the angle between the incoming magnetic field lines increases the outflow will become magnetically dominated from being kinetically dominated in the anti-parallel case.

The main conclusions in brief are that the relativistic tearing mode has a linear growth rate dependent on the wavenumber. The wavenumber corresponding to the maximum growth rate is predicted by the boundary layer analyses for the tearing mode in magnetodynamics. The linear growth rates found in the simulations also support the relativistic tearing mode being a candidate for powering bursts in compact relativistic objects. The simulations for relativistic Petschek reconnection confirm the order of magnitude calculations by Lyubarsky in [29].

## 6.2 The relativistic tearing mode

The order of magnitude calculations of Lyubarsky in [29] and detailed in chapter 4 show that the Sweet-Parker model generalises in a straightforward way to the relativistic case. The main change is that the Alfvén speed in the non-relativistic case is replaced by the speed of light for the relativistic case. This is not surprising if the relativistic Alfvén speed  $v_a$ , defined as

$$v_a = \frac{B}{\sqrt{B^2 + w}}, \quad (6.1)$$

tends to one in the highly magnetised environment. This is partly supported by the numerical results in chapter 4. The deviation seems to be the result that the current sheet was found to be compressible, in contradiction with the analytical results. This caused the numerical outflow velocities to be in poor agreement with the analytic predictions. The inflow was less affected, being at most a factor of 3 out. This is to be expected, as the effects of compressibility will be entirely inside the current sheet. As the pressure balance across the current sheet is determined by the external magnetic field, the extra compressed plasma in the sheet will not affect it much. The fact that the inflow region is not completely magnetically dominated will also affect this. If the magnetisation factor is raised to a large enough value, this effect is expected to nearly completely vanish. These

results are shown in table 4.5. The numerical outflow is drastically affected by these effects. The compression allows more plasma to leave the current sheet at a lower speed, whilst conserving the mass flux. A greater magnetisation parameter would also serve as a larger store of magnetic energy to be transferred to the kinetic energy of the plasma after reconnection, which would increase the speed of the outflow. These results are shown in table 4.6.

As in the non-relativistic case, if a  $B_z$  component of the magnetic field is added, it is found both analytically and numerically to not affect the model as shown in section 4.1.1 analytically and section 4.2.1 where the force-free current sheet is compared to the Harris current sheet.

Contrary to the order of magnitude calculations for the Sweet-Parker and Petschek reconnection, the analysis of the tearing mode was not a straightforward generalisation.

If the standard approach is taken, by neglecting higher order terms in  $\mu_c$ , then the induction equation and the condition for a force-free magnetic field is acquired. This does not allow analysis of the relativistic tearing mode and is not a closed system. An approach to analyse the relativistic tearing mode is to use the fact that the dimensional unit for the plasma beta is involved in the equations and use the fact that it is small. If this approach is taken then the equations found are the non-relativistic magnetohydrodynamics induction equation and the momentum equation is found to be from magnetodynamics. This is still not a closed system, though it suggests using the analysis of the tearing mode in the magnetodynamical case to present the results. This has good agreement for large values of the magnetisation parameter (and lower plasma beta's) and the Lundquist number. The maximum growth rate was found to be given by the non-dimensionalised wavenumber  $\bar{k}$ ,

$$\bar{k} = L_u^{-\frac{1}{4}}, \quad (6.2)$$

as predicted by equation 4.78 of the magnetodynamical analysis. The growth rate for this

wavenumber is much lower than predicted. This will be due to the plasma pressure that is not present in the magnetodynamical case. This is shown in figures 4.18 and 4.19.

Part of the motivation for numerical studies of the relativistic tearing mode were the interesting results found by Komissarov et al. in [27], for the tearing mode in relativistic magnetodynamics. This produced the question of whether this was an appropriate approach to the linear growth phase where the plasma is expected to be magnetically dominated. This was not found to be the case. With magnetohydrodynamics the rate was found to be significantly slower as illustrated in figure 4.26. The main cause of this was found to be the plasma pressure. In the magnetodynamic simulations the plasma pressure was absent and the decrease in magnetic pressure inside the current due to reconnection lead to a pressure difference pushing the magnetic field lines at a faster rate into the current sheet. This increased the rate of reconnection. In the magnetohydrodynamics case the plasma pressure increased inside the current sheet to give a near constant total pressure. With the pressure balance across the current sheet the inflow velocity will initially be entirely due to the motion of the magnetic field lines diffusing towards the current sheet causing an inflow by the frozen in field effect. There is further evidence of this in the isothermal simulations. To create the isothermal environment, at the end of each time step the plasma pressure was reset to

$$p = \rho T_{iso}, \quad (6.3)$$

where  $T_{iso}$  is the constant temperature desired. This kept the pressure reduced and the reconnection rate and rise time was seen to rise. This is shown in figure 4.18 and table 4.4. As the plasma pressure was reduced, it allowed a larger density in the current sheet. This is due to the reduced plasma pressure in the current sheet exerting a smaller force on the plasma giving a smaller outflow than expected and allowing much greater compression of the plasma. This is shown in the greater inflow velocity for the fastest growing isothermal growth rate and slower outflow shown in tables 4.5 and 4.6 in comparison to the standard

case.

The plasma beta was varied to see what effect it (and hence the magnetisation parameter as the background magnetic field strength is controlled by the plasma beta in the code) will have on the relativistic tearing mode. In varying the plasma beta from 0.32 to 0.05 the growth rate and development of the tearing mode was found to increase. As shown in figures 4.26 and 4.27, the isothermal case is a upper limit on the reconnection rate for the relativistic tearing mode. The magnetisation parameter was also varied independent of the plasma beta. This was done by increasing the density from 0.1 to 0.5. This was unchanged in the outflow, reconnection electric field and very similar for the linear growth rates. The inflow velocity was slower matching the greater background density for the same inflow momentum. The dispersion relation is different than from when the density is equal to the pressure. This is due to the inaccuracies in determining the linear growth rates.

In section 4.2.7 the tables 4.5 and 4.6 show the inflow and outflow velocity respectively. These are promising, showing good agreement for the inflow velocity but a slower than expected outflow velocity. It is expected that if the background magnetisation parameter were increased it would provide a reservoir of magnetic energy which when converted in the reconnection event would power the outflow velocity to greater speeds.

With the plasma beta not low enough to get the predictions of section 4.1.1 accurately, the growth rates still compare favourably to the observed growth rates for magnetars presented in [31]. This is shown in table 4.4. From the convergence of the growth rate and saturation of the relativistic tearing mode shown in figure 4.26, it is expected that the growth rates will increase but not exceed the value found for the isothermal simulations. This puts the tearing mode as an ideal candidate for the mechanism powering flares in magnetars, if the current accuracy of observations and the fact that these simulations were not calibrated towards this end is taken into consideration. The evidence against the relativistic tearing mode powering flares in magnetars comes from the fact that the outflow is expected to be highly relativistic, up to values of  $\gamma \sim 10 - 20$  (see [31]). This may be

caused by a mechanism acting on the released photon-pair plasma fire ball (described in detail in [46]) or from the relativistic tearing mode activating some anomalous resistivity and becoming relativistic Petschek reconnection. If the anomalous resistivity is based on the electron-ion drift velocity as described in [50], then this could happen as a natural progression as this is expected to grow at the reconnection point in the tearing mode.

The Lundquist number was varied by changing the value of the resistivity from the standard value of  $\eta = 10^{-3}$  to  $\eta = 10^{-4}$  giving relativistic Lundquist numbers of  $L_u = 10^2$  and  $10^3$ . The results where the relativistic Lundquist number was increased had a faster growth rate for the perturbation to the magnetic field. This is expected from 4.79 and due to the fact that the inflow region is closer to the ideal state. As indicated in figure 4.30, there is secondary tearing which is not present for the lower relativistic Lundquist values. This will be due to the wavelength being longer in the recorded reconnection electric field graph for the larger relativistic Lundquist number. This gives a longer thinned current sheet which is susceptible to secondary tearing.

When the growth rate reaches a large enough value the non-linear terms set in. This causes the growth of the perturbation to saturate and then start to decrease to a steady state. The point when the non-linear terms kick in depends on the wave length of the perturbation. This is shown for the various cases in figures 4.22 for the standard case. As the development of the structure of the relativistic tearing mode is slow for the different values of the plasma beta and relativistic Lundquist number, the current sheet is still quite thick and magnetic islands are not formed as shown in figure 4.5. This slow development and relatively thick current sheet stops secondary tearing from occurring. For the isothermal case and for magnetodynamics the plasma pressure is reduced and magnetic islands form with a very thin current sheet between them. This is susceptible to secondary tearing which is shown for the isothermal case in figure 4.6 and in the growth rate of the perturbation for magnetodynamics in figure 4.26.

From the linear growth rates the dispersion relation can be discerned. This was done using

the linear analysis of the tearing mode for magnetodynamics presented in section 4.1.2. Figures 4.18 and 4.19 both show the applicability of this analysis. As the plasma beta decreases the agreement increases, with the maximum moving to the origin and growing. Increasing the relativistic Lundquist number was found to fit the framework of the tearing mode in magnetodynamics quite accurately and is reminiscent of the results found in [27]. The greater agreement for the larger relativistic Lundquist number is due to the larger separation between the maximum wavenumber and cut off wavenumber. This is shown in figure 4.19. If the relativistic Lundquist number were to be further increased, it is expected to give better agreement, but not significantly so.

### 6.3 Relativistic Petschek reconnection

The order of magnitude calculations for relativistic Petschek reconnection are a straightforward generalisation of the non-relativistic case, with the Alfvén speed being replaced by the speed of light. The numerical simulations, whilst lacking in the necessary resolution, support this as shown in table 5.1. The main difference is the effect of a  $B_z$  component of the magnetic field. This is introduced as a fraction of the constant inflow magnetic field  $B_0$  as  $B_z = \alpha B_0$ , where  $\alpha$  is the angle the inflowing field makes with the  $x$  axis. When

$$\alpha \ll \frac{1}{2\sqrt{\varsigma}}, \quad (6.4)$$

the  $B_z$  component stays small and does not affect Petschek reconnection. Since the magnetisation parameter  $\varsigma$  will typically be large, this limit will be violated for small values of  $\alpha$  and the  $B_z$  component will be stretched and increase in value across the shocks. When this happens the structure of the relativistic Petschek reconnection is significantly altered. Rotational shocks now appear separating the inflow region from the slow shocks. This is to deal with stretching of the  $B_z$  component of the magnetic

field connecting the upper and lower regions. The stretching of the  $B_z$  component of the magnetic field requires energy which is taken from the reconnecting part of the magnetic field. This leaves the outflow being dominated by the Poynting flux instead of the normal result of reconnection, where the resulting plasma is dominated by the kinetic energy flux. The outflow is also found to have a larger angle between the slow shocks and a slower outflow velocity. The reconnection rate is unchanged though as the inflow region will be unchanged and the same amount of magnetic flux enters into the reconnection region as for the anti-parallel case.

As well as comparing relativistic and non-relativistic magnetohydrodynamical models of magnetic reconnection, the simulations of relativistic Petschek reconnection were directed towards confirming the order of magnitude calculations of Lyubarsky in [29]. There were difficulties in setting up the Petschek reconnection.

These include choosing a plasma beta, magnetisation parameter the state variables and the magnitude of the anomalous resistivity. The background resistivity was set to  $10^{-2}$  as when it was set lower relativistic Petschek reconnection did not work no matter the setup. This seems to be due to the stronger inflow creating a greater difference between the magnetically dominated inflow and the matter dominated outflow. Once the resistivity was set to  $10^{-2}$  the choice of the other parameters were chosen. The plasma beta controlled the pressure balances. As the resistivity was higher it allowed a lower plasma beta of 0.03 and relativistic Petschek reconnection to still occur. Within this choice of parameters the state variables were chosen. The plasma pressure was kept low to keep the inflow dominated by the magnetic pressure. With this the density was left to choose. Originally it was set large. This did not work which was thought to be due to accelerating the large amount of plasma through the reconnection process. Finally this was set to the same value as the plasma pressure. The magnetisation parameter was varied by changing state variables so that they are not equal. The simulations ran only for a short period of time, which was not long enough to take any measurements. The state variables not being equal seemed



to exacerbate the strange behaviour at the boundaries documented in section 3.6.2. This led to all the simulations of relativistic Petschek reconnection being done with the state variables equal.

The anomalous model shown in section 5.2.1 was found to be stable and consistently providing results. Attempts were made at generalising this to a resistivity dependent on the electron-ion drift velocity  $V_D$ , where the electron-ion drift velocity is given by

$$V_D = \frac{J}{\rho}. \quad (6.5)$$

This was done in accordance with the conditions prescribed by Ugai in [50], that

$$\frac{\partial \eta}{\partial V_D} > 0 \quad \text{for } V_D > V_C \quad \text{and} \quad \eta = \text{const} \quad \text{for } V_D < V_C, \quad (6.6)$$

where  $V_C$  is a threshold value. This was done with the standard model with anti-parallel magnetic field lines in the inflow region and, with or without a perturbation, did not produce reconnection. Any region affected by the enhanced reconnection was found to rapidly diffuse and, if relativistic Petschek reconnection was triggered, the anomalous resistivity would affect the outflow region and end the reconnection. This was done for various different models and no qualitative difference was found between them as predicted in [50].

The anomalous resistivity model detailed in section 5.2.1 was then used to make preliminary investigations into relativistic Petschek reconnection. This found the simulations to be both numerically intensive and with some restrictions. The length of the domain was also a limiting factor on the simulations. The length of the domain needed to be long as it was found that where the outflow moves into the unperturbed plasma and the boundary it would cause the simulations to crash. This led to a compromise between letting the reconnection fully develop and producing reasonable simulation times and size of the data files. As such the  $x$  domain was set as  $[-16, 16]$ .

With a working model, simulations were then made and compared to the predictions of [29] which were reproduced in section 5.1. When the magnetic field was inclined at a small angle  $\alpha$  and when  $2\alpha\sqrt{\zeta} \sim 1$ , the predictions were in good agreement with the simulations. This was not the case when  $\alpha \ll 1/2\sqrt{\zeta}$ . Here the numerical resolution was too low to resolve the system accurately enough to verify the analytical predictions. Since the simulations were done with a staggered grid, getting finer towards the centre and did not provide the increased resolution needed in the areas of interest, it suggests using an adaptive grid to give the much higher resolution needed in the current sheet compared to the inflow region. In either case the reconnection rate is calculated from the inflow region, where there is sufficient resolution, and is as predicted for all the simulations of relativistic Petschek reconnection with small  $\alpha$ .

The numerical simulations showed that when the angle of inclination of the magnetic field in the inflow  $\alpha$  obeys  $\alpha \ll 1/2\sqrt{\zeta}$  Petschek reconnection generalises in a straightforward way from the non-relativistic case, with the magnetic energy being efficiently liberated at slow shocks, converting the reservoir of magnetic energy into kinetic energy and heating. This is illustrated in figure 5.26. This shows that in this regime relativistic Petschek reconnection is a viable mechanism for powering relativistic flares.

When the angle of inclination of the magnetic field is  $2\alpha\sqrt{\zeta} \sim 1$ , Petschek reconnection deviates from the non-relativistic case. The  $B_z$  component of the magnetic field now provides a magnetic pressure inside the current sheet which thickens the sheet and leaves the outflow energy density dominated by the Poynting flux. This is illustrated again in figure 5.26. As  $\alpha$  increases, the time for the structure of relativistic Petschek reconnection to develop and to reach the boundaries of the domain increases and the rise time increases. It is not immediately obvious whether relativistic Petschek reconnection with  $B_z \neq 0$  can power flares from relativistic objects. This however does not exclude the magnetic energy being liberated at a later point either by waves or through further reconnection. The further liberation of magnetic energy is beyond the scope of this work.

When the angle of inclination is  $\alpha \gg 1/2\sqrt{\zeta}$  there is clear evidence of reconnection occurring at a much reduced rate. This is shown in figure 5.24. The development of the structure of relativistic Petschek reconnection and the time taken to reach the boundaries of the domain are remarkably slow, even in comparison to the smaller  $\alpha$  cases. The outflow is magnetically dominated as only a small portion of the magnetic energy is converted to kinetic energy. Though it is unlikely that relativistic reconnection in this regime will power any flares, it is suggestive that a rotation of the incoming magnetic field towards the anti-parallel case from this initial state may trigger relativistic Petschek reconnection which could power high energy bursts.

The relativistic Lundquist number was only varied once due to the intensity of the simulations. This was done for the non anti-parallel case with a value of  $\alpha = \frac{\pi}{6}$ . The agreement with the order of magnitude predictions was much better for the larger value of the relativistic Lundquist number. This is likely due to the sharper resolution of the various shocks, which will convert the variables across them closer to the theoretical predictions.

In comparing Petschek reconnection to the relativistic case when the incoming magnetic field lines are anti-parallel it is a straightforward generalisation. If a small  $B_z$  component is included in the inflow given by  $B_z = \alpha B_0$  and the condition  $\alpha \ll 1/2\sqrt{\zeta}$  is violated then the relativistic case is not a generalisation of the non-relativistic one. When this condition is violated the structure of the relativistic Petschek reconnection is changed. The changes are, the formation of relativistic rotational shocks outside of the relativistic slow shocks, a widening of the outflow with a widening of the angle between the relativistic slow shocks, a reduction in the outflow velocity and hence the Lorentz factor. The outflow energy flux also changes from being kinetically dominated to being dominated by the Poynting flux. The reconnection rate is unaffected as it is determined by the inflow velocity and the dynamics at the point of symmetry between the two shocks. The discrepancy in this work with the reconnection rate comes from the reduction in the anti-

parallel part of the magnetic field to accommodate the non-zero  $B_z$  component of the magnetic field and keep the inflow magnetic pressure constant.

## 6.4 Future research

An improvement upon this work would be the further development of relativistic resistive magnetohydrodynamical codes to deal with a larger magnetisation parameter (to get more accurate results for the relativistic tearing mode), a larger Lundquist number and to deal with the stiff resistive term more effectively. Progress has already been made in dealing with the stiff term whilst this research was underway with the work of Palenzuela et al. in [35] where an implicit-explicit Runge-Kutta method is applied to deal with the stiff term. This is done by treating the stiff term with an implicit discretisation and an explicit one for the non-stiff terms. This shows stability across a greater range of Lundquist numbers and effectively deals with the stiff term in all the tests presented. This code has not been used to work on relativistic reconnection as of the time of writing.

Also whilst this research was being conducted work was done by Zenitani et al. on relativistic magnetic reconnection using a magnetohydrodynamical two fluid model of electrons and positrons with an inter-species friction term in the momentum equation which provides an effective resistivity. This is presented in [53]. Their simulations went straight to relativistic Petschek reconnection and are quantitatively similar to this work. They did not have a problem with the outflow interface passing through the edge of the domain. They also achieved slightly larger magnetisation parameters of  $\varsigma = 100$ . They did not investigate the angle of the inflow magnetic field or the relativistic Lundquist number.

The linear analysis of the tearing mode in relativistic resistive magnetohydrodynamics produced the two equations used by Furth et al. in [11] for non-relativistic magnetohydrodynamics and by Komissarov et al. in [27] for magnetodynamics.

Unfortunately one equation was from each regime (see equations 4.33 and 4.37). It would then be of interest to investigate the full dispersion relation for the full relativistic resistive magnetohydrodynamical equations without any assumptions to see what this looks like and how it compares to that found in the non-relativistic and magnetodynamical cases.

As suggested by the low outflow velocity for the relativistic tearing mode compared to observations, it would be instructive to trigger relativistic Petschek reconnection from the relativistic tearing mode. This would probably be dependent on either the current density or the electron-ion drift velocity  $V_D$  passing a threshold at the X-point. This should be done first for the anomalous resistivity profile used in the Petschek simulations then using a resistivity directly dependent on  $V_D$ .

With relativistic Petschek reconnection occurring at large values of  $\alpha$ , it would be instructive to investigate starting reconnection at a large value of  $\alpha$  and then, when this was set up, rapidly reducing the angle to see if this could act as an effective trigger for the observed rise times of flares from relativistic objects.

It would be of interest, both in the relativistic tearing mode and relativistic Petschek reconnection to enforce an inflow on the top and bottom boundaries to create a higher inflow velocity. By increasing the inflow velocity it would allow the maximum reconnection rate to be determined for the relativistic tearing mode by finding how the plasma pressure in the current sheet reacts to the increased incoming plasma and by the frozen in magnetic field, the incoming magnetic flux. For relativistic Petschek reconnection it would be of interest to see if the width of the outflow jet is affected and again the maximum amount of magnetic flux that Petschek reconnection can reconnect.

With the natural three dimensional nature of electromagnetic fields, it would be prudent to perform three dimensional simulations to check that the two and a half dimensional simulations are valid and to see if any new behaviour is present.



# Appendices

## A Estimation of the relativistic Lundquist number for magnetars

First the resistivity is estimated by a combination of a typical velocity and length of the system,

$$\eta = c\delta. \quad (\text{A.7})$$

The typical length scale itself can be estimated as  $\delta = c/\omega_e$ , where  $\omega_e$  is the electron skin depth. With this the relativistic Lundquist can then be estimated by

$$L_u = \frac{lc}{\eta} = \frac{l}{\delta} = \frac{l\omega_e}{c}, \quad (\text{A.8})$$

where  $l$  is the width of the current sheet.

An estimate of the electron skin depth is then needed in terms of none of the parameters of the system. If Gauss's law is considered

$$\nabla \cdot \mathbf{E} = 4\pi q, \quad (\text{A.9})$$

and the electric field is estimated as  $E$ , the derivative is estimated as a length  $r$  and the charge density as a combination of the number density and the charge of an electron,  $q = ne$  then

$$\frac{E}{r} = 4\pi en. \quad (\text{A.10})$$

The electric field will be generated by the rotation of the magnetar and will be a fraction of the magnetic field  $E = \lambda B$ , where  $\lambda$  will be less than 1 and is a measure of the rotation of the magnetar. Using this Gauss's law is then

$$\frac{\lambda B}{r} = 4\pi en. \quad (\text{A.11})$$

Then using the definition of the electron skin depth and the estimation of Gauss's law, it can be estimated as

$$\omega_e^2 = \frac{4\pi e^2 n}{m} = \frac{\lambda e B}{mr}. \quad (\text{A.12})$$

Substituting this into the equation found for the relativistic Lundquist number, equation A.8, it becomes

$$L_u = \frac{l}{c} \left( \frac{\lambda e B}{mr} \right)^{\frac{1}{2}}, \quad (\text{A.13})$$

as the derivative length will be around the radius of a neutron star  $r \approx R_{NS}$  and then on rearranging

$$L_u = \left( \frac{l}{R_{NS}} \right) \left( \frac{B}{B_Q} \right)^{\frac{1}{2}} \lambda^{\frac{1}{2}} \left( \frac{e B_Q R_{NS}}{mc^2} \right)^{\frac{1}{2}}, \quad (\text{A.14})$$

where  $B_Q$  is the quantum magnetic field. The parameters in the final parentheses are all known with the charge on an electron as  $e = 4.8033 \times 10^{-10}$  Statcoulomb, the mass of an



electron as  $m = 9.0109 \times 10^{-28}$  g and the speed of light as  $c = 2.998 \times 10^{10}$   $cm s^{-1}$  or can be estimated as  $B_Q = 4 \times 10^{13}$  Gauss,  $R_{NS} = 10^6$  cm. This finally gives

$$L_u = 1.54 \times 10^8 \left( \frac{l}{R_{NS}} \right) \left( \frac{B}{B_Q} \right)^{\frac{1}{2}} \lambda^{\frac{1}{2}}. \quad (A.15)$$

The prefactor roughly represents a maximum value for the relativistic Lundquist number. As  $l \approx R_{NS}$ ,  $B \sim B_Q$  and  $\lambda^{\frac{1}{2}}$  will be small, around  $\frac{1}{10}$  the relativistic Lundquist number will be around  $10^6$ .

## B Estimation of the magnetisation parameter for magnetars

To estimate an upper limit for the magnetisation parameter the minimum density is found using the method by Goldreich and Julian in [18]. To do this Gauss's law

$$\nabla \cdot \mathbf{E} = 4\pi q \quad (\text{B.16})$$

is rearranged to give an estimate of the electric field as

$$q = \frac{\nabla \cdot \mathbf{E}}{4\pi} = \frac{E}{4\pi R_{NS}} = \frac{\lambda B}{4\pi R_{NS}}, \quad (\text{B.17})$$

where the derivative has been replaced by the length scale of the system, the radius of a neutron star and the electric field is expected to be generated by the rotation of the magnetic field and will be a fraction of its strength  $E = \lambda B$ , where  $\lambda$  is a measure of the rotation of the star.

The number density  $n$  is then given by

$$n = \frac{q}{e} = \frac{\lambda B}{4\pi e R_{NS}}, \quad (\text{B.18})$$

where  $e$  is the charge on an electron. Hence the rest mass density is

$$\rho c^2 = m_e n c^2 = \frac{\lambda B m_e c^2}{4\pi e R_{NS}}, \quad (\text{B.19})$$

where  $m_e$  is the mass of an electron.

Then the upper limit on the magnetisation parameter may be estimated as

$$\varsigma = \frac{B^2}{8\pi} \bigg/ \frac{\lambda B m_e c^2}{4\pi e R_{NS}} = \frac{B e R_{NS}}{2\lambda m_e c^2} \quad (\text{B.20})$$

or by using the definition of the cyclotron frequency

$$\omega_B = \frac{eB}{m_e c}, \quad (\text{B.21})$$

as

$$\varsigma = \frac{\omega R_{NS}}{2\lambda c}. \quad (\text{B.22})$$

If the constants  $e = 4.8033 \times 10^{-10}$  Statcoulomb,  $m_e = 9.0109 \times 10^{-28}$  g and  $c = 2.998 \times 10^{10}$  cm s<sup>-1</sup> and the estimates for a magnetar where  $B = 4 \times 10^{13}$  Gauss,  $R_{NS} = 10^6$  cm and a typical rotational frequency of  $\lambda = 10^{-1}$  then the upper limit from equation B.20 is

$$\varsigma = 10^{17}. \quad (\text{B.23})$$

The Goldreich Julian estimation does not take into account matter produced through pair production as the charges cancel out. The multiplicity factor was found by Hibschan and Arons in [21] for pulsars to be in the range 10 – 100 which taking the upper value of the range gives a lower limit for the magnetisation parameter as  $10^{14}$  and hence it will be in the range

$$10^{14} \leq \varsigma \leq 10^{17}. \quad (\text{B.24})$$

## C Estimation of the plasma beta for magnetars

To estimate the lower limit on the plasma beta the ideal gas law

$$p = R\rho T, \quad (\text{C.25})$$

is used with the density given the Goldreich-Julian approach which from appendix B is

$$\rho = \frac{\lambda B m_e}{4\pi e R_{NS}}. \quad (\text{C.26})$$

Using these two equations the plasma beta is given by

$$\beta = \frac{8\pi p}{B^2} = \frac{2RT}{B} \cdot \frac{\lambda m_e}{e R_{NS}}. \quad (\text{C.27})$$

The constants  $e = 4.8033 \times 10^{-10}$  Statcoulomb,  $m_e = 9.0109 \times 10^{-28}$  g,  $c = 2.998 \times 10^{10}$  cm s<sup>-1</sup> and the gas constant  $R = 8.314 \times 10^7$  erg mol<sup>-1</sup> K<sup>-1</sup> are known and the estimates for a magnetar are  $B = 4 \times 10^{13}$  Gauss,  $R_{NS} = 10^6$  cm and a typical rotational frequency of  $\lambda = 10^{-1}$  then only the temperature is needed.

In [46] the temperature of the magnetosphere of a magnetar is shown to be  $\approx 10$  keV. To convert this kelvin, it is first converted to joules by

$$1\text{K} = 1.380658 \times 10^{-23}\text{J}, \quad (\text{C.28})$$

and then to electron volts to joules by

$$1\text{eV} = 1.60217733 \times 10^{-19}\text{J}, \quad (\text{C.29})$$

which gives one electron volt in kelvin as

$$1\text{eV} = 11.604447517 \times 10^3\text{K}, \quad (\text{C.30})$$

and hence 10keV is

$$10\text{keV} = 1.1604447517 \times 10^8\text{K} \approx 10^8\text{K}. \quad (\text{C.31})$$

Then, on substituting these values into equation C.27 gives the lower limit for the plasma beta as

$$\beta = 7.79 \times 10^{-21} \approx 10^{-20}. \quad (\text{C.32})$$

As the density was found via the Goldreich-Julian method, the matter missed is accounted for by the multiplicities as in appendix B which at its maximum is  $10^3$  gives the range on the plasma beta is

$$10^{-20} \leq \beta \leq 10^{-17}. \quad (\text{C.33})$$



# Bibliography

- [1] S. K. Antiochos, C. R. DeVore, and J. A. Klimchuk, *A model for solar coronal mass ejections*, The Astrophysical Journal **510** (1999), 485–493.
- [2] A. M. Beloborodov and C. Thompson, *Corona of Magnetars*, The Astrophysical Journal **657** (2007), 967–993.
- [3] N. Bessho and A. Bhattacharjee, *Collisionless reconnection in an electron-positron plasma*, Physical Review Letters **95** (2005), 245001–+.
- [4] T. G. Cowling, *Solar electrodynamics*, Electrodynamic phenomena in cosmical physics (B. Lehnert, ed.), International Astronomical Union symposium, vol. 6, 1958, pp. 105–113.
- [5] W. Daughton and H. Karimabadi, *Collisionless magnetic reconnection in large-scale electron-positron plasmas*, Physics of Plasmas **14** (2007), 072303–+.
- [6] W. Daughton, J. Scudder, and H. Karimabadi, *Fully kinetic simulations of undriven magnetic reconnection with open boundary conditions*, Physics of Plasmas **13** (2006), 072101–+.
- [7] J. F. Drake, M. A. Shay, and M. Swisdak, *The Hall fields and fast magnetic reconnection*, Physics of Plasmas **15** (2008), 042306–+.

- [8] R. C. Duncan and C. Thompson, *Formation of very strongly magnetised neutron stars - Implications for gamma-ray bursts*, The Astrophysical Journal **392** (1992), 9–13.
- [9] D. Eichler, Y. Lyubarsky, C. Thompson, and P. M. Wood, *Magnetars in the afterglow era*, Pulsars, AXPs and SGRs Observed with BeppoSAX and other observatories (G. Cusumano, E. Massaro, and T. Mineo, eds.), 2003, pp. 215–222.
- [10] L. Ferrario and D. Wickramasinghe, *Origin and evolution of magnetars*, Monthly Notices of the Royal Astronomical Society **389** (2008), 66–70.
- [11] H. P. Furth, J. Killeen, and M. N. Rosenbluth, *Finite-resistivity instabilities of a sheet pinch*, Physics of Fluids **6** (1963), 459–484.
- [12] C. F. Gammie, J. C. McKinney, and G. Tóth, *Harm: A numerical scheme for general relativistic magnetohydrodynamics*, The Astrophysical Journal **589** (2003), 444–457.
- [13] G. Ghisellini, A. Celotti, G. Fossati, L. Maraschi, and A. Comastri, *A theoretical unifying scheme for gamma-ray bright blazars*, Monthly Notices of the Royal Astronomical Society **301** (1998), 451–468.
- [14] D. Giannios, D. A. Uzdensky, and M. C. Begelman, *Fast TeV variability in blazars: jets in a jet*, Monthly Notices of the Royal Astronomical Society **395** (2009), L29–L33.
- [15] ———, *Fast TeV variability in blazars: jets in a jet*, Monthly Notices of the Royal Astronomical Society **395** (2009), 29–33.
- [16] R. Gill and J. Heyl, *The birthrate of magnetars*, Monthly Notices of the Royal Astronomical Society **381** (2007), 52–58.



- [17] S. K. Godunov, *A finite difference method for the computation of discontinuous solutions of fluid dynamics*, Mathematics Sbornik **47** (1959), 271–306, (translated to English by US joint publication resource service, JPRS 7226, in 1969).
- [18] P. Goldreich and W. H. Julian, *Pulsar electrodynamics*, The Astrophysical Journal **157** (1969), 869–+.
- [19] H. Harten, P. D. Lax, and B. van Leer, *On upstream differencing and Godunov-type schemes for hyperbolic conservation laws*, SIAM Review **25** (1983), 35–61.
- [20] L. N. Hau and S. W. Chiou, *On the linear and nonlinear resistive tearing-mode instabilities*, Journal of Geophysical Research **106** (2001), 8371–8380.
- [21] J. A. Hirschman and J. Arons, *Pair production multiplicities in rotation-powered pulsars*, The Astrophysical Journal **560** (2001), 871–884.
- [22] A. Jeffrey and V. P. Korobeinikov, *Formation and decay of electromagnetic shock waves*, Zeitschrift Angewandte Mathematik Physik **20** (1969), 440–447.
- [23] V. M. Kaspi, *Magnetars*, Radio Pulsars (M. Bailes, D. J. Nice, and S. E. Thorsett, eds.), Astronomical Society of the Pacific Conference Series, vol. 302, 2003, pp. 151–158.
- [24] S. S. Komissarov, *A Godunov-type scheme for relativistic magnetohydrodynamics*, Monthly Notices of the Royal Astronomical Society **303** (1999), 343–366.
- [25] ———, *On some recent developments in numerical methods for relativistic mhd*, Relativistic Jets: The common physics of AGN, microquasars, and gamma-ray bursts (P. A. Hughes and J. N. Bregman, eds.), American Institute of Physics Conference Series, vol. 856, 2006, pp. 129–149.
- [26] ———, *Multi-dimensional numerical scheme for resistive relativistic mhd*, Monthly Notices of the Royal Astronomical Society **382** (2007), 995–1004.

- [27] S. S. Komissarov, M. Barkov, and M. Lyutikov, *Tearing instability in relativistic magnetically dominated plasmas*, Monthly Notices of the Royal Astronomical Society **374** (2007), 415–426.
- [28] B. C. Low, *Resistive diffusion of force-free magnetic fields in a passive medium*, The Astrophysical Journal **181** (1973), 209–226.
- [29] Y. E. Lyubarsky, *On the relativistic magnetic reconnection*, Monthly Notices of the Royal Astronomical Society **358** (2005), 113–119.
- [30] M. Lyutikov, *Explosive reconnection in magnetars*, Monthly Notices of the Royal Astronomical Society **346** (2003), 540–554.
- [31] M. Lyutikov, *Magnetar giant flares and afterglows as relativistic magnetised explosions*, Monthly Notices of the Royal Astronomical Society **367** (2006), 1594–1602.
- [32] M. Lyutikov and D. Uzdensky, *Dynamics of relativistic reconnection*, The Astrophysical Journal **589** (2003), 893–901.
- [33] L. Maraschi, G. Ghisellini, and A. Celotti, *A jet model for the gamma-ray emitting blazar 3C 279*, The Astrophysical Journal Letters **397** (1992), L5–L9.
- [34] M. Øieroset, T. D. Phan, M. Fujimoto, R. P., and R. P. Lepping, *In situ detection of collisionless reconnection in the Earth’s magnetotail*, Nature (2001), 414–417.
- [35] C. Palenzuela, L. Lehner, O. Reula, and L. Rezzolla, *Beyond ideal MHD: towards a more realistic modelling of relativistic astrophysical plasmas*, Monthly Notices of the Royal Astronomical Society **394** (2009), 1727–1740.
- [36] D. M. Palmer, S. Barthelmy, N. Gehrels, R. M. Kippen, T. Cayton, C. Kouveliotou, D. Eichler, R. A. M. J. Wijers, P. M. Woods, J. Granot, Y. E. Lyubarsky, E. Ramirez-Ruiz, L. Barbier, M. Chester, J. Cummings, E. E. Fenimore, M. H. Finger, B. M.

- Gaensler, D. Hullinger, H. Krimm, C. B. Markwardt, J. A. Nousek, A. Parsons, S. Patel, T. Sakamoto, G. Sato, M. Suzuki, and J. Tueller, *A giant  $\gamma$ -ray flare from the magnetar SG 1806 - 20*, *Nature* **434** (2005), 1107–1109.
- [37] E. N. Parker, *Sweet's mechanism for merging magnetic fields in conducting fluids*, *Journal of Geophysical Research* **62** (1957), 509–520.
- [38] H. E. Petschek, *Magnetic field annihilation*, NASA Special Publication **50** (1964), 425–439.
- [39] E. Priest and T. Forbes (eds.), *Magnetic reconnection : MHD theory and applications*, Cambridge University press, 2000.
- [40] M. Semenov, I. V. Kubyshkin, V. V. Lebedeva, R. P. Rijnbeek, M. F. Heyn, H. K. Biernat, and C. J. Farrugia, *A comparison and review of steady-state and time-varying reconnection*, *Planetary and Space Science* **40** (1992), 63–87.
- [41] A. N. Simakov and L. Cacán, *Quantitative, comprehensive, analytical model for magnetic reconnection in Hall magnetohydrodynamics*, *Physical Review Letters* **101** (2008), 105003–+.
- [42] B. V. Somov (ed.), *Fundamentals of cosmic electrodynamics*, Astrophysics and Space Science Library, vol. 191, 1994.
- [43] G. Strang, *On the construction and comparison of difference schemes*, *SIAM Journal on Numerical Analysis* **5** (1968), 506–517.
- [44] P. A. Sweet, *The neutral point theory of solar flares*, Electromagnetic phenomena in cosmical physics (B. Lehnert, ed.), International Astronomical Union symposium, vol. 6, 1958, pp. 123–134.
- [45] ———, *The production of high energy particles in solar flares*, *Il Nuovo Cimento* **8** (1958), 188–196.

- [46] C. Thompson and R.C. Duncan, *The soft gamma repeaters as very strongly magnetised neutron stars = I. Radiative mechanism for outbursts*, Monthly Notices of the Royal Astronomical Society **275** (1995), 255–300.
- [47] E. F. Toro, *Riemann solvers and numerical methods for fluid dynamics*, 2 ed., Springer - Verlag, 1999.
- [48] G. Tóth, *The  $\nabla \cdot \mathbf{B} = 0$  constraint in shock-capturing magnetohydrodynamical codes*, Journal of Computational Physics **161** (2000), 605–652.
- [49] S. Tsuneta, *Structure and dynamics of magnetic reconnection in a solar flare*, The Astrophysical Journal **456** (1996), 840–+.
- [50] M. Ugai, *Global dynamics and rapid collapse of an isolated current-sheet system enclosed by free boundaries*, Physics of Fluids **29** (1986), 3659–3667.
- [51] D. A. Uzdensky, *Magnetic reconnection in astrophysical systems*, ArXiv Astrophysics e-prints (2006).
- [52] A. A. Vlasov, *On vibration properties of electron gas*, Soviet Physics-JETP **8** (1938), 444–470.
- [53] S. Zenitani, M. Hesse, and A. Kilmas, *Two-fluid magnetohydrodynamical simulations of relativistic magnetic reconnection*, The Astrophysical Journal **696** (2009), 1385–1401.